

MODELLING OF HYDROGEN ASSISTED STRESS CORROSION CRACKING

Submitted in partial fulfillment of the requirements

for the degree of

Doctor of Philosophy

of the

Indian Institute of Technology Bombay, India

and

Monash University, Australia

by

Nilesh Ramkrishna Raykar

Supervisors:

Professor S. K. Maiti

Department of Mechanical Engineering

Indian Institute of Technology Bombay, India

Professor Raman Singh

Department of Mechanical and Aerospace Engineering

Monash University, Australia



*The course of study for this award was developed jointly by
the Indian Institute of Technology Bombay and Monash University, Australia
and given academic recognition by each of them.*

The programme was administered by The IITB-Monash Research Academy.

(Year 2013)

Thesis Approval

This thesis entitled **Modelling of Hydrogen Assisted Stress Corrosion Cracking** by Nilesh R. Raykar is approved for the degree of Doctor of Philosophy.

Examiners



Supervisor(s)



Chairman



Date: 30/09/2013

Place: Mumbai

Declaration

I declare that this written submission represents my ideas in my own words and where others' ideas or words have been included, I have adequately cited and referenced the original sources. I also declare that I have adhered to all principles of academic honesty and integrity and have not misrepresented or fabricated or falsified any idea/data/fact/source in my submission. I understand that any violation of the above will be cause for disciplinary action by the Institute and can also evoke penal action from the sources which have thus not been properly cited or from whom proper permission has not been taken when needed.

Notice 1

Under the Copyright Act 1968, this thesis must be used only under the normal conditions of scholarly fair dealing. In particular no results or conclusions should be extracted from it, nor should it be copied or closely paraphrased in whole or in part without the written consent of the author. Proper written acknowledgement should be made for any assistance obtained from this thesis.

Notice 2

I certify that I have made all reasonable efforts to secure copyright permissions for third-party content included in this thesis and have not knowingly added copyright content to my work without the owner's permission.



Nilesh R. Raykar

IITB ID: 08410402

Monash ID: 22154787

September 2013

Abstract

Modelling of hydrogen assisted stress corrosion cracking (HASCC) within the framework of mechanics is very important for its control and avoidance. The main focus of this study is to develop suitable approach for modelling and analysis of stable crack growth through high strength steels under HASCC.

A new strategy based on combined analytical/numerical solution and finite element based cohesive zone model (CZM) has been developed. This has helped to couple analysis of hydrogen diffusion and crack growth during HASCC. The strategy has been applied to study crack growth in compact tension (CT) specimens. The solution to diffusion process is obtained through either an analytical or a numerical solution to the governing differential equation. The crack growth is analysed by CZM. For the analytical solution, both one- and two-dimensional approximations of the domain have been considered. The new CZM strategy, termed as hydrogen concentration dependent cohesive zone model (HCD-CZM), has been used for both CT and circumferentially notched tensile (CNT) round specimens.

The CNT specimen has been employed for the first time to obtain the fracture toughness data of high strength steel under internal and external supply of hydrogen. The experimental scheme involving CNT specimen under slow strain rate loading is demonstrated as a valid experimental procedure for study of HASCC for high strength steels. Both types of HASCC, internal hydrogen assisted cracking (IHAC) and hydrogen environment assisted cracking (HEAC), are found to induce a proportionate drop in fracture toughness under higher hydrogen concentration near the crack tip. The experimentally obtained lowest fracture toughness data compare favourably with lower range of published threshold values for the similar material. The experimental average crack growth rates too agree with the reported data for the material.

For CT specimens, both schemes of analysis of diffusion, excluding or including the effect

of hydrostatic stress and plastic strain, predict variation of crack opening displacement with crack growth with good accuracy. Diffusion solution based on one- and two-dimensional analyses do not significantly alter the prediction of crack growth. The effect of hydrostatic stress on the distribution of hydrogen concentration is observed to be significant as long as plastic strain is less than 5%. The study has given rise to an important correlation between hydrogen concentration dependent strength reduction and plastic strain rate. A new modelling technique is presented for the CNT specimen with eccentrically placed ligament using two-dimensional finite element approximations; this has considerably simplified analysis of the problem which otherwise would require a three-dimensional solution. For CNT specimens, the HCD-CZM approach employing both analytical and finite difference based diffusion solutions predicted the critical fracture toughness in agreement with experimental results. In this case too, the inclusion of hydrostatic stress in the diffusion analysis has been found to have not so significant influence on the prediction of experimental observations. The K -resistance curve obtained for the case is included. The proposed HCD-CZM has been found to satisfactorily handle variation in specimen geometry, material and source of hydrogen supply.

The thesis is divided into six chapters dealing sequentially with introduction, literature review, experiments with CNT specimen, analysis of CT specimens, modelling of CNT specimens and conclusions.

Keywords: Modelling of hydrogen assisted stress corrosion cracking (HASCC) of high strength steels; Hydrogen concentration dependent cohesive zone model for prediction of crack growth behaviour; Influence of hydrostatic stress and plastic strain on crack growth under HASCC; Circumferentially notched tensile (CNT) test for investigation into hydrogen assisted cracking.

Contents

Declaration	ii
Abstract	iii
Nomenclature	xiii
1 Introduction	1
1.1 Introduction and Motivation	1
1.2 Aims and Scope	4
1.3 Outline of the Thesis	5
2 Literature Review	6
2.1 Introduction	6
2.2 Environmentally Assisted Cracking (EAC) and Hydrogen Assisted Stress Corrosion Cracking (HASCC)	6
2.2.1 Hydrogen damage and HASCC	11
2.2.2 Typical failures due to HASCC	11
2.3 Features and mechanisms of HASCC	13
2.3.1 Types of HASCC	13
2.3.2 Influencing parameters	14
2.3.3 Mechanisms	16
2.4 Mitigation	17
2.5 Mechanistic Models of HASCC	19
2.5.1 Classical models	19
2.5.2 Crack growth studies based on fracture mechanics	24
2.5.3 Cohesive zone models	27

2.5.4	Overview of cohesive zone models	36
2.6	Experimental methods	37
2.6.1	Classical experiments	37
2.6.2	Fracture mechanics based tests	38
2.6.3	Tests with circumferentially notched tensile (CNT) specimen	45
2.6.4	Experimental studies for grade 4340 steel	47
2.7	Closure	47
3	Experimental Study	50
3.1	Introduction	50
3.2	Test procedure	50
3.2.1	Test specimen	51
3.2.2	Fatigue pre-cracking	53
3.2.3	Test arrangement	54
3.2.4	Test details	56
3.3	Determination of K_I	56
3.3.1	Computation of d and e_1	61
3.3.2	Validity requirements	63
3.4	Results and discussion	63
3.4.1	IHAC tests	64
3.4.2	Analysis of hydrogen distribution during IHAC tests	65
3.4.3	HEAC and combined IHAC-HEAC tests	67
3.4.4	Crack growth rate	70
3.4.5	Fractography	73
3.5	Closing remarks	75
4	Analysis of HASCC through CT specimen	76
4.1	Introduction	76
4.2	Scheme I for HASCC modelling	76
4.2.1	Specimen geometry and material	78
4.2.2	Analytical solution to diffusion equation	79

4.2.3	Finite element (FE) model	86
4.2.4	Comparison of predicted results with experimental data	89
4.3	Scheme II for HASCC modelling	95
4.3.1	Modifications in scheme I	96
4.3.2	Finite difference solution to the diffusion equation	98
4.3.3	Finite element (FE) based CZM	101
4.3.4	Implementation of HCD-CZM in ABAQUS®	101
4.3.5	Results and discussion	102
4.4	Closing remarks	107
5	Analysis of HASCC through CNT specimen	110
5.1	Introduction	110
5.2	HCD-CZM model for cylindrical geometry	110
5.2.1	Analysis of crack growth	111
5.2.2	Diffusion of hydrogen	112
5.3	Study of crack growth	113
5.3.1	Overview of scheme of analysis	113
5.3.2	Finite element based CZM for crack growth	113
5.3.3	Coupling of crack growth and diffusion analyses	117
5.3.4	Boundary and initial conditions for diffusion analysis	120
5.3.5	FDM based solution to diffusion equation	122
5.3.6	Analytical solution to diffusion equation	123
5.4	Results and discussion	125
5.5	Closing remarks	133
6	Conclusions	134
6.1	Introduction	134
6.2	Discussion	134
6.3	Conclusions	137
6.4	Contributions	139
6.5	Suggestions for future work	140

Appendix I	Commonly used HASCC test standards	141
Appendix II	Details of experimental arrangement	143
Appendix III	Sample USDFLD code for analysis of CT specimen	151
References		153
Publications by candidate		167
Acknowledgements		168

List of Tables

Table 2.1	Comparison of test techniques using CNT and traditional specimens. . . .	46
Table 3.1	Chemical composition of AS-4340 steel	52
Table 3.2	Experimental details.	58
Table 3.3	Calculated values of K_{Ic}^H and compliance with validity requirements. . . .	64
Table 3.4	Crack growth rate calculations.	72
Table 4.1	Values of strength reduction factor μ	93
Table 4.2	Comparison of experimental δ_5 with different theoretical predictions. . .	94
Table 4.3	Strength reduction factor μ obtained through scheme I and II.	102
Table 4.4	Comparison of hydrogen concentration C_{avg} and estimation of μ	108
Table 5.1	Experimental and predicted K_{Ic}^H in MPa.m ^{1/2}	131

List of Figures

Fig. 2.1	Interrelationship between types of EAC	8
Fig. 2.2	Illustration of simple electrochemical cell.	9
Fig. 2.3	HASCC failure of steel bolts.	9
Fig. 2.4	Schematic diagram of film rupture or slip dissolution model.	10
Fig. 2.5	SCC in stainless steel used for food processing vessel.	10
Fig. 2.6	Hydrogen related failure of components	13
Fig. 2.7	Variation of crack growth rate da/dt against stress intensity factor K	15
Fig. 2.8	Schematic representation of HELP and HEDE mechanisms.	17
Fig. 2.9	Processes occurring during HASCC	20
Fig. 2.10	Model of HASCC using fictive tensile specimens.	22
Fig. 2.11	Notch specimen geometry for u-notched round bar.	22
Fig. 2.12	Subdivision of hydrogen supply in hydrogen partitioning model.	23
Fig. 2.13	Modelling of tendon wire with thumbnail shaped crack.	25
Fig. 2.14	Multi-physics events in hydrogen induced cracking.	26
Fig. 2.15	Illustration of cohesive zone model.	28
Fig. 2.16	Measurement of CTOD δ_5 for CT specimen.	30
Fig. 2.17	Experiments on duplex stainless steel in hydrogen environment.	31
Fig. 2.18	Finite element model for disk pressure test.	31
Fig. 2.19	Model for HASCC of CT specimen.	32
Fig. 2.20	Void cell based model.	33
Fig. 2.21	Quantum-mechanically informed model.	34
Fig. 2.22	Crack surface evolution using multi-scale model.	35
Fig. 2.23	TSL for fatigue loading under hydrogen environment.	36
Fig. 2.24	Disk pressure test cell.	38

Fig. 2.25	Notched C-ring specimen with loading bolt.	39
Fig. 2.26	Types of test specimens for fracture mechanics based tests.	40
Fig. 2.27	Test specimen types in ASTM E1681.	41
Fig. 2.28	Double beam specimen in ASTM G168.	42
Fig. 2.29	Example of SSRT test machine.	43
Fig. 2.30	Schematic of step loading profile for high strength steels.	44
Fig. 2.31	Dimensions of a typical CNT specimen.	45
Fig. 3.1	Experimental set-up.	51
Fig. 3.2	Dimensions of CNT specimen (in mm).	52
Fig. 3.3	Experimental engineering stress-strain curve for AS-4340 material.	52
Fig. 3.4	Schematic of rotating bending machine used for fatigue pre-cracking.	53
Fig. 3.5	Details of experimental arrangement.	55
Fig. 3.6	Electrical connection diagram.	57
Fig. 3.7	Eccentricity of fatigue pre-crack profile.	59
Fig. 3.8	Geometry of CNT specimen.	60
Fig. 3.9	Profile projector used to measure crack size	62
Fig. 3.10	Geometric analysis of pre-crack profile.	62
Fig. 3.11	K_{Ic}^H vs. hydrogen pre-charging span results for IHAC.	66
Fig. 3.12	Finite element mesh and boundary conditions.	66
Fig. 3.13	Normalised hydrogen concentration distribution.	67
Fig. 3.14	Plots of $(1 - C_{avg})$ and K_{Ic}^H with hydrogen pre-charging time.	68
Fig. 3.15	K_{Ic}^H vs. cross-head speed for HEAC.	69
Fig. 3.16	K_{Ic}^H vs. cross-head speed for combined IHAC and HEAC.	69
Fig. 3.17	Typical load vs elongation variation (specimen S15).	70
Fig. 3.18	Typical load vs time variation (specimen S15).	71
Fig. 3.19	Plot of crack growth rate vs. loading speed.	72
Fig. 3.20	SEM fractographs of CNT specimen.	74
Fig. 4.1	Stress-strain curves for FeE690T.	79
Fig. 4.2	Polynomial representing initial conditions to diffusion equation.	81

Fig. 4.3	Solution domain and boundary conditions for diffusion equation.	82
Fig. 4.4	Concentration at crack tip with $C=1$ at outer boundaries.	83
Fig. 4.5	Concentration contours with $C=1$ at outer boundaries, $t = 440$ h	84
Fig. 4.6	Finite element discretisation for CT specimen.	87
Fig. 4.7	Effect of mesh size on results.	88
Fig. 4.8	Concentration dependent TSL and effect of strength reduction factor μ . . .	88
Fig. 4.9	Comparison of results, for $D_{eff} = 2.5 \times 10^{-6}$ mm ² /s and constant μ	89
Fig. 4.10	Experimental D_{eff} vs ϵ_p data.	90
Fig. 4.11	Plastic strain ahead of crack tip.	91
Fig. 4.12	Comparison of results, $D_{eff} = 2.0 \times 10^{-5}$ mm ² /s and variable μ	91
Fig. 4.13	Comparison of results, $D_{eff} = 5.5 \times 10^{-6}$ mm ² /s and variable μ	92
Fig. 4.14	Variation of μ with $\dot{\epsilon}_p$	93
Fig. 4.15	Predicted values of normalised hydrogen concentrations in crack ligament. .	94
Fig. 4.16	Experimental data of N_T vs. ϵ_p	97
Fig. 4.17	Finite difference scheme used in HCD-CZM.	99
Fig. 4.18	Flow-chart of subroutine USDFLD.	103
Fig. 4.19	Comparison of results with and without stress-strain effect.	104
Fig. 4.20	Variation of C_L , C_T , σ_h and ϵ_p near crack tip, rate of loading = 0.001 mm/h. .	104
Fig. 4.21	Variation of C_L , C_T , σ_h and ϵ_p near crack tip, rate of loading = 0.01 mm/h. .	105
Fig. 4.22	Variation of C_L , C_T , σ_h and ϵ_p near crack tip, rate of loading = 0.1 mm/h. .	105
Fig. 4.23	Comparison of C with and without σ_h effect for loading rate of 0.001 mm/h. .	106
Fig. 4.24	Comparison of C with and without σ_h effect for loading rate of 0.01 mm/h. .	106
Fig. 4.25	Comparison of C with and without σ_h effect for loading rate of 0.1 mm/h. .	107
Fig. 5.1	Triangular TSL used in analysis.	111
Fig. 5.2	Eccentric crack edge profile in CNT specimen.	114
Fig. 5.3	Geometry for 2D analysis of CNT specimen.	115
Fig. 5.4	Finite element discretisation for CNT specimen.	116
Fig. 5.5	Approximation for thickness of elements in 2D FE analysis.	118
Fig. 5.6	Hydrogen distribution and element arrangement on bending plane.	119
Fig. 5.7	Boundary and initial conditions for axisymmetric diffusion analysis.	120

Fig. 5.8	Typical hydrogen concentration and σ_h distributions during IHAC test. . .	127
Fig. 5.9	Typical hydrogen concentration and σ_h distributions during HEAC test. . .	127
Fig. 5.10	Predicted K_{Ic}^H for IHAC using FDM and analytical approaches.	128
Fig. 5.11	Predicted K_{Ic}^H for HEAC using FDM and analytical approaches.	129
Fig. 5.12	Predicted K_{Ic}^H for IHAC+HEAC using FDM and analytical approaches. . .	130
Fig. 5.13	Typical K -resistance curves obtained through FE analysis.	132
Fig. II.1	CNT specimen.	144
Fig. II.2	Environmental cell.	145
Fig. II.3	Measurement arm.	146
Fig. II.4	Miscellaneous items.	147
Fig. II.5	LVDT clamps.	148
Fig. II.6	Locator piece.	149
Fig. II.7	Procedure for setting up the experiment.	150

Nomenclature

Arabic letters

a	crack length
a_0	initial crack length
$da/dt, \frac{da}{dt}$	crack growth rate
Δa	crack growth
\bar{a}	corrected crack size
a_{f_i}	depth of fatigue pre-crack for i^{th} point
a_{m_i}	depth of machined notch for i^{th} point
a_1, a_2, \dots	coefficient of polynomial for 2D diffusion analysis for CT specimen
$\Delta a_r, \Delta a_l$	crack growth in CNT specimen
b_0, b_1, \dots	coefficients of polynomial for 1D diffusion analysis for CT specimen
d	ligament diameter
e_1	eccentricity of ligament
l_{cz}	cohesive zone size
p_0, p_1, \dots	coefficients of polynomial fitting hydrogen distribution in CNT specimen
r	radial distance/coordinate
r_y	Irwin correction factor
t	time
Δt_f	span of time taken for total failure after attaining maximum load
v_{pl}	plastic component of crack mouth opening displacement
w_1, w_2	thickness of finite elements in CNT specimens
Δx	distance between finite difference grid points

z	distance between load-line and measuring position for crack mouth opening displacement
A_{pc}	area bounded by pre-crack profile
A_{wi}	area of i^{th} radial sector of ligament
$B_{m,n}^i$	Fourier coefficients for 2D diffusion analysis
C, C_H	concentration of hydrogen
C_{abs}	absolute hydrogen concentration inside material
C_{avg}	average hydrogen concentration over a span ahead of crack tip
C_{avg}^a, C_{avg}^b	average hydrogen concentration over a span ahead of crack tip with and without hydrostatic stress effect
C_{env}	environmental concentration of hydrogen
C_L	concentration of hydrogen in lattice
C_{L0}	concentration of hydrogen in environment
C_T	concentration of hydrogen in reversible trap sites
C_{T0}	equilibrium concentration in traps corresponding to C_{L0}
C_{tot}	total hydrogen concentration in material
$(C_{tot})_{env}$	total hydrogen concentration in environment
D	outside diameter of CNT specimen
D_{eff}	effective diffusivity
D_H	damage factor due to hydrogen
D_L	stress and concentration independent lattice diffusivity
D_m	damage variable for fatigue crack propagation
E	modulus of elasticity
E_m^i	Fourier coefficients for 1D diffusion analysis
F_0, F	geometric factors for CNT specimen
H	height of domain for CT specimen study
H_0, H_1	Struve functions

J_0, J_1	Bessel functions of the first kind of order zero and one
\mathbf{J}_H	flux of hydrogen concentration
K	stress intensity factor
dK/dt	rate of loading in terms of stress intensity factor
K_I	mode I stress intensity factor
K_{Ic}	fracture toughness
K_{Ic}^H	fracture toughness under hydrogen environment
K_R	fracture resistance
K_{TH}	threshold stress intensity factor
K_{tr}	trap equilibrium constant
L, L_1	length of domain for diffusion calculation
M	model constant to calculate cohesive zone size
M_{xi}, M_{yi}	area moment of i^{th} ligament sector about X and Y axes
N_L	number of solvent lattice atoms per unit volume
N_T	number of traps per unit volume
P	axial load
P_{FFS}	fast fracture strength during incremental step loading test
P_{max}	maximum axial load taken by CNT specimen
P_{th-n}	threshold load during n^{th} step of incremental step loading test
R	universal gas constant
R_1	radius of crack tip in CNT specimen
T	cohesive strength
T_0	maximum cohesive strength
T_a	absolute temperature
V_H	partial molar volume of hydrogen in metal
W	width of specimen
\bar{X}, \bar{Y}	coordinates of centroid of ligament area

Greek letters

α	factor employed in SIF calculation for CNT specimen
$\alpha_1, \beta_1, \gamma_1, \zeta_1, \eta_1$	factors of finite difference solution to diffusion equation
$\alpha_k, \alpha_{k_1}, \alpha_{k_i}$	positive roots of Bessel functions
α_{tr}	number of hydrogen atom sites per trap
β	number of NILS per solvent atom
δ_0	critical separation
δ_1, δ_2	parameters of trapezoidal traction separation law
δ_5	modified crack tip opening displacement
δ_{COD}	critical crack opening displacement
δ_g	elongation of specimen over gauge length
$\Delta\delta_{pre}$	displacement amplitude of loading cycle
$\dot{\epsilon}$	strain rate
ϵ_p	plastic strain
$\dot{\epsilon}_p$	plastic strain rate
$\lambda_{m,n}$	factor in 2D diffusion analysis
μ	cohesive strength reduction factor
μ^a, μ^b	cohesive strength reduction factors with and without hydrostatic stress effect
ν	Poisson's ratio
σ_b	bending stress
σ_h	hydrostatic stress
σ_N	average axial stress across ligament
σ_t	tensile stress
σ_Y	tensile yield strength
θ_i	angular location of centroid of i^{th} ligament sector
Γ_0	cohesive energy

$(\Gamma)_{Ic}$	critical cohesive energy
$(\Gamma)_{TH}$	threshold cohesive energy

Abbreviations

AIDE	adsorption induced dislocation emission
CCT	center cracked tension
CF	corrosion fatigue
CNT	circumferentially notched tensile (specimen)
CT	compact tensile (specimen)
CTOD	crack tip opening displacement
CVN	Charpy v-notch
CZM	cohesive zone model
DCB	double cantilever beam
EAC	environmentally assisted cracking
FD	finite difference
FDM	finite difference method
FEM	finite element method
FPZ	fracture process zone
GDP	gross domestic product
HAC	hydrogen assisted cracking
HASCC	hydrogen assisted stress corrosion cracking
HAZ	heat affected zone
HCD-CZM	hydrogen concentration dependent cohesive zone model
HEAC	hydrogen environment assisted cracking
HEDE	hydrogen enhanced decohesion
HE	hydrogen embrittlement
HELP	hydrogen enhanced localised plasticity
HIC	hydrogen induced cracking

HSC	hydrogen stress cracking
IHAC	internal hydrogen assisted cracking
LME	liquid metal embrittlement
LVDT	linear variable differential transducer
NILS	normal interstitial lattice site
SCC	stress corrosion cracking
SEM	scanning electron microscope
SENT	single edge notched tension (specimen)
SSC	sulphide stress cracking
SSRT	slow strain rate tension
TSL	traction separation law
WOL	wedge opening loading (specimen)
X-FEM	extended FEM

Chapter 1

Introduction

1.1 Introduction and Motivation

Corrosion leads to enormous loss of property and lives annually. The loss may account up to 5% of the GDP in some countries (Koch et al., 2002; Bhaskaran et al., 2003). Because of this enormity of loss, the corrosion has attracted attention for study from the early stage of industrialisation (Fontana, 2005; Shipilov, 2007). The initial phase of studies was dominated by experimentation, proof testing and development of application-specific mitigation strategies. Some of the measures that have developed through such efforts include development of purpose built materials, tailor-making manufacturing processes, protective coating, inhibitors, changes in component design, etc. (Staehle, 2000; Turnbull, 2000; Freeman, 2003; Gangloff, 2003; Gangloff, 2006; Louthan, 2008; Cwiek, 2010; Pidaparti and Patel, 2011).

Corrosion in the presence of stresses in materials leads to an increase in severity and sudden failure by cracking. This is a matter of great concern. The discipline of environmentally assisted cracking (EAC) concerns understanding, prevention and control of such cracking (Parkins, 1975; Ford, 1996; Kane, 2000; Rhodes, 2001; Craig, 2003*b*). The cracking under the combined action of hydrogen, corrosion and stress, i.e., hydrogen assisted stress corrosion cracking (HASCC), needs careful handling due to its safety and reliability implications. Hydrogen related corrosion damages constitute a considerable part of the total corrosion damages. This has made HASCC an important issue in its own right. The gradual emergence of hydrogen as a source of clean energy (Hudson et al., 2009) has added further interest in the study

of HASCC. It has become very difficult to eliminate HASCC completely because hydrogen, due to its small size and great mobility, finds its way into the material during manufacturing, and/or service (Woodtli and Kieselbach, 2000; Cwiek, 2010; Wanhill et al., 2011; Shirband et al., 2011). The present study is concerned with HASCC.

The HASCC involves chemical, mechanical and metallurgical processes (Gangloff, 2003). The chemical process controls release of damaging elements, like hydrogen in the case of HASCC, from the medium, its ingress into the material of a component and further transport inside the material. The process is influenced by the concentration of the element in the medium, and its temperature, motion, pressure, etc. The transport of corrosive element inside the material is influenced by the material's mechanical properties, stress-strain state, and geometry. Metallurgical factors like composition of materials, grain structures, heat treatments, and coatings, if any, too influence the process.

For a component with a crack, the HASCC gets significantly dominated by the physical and mechanical state of material around the crack tip (Lynch, 2007; Gangloff, 2009). The elements of mechanical environment consist of levels of stresses and weakening of the material, if any, near the crack tip. The higher levels of stresses result in higher transport of hydrogen towards the tip. This, in turn, facilitates weakening of material's cohesive strength.

Although experimental approach is very important for the study of EAC, it is very expensive as well as time consuming. It becomes uneconomic to try to obtain solution for each and every practical situation. This has motivated development of mechanics based models, which can include different process parameters and help to assess their influence on HASCC. The models are also useful for prediction of crack growth even under new situations and can help to reduce the number of experiments (Scheider et al., 2008; Olden et al., 2008). The models are built by capturing the underlying chemical and mechanical activities. The fracture criterion for crack growth can be defined in terms of fracture toughness K_c or its equivalent, such as, critical crack tip opening displacement δ_c , critical J-integral J_c (Bhowmik et al., 2013), J-integral based on stretch zone width ahead of crack tip J_{SZWc} (Saxena et al., 2010), critical fracture energy based on cohesive zone model (CZM) (Cornec et al., 2003; Banerjee and Manivasagam, 2009), etc. Though CZM can accommodate a lot of parameters related to process and specimen or component geometry, this approach has not been fully exploited. This has provided some motivation

for the present study.

The stress field in a component affects the diffusion of hydrogen through hydrostatic component of the local stress tensor, the plastic strain distribution and the imposed strain rate (Krom et al., 1999; Taha and Sofronis, 2001). Further, any non-uniform concentration distribution of hydrogen leads to varying degree of degradation of material's strength. Thus the underlying actions are very intertwined and any uncoupled analysis becomes insufficient for modelling of the situation.

The governing equations involve a large number of material and process related parameters. It is rarely possible to have values of full set of data for any given situation. In most modelling approaches only two issues, diffusion of hydrogen towards the crack tip and accelerated crack growth due to hydrogen embrittlement of material, are accommodated.

Some meaningful solutions have been obtained by ignoring the full coupling between stress-strain field and diffusion process (Olden et al., 2008; Scheider et al., 2008; Toribio et al., 2011). This simplification leads to governing equations, which can be easily tackled analytically. Thereby the solution time for the HASCC problems can be reduced. No attempts have been so far made to exploit this possibility. Particularly, strategies combining analytical or finite difference solutions for the diffusion and crack growth study through finite element method have not been examined. This opens up possibilities of fresh investigations.

According to the current state of the art, many investigators (Serebrinsky et al., 2004; Scheider et al., 2008; Olden et al., 2009) have attempted to understand the HASCC considering laboratory scale experiments involving compact tension (CT) or other standard specimens and simultaneous modelling of crack growth. Thereby influence of a number of parameters have been evaluated, others, e.g. plastic strain rate, concentration dependent degradation, etc., are yet to be examined. This issue too has motivated the present study.

Fracture testing under HASCC has been mostly done to evaluate threshold fracture toughness K_{TH} and collect crack growth rate data under varying environmental conditions (Gangloff, 2003). In general, determination of K_{TH} involves long duration tests. Development of any strategy that can help to reduce the duration of test is highly welcome. Such an issue requires exploration.

Of late, circumferentially notched tensile (CNT) specimens have been shown to offer promise

for a simple and inexpensive approach for generating fracture toughness data under corrosive environments (R.K. Singh Raman et al., 2006; Rihan et al., 2006). Whether it is possible to collect HASCC data using such specimens is worth investigating.

The HASCC testing with CNT specimens involves diffusion of hydrogen and crack propagation. Both occur in three dimensions. Whether the diffusion and crack extension through such geometry can be modelled is another problem open for investigations. Such an exercise involves three stages of investigation for any material-environment combination. In the first stage, experiments have to be done with suitable specimen geometry to collect data related to load-deflection, or load-crack growth, or crack opening displacement-crack growth, etc. In the second stage, some of the test cases have to be utilised to settle a set of process parameters, e.g., diffusivity, cohesive strength, critical crack opening displacement, concentration dependent cohesive strength reduction/degradation factor, etc. In the third stage, the modelling is employed to predict data for the remaining situations.

1.2 Aims and Scope

Keeping in view of the issues discussed, the objectives of present study have been set as follows.

- (a) To develop an improved and more effective mechanistic model for predicting crack growth in high strength steels under HASCC using cohesive zone modelling combined with analytical and numerical techniques for diffusion analysis.
- (b) To explore feasibility of employing circumferentially notched tensile (CNT) specimens to determine fracture toughness and generate crack growth data for high strength steel, e.g., AISI 4340 steel, under HASCC conditions.
- (c) To investigate influence of hydrostatic stress, equivalent plastic strain and plastic strain rate on crack growth under HASCC using the model.
- (d) To examine the possibility of implementing a single modelling approach to predict HASCC for different grades of steel and geometric shapes.
- (e) To demonstrate accuracy as well as suitability of the new mechanistic model based on the experimental data.

Theoretical and experimental studies have been carried out to examine mode I stable crack growth under HASCC at room temperature under quasi-static loading. Two grades of steels with different yield strengths have been examined and crack growth in rectangular and cylindrical specimens have been studied. Effects of two modes of supply of hydrogen, either from within material or from outside environment, have been investigated. The modelling approach focuses on two dominant processes involved in HASCC, diffusion of hydrogen through material and crack growth promoted by the diffused hydrogen. Other processes, such as, hydrogen generation reactions in environment, transport of hydrogen through environment, surface adsorption of hydrogen have been neglected.

1.3 Outline of the Thesis

The thesis is divided into six chapters. Chapter 1 gives introduction, motivation, aims and scope of the present study. A review of relevant literature leading to problem identification is presented in Chapter 2. Chapter 3 describes the experimental work performed using CNT specimen to obtain fracture data for a high strength steel under different conditions of HASCC. Such data are later used for refinement and validation of the proposed model. Chapter 4 deals with development of a new modelling strategy for analysis of hydrogen assisted cracking in a compact tension specimen. The effects of parameters influencing HASCC, i.e., hydrostatic stress, equivalent plastic strain and plastic strain rate, have been examined. The model has been verified through the experimental data using CNT specimens of a different grade of steel, which is reported in Chapter 5. The influence of hydrostatic stresses on the crack growth has been also examined in this chapter. Chapter 6 presents a discussion of the results, main conclusions, main contributions of the study, as well as suggestions for further studies.

Chapter 2

Literature Review

2.1 Introduction

This chapter examines the important approaches for modelling crack growth under hydrogen environment and experimental investigations into the similar problems. This has been done with a view to emphasise the importance of the present study.

2.2 Environmentally Assisted Cracking (EAC) and Hydrogen Assisted Stress Corrosion Cracking (HASCC)

Environmentally assisted cracking (EAC) deals with failures due to different types of environments including hydrogen. Williams et al. (1977) define “environmentally assisted cracking” (EAC) as a case of initiation and growth of cracks under simultaneous action of applied stress (static or cyclic, including residual stress as well) and corrosive environment. Scientific interest in EAC dates back to late 1800s, driven by recurring events of season cracking of brass cartridges and explosions of riveted boiler shells from caustic embrittlement. During this period, the prominent role of hydrogen amongst other damaging environments was identified. In 1874, probably the first published case of EAC was recorded (Shipilov, 2007) covering an experimental study by Johnson (1874). It demonstrated the detrimental effects of acid and hydrogen on ductility of iron wire. In the same year, Osborne Reynold explained the case on the basis of

role played by hydrogen in the damage. Despite such an early start and the subsequent extensive research, the work on EAC and hydrogen damage is ongoing. The comprehensive solution keeps eluding mostly due to involvement of large number of complex damage processes and also because of steady evolution of new material-environment combinations.

Four major types of EAC are recognised (Anderson, 2002; Lynch, 2003). The first type, “Hydrogen Embrittlement (HE)” is characterised by loss of bond strength of metal due to presence of atomic hydrogen inside material micro-structure; stresses may or may not be present. The second type is “Stress Corrosion Cracking (SCC)” and refers to crack growth under tensile and/or shear stresses, driven by physical removal of material through chemical dissolution at the crack tip. “Corrosion Fatigue (CF)” is the third type where fatigue crack growth is accelerated by chemical environment. The fourth type of EAC is “Liquid Metal Embrittlement (LME)”. In LME electrochemical reaction is not involved unlike the prior three situations. The liquid metal penetrating through the grain boundaries of solid metal causes the crack growth which can be very rapid. HE, SCC and LME occur under non-cyclic loading and differ in terms of the nature of environment involved; CF includes effects of cyclic loading and may include any type of environment. Amongst the four types, the frequency of failures is recorded highest for SCC, followed by CF, HE and LME respectively (Lynch, 2003). LME involves distinctly separate processes than the other three and it is not covered in this review.

HE, SCC and CF are not mutually exclusive; they do overlap, in which case, the amount of damage is multiplied. Stansbury and Buchanan (2000) have illustrated the interrelationship between SCC, HE and CF using a Venn diagram (Ford, 1982) as shown in Fig. 2.1. As can be seen from the diagram, it is possible to have concurrent presence of two or even three forms of EAC. Hydrogen assisted stress corrosion cracking (HASCC) involves presence of both HE and SCC.

Corrosion is a vital process through which environment interact with metals during both HASCC and SCC. Corrosion can be aqueous or dry and it can be classified into eight forms based on appearance of corroded metal (Fontana, 2005); SCC and HE are the two of these eight forms. All aqueous corrosion processes involve electrochemical reactions. The reaction takes place as a result of development of simple electrochemical cells at numerous locations on the surface exposed to corrosion. A typical cell consists of anode and cathode which are electrically

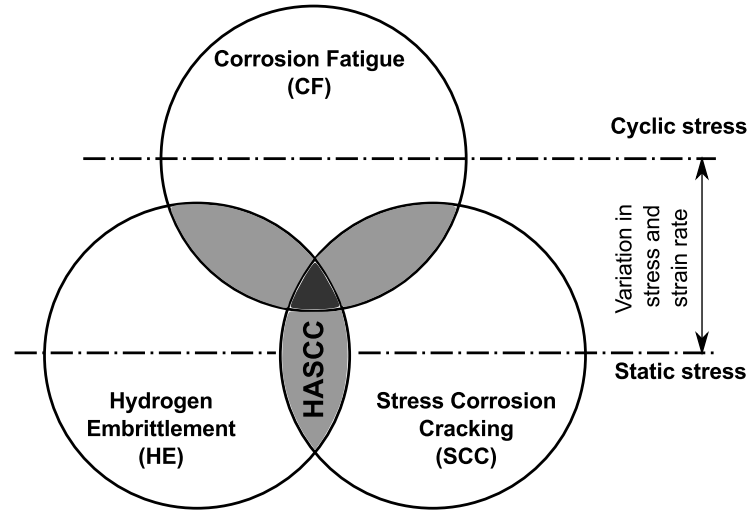
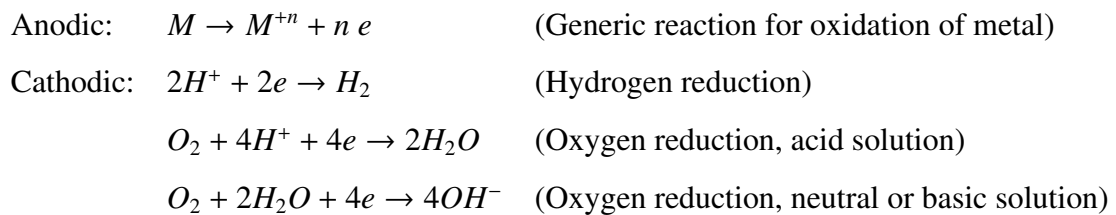


Fig. 2.1 Interrelationship between three main types of EAC (adapted from Ford, 1982)

connected to one another and are immersed in conductive medium called electrolyte (Fig. 2.2). Metal atoms from anode give up electrons and get released into the electrolyte as ions. The electrons flow to the cathode. The electrochemical cell involves two reactions, oxidation and reduction. An oxidation or anodic reaction involves release of electrons; on the contrary, the reduction or cathodic reaction involves consumption of electrons. As a result, anode corrodes. Both anodic and cathodic reactions always proceed at the same rate. Typical examples of these reactions are given below:



HASCC and SCC mainly differ in terms of the type of corrosion reaction which drives crack growth. Cathodic reaction influences crack growth during HASCC as opposed to SCC where anodic reaction is the driver (Jones, 2003). The most common cathodic reaction is reduction of H^+ into hydrogen H_2 . During HASCC, this reaction generates atomic hydrogen which subsequently embrittles material around the crack tip and promotes accelerated crack growth. This process is explained further in section 2.3.3 of this chapter. Fig. 2.3 shows typical view of cracking developed due to HASCC in steel bolts subjected to acidic chlorides and polymer solution environment.

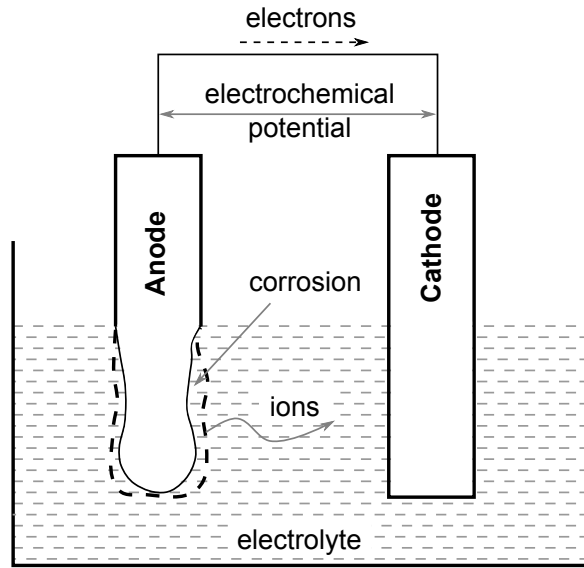


Fig. 2.2 Illustration of simple electrochemical cell (Anderson, 2002).

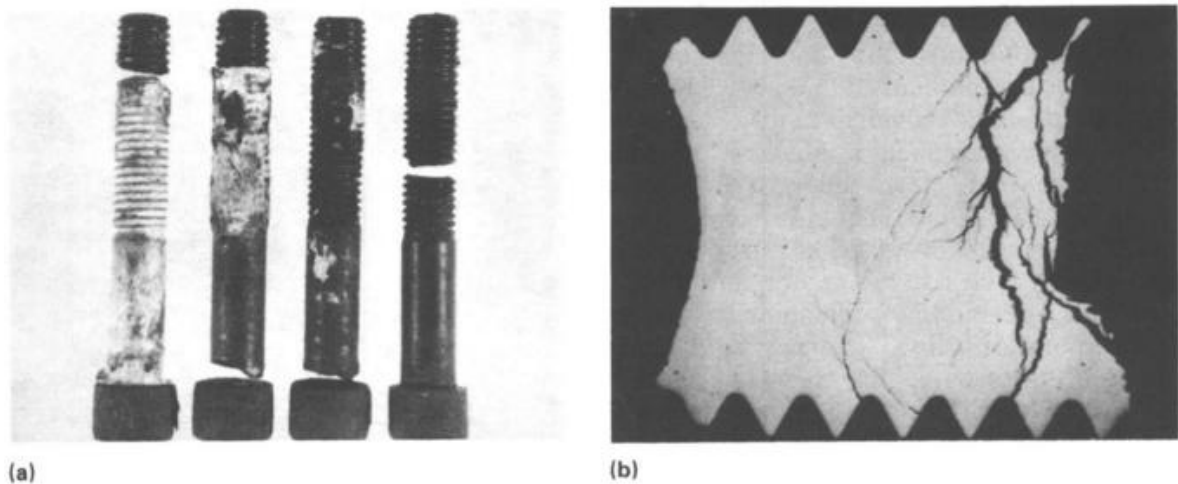


Fig. 2.3 HASCC failure of steel bolts. (a) Overall view (b) Longitudinal section through one of the bolts (Akstens et al., 1990).

During SCC, anodic dissolution of metal at the crack tip promotes crack growth. Passivity of metal plays an important role in SCC. Passivity refers to the loss of chemical reactivity by metals under particular environmental conditions. This effect mostly owes to the formation of an extremely thin passive film on metal surface. Film rupture or slip-dissolution mechanism (Ford, 1982; Newman, 1995; Magnin, 1995; Jones, 2003) is one of the most common mechanisms used to explain SCC. This mechanism assumes that external stress causes rupture of the passive film at the crack tip through evolution of a slip step, thereby exposing bare metal to corrosive

media. The crack growth occurs through anodic dissolution of metal until the exposed surface is repassivated. Crack growth progresses by cyclic process of film rupture, dissolution and film repair (Fig. 2.4). Typical failure due to SCC of a stainless steel food industry process vessel is shown in Fig. 2.5.

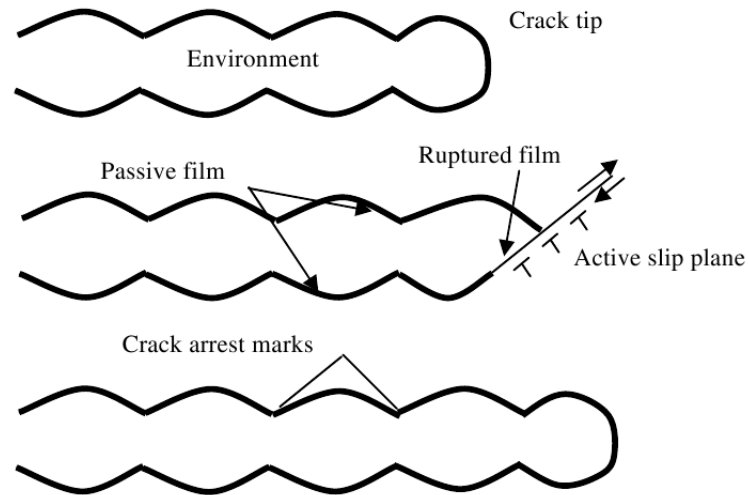


Fig. 2.4 Schematic diagram of film rupture or slip dissolution model (Anderson, 2002).



Fig. 2.5 SCC in stainless steel used for food processing vessel (Elliott, 2003).

Although HASCC may have features of both HE and SCC, the crack growth is dominated by hydrogen driven mechanism (Gangloff, 2003). In general, the models of HASCC do not include SCC processes such as film rupture/repair.

2.2.1 Hydrogen damage and HASCC

Damages to metals due to hydrogen are of multiple types. Several ways are proposed to categorise them (Oriani et al., 1985; Craig, 2003a; Fontana, 2005; Cwiek, 2010; Wanhill et al., 2011). The types suggested by Craig (2003a) are: hydrogen embrittlement (HE), hydrogen attack, blistering, shatter-cracks, fish-eyes, micro-perforations and hydride formation. The main difference between HE and others is in terms of the state of hydrogen; hydrogen remains in atomic state during HE whereas in others it transforms into molecular forms. Although the damaging effects of hydrogen on metal are widespread and dreaded, a few positive effects of hydrogen include improved microstructure, mechanical properties and formability of metals (Eliaz et al., 2000).

Different terminologies are used in the literature to denote HE which can be sometimes confusing. These terminologies are either synonymous to HE or refers to a specific sub-category. Hydrogen assisted cracking (HAC), hydrogen induced cracking (HIC) are synonymous to HE. Sulphide stress cracking (SSC) indicates cracking of steels in hydrogen sulphide environment. Hydrogen stress cracking (HSC) describes HE in the presence of stress. Hydrogen assisted stress corrosion cracking (HASCC) indicates simultaneous presence of hydrogen, corrosive medium and stress. The HASCC is of main interest here and it includes HSC as well.

2.2.2 Typical failures due to HASCC

The failures under HASCC are usually catastrophic; crack growth is rapid and almost undetectable. Failures due to the combined effect of hydrogen, corrosion and stress occur in many industries and applications. These constitute a significant portion of general corrosion-assisted failures in industries. For example, around one-fourth of the failures in petroleum refining industry are associated with the influence of hydrogen (Shirband et al., 2011). Typical failures arising out of HASCC are presented in the following.

Aviation: Cracking of aircraft propeller retaining bolts originating from incorrect cadmium plating process (Fig. 2.6a) is discussed by Lynch (2003); a similar case for steel nuts in aircraft wing structure is covered by Freeman (2003); case histories of failure of various aircraft components have been analysed in detail by Wanhill et al. (2011).

Marine: Failure of sub-sea duplex stainless steel manifold is discussed by Wintle and Pargeter (2005); hydrogen induced premature failure of a 17 tons cast steel anchor fluke (Fig. 2.6b) is investigated by Hassan (2010); a study conducted to evaluate effect of hydrogen permeation on the failure of steels in seawater and marine mud is presented by Benson and Edyvean (1998).

Power: Failure of different steel components in a power plant are presented by Dayal and Parvathavarthini (2003); a case of failure of riser water wall tube (Fig. 2.6c) due to hydrogen is discussed by Ahmad and Purbolaksono (2010).

Petrochemical: Investigation of an explosion of tower vessel in a refinery (Fig. 2.6d), which originated from a hydrogen induced crack in a weld-joint, is discussed by Wintle and Pargeter (2005); problems encountered in petrochemical plants such as ammonia and methanol are presented by Prescott and Shannon (2001) and Kain et al. (2007); hydrogen assisted cracking of steam drum used in refinery and petrochemical industry is analysed by Sujata et al. (2009); and failure of a stationary oil storage tank is discussed by Kim et al. (2009).

Nuclear power: Failure of zirconium alloy clad tubes used for providing an air-tight enclosure to radioactive fuel under different conditions in nuclear industry have been reported by Alam et al. (2011); analysis of a severe accident of pressurised water reactor involving hydrogen damage has been presented by Prior et al. (1991).

Miscellaneous: Failure of storage tank for compressed hydrogen under fatigue loading is described by Woodtli and Kieselbach (2000); and cracking in an underground low carbon steel pipeline under pressure due to hydrogen evolved during corrosion reaction is described by May and Bagnall (2007).

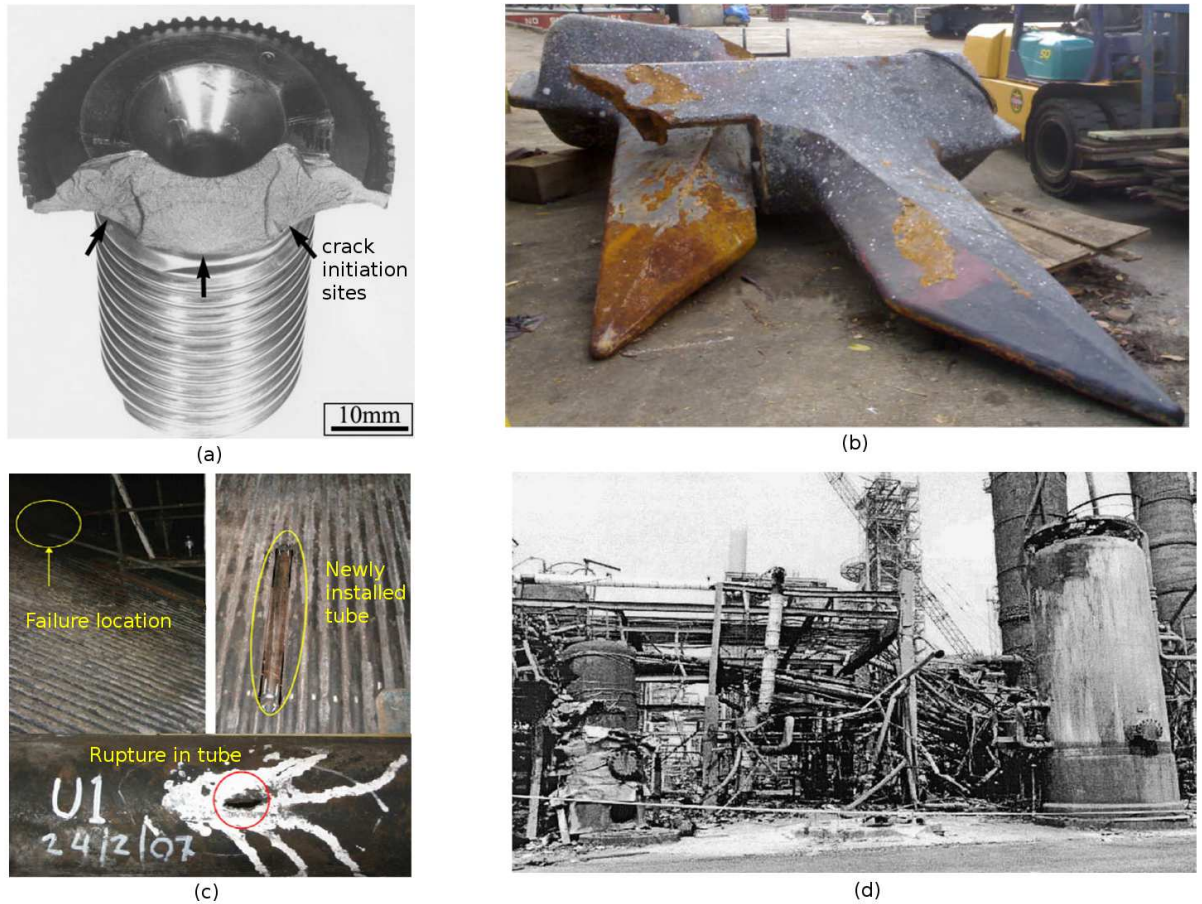


Fig. 2.6 Hydrogen related failure of components: (a) aircraft propeller retaining bolt (Lynch, 2003); (b) a 17 tons cast steel anchor fluke (Hassan, 2010); (c) riser water wall tube (Ahmad and Purbolaksono, 2010); (d) tower vessel explosion in refinery (Wintle and Pargeter, 2005).

2.3 Features and mechanisms of HASCC

HASCC is very complex. It is influenced by a large number of parameters and underlying processes.

2.3.1 Types of HASCC

The source of hydrogen during HASCC can be either inside the material or outside environment. Accordingly, two types of HASCC are defined: internal hydrogen assisted cracking (IHAC) and hydrogen environment assisted cracking (HEAC). In IHAC, the hydrogen is available from within the material. The hydrogen may build up in the metal during manufacturing

processes (welding, casting, heat treatment, electro-plating) or through previous exposures (hydrogen from process gas, corrosion attack). In HEAC, the hydrogen enters from the outside environment (gaseous hydrogen, corrosion reaction, cathodic protection) under the action of loading. Both IHAC and HEAC can occur simultaneously in some situations. In either case, the primary damage due to hydrogen during HASCC is localised in a region just ahead of the crack tip, termed as fracture process zone (FPZ). From the point of view of modelling, HEAC differs from IHAC in the mode of hydrogen transport. In HEAC, crack geometry, solute chemistry and electrochemical reaction determine the transport of hydrogen from environment up to the crack tip. Subsequent hydrogen transport within the material up to the FPZ is identical for both IHAC and HEAC and is governed by material micro-structure and stress field.

2.3.2 Influencing parameters

The parameters influencing crack growth under HASCC can be categorised as mechanical, metallurgical and chemical. Amongst mechanical parameters, stress intensity factor (K) has a significant effect on crack growth rate da/dt . For every material-environment combination, there exists a threshold stress intensity factor K_{TH} below which da/dt is practically zero. The typical variation of da/dt against K shows three distinct regions (Fig. 2.7): first, for K 's just above K_{TH} , the crack growth rate da/dt increases with K (stage I); second, for intermediate K 's, da/dt is either constant or rises slowly with K (stage II), and third, for high K 's, da/dt again rises rapidly with K (stage III). This variation of da/dt against K is distinct for a material and environment combination. This characteristic variation provides two important directions for damage control; the threshold stress intensity factor K_{TH} below which no damage growth would occur, and the curve of da/dt vs. K which can be used to predict residual life in the presence of a crack. Loading rate, measured in terms of either dK/dt or strain rate $\dot{\epsilon}$ is another factor which affects crack initiation and growth. For higher loading rates, hydrogen has shorter time to travel to the FPZ and cause damage, thus resulting in higher K_{TH} and smaller da/dt . Hydrostatic stress σ_h and plastic strain ϵ_p are the primary parameters, which govern the distribution of hydrogen around the crack tip and da/dt . The modes (I, II, III) of loading on a crack (Jones et al., 2001), loading sequence and load cycling too affect the crack growth (Gangloff, 2003).

The metallurgical parameters, such as, microstructure, composition, impurity level, etc., that

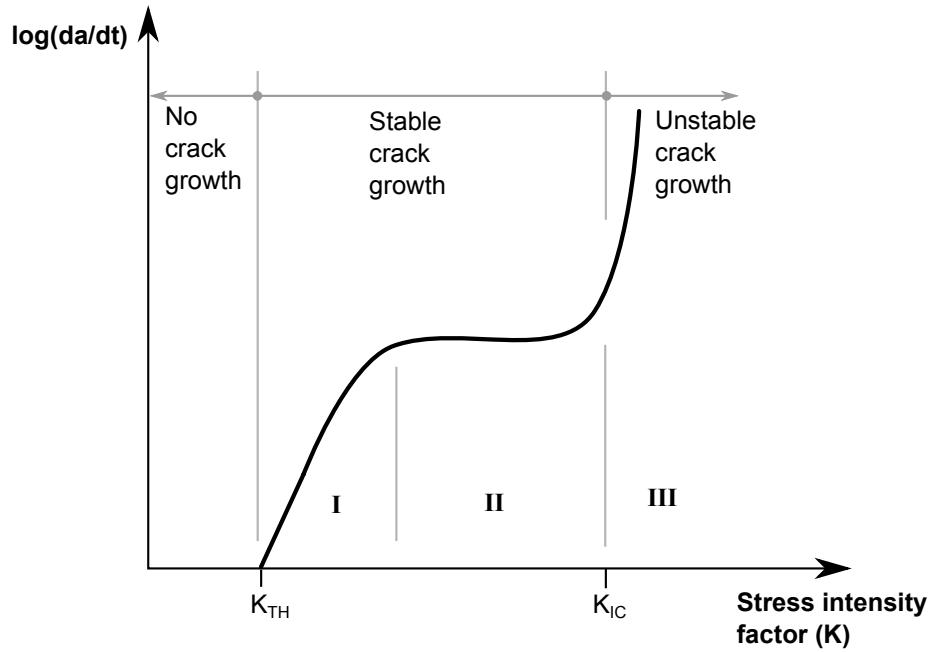


Fig. 2.7 Variation of crack growth rate da/dt against stress intensity factor K .

influence HASCC are generally accounted during selection of material for a specific service condition. However, no quantitative model of HASCC incorporate these parameters explicitly. The material microstructure, which is usually represented in the model by yield strength, is correlated to K_{TH} in the case of steels. For low strength steels, a large gain in K_{TH} is obtained by a small increase in the yield strength; for high strength steels the effect of increasing yield strength on K_{TH} is not significant (Gangloff, 2003). Grain size is another metallurgical parameter which affects K_{TH} . The reduction of grain size increases K_{TH} . Material purity too influences HASCC. Specially, for moderate strength steels (with $\sigma_Y < 1000$ MPa), purity enhances HASCC resistance; for steels of high strength, this is an insignificant parameter.

The chemical parameters affecting crack growth under HASCC are diffusible hydrogen concentration C_H , environmental hydrogen supply and temperature. C_H is an important modelling parameter. It accounts for three regions wherein hydrogen resides within material: lattice, reversible trap sites (dislocations, grain boundaries, phase boundaries) and irreversible trap sites (interface between non-metallic inclusions, precipitates and voids). C_H is the sum of concentration C_L of hydrogen present in lattice and the concentration C_T in the reversible trap sites. The transport of hydrogen within a material lattice is governed by diffusion equation (Taha and

Sofronis, 2001):

$$\frac{\partial C_L}{\partial t} = \vec{\nabla} \cdot (D_{eff} \vec{\nabla} C_L) - \vec{\nabla} \cdot \left(\frac{D_{eff} V_H}{RT_a} C_L \vec{\nabla} \sigma_h \right) - f(\dot{\epsilon}_p) \quad (2.1)$$

$$\vec{\nabla} = \left(\frac{\partial}{\partial x} \vec{i} + \frac{\partial}{\partial y} \vec{j} \right)$$

where D_{eff} is effective diffusivity of material, V_H is partial molar volume of hydrogen in metal, R is universal gas constant, T_a is absolute temperature in degree Kelvin, σ_h is hydrostatic stress and $f(\dot{\epsilon}_p)$ is a function accounting for the effect of plastic strain rate. Amongst these, D_{eff} is the most critical. Environmental hydrogen supply is important during HEAC; the amount of environmental hydrogen adsorbed on the crack surfaces before its further diffusion into the material affects the crack growth. The hydrogen supply is decided by hydrogen pressure in gaseous environments and pH, or cathodic polarisation¹, in aqueous environments. Temperature, which is another process parameter, affects both IHAC and HEAC; in general K_{TH} increases and da/dt decreases with increase in temperature.

2.3.3 Mechanisms

A number of mechanisms are proposed (Oriani, 1978; Hirth, 1980; Magnin, 1995; Gangloff, 2003; Cwiek, 2010) to describe HE. These are also applicable to HASCC. There are three main mechanisms supported by experimental and theoretical work especially for steels, nickel and titanium alloys (Lynch, 2007): hydrogen enhanced decohesion (HEDE), hydrogen enhanced localised plasticity (HELP) and adsorption induced dislocation emission (AIDE). For materials such as Zr, Nb, V and Ta, mechanisms based on formation of brittle hydrides and their fracture are widely accepted. The hydride based mechanisms are not of concern here.

The HEDE mechanism results in weakening of cohesive or bond strength between metal atoms because of solute hydrogen present in metal structure. It may also be visualised as a process of tensile separation of atoms after reaching hydrogen concentration dependent critical distance between them (Fig. 2.8a). The weakening of strength is maximum near the FPZ where the hydrogen concentration is the highest.

According to HELP mechanism, due to high diffusivity of hydrogen in certain materials

¹the part of electric cell where polarisation occurs at the cathode

(including steels), the hydrogen distribution readily adjusts itself such that the total elastic energy is minimised when dislocations approach obstacles (Fig. 2.8b). The presence of solute hydrogen introduces localised plasticity in the material around mobile dislocations and obstacles. This enhances the mobility of dislocations, which, in turn, facilitates faster crack growth. More crack growth occurs due to more localised micro-void coalescence as compared to the less localised one observed in benign environment (Lynch, 2007).

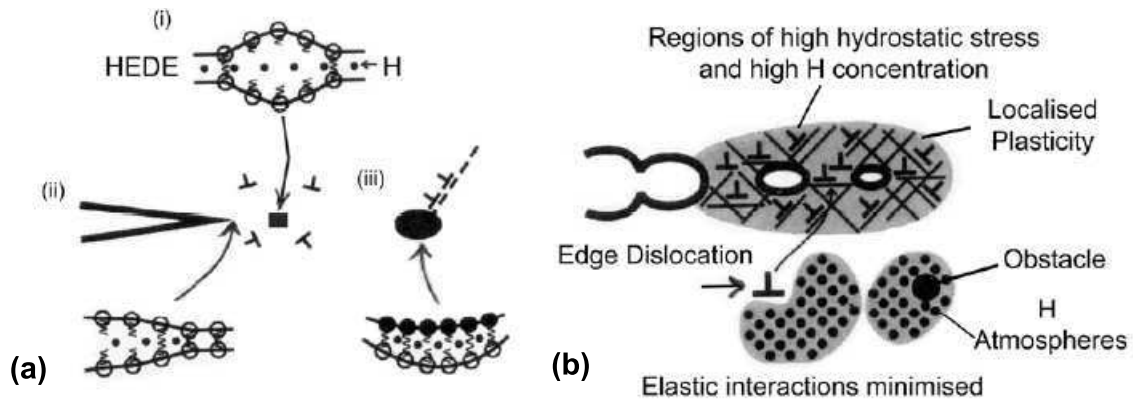


Fig. 2.8 Schematic representation. (a) HEDE mechanism involving tensile separation of metal atoms at (i) lattice (ii) crack tip and (iii) particle-matrix interface. (b) HELP mechanism involving micro-void coalescence and localised plasticity region. (Lynch, 2007).

The AIDE mechanism relates to the effect of adsorbed hydrogen on the surface of crack close to tip rather than the solute hydrogen considered in the earlier mechanisms. The adsorbed hydrogen lowers the inter-atomic bond strength, which leads to emission of dislocations from crack tip and results in crack growth.

Amongst the three mechanisms, HEDE is considered to be the most dominant mechanism of HASCC (Oriani, 1987). This is the reason why HEDE has been included in majority of HASCC models.

2.4 Mitigation

Three strategies adopted for mitigation of HASCC relate to the three factors - material, stress and hydrogen environment. Often two or more of these strategies are combined to arrive at a more effective solution.

Resistance of different materials against HASCC has been experimentally determined and a database already exists and it has been constantly building up. The mitigation strategy focussing on materials is benefited by this data. This database too provides guidance for development of new materials.

An exhaustive set of data pertaining to carbon and alloy steels, austenitic steels, aluminium alloys and copper alloys related to hydrogen assisted fracture in gaseous environment is given by San Marchi and Somerday (2008). Baboian and Treseder (2002) present HASCC behaviour of various types of hydrogen damages based on testing typical material and environment combinations. Craig (2003a) and Oriani et al. (1985) have presented both test and empirical data of iron based alloys under hydrogen environment. Freeman (2003) has given information related to hydrogen degradation characteristic of Fe, Ni, Al, Cu, Ti alloys.

The threshold stress intensity factor K_{TH} level strategies are adopted at the design stage by focussing on maintaining applied load levels low. This is also sometimes coupled with heat-treatment to reduce the residual stresses in the material.

Prevention or reduction of environmental hydrogen levels within material is frequently the basis for some mitigation strategies (Cwiek, 2010; Freeman, 2003). This is achieved through suitable control of hydrogen ingress during fabrication. Further, use of clean, preheated, low hydrogen electrodes and appropriate pre- and post-heating cycle are of help in this connection. Paint, rust and grease present at the welding site act as sources of hydrogen. Therefore their elimination from the site is beneficial. Hydrogen entry during operations such as electroplating or pre-service pickling is unavoidable and it is addressed through a proper bake-out procedure. Resorting to protective coatings is yet another way to check hydrogen entry.

There are numerous alternatives to reduce the ingress of hydrogen in service. First, steel component surfaces can be coated with Cd, Au, Ag, Pt, Cu, Al and austenitic steels to reduce diffusion of external hydrogen. Second, Ti or P ion implantation on steel surface too acts as atomic traps for hydrogen in the surface layer, thereby reducing its entry into the steel substrate. Third, the presence of elements like As, Se, Te, S, Sn, Hg, Pb and Bi in steels and environment is avoided to eliminate possibility of any reduction in hydrogen recombination reaction which can increase the supply of diffusible atomic hydrogen.

Other methods include corrosion inhibitors and redesigning. Corrosion inhibitors help to re-

duce the corrosion reaction and hence quantity of hydrogen generation. Changes in design are employed to eliminate certain design details which increase corrosion induced hydrogen generation, e.g., improper drainage, presence of dead pockets, non-continuous welding of horizontal members, etc., (Baboian and Treseder, 2002).

The HASCC mitigation strategies too draw on the understanding of crack growth behaviour through a material and appropriate modelling. These models can help to build adequate safety margins during design and set proper in-service inspection schedules during operation. In addition, modelling can help to reduce time consuming and costly experiments.

2.5 Mechanistic Models of HASCC

The mechanistic models are built on processes occurring during HASCC (Fig. 2.9). Two processes, diffusion of hydrogen to FPZ from lattice/trap sites and crack growth, are common to IHAC and HEAC. Additional ones specific to HEAC are transport of reactants towards crack tip, generation of hydrogen through chemical reaction and adsorption of hydrogen on the crack surfaces. The models may include effects of other parameters indicated earlier in section 2.3.2. In general, a limited number of these processes and parameters are accommodated in a model to keep complexity under control. Although film rupture and metal dissolution are present in SCC, HE only dominates the crack growth (Gangloff, 2003). In dealing with HE, this is the basis for neglecting some factors which would otherwise be important for SCC but not HE.

The mechanistic models employed to predict the crack growth under HASCC can be grouped under two categories (Gangloff, 2009, 2003). The first group is helpful to predict the threshold stress intensity level K_{TH} below which no crack growth occurs. The second group helps to predict the rate of crack propagation da/dt to estimate the remaining life of a component in service. The second group is of special interest here.

Some of the models are presented in the three following sections.

2.5.1 Classical models

The earliest models date back to 1950s and some of them are listed by Gerberich et al. (1988). For example, Frohmberg et al. (1954) correlated the experimentally observed reduction in duc-

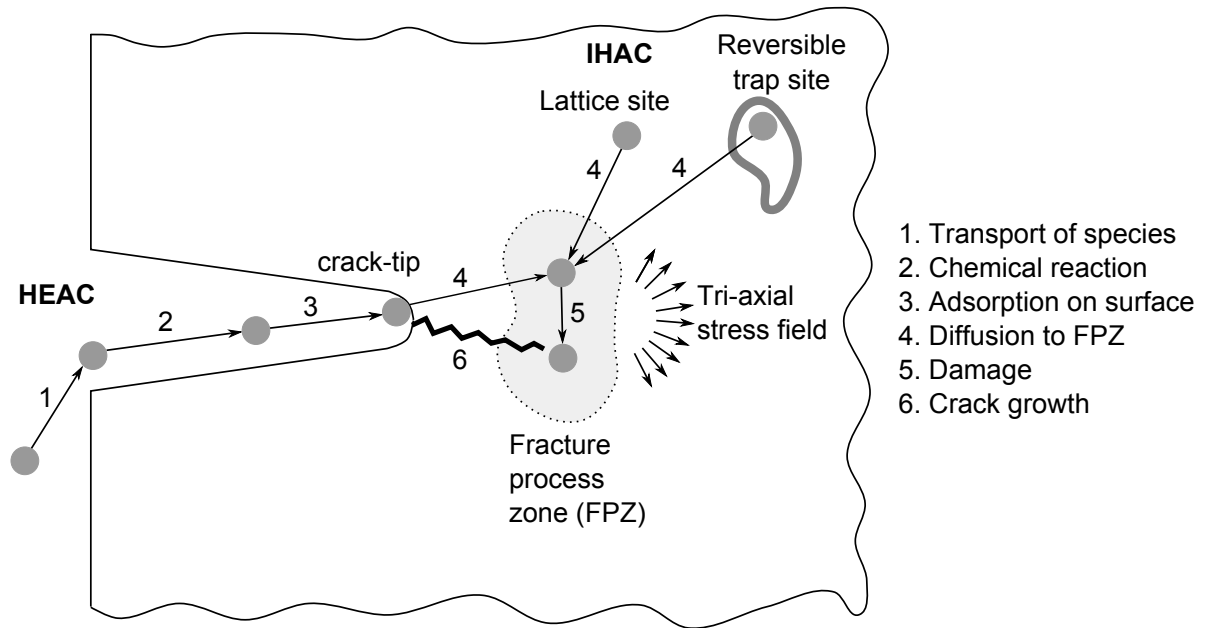


Fig. 2.9 Processes occurring during HASCC (adapted from Anderson, 2002).

tility of steel to the depth of hydrogen penetration and degree of severity of hydrogen embrittlement. A collection of such models and the description of complexities involved in the process of solution is presented by Turnbull (1993). Classical models have used a wide variety of concepts to suit the situations and goals. Some are given below.

- (a) Models which provide for coupling between diffusion of hydrogen and stress-strain fields are important for HASCC modelling. In fact, some studies exclusively focus on this particular aspect (Sofronis and McMeeking, 1989; Turnbull et al., 1996; Yokobori et al., 1996; Krom et al., 1999; Taha and Sofronis, 2001; Toribio et al., 2011). The method of Sofronis and McMeeking (1989) is widely adopted in many studies.
- (b) Many of the classical models have employed critical value of hydrogen concentration near the crack tip as a crack growth criterion.

A quantitative method to predict K_{TH} , using critical hydrogen concentration as the primary basis and yield strength, initial concentration and stress distribution as the secondary variables, has been developed by Gerberich and Chen (1975). A related approach based on threshold hydrogen pressure necessary to result in crack propagation was adopted by Oriani and Josephic (1974).

The critical value of hydrogen concentration computed over a distance, which is decided based on grain or cell size, has been employed as the fracture criterion by Toribio and Kharin (2006) to predict the effect of residual stress distribution upon operating life of steel wires used in pre-stressed reinforced concrete. Realistic values of residual stresses measured in-situ were incorporated in the finite element representation of the steel wire. This criterion has also been adopted by Van Leeuwen (1974); Doig and Jones (1977) and Wang et al. (2006).

- (c) Some of the approaches have employed crack growth criteria based on critical strain near the crack tip.

Moody et al. (2001) have used the critical strain criterion in their model to examine the effect of temperature on hydrogen induced crack growth in iron based superalloy. The model had three components: (i) computation of stress-strain field and stress intensity factor in the presence of an assumed micro-crack ahead of the main crack; (ii) evaluation of hydrogen distribution at slip-band intersections around the micro-crack using diffusion calculations and (iii) fracture along slip-band segments. The fracture occurred when the strain reached hydrogen concentration dependent critical level. The model was able to predict accurately the experimentally determined temperature effects on crack growth.

A method based on critical strain in fictive tensile specimens (Fig. 2.10) is given by Boellinghaus et al. (2001) and Viyanit and Boellinghaus (2007). The fictive elements are kept along crack path and these elements fail after attaining critical strain. This consideration resembles the basis of cohesive zone modelling.

Kim et al. (2012) too proposed a scheme to simulate HASCC using fracture strain as the criterion. The critical strain was, however, selected based on crack tip constraint given by hydrostatic or mean stress. They considered coupling between diffusion and stress analysis through thermo-mechanical coupling feature of FE software and the equivalence of parameters associated with diffusion and thermal conduction. The predicted results were found to be in agreement with experimental data on high strength steel obtained through compact tension (CT) specimens.

Gutierrez-Solana et al. (1993) and Hall (2007) have also employed this criterion. An

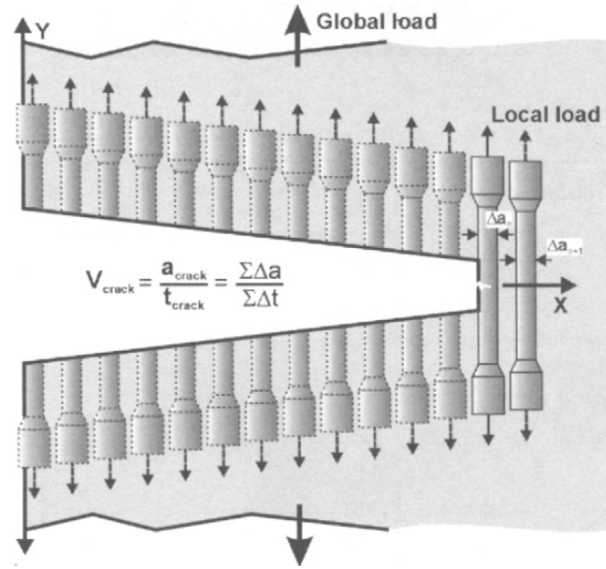


Fig. 2.10 Model of HASCC using fictive tensile specimens (Viyanit and Boellinghaus, 2007).

associated approach employing critical stress as failure criterion has been presented by Akhurst and Baker (1981).

- (d) Time to failure under hydrogen environment, determined experimentally for different uni-axial loading rates, was taken as the condition for fracture by Toribio et al. (2011). An optimised strategy to minimise computational efforts during finite element based modelling of hydrogen assisted fracture in u-notched round steel bars (Fig. 2.11) was investigated. Distribution of diffused hydrogen was obtained using multiple, gradually refined one and two dimensional analytical and FE approaches.

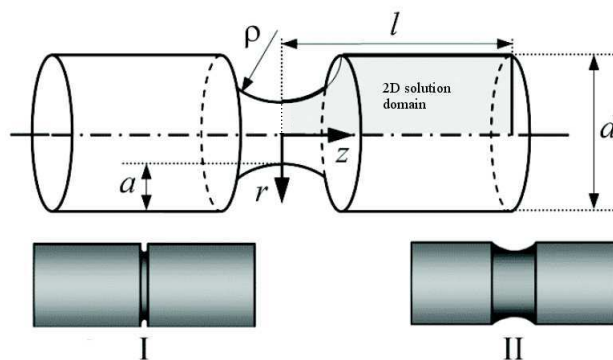


Fig. 2.11 Notch specimen geometry for u-notched round bar (Toribio et al., 2011). 'I' and 'II' illustrate typical range of u-notch shapes studied.

(e) Approach based on computation of rate of hydrogen supply through microstructural elements is employed by the hydrogen partitioning model developed by Gao and Wei (1985). The model determines the distribution or partitioning of hydrogen amongst the microstructural elements, such as, grain boundaries and matrix (Fig. 2.12), and relates such data to variation of crack growth rate. A related strategy based on role of material

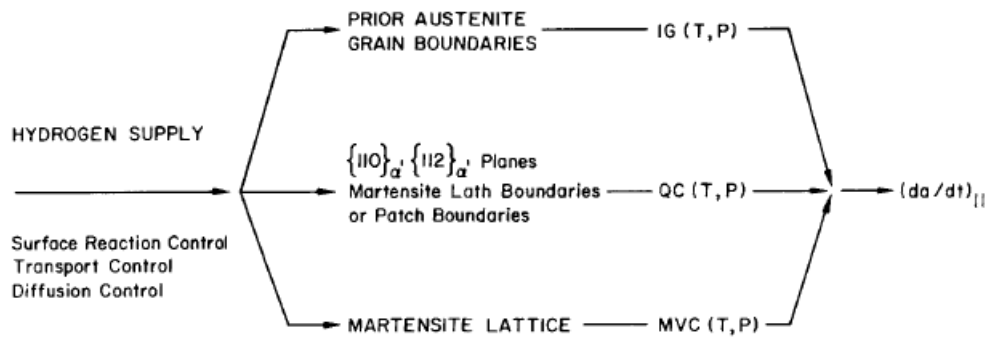


Fig. 2.12 Subdivision of hydrogen supply in hydrogen partitioning model (Gao and Wei, 1985).

micro-structure on hydrogen transport and embrittlement during the inter-granular stress corrosion cracking of Nickel based alloy has been presented by Smith (2000).

Investigation of IHAC in ultra-high strength steel AERMET 100 for different levels of internal diffusible hydrogen by Thomas et al. (2003) is yet another example of microstructural approach. The study was based on an analytical model and computer simulation of dislocation structure around crack tip, for prediction of both K_{TH} and da/dt .

(f) A few approaches have adopted an atomic scale simulation. Tan (2002) has presented a collection of concepts for multi-scale analysis of fracture and corrosion including those for studying interactions between hydrogen and material plasticity.

A unified concept applicable to three types of EAC–SCC, HE and LME, has been proposed by Liu (2008). This is based on the fact that valence electrons available through hydrogen or liquid metal or chemical environment decrease the misfit energy across slip planes, which leads to enhanced crack tip plastic deformation and crack growth.

A theoretical model of SCC including the effect of hydrogen lodged at grain boundaries, based on molecular-statics simulation, has been proposed by Arnoux (2010).

Young et al. (2005) developed an equation based on micro-structural study, fracture mechanics analyses and atomistic modelling applicable for prediction of crack growth rate in A600 type Ni-alloy exposed to high purity high temperature deaerated water where crack growth is governed predominantly by HE. The effectiveness of the approach has been checked through experimental crack growth rate data.

- (g) Some of the approaches specifically deal with examination of solute chemistry near the crack tip for subsequent calculation of corrosive attack by the chemicals (Turnbull, 1997, 2001*a,b*; Vankeerberghen et al., 2001; Mousson et al., 2004). These have been used for prediction of SCC (Vankeerberghen, 2004; Gavrilov et al., 2007). Although the solute chemistry is relevant for establishing environmental hydrogen concentration during HEAC, these approaches have not yet been adopted for such purpose.
- (h) A set of empirical methods relevant for prediction of SCC and HE in nuclear reactor components has been presented by Mohanty et al. (2012).

2.5.2 Crack growth studies based on fracture mechanics

The advances in scientific understanding of material damage and fracture mechanics have provided a strong impetus to the development of models for EAC and HASCC. Computational techniques commonly used in conjunction with the principles of fracture mechanics include finite element method (FEM), extended finite element method (X-FEM) and meshless method. Fracture mechanics based crack growth models may use a criterion based on, for example, stress intensity factor K , fracture energy or J -integral and crack tip opening displacement (CTOD). A few representative approaches are given below.

- (a) Significant number of models use hydrogen concentration dependent critical stress intensity factor as criterion for crack growth.

An early study to relate hydrogen assisted cracking and fracture mechanics principles was due to Johnson and Paris (1968). They observed that, for high strength steels in water, stress intensity factor K_I is a controlling parameter for crack growth. They proposed a model based on a unique relationship between crack growth rate da/dt and K_I for a given material-environment combination.

The growth of a penny shaped crack located fully inside wall of a steel cylindrical pressure vessel was analysed using coupled diffusion-stress approach by Krom et al. (1997). The crack faces were subjected to pressure exerted by gaseous hydrogen trapped inside crack volume. The build-up of hydrogen pressure within crack due to diffusion from the surrounding metal was computed. The failure was considered to occur when K_I for the crack attained the material fracture toughness. The influence of diffusivity, solubility, fluctuations of hydrogen input and crack geometry were accounted for.

Corrosion enhanced plasticity model (Magnin et al., 1997), utilising critical stress intensity factor as a crack growth criterion, has helped in numerical simulation of hydrogen-dislocation interactions at the crack tip for austenitic stainless steel. Further studies in this direction are reported by Delafosse and Magnin (2001) and Chateau et al. (2002).

A case study of a steel tendon wire used in pre-stressed structures exposed to hydrogen attack was presented by Cho and Kim (2008). In this study, an initial thumbnail crack was considered. The diffusion and stress calculations were decoupled, i.e., analysis of diffusion and stress distribution (Fig. 2.13) were done employing separate finite element schemes. Three crack growth criteria - fracture toughness of material, critical tensile

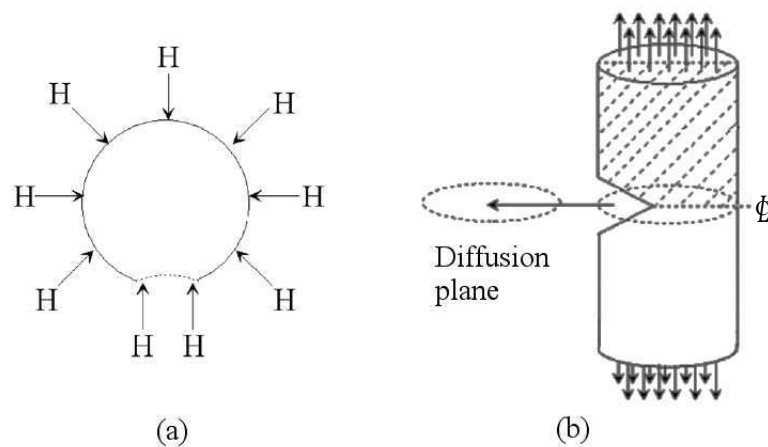


Fig. 2.13 Modelling of tendon wire with thumbnail shaped crack (Cho and Kim, 2008). Geometry considered in model is shown for: (a) diffusion study and (b) fracture analysis.

strain and limiting value of equivalent hydrogen pressure near the crack tip - were considered.

A finite element simulation of hydrogen induced cracking in steel pipes with an assumed

penny shaped crack subjected to hydrogen sulphide environment was reported by Traidia et al. (2012). They evaluated the diffusion of hydrogen into crack cavity and the subsequent pressure built up. They considered diffusion of atomic hydrogen, recombination of atomic hydrogen to form gas molecules and pressure built-up in the crack cavity as the sequence of phenomena preceding every event of crack growth (Fig. 2.14). Further, hydrogen concentration dependent fracture toughness was utilised as the criterion of crack growth.

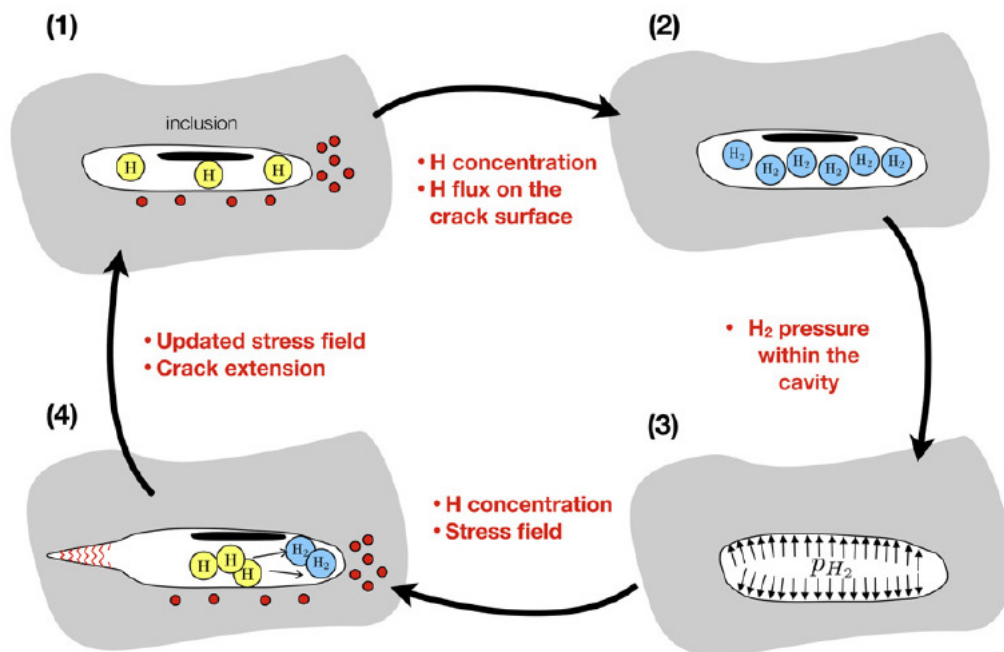


Fig. 2.14 Multi-physics events in hydrogen induced cracking (Traidia et al., 2012): (1) to (4) represent cyclic stages, i.e., hydrogen diffusion, pressure-built-up, mechanical loading and crack growth respectively.

(b) Some of the approaches employ critical fracture energy as basis for crack growth study.

Kameda (1986) developed a microscopic model of hydrogen induced intergranular cracking of high strength steels under constant load conditions using fracture energy approach. The strain energy available at the crack tip for driving crack growth is computed using fracture mechanics principles. The energy required to create new surfaces or boundaries during crack growth is thermodynamically calculated considering the linear dislocation arrays along crack plane and an analytically calculated distribution of hydrogen atoms

ahead of the crack tip. A stable crack growth occurs when the energy equilibrium is disturbed.

A technique that can work for both SCC and HASCC simulation has been proposed by McLaughlin (1997). He has proposed an approach based on critical strain energy density for dislocation emission near the crack tip.

Carrasco et al. (2012) numerically modelled crack growth in edge cracked steel specimen under HE using critical energy release rate as damage criteria. The damage model factored deterioration in fracture properties of material ahead of crack tip due to hydrogen appropriately. This factoring was based on experimental data.

- (c) Crack tip opening displacement (CTOD) has been adopted as a criterion for crack growth during some investigations. For a pipe with inner surface crack subjected to internal pressure, Takayama et al. (2011) have obtained numerically a correlation between the maximum steady state hydrogen concentration at the crack tip and the CTOD. This type of relations can be exploited in other situations.

2.5.3 Cohesive zone models

The schemes of analysis based on fracture mechanics have been generally successful and provided sufficiently accurate prediction for HASCC. However, the classical approaches have been based on single parameter characterisation of fracture in terms of plane strain fracture toughness or J -integral. These are incapable of taking care of variations arising from stress state, plane stress to plane strain, distribution of hydrogen concentration ahead of crack tip, etc. To overcome some of the problems, the concept of T -stress and utilisation of constraint-specific fracture toughness data were suggested (Cornec et al., 2003). These schemes are, however, computationally more rigorous and expensive. Methods employing cohesive zone model help to overcome these shortcomings and extend the scope of fracture toughness based classical fracture mechanics.

The cohesive zone model (CZM) incorporates the effects of damage processes occurring within process zone around the crack tip. The CZM was introduced by Barenblatt (1962) to simulate crack growth through brittle materials. It has been later developed to study ductile

tearing process. The model is founded on gradual separation/decohesion of atomic bonds. The corresponding variation of cohesive force with increasing distance is represented by a suitable traction separation law (TSL). This law relates cohesive force with displacement within material. The CZM model is applied to a narrow region immediately ahead of the tip on the path of crack extension. The progressive damage to the load carrying capacity of material and subsequent formation of crack surfaces take place inside the narrow region, called cohesive zone.

A schematic of CZM is depicted in Fig. 2.15. The crack growth occurs through generation

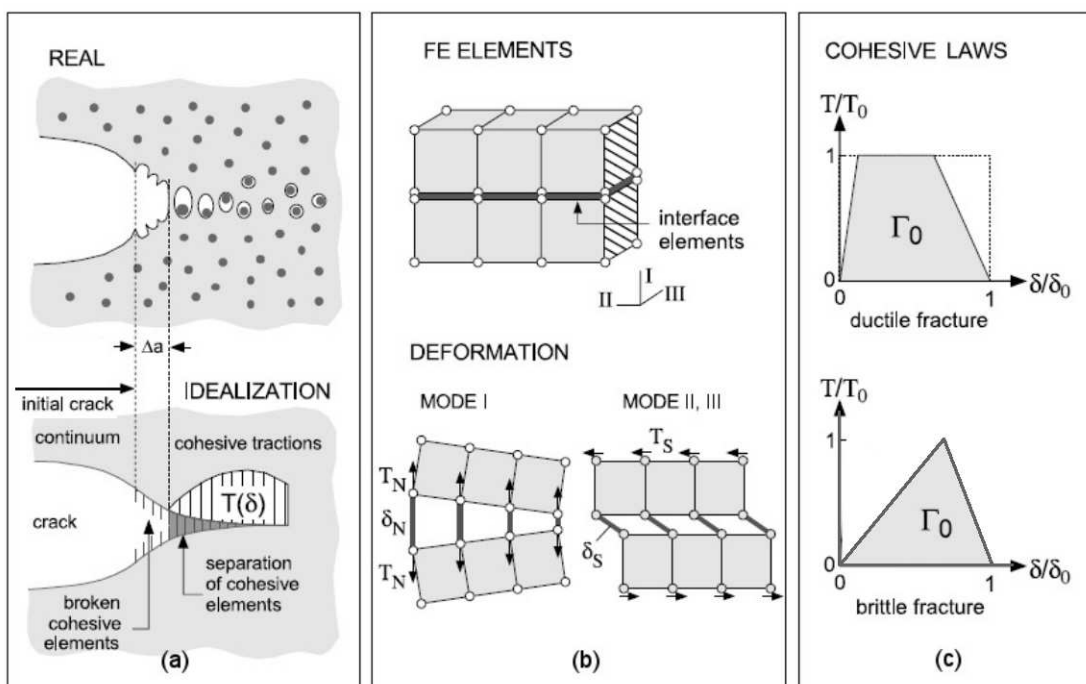


Fig. 2.15 Illustration of cohesive zone model. (a) Representation of ductile tearing process (Cornec et al., 2003). (b) FE discretisation and deformation stages (Cornec et al., 2003). (c) Traction separation laws for ductile and brittle materials.

of voids and their coalescence ahead of the crack tip. This process causes a gradual separation of crack faces and corresponding loss of traction acting on the ligament ahead of previous crack tip (Fig. 2.15a). In the finite element implementation of CZM, a series of interface elements are laid along the prospective crack path (Fig. 2.15b). The interface elements undergo progressive damage in accordance with TSL and ultimately the element disappears resulting in crack growth. The CZM is a phenomenological model and the shape of TSL may be chosen suitably. Fig. 2.15c presents typical shapes of TSL chosen for ductile and brittle materials. Tvergaard

and Hutchinson (1992) have observed a relatively weak dependence of shape of TSL curve on prediction of fracture behaviour.

The CZM helps to avoid modelling of stress singularity at the crack tip. This feature simplifies the analysis of crack growth. The material damage is represented by using any two of the parameters: cohesive energy Γ_0 , cohesive strength T_0 and critical separation δ_0 . The cohesive energy represents the amount of energy supplied to a unit of material for its complete separation leading to a crack extension. The damage due to hydrogen is sometimes quantified by the extent of reduction in the cohesive energy proportionate to local hydrogen concentration.

Some of the approaches based on CZM are given below. Approaches (a), (b), (c) and (d) are basic and include the essential interaction between diffusion and crack growth processes; (e) and (f) include an advanced analysis with addition of an extra process or a mechanism of HASCC; (g) and (h) employ specialised knowledge, such as, quantum mechanics or behaviour of polycrystalline structure; and (i) addresses fatigue crack growth.

(a) Simulation of crack growth in CT specimen (Scheider et al., 2008)

Scheider et al. (2008) simulated stable crack growth in compact tension (CT) specimens of a medium strength steel under hydrogen charging conditions. The loading was done at different displacement rates. Variation of modified crack tip opening displacement δ_5 , which is displacement between two points lying 2.5 mm off the crack plane (Fig. 2.16), with crack growth Δa were experimentally measured. The analysis was carried out by performing diffusion and crack growth calculations sequentially. The effects of hydrostatic stress and plastic strain, if any, on diffusion process were neglected. The TSL parameters, material diffusivity and cohesive strength reduction factors were determined by combined numerical-experimental study. This work was extended by Falkenberg et al. (2010) to account for the coupling effect of hydrostatic stress and plastic strain on diffusion.

(b) Analysis of notched flat tensile specimens of duplex stainless steel (Olden et al., 2008)

Crack growth in 25% Cr duplex stainless steel in U and V notched flat tensile specimens subjected to constant tensile stress while immersed in sea water was investigated by Olden et al., (2008). Diffusion and crack growth were analysed separately. The time for crack initiation

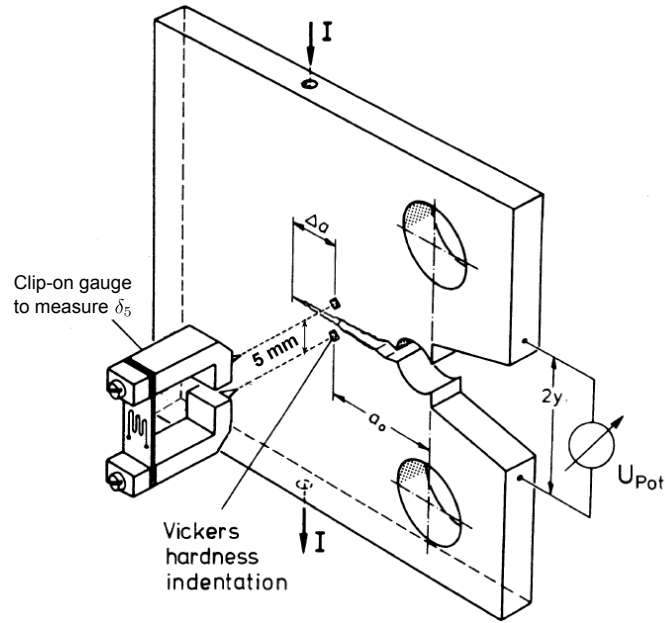


Fig. 2.16 Measurement of CTOD δ_5 for CT specimen (Dietzel et al., 2005).

was predicted and compared with experimental data. The model was reported to be sensitive to mesh size and an upper limit on mesh size was recommended. The authors evaluated the suitability of linear and polynomial hydrogen concentration dependent TSLs. Polynomial TSL was found more suitable.

(c) Study of crack growth in SENT specimens (Olden et al., 2009)

Laboratory experiments using 25% Cr stainless steel specimens to study influence of hydrogen evolved during cathodic protection and FE simulation of the tests were carried out by Olden et al. (2009). Single edge notched tensile (SENT) specimens were used for the experiments (Fig. 2.17). The simulation was done in three steps at every increment of time. In the first step, an elastic-plastic stress analysis was carried out to obtain distribution of hydrostatic stress and plastic strain. In the second step, diffusion analysis was done utilising the stress-strain data to obtain the hydrogen concentration distribution. In the last step, CZM based crack growth analysis was performed employing the hydrogen concentration data. Influence of hydrogen on TSL was incorporated through a polynomial multiplier (Serebrinsky et al., 2004). The results predicted by the model were in close agreement with experimental results.

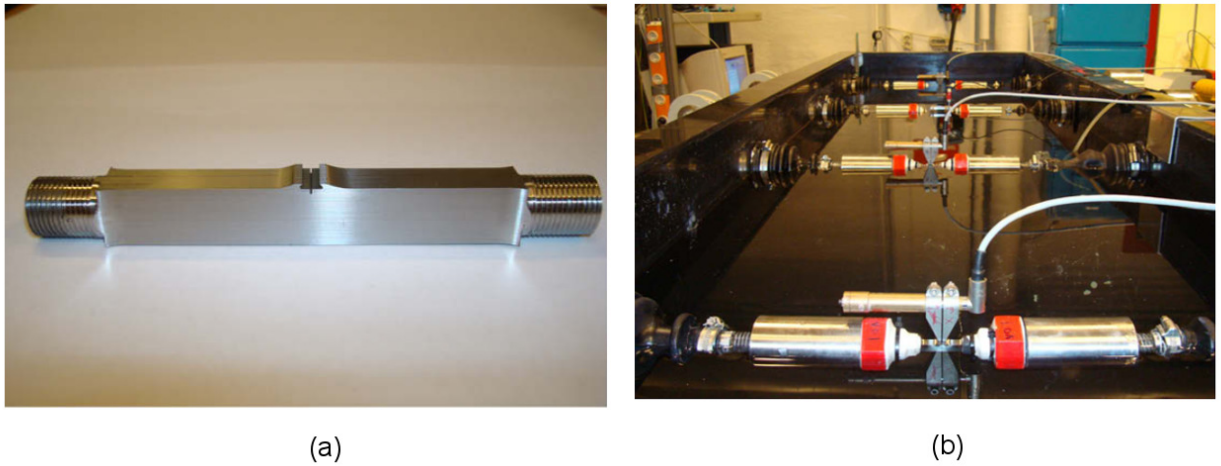


Fig. 2.17 Experiments on duplex stainless steel in hydrogen environment (Olden et al., 2009).
 (a) SENT test specimen. (b) Test rig with hydrogen charging arrangement in slowly circulating artificial sea water.

(d) Simulation of disk pressure test (Charles et al., 2012)

Disk pressure test is used to characterise metal's resistance to hydrogen embrittlement. In this test, a thin disk is subjected to bulging using pressure from inert and hydrogen gases until rupture. The ratio of rupture pressures observed for inert and hydrogen gases represents hydrogen embrittlement susceptibility of the metal. Charles et al. (2012) simulated this test for a nickel alloy and steel. Fig. 2.18 shows schematically the geometry and boundary conditions used. The crack emerging in the disk is subjected to mixed-mode loading. Accordingly, the

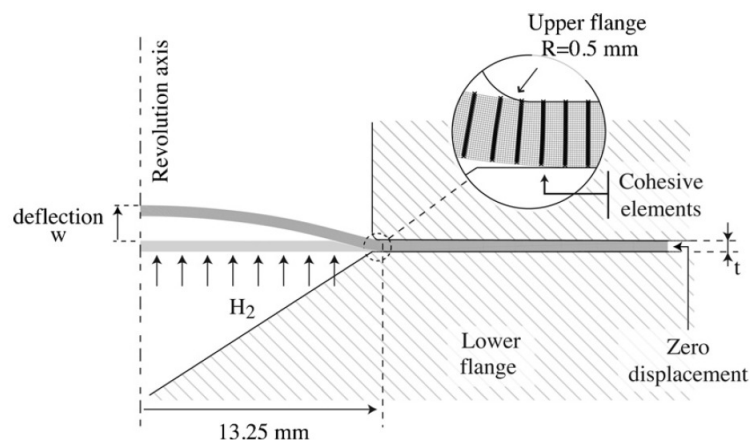


Fig. 2.18 Schematic of finite element model for disk pressure test (Charles et al., 2012).

TSL used in the model included variation of both normal and shear tractions. The predicted

load-displacement curve as well as fracture features agreed with experimental data.

(e) Approach with inclusion of surface absorption process (Brocks et al., 2012)

The hydrogen available in the environment is gradually absorbed through a boundary layer of passivation or corrosion products to the surface near the crack tip. Brocks et al. (2012) extended the work by Scheider et al. (2008) to additionally include the surface absorption driven variation of hydrogen concentration at the crack tip during crack growth simulation in CT specimen (Fig. 2.19). The surface absorption was implemented by chemisorptions model. The method

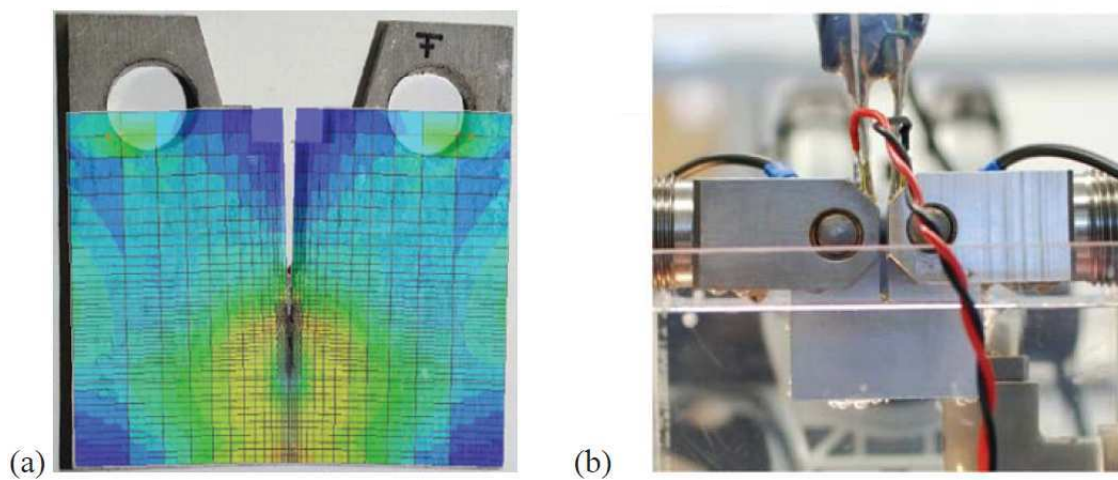


Fig. 2.19 Model for HASCC of CT specimen (Brocks et al., 2012). (a) FE model overlaid on test specimen. (b) Test apparatus.

covered the coupling effects through in-built thermo-mechanical-coupled scheme of analysis available in ABAQUS[®] code.

(f) Void cell based model (Ahn et al., 2007)

Ahn et al. (2007) have presented a scheme of ductile crack growth study through pressure vessel steel A533 where microstructural effects (void growth and coalescence) are evaluated considering a separate cell of cylindrical shape with spherical void. The axisymmetric void cell model was subjected to stress conditions and uniform initial hydrogen concentration corresponding to the starting stress state and hydrogen distribution. The response of void cell model was transformed to develop the TSL. The TSL was then employed with regular 2-D cohesive elements

(Fig. 2.20). The model included softening of elastoplastic response of material due to HELP

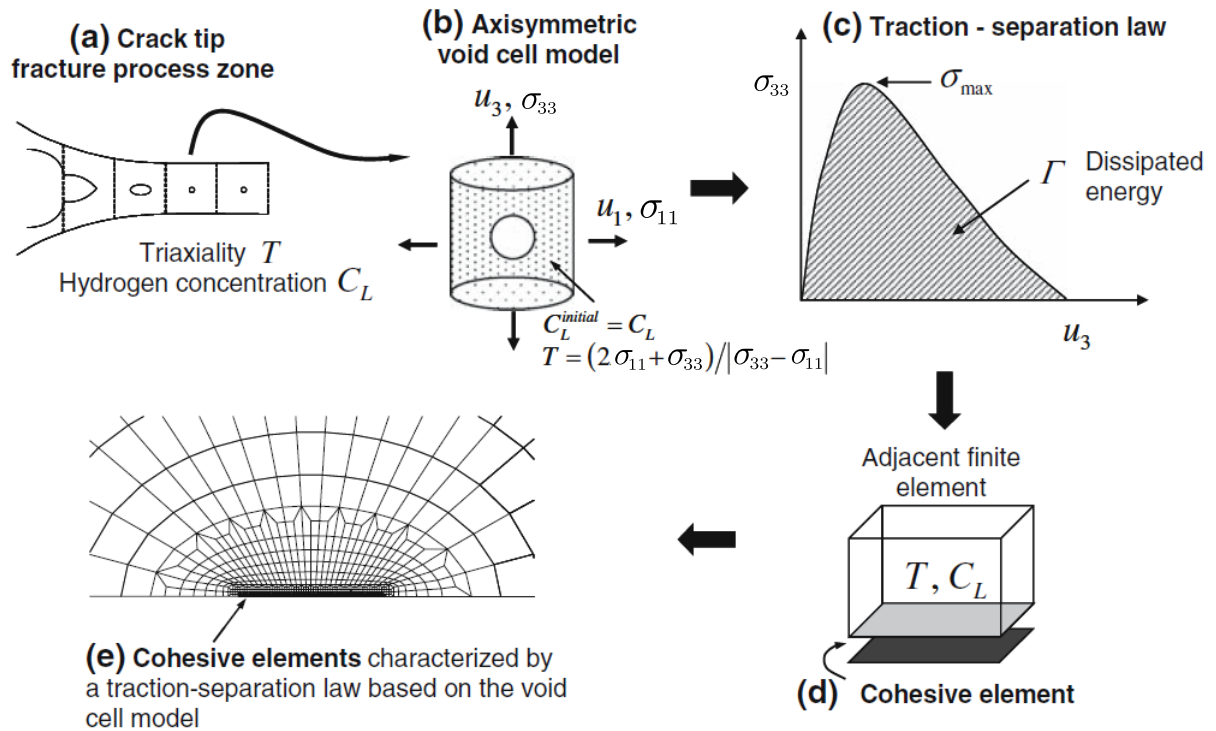


Fig. 2.20 Void cell based model (Ahn et al., 2007).

mechanism. In this case too crack growth was considered to be linking of multiple voids and the crack tip. The predicted results were in agreement with experimental observations for steels for common usage in process industry.

(g) Model with quantum mechanics based TSL (Serebrinsky et al., 2004)

A model of this type has been employed to analyse crack growth in center cracked tension (CCT) specimen (Fig. 2.21a) of high strength steel AISI 4340 (Serebrinsky et al., 2004) under hydrogen environment. The variation of traction with separation was triangular. The TSL was derived through quantum mechanics approach where cohesive traction and separation were based on energy of structurally relaxed surface and elastic modulus of single pair of atomic planes. The drop in cohesive traction due to hydrogen was accommodated by a polynomial multiplier. The multiplier involved a ratio of actual and saturation hydrogen concentration. The computation of hydrogen transport coupled with stress analysis enables accounting for the effect of hydrostatic stress. A typical set of results is presented in Fig. 2.21b. Some of the results have

been reported to have good agreement with experimental results.

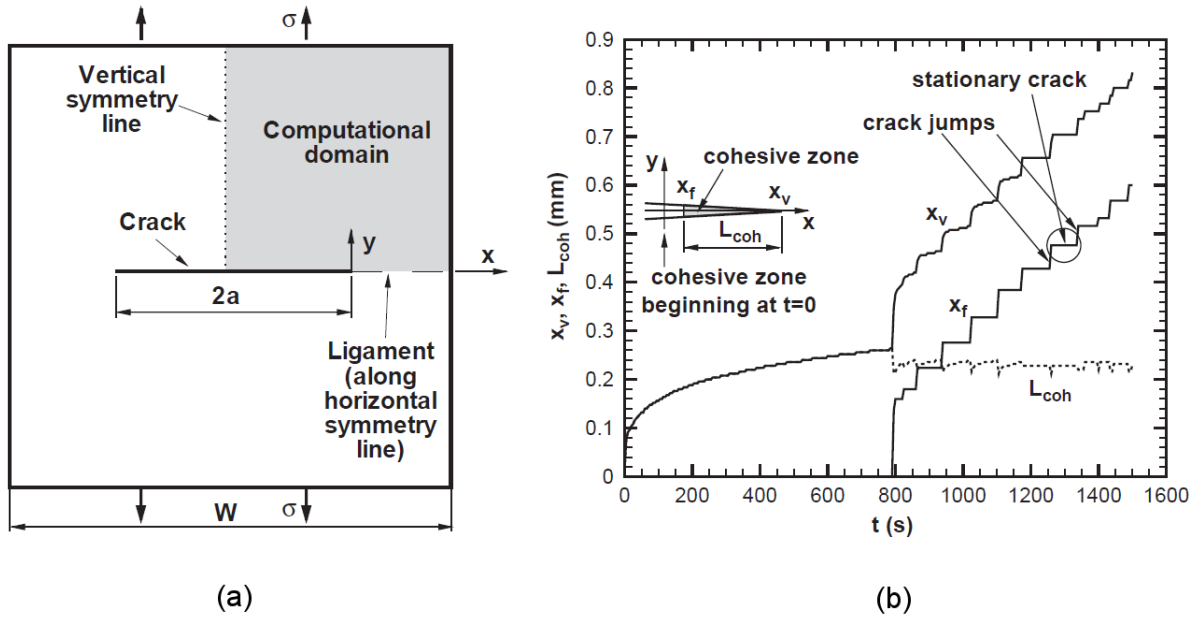


Fig. 2.21 Quantum-mechanically informed model (Serebrinsky et al., 2004). (a) Geometry analysed. (b) Crack growth results. $L_{coh} = x_v - x_f$ where x_f is position of crack tip and x_v is location of the point along cohesive zone beyond which separation is zero.

(h) Multi-scale model with polycrystalline structure mesh (Rimoli and Ortiz, 2010)

A three-dimensional model for prediction of intergranular crack growth under conditions of hydrogen embrittlement for a double-cantilever test specimen, incorporating polycrystalline structure along crack path, was presented by Rimoli and Ortiz (2010). The crystal structure was represented by computational mesh; the texture of poly-crystals is random and grain material was considered elastically anisotropic and deformed plastically by crystallographic slip. Grain boundary embrittlement was accommodated by hydrogen concentration dependent CZM. The hydrogen diffusion along grain boundaries was modelled using basic form of diffusion equation without coupling with stress field. The prediction of time for crack initiation and crack growth details (Fig. 2.22) were in line with experimental observations. The model helped to estimate K_{TH} .

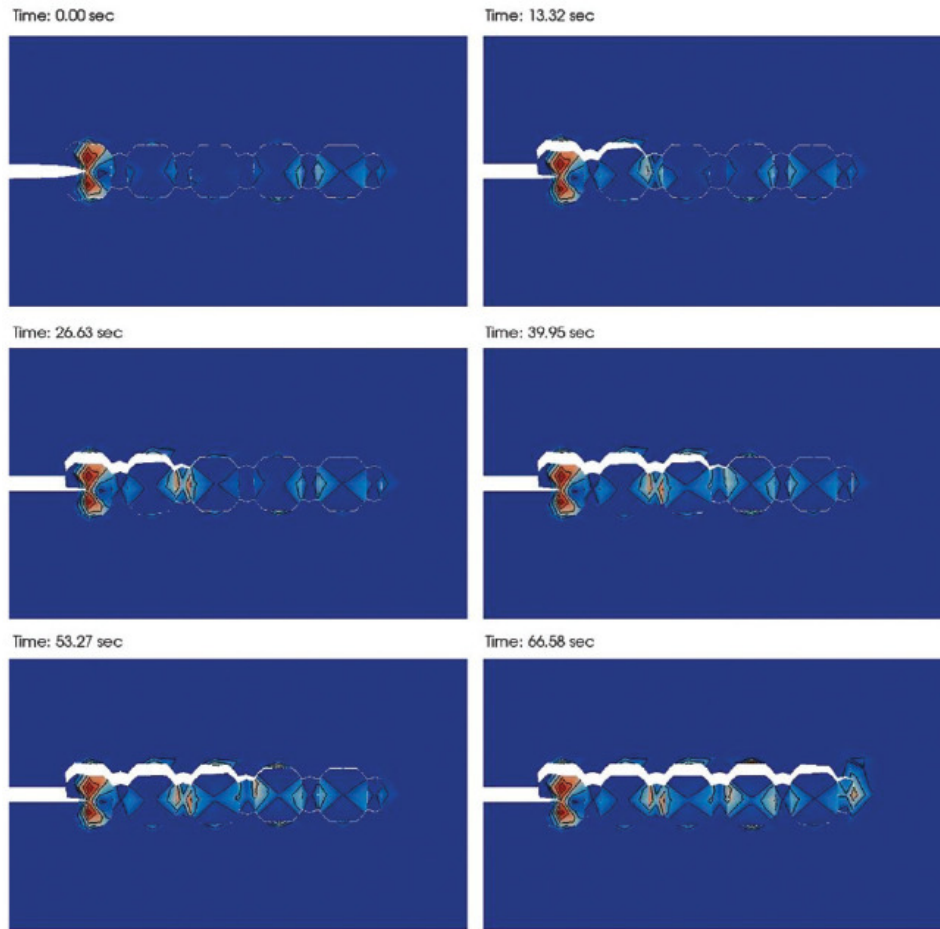


Fig. 2.22 Crack surface evolution in double cantilever specimen using multi-scale model (Rimoli and Ortiz, 2010).

(i) Analysis of fatigue crack growth under hydrogen environment (Moriconi et al., 2011)

A model for prediction of crack growth in compact tension (CT) specimen under fatigue loading was developed by Moriconi et al. (2011). The TSL employed for CZM incorporated damages due to both hydrogen concentration distribution and cyclic loading. The degradation of material was represented by damage variable D_m . $D_m = 0$ indicated no damage and $D_m = 1$ indicated full damage. The model assumed increase in D_m during loading phase of cycle and D_m remained constant during unloading. Fig. 2.23a shows typical progressive drop in cohesive traction resulting from each cycle of loading of displacement amplitude $\Delta\delta_{pre}$. The TSL was adjusted to incorporate the effect of hydrogen concentration (Fig. 2.23b). The analysis involved coupling of diffusion and crack growth processes.

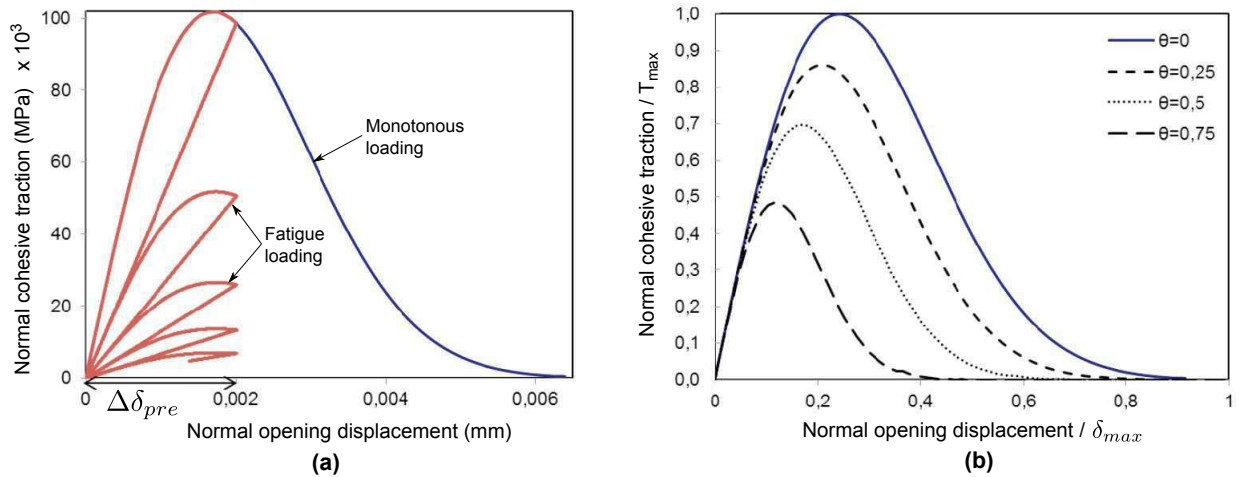


Fig. 2.23 TSL for fatigue loading under hydrogen environment (Moriconi et al., 2011). (a) TSL for monotonous loading and for fatigue loading, where $\Delta\delta_{pre}$ - prescribed displacement amplitude. (b) TSL for different values of normalised hydrogen concentration θ .

2.5.4 Overview of cohesive zone models

Most CZM models have helped to analyse crack growth or crack growth rate da/dt . Rimoli and Ortiz (2010) have additionally predicted K_{TH} . Each CZM model has been targeted for specific geometry. Since the CZM inherently represents damage as a decohesion process, it has been possible to incorporate HEDE mechanism easily. Models by Ahn et al. (2007) and Brocks et al. (2012) have included HELP mechanism. Hydrostatic stress and plastic strain/strain rate have been recognised as two important parameters. Scheider et al. (2008) and Rimoli and Ortiz (2010) have however ignored the effect of hydrostatic stress during diffusion calculations. The schemes of analysis mostly treat diffusion and crack growth uncoupled and utilise sequential approach for study. Charles et al. (2012) and Brocks et al. (2012) report fully coupled analysis. This has helped in enhancing speed of calculations. Majority of models try to settle two 'open' parameters: effective diffusivity D_{eff} and a factor representing reduction in cohesive strength with increase in hydrogen concentration, through a comparison of predicted and measured data.

2.6 Experimental methods

The experimental methods are used to generate data for HASCC design calculations, examine effectiveness of a prevention/control strategy, investigate into behaviour of a new material-environment combination, understand fundamental processes underlying the damage, etc. Different techniques are employed to determine threshold load, evaluate sub-critical crack growth kinetics, measure changes of ductility, study microstructural changes and evaluate electrochemical parameters (Raymond, 1972; Dean et al., 1982; Katz et al., 2000; Interrante and Raymond, 2005). A list of common practices for HASCC testing is given in Appendix I.

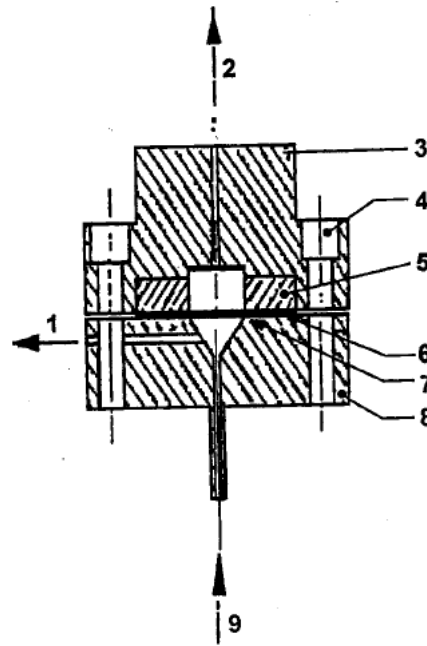
The experimental methods related to study of crack growth and determination of threshold load are in general based on fracture mechanics. Tests are performed with pre-cracked specimens.

2.6.1 Classical experiments

These experiments are mostly done employing smooth specimens. Their main focus is to evaluate HASCC qualitatively. Some are focussed to measure hydrogen concentration within material to monitor evolution of damage. ASTM F113 test method provides guidelines to measure diffusible hydrogen in steels at room temperature through Barnacle electrode. ASTM F326 standard gives methods to electronically detect hydrogen in plating bath using Lawrence gauge. Thereby quantity of hydrogen absorbed by the steel parts undergoing plating in the bath is obtained (Interrante and Raymond, 2005).

The accuracy of measurement of hydrogen concentration obtained through above direct methods is not sufficient in many cases to assess the damage due to HASCC. This has given way to measure hydrogen damage employing mechanical load tests, which are often more accurate as well as less expensive. The mechanical tests measure either difference in loads required to fracture a specimen in hydrogen and inert environment, or ascertain the ability of a specimen to withstand the environment without fracture for a fixed duration. The disk pressure test (as per ASTM F1459) employs a disk in the standard test cell (Fig. 2.24). The cell is pressurised upto rupture of the disk, first using hydrogen and then using helium gas. The ratio of two bursting pressures gives the measure of susceptibility of the material to HASCC. ASTM F519 provides

a test method to evaluate level of hydrogen present during plating/coating processes and service environments. Test specimens of specified geometry made from 4340 grade steel are installed in the plating bath along with the regular batch of items for plating. The level of hydrogen in the bath is acceptable if the test specimens are able to stand the medium for 200 hours without fracture. Six types of test specimens and three loading methods are specified. A typical notched C-ring type specimen with loading bolt is shown in Fig. 2.25.



- | | |
|--|-----------------|
| 1. Port for evacuation and flow adjustment | 6. Disk |
| 2. Discharge port | 7. O-ring |
| 3. Upper flange | 8. Lower flange |
| 4. Bolt | 9. Gas inlet |
| 5. High strength steel ring | |

Fig. 2.24 Disk pressure test cell (ASTM Standard, 2012a).

2.6.2 Fracture mechanics based tests

Fracture mechanics based tests involve specimens that contain a machined notch which is grown into a sharp crack by fatigue loading. This process is also known as pre-cracking. The tests are conducted with specimens of various shapes and employing different types of loading.

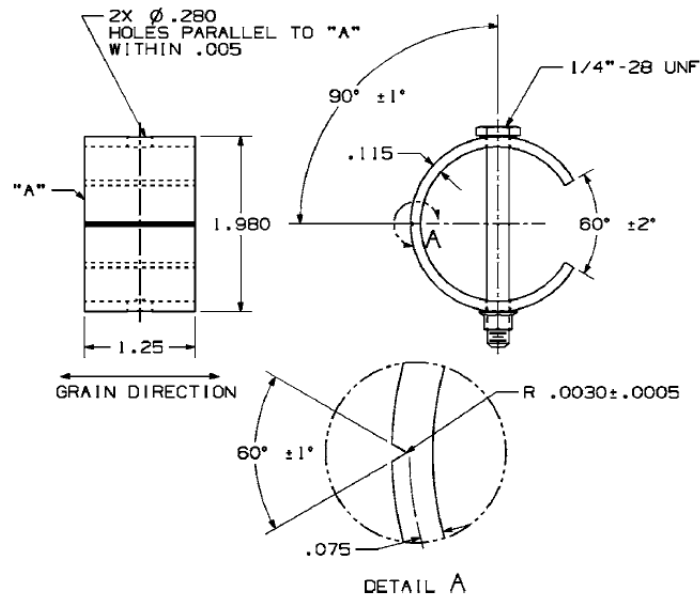


Fig. 2.25 Notched C-ring specimen with loading bolt (ASTM Standard, 2012c).

Types of test specimens

The shape of test specimens is selected based on material availability, shape of product, load capacity of test apparatus, etc. Fig. 2.26 shows different types of recommended standard test specimen geometries. A number of other specimens, e.g., center cracked, double edge cracked, surface cracked, taper single edge cracked and circumferentially notched tensile (CNT) round geometries, are also considered to meet specific needs of investigation.

Types of loading

Commonly employed loadings are: (i) constant force or displacement, (ii) rising force or displacement, (iii) slow strain rate, (iv) step load, (v) cyclic load, and (vi) controlled stress intensity factor K .

Selection of a loading type depends on the intent of experiments. Typically rising force/displacement or slow strain/step loading provides an accelerated determination of kinetics of crack growth as compared to constant loading tests. Particularly, crack growth rate (da/dt) data obtained by rising force/displacement tests correspond to values in the stage-I and II behaviour obtained through long duration tests (Gangloff, 2003). Thus, there is substantial time saving possible by such tests (Dietzel and Mueller-Roos, 2001).

FRACTURE MECHANICS, FATIGUE PRECRACKED SPECIMEN GEOMETRIES FOR HYDROGEN EMBRITTLEMENT

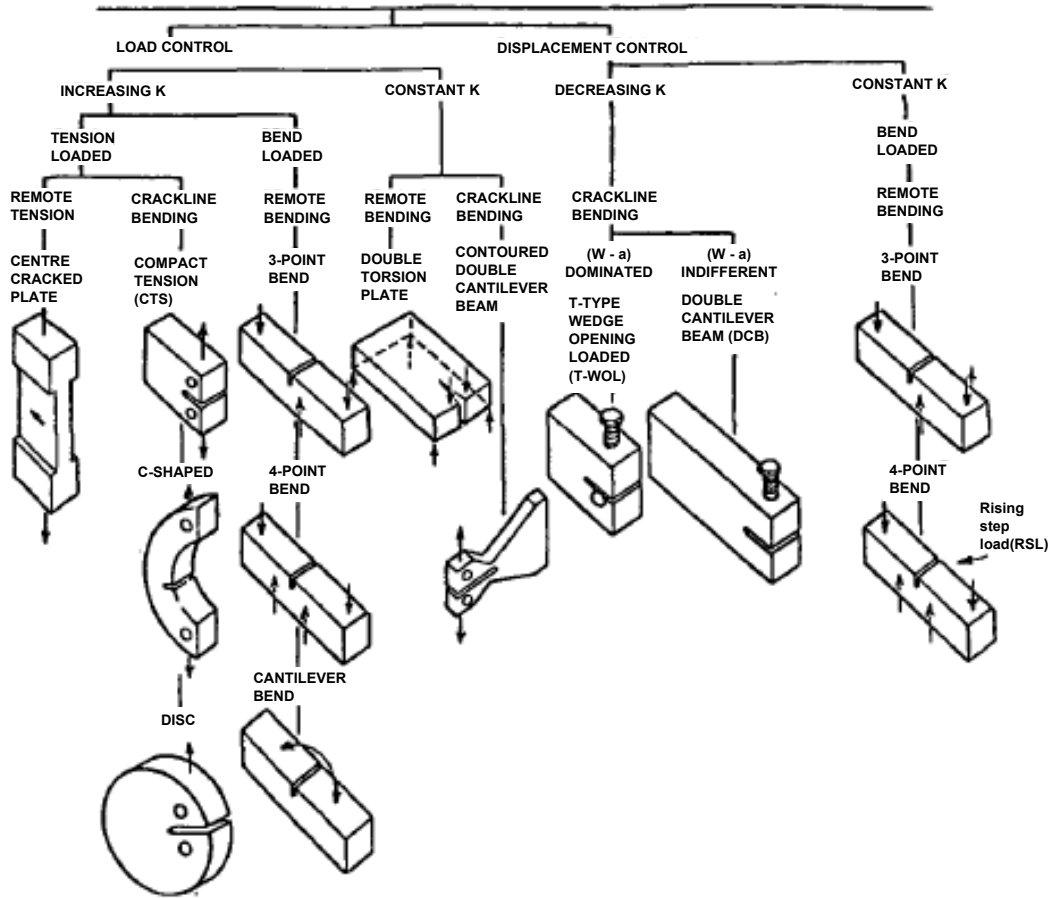


Fig. 2.26 Types of test specimens for fracture mechanics based tests (Interrante and Raymond, 2005).

Some of the main test procedures categorised by their intent and loading type are given below.

(a) Determination of threshold stress intensity factor K_{TH} employing constant force or displacement loading

Standard ASTM E1681 (2011) covers procedures for determination of threshold stress intensity factor K_{TH} for metals under environmentally assisted cracking conditions. It recommends single edge notched cantilever beam test specimen or compact tension (CT) specimen subjected to constant force loading, or modified bolt-loaded compact specimen or wedge opening load (WOL) specimen. The WOL specimen is loaded through imposition of constant displacement.

The specimens with constant force loading (Fig. 2.27a,b) are subjected to dead weight or loaded through other means of applying constant load. The specimens for constant displacement loading (Fig. 2.27c) are subjected to fixed crack mouth opening displacement by means of a bolt. The specimens are kept under loading inside the environment chamber for a prescribed duration, typically 10,000 hours for low strength steels, and 5,000 hours for high strength steels. The stress intensity factor applied to the specimen is calculated using the appropriate relation of linear elastic fracture mechanics. Tests are repeated until the highest load, for which no crack growth or failure occurs till the end of the test, is obtained. The stress intensity factor corresponding to this maximum load is the required threshold stress intensity factor K_{TH} for the material-environment combination. Due to the long duration of the test and the requirement of a large number of tests to arrive at K_{TH} , these tests turn out to be expensive.

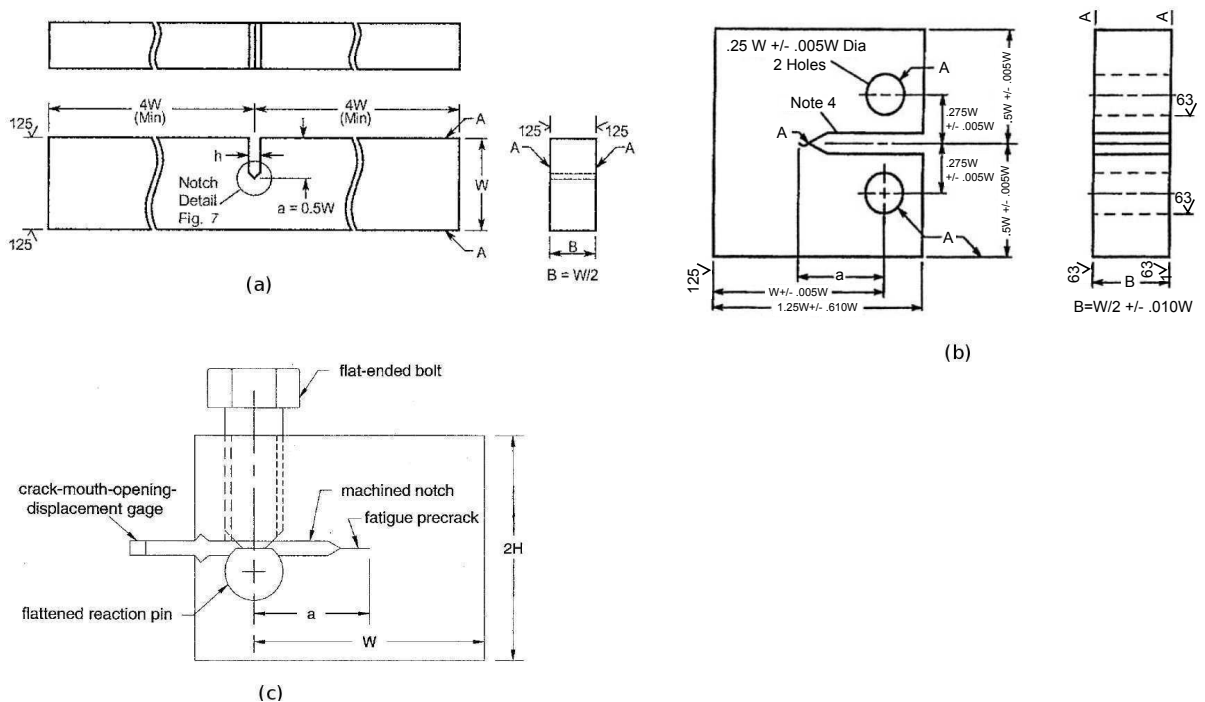


Fig. 2.27 Test specimen types in ASTM E1681 (ASTM Standard, 2011): (a) Single edge notched. (b) Compact tension. (c) Bolt-load compact.

(b) Determination of crack growth rate using constant force or displacement loading

The double beam specimens (ASTM G168; 2006b), known as double-cantilever beam (DCB) formerly, were developed primarily for measuring crack growth rate (Interrante and Raymond,

2005). These specimens (Fig. 2.28) too can be used for determination of K_{TH} , da/dt vs. K relation, and measure K -independent (stage II) crack growth rate (Fig. 2.7), if any. The specimens are loaded either under constant displacement or force. The test is started by applying a pre-defined stress intensity factor (K), which is calculated with the help of linear elastic stress analysis as per guidelines of the standard. During the test, crack length is measured at some suitable intervals to plot the crack growth behaviour. Test durations vary depending on material and purpose of the test.

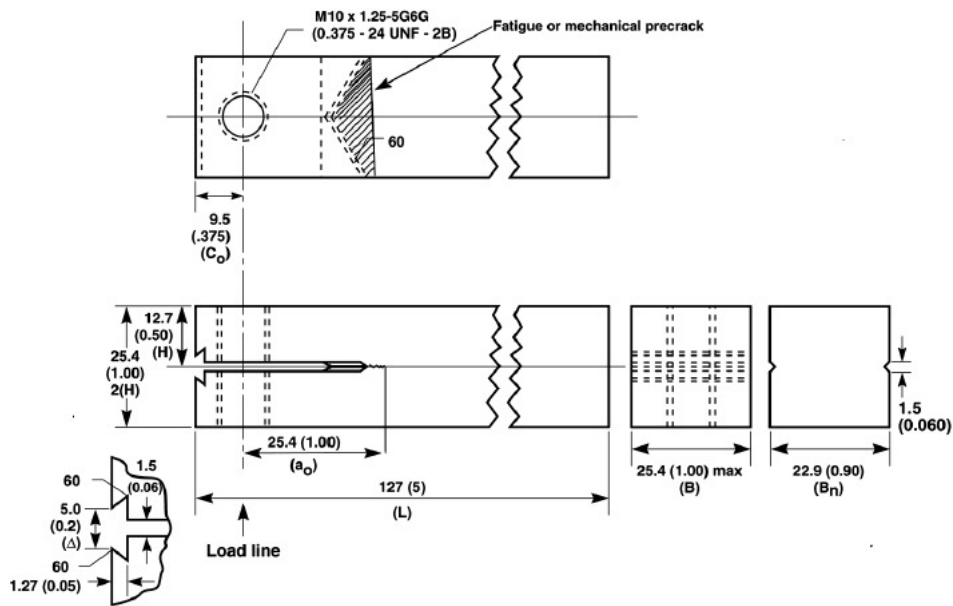


Fig. 2.28 Double beam specimen in ASTM G168 (ASTM Standard, 2006b).

A contoured double cantilever beam test specimen (Fig. 2.26), whose section depth gradually increases away from the crack tip, is sometimes recommended to facilitate crack growth under constant K .

(c) Comparative evaluation of EAC resistance with slow strain rate loading

Standard ASTM G129 (2006a) provides procedure for employing axially loaded smooth tensile specimens or pre-cracked fracture specimens, for study of environmentally assisted cracking. This test allows a rapid screening or a comparative evaluation of environmental or metallurgical variables on EAC resistance. The measures of EAC susceptibility for smooth specimens could be the maximum load, time to failure, change in ductility (elongation or reduction in area),

stress-strain curve, difference in physical appearance; whereas the measures for pre-cracked specimens could be K at failure, notch tensile strength, microstructural appearance of fractured surface. During the test, the specimen is subjected to a rising strain at a sufficiently low rate (10^{-4} to 10^{-7} s $^{-1}$) which allows sufficient time for the action of environment to stabilise. The tests are done with multiple specimens under different strain rates to gather sufficient data for a proper understanding of material behaviour. These tests are continued until the specimen fractures. A typical experimental set-up is shown in Fig. 2.29.

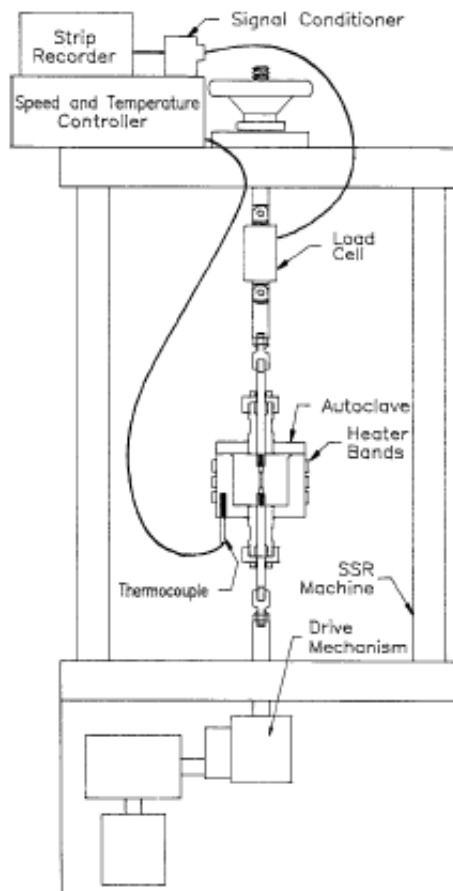


Fig. 2.29 Example of SSRT test machine (ASTM Standard, 2006a).

(d) Determination of threshold stress intensity factor K_{TH} employing incremental step loading

Standard ASTM F1624 (2012b) is used to establish K_{TH} for steels under hydrogen embrittlement conditions. It bridges gap between the long duration tests prescribed by ASTM E1681 and

relatively fast test under ASTM G129. This test can give K_{TH} within one week as compared to 10,000/5,000 hours required for low/high strength steels by ASTM E1681 standard and a few days by ASTM G129 standard. The data obtained by this test is more accurate and comes closer to the data obtained by the long term tests as per ASTM E1681. The test is carried out under displacement control, rising incrementally at slow strain rate. The specimen geometry can conform to that specified by ASTM E399 (ASTM Standard, 2010) for standard fracture toughness testing or irregular shaped.

In the test, the fast fracture strength P_{FFS} of material is determined by loading one specimen as per standard tensile test procedure. Thereafter, each test specimen is subjected to a load profile represented by $\#/\%P_{max}/hrs$, where $\#$ is the number of steps, $\%P_{max}$ is the percent of maximum anticipated load at each step and hrs is the hold time for each step. For example, loading profile 20/5/1 is prescribed for high strength steels with hardness >54 HRC (Fig. 2.30). This data indicates that there are 20 steps of magnitude 5% of P_{FFS} each and the hold time is

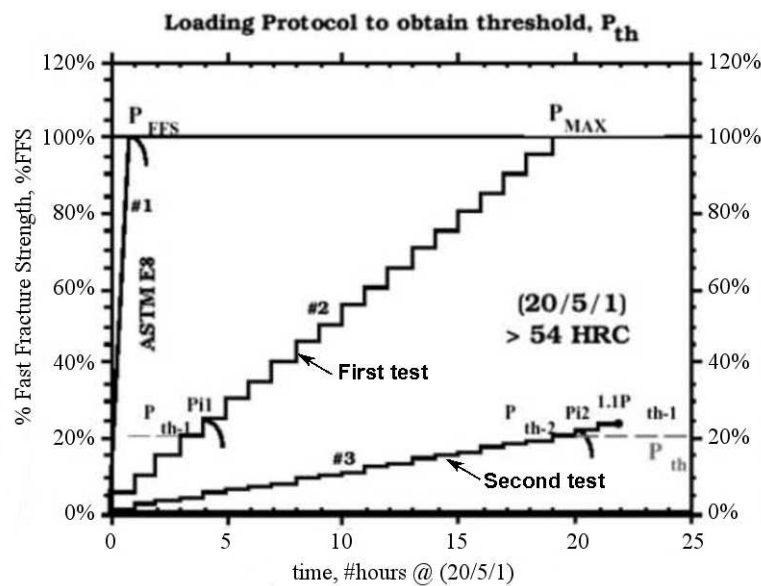


Fig. 2.30 Schematic of step loading profile for high strength steels with hardness >54 HRC (ASTM Standard, 2012b).

1 hour. During every test, the threshold load P_{th-n} corresponding to the step before onset of crack growth is recorded. This gives P_{th-1} from the first test. For the second test, P_{max} is set to 1.1 times P_{th-1} . This leads to a substantial reduction in step size. From the second test, the threshold load is obtained as P_{th-2} (Fig. 2.30). The next test can be done along similar lines.

The final threshold load is obtained when difference in the two subsequent threshold loads is less than 5% of P_{FFS} . The threshold stress intensity factor K_{TH} is calculated using the final threshold load and the relation given in the standard.

2.6.3 Tests with circumferentially notched tensile (CNT) specimen

Circumferentially notched tensile (CNT) test specimen is a relatively new application of small-size round specimens for fracture mechanics based investigation on EAC. Although round specimens have been in place for regular crack propagation studies for quite some time (ASTM special committee, 1962; Srawley and Brown Jr., 1964; Ibrahim and Stark, 1990), its adoption for EAC testing is relatively recent.

Typical dimensions of CNT specimen are shown in Fig. 2.31. The specimen has a machined v-notch in the thread-free segment. A circumferential fatigue pre-crack is introduced at the root of notch by loading it, for example, on a rotating-bending machine. The pre-cracked specimen is subjected to either constant load, constant displacement or slow strain rate loading to determine the EAC growth properties. The CNT test technique has been successfully employed in studies on stress corrosion cracking for determination of K_{TH} and crack growth rate (da/dt) (R.K. Singh Raman et al., 2006, 2007a, 2007b; Rihan et al., 2007; Ibrahim et al., 2008; Wu et al., 2009).

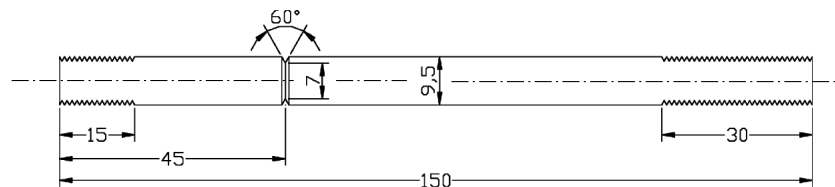


Fig. 2.31 Dimensions of a typical CNT specimen (R.K. Singh Raman et al., 2007b).

While the common test specimens (CT, DCB, WOL, etc.) and their associated experimental procedures are well established and standardised, they have certain limitations: the specimen size required is large and relatively intricate in shape and hence expensive to manufacture. Each test specimen requires large quantity of material in order to meet the plane strain validity requirements. Consequently the load required for testing is considerably high. The experimental technique involving circumferentially notched tensile (CNT) specimens offers an attractive alternative because of ease of fabrication of cylindrical shape. The smaller cross-sectional size of

such specimens gives rise to smaller load and quantity of material per specimen (Rihan et al., 2005, 2006). A detailed comparison of CNT with traditional test specimens (Table 2.1) is presented by Pal (2010). He indicates some advantages of the CNT specimen.

Table 2.1 Comparison of test techniques using CNT and traditional specimens (adapted from Pal, 2010).

Attribute	CT and DCB specimen	CNT specimen
(a) Specimen Geometry		
Thickness requirements	Required thickness for plane strain condition changes with the material	Plane strain conditions are inherently satisfied for any thickness
Valid plane strain condition	Depends on the thickness of the specimen, the minimum thickness requirement is 20mm	Satisfied for 9.5 mm diameter because of no end effect and absence of plane stress zone (Stark and Ibrahim, 1992)
Shape	Intricate	Simple
K_{Ic} of thin components	Not possible to produce valid K_{Ic} data	Possible to produce valid K_{Ic} using 8.4 mm specimen (Ibrahim and Stark, 1987)
K_{Ic} of weld and HAZ	Difficult to produce valid K_{Ic} data	Potential to produce valid K_{Ic} data
Loading device	Heavy machinery required	Light machinery required
(b) Validity of K_{Ic} results		
Crack branching	May invalidate K_{Ic} data	Crack is constrained to propagate in one plane only
Crack blunting	No	No
Specimen end effects in Plane Stress Zone	Yes	No (There is no end in cylinder geometry)
(c) Time and cost of testing		
Time of testing to determine K_{TH}	High	In short span of time, many specimens can be loaded and K_{Isc} can be determined. A reasonable K_{TH} value can be obtain within two months
Cost of specimen fabrication	High	Low (20% of the cost of CT specimens)
Overall cost effectiveness of test	No	Yes

2.6.4 Experimental studies for grade 4340 steel

HASCC experimental studies have been mostly focussed on determination of properties of high strength steels due to their widespread applications in major industries. Gangloff (2003) has mentioned some of the important works in this area. AISI 4340 steel is a high strength steel which is extensively used for structural applications in aviation and marine applications. This is a martensitic steel with yield strength ranging from 1000 to 2000 MPa depending on heat treatment employed. It has been very widely experimented with.

Early works related to K_{TH} and da/dt determination of 4340 grade steel were carried out by Brown and Beachem (1965) and Van Der Sluys (1969). In a unique study McNitt et al. (1972) exploited the proneness of 4340 steel towards hydrogen embrittlement to induce pre-cracking in a round-hollow notched specimen. The specimens were later tested to determine fracture toughness in air. Sandoz (1972) conducted an investigation to evaluate the effect of mode of hydrogen supply, alloying elements and corrosion potential on its HASCC behaviour. Gerberich et al. (1975) and Simmons et al. (1978) experimentally demonstrated correlation between hydrogen diffusion and rate of crack growth. Effect of hydrogen source on crack initiation was studied by Page and Gerberich (1982). The effect of steel composition and hydrogen pressure on K_{TH} was studied by Bandyopadhyay et al. (1983). Macdonald and Chung (1985) studied effect of sudden change in applied stress intensity on da/dt for the material. Effect of temperature and micro-structure on crack growth under IHAC was examined by Gerberich et al. (1988). Kalnaus et al. (2011) have studied the behaviour of the steel at different concentrations of NaCl solution.

All the reported studies under HASCC for this material have been conducted with CT, WOL or DCB specimen. Though round specimens have been employed for non-environmental tests, they have not yet been adopted for HASCC experiments.

2.7 Closure

The literature review clearly indicates the magnitude of problems faced by industries from hydrogen assisted stress corrosion cracking (HASCC) of high strength metals, and the different approaches available for addressing the issue. The review also shows the vast utility of the

mechanistic modelling as the rational approach in the scheme to mitigate HASCC.

The reported studies have focused on modelling as well as experimental investigations. The modelling has mostly considered two processes, hydrogen diffusion and crack growth, as central to HASCC. Studies have been carried out to understand crack growth phenomenon in conjunction with the diffusion mechanism. Some studies were directed to determine the threshold stress intensity factor (K_{TH}) and others were concerned with the determination of crack growth rate (da/dt). Generally, the crack growth analysis uses K_{Ic} or δ_{COD} as failure criteria. This approach does not offer a convenient way of inclusion of the effect of local hydrogen concentration on the crack growth. On the contrary, an approach based on cohesive zone model (CZM) does not suffer from such limitations. Notably some of the studies have been carried out by more than one research groups. This has helped in developing confidence in the findings.

To analyse the problem of HASCC, it is necessary to examine and understand the mechanism of diffusion of hydrogen into, and within the material, plus the process of simultaneous crack extension. The diffusion of hydrogen leads to weakening of material's cohesive strength and an accelerated crack extension, and the extension of crack, thereby creating new surfaces, leads to further diffusion of hydrogen. Thus the two processes are interdependent.

Study based on effective coupling between the diffusion and crack growth processes is crucial to get a complete understanding of HASCC. Majority of schemes of analysis have neglected the full coupling, resorting to separate analyses of diffusion and crack growth in sequence. Both the stages have been handled by numerical methods. Particularly, in recent works, the finite element method (FEM) has been found very handy for the diffusion stage and FEM based CZM suitable for the crack growth stage. The diffusion equation, when employed for a specific geometry and simplified to eliminate the interdependencies, is amenable for analytical solution. An analytical solution to the diffusion equation had been employed in some classical models. Some investigators have adopted finite difference method (FDM) to solve the full-scale diffusion equation with the involvement of stress-strain terms or interdependencies. The analytical solutions may be obtained in one- or two-dimensions. The effectiveness of coupling one- or two-dimensional analytical solutions with crack growth analysis is not known. Whether the analytical or FDM solutions can be more gainfully combined with crack growth analysis remains an open issue. The combined analytical and CZM approach or FDM and CZM approach can

bring down the time for analysis substantially. To assess the exact benefits fresh investigations are required.

The coupling between diffusion and crack growth processes has been attempted either through sequential computation of the two processes (Olden et al., 2009, 2012) or through elaborate coupled-FE procedures (Taha and Sofronis, 2001; Ahn et al., 2007) or by employing equivalent thermo-mechanical-coupled approach (Kim et al., 2012; Brocks et al., 2012). The sequential approaches are generally tedious and slow whereas the other two approaches are fast but demand more complex computational procedure. An intermediate strategy based on combined analytical/FDM and CZM approach, which balances speed, accuracy and computational resources, is worth investigating.

The earlier studies have helped to identify important process parameters, e.g., hydrogen concentration, effective diffusivity, hydrostatic stress, plastic strain, plastic strain rate, etc. The CZM based approaches have permitted to accommodate easily some of these parameters in the analysis. Study to investigate the influence of more parameters on the accuracy of crack growth is open for investigations.

The reported experimental studies have made use of a wide variety of specimen geometries and materials. Circumferentially notched tensile (CNT) specimens have been used for measurement of fracture toughness K_{Ic} . Even such specimens have been recently utilised for measurement of SCC growth data (R.K. Singh Raman et al., 2006; Ibrahim et al., 2008). However, CNT specimens have not yet been employed for investigation into HASCC under combined conditions of internal hydrogen assisted cracking (IHAC) and hydrogen environment assisted cracking (HEAC). Whether crack growth through such specimens can be modelled and analysed requires an examination. Further, to examine the accuracy of the results, both experimental and combined analytical-numerical studies are required.

Although, individual modelling approaches to handle rectangular and cylindrical geometries, brittle and ductile materials and IHAC and HEAC type of hydrogen supply, are available, whether a common approach is suitable for both situations requires an examination.

Keeping in view all the above, studies have been undertaken here along the lines stipulated in section 1.2.

Chapter 3

Experimental Study

3.1 Introduction

This chapter gives the details of experimental investigations carried out with circumferentially notched tensile (CNT) specimens. The experiments were conducted using CNT specimens of AS-4340 steel, which is a high strength steel often employed, for example, for landing gear of aircraft. The test was carried out in neutral 3.5% NaCl solution at room temperature.

The testing was employed for determination of critical stress intensity factor K_{Ic}^H , under the conditions of IHAC, HEAC and combined IHAC-HEAC¹. Rising displacement loading was employed to study loading rate effect on HASCC kinetics. The data collected through the experiments was further utilised to establish the accuracy of theoretical predictions, which are presented in chapter 5.

3.2 Test procedure

The experimental set-up (Fig. 3.1) consisted of a loading arrangement, CNT test specimen, environmental cell, and instrumentation to measure load and specimen elongation. The set-up was specifically designed for this study. The loading axis was vertical. The machine was

¹Most data reported in this chapter have been published in the following paper.

Raykar N. R., R. K. Singh Raman, Maiti S.K., Choudhary Lokesh (2012), 'Investigation of hydrogen assisted cracking of a high strength steel using circumferentially notched tensile test', *Material Science and Engineering A*, **547**, 86-92.

operated by an electric DC motor with reduction gear box to achieve cross-head linear speeds between 0.1 mm/h and 0.0015 mm/h. The tensile load was applied to the test specimen through gradual motion of the cross-head. The machine had a rated axial load capacity of 6000 N. The test specimen and other load bearing components in the set-up were sized accordingly.

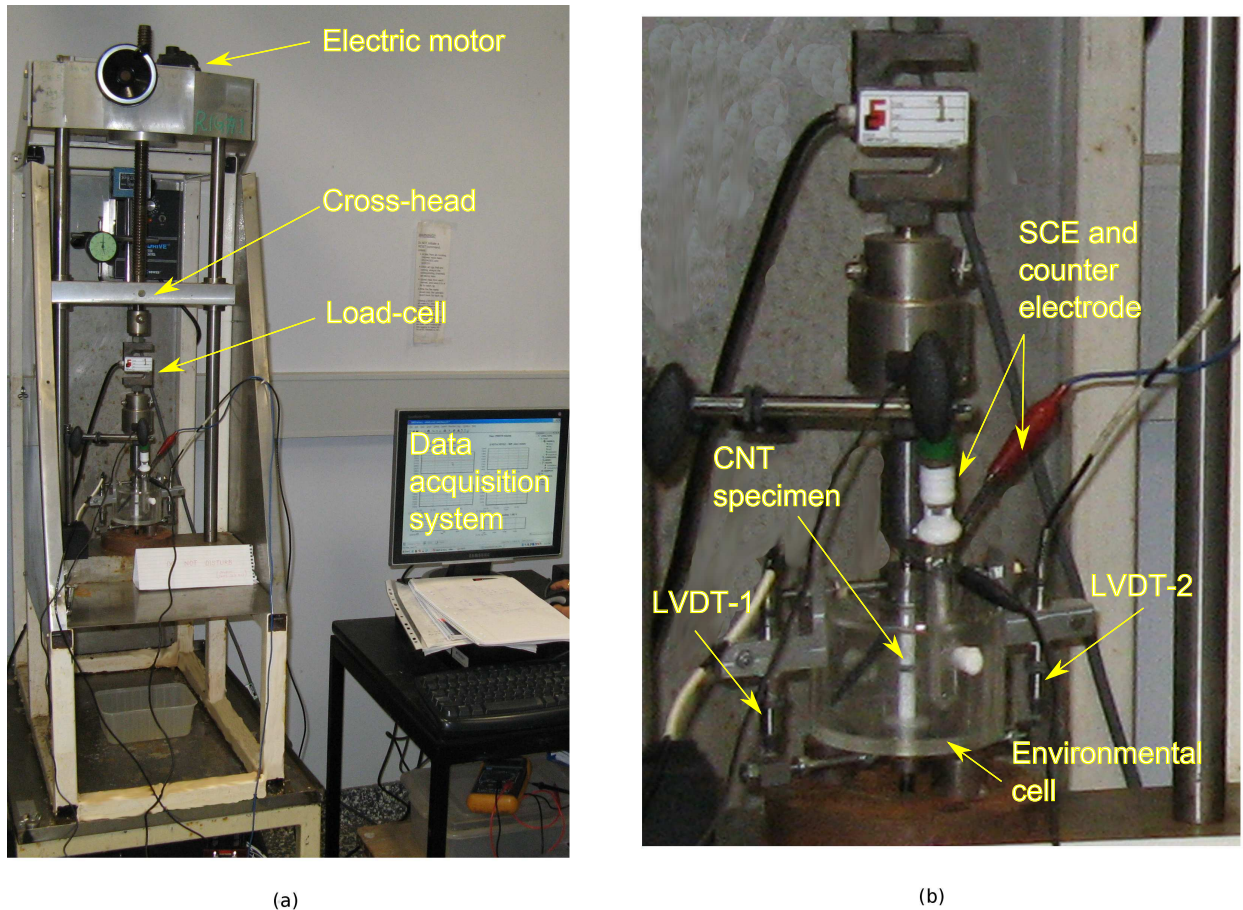


Fig. 3.1 Experimental set-up. (a) Overall view. (b) Arrangement near test specimen.

3.2.1 Test specimen

The test specimens were machined from bars of AS-4340 steel. The composition of the material is given in Table 3.1. The final specimen size is 7 mm outside diameter and 5 mm notch root diameter (Fig. 3.2). The specimen dimensions were restricted taking note of the machine load capacity. The shape of test specimen was modified from the conventional design (Fig. 2.31) to facilitate its adoption in the set-up. The specimens were heat treated by normalising at 835 °C for 0.5 hour and followed by tempering at 300 °C for 2 hours. The mechanical properties of

Table 3.1 Chemical composition (weight %) of AS-4340 steel.

C	Si	Mn	Cr	Mo	Ni	S	P	Fe
0.40	0.25	0.70	0.80	0.25	1.80	0.025	0.025	balance

the material after heat treatment were determined by tensile test (ultimate tensile strength 1740 MPa, yield strength 1525 MPa and hardness 48 HRC). Engineering stress-strain curve obtained through the test is shown in Fig. 3.3. The specimens were fatigue pre-cracked after the heat treatment to generate a sharp circumferential crack at the root of the machined notch.

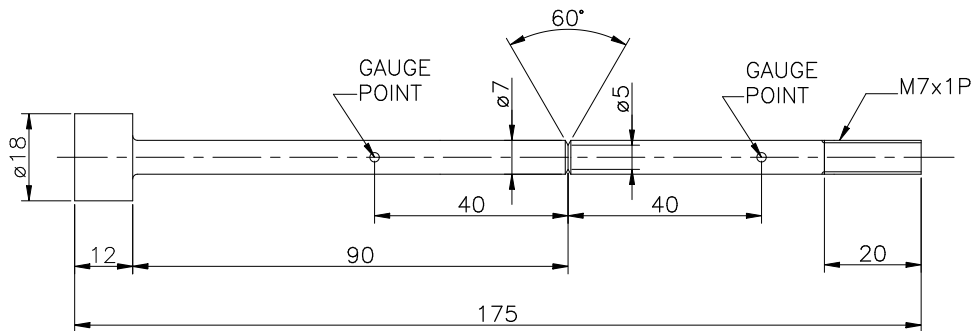


Fig. 3.2 Dimensions of CNT specimen (in mm).

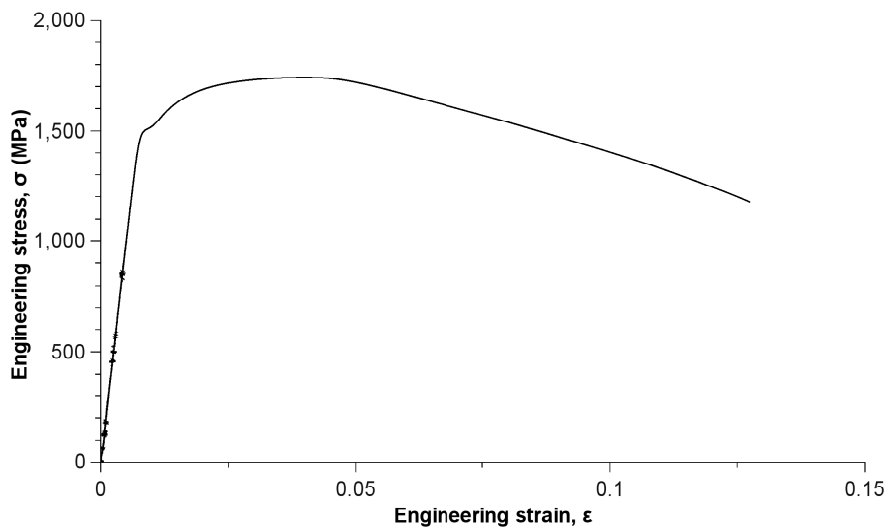


Fig. 3.3 Experimental engineering stress-strain curve for AS-4340 material.

3.2.2 Fatigue pre-cracking

A rotating bending machine (Fig. 3.4) was used for fatigue pre-cracking. The machine was driven by an electric motor. It had a spindle for holding the test specimen. Eight choices for the speed were available. The specimen was held fixed at one end and the other end was free. The

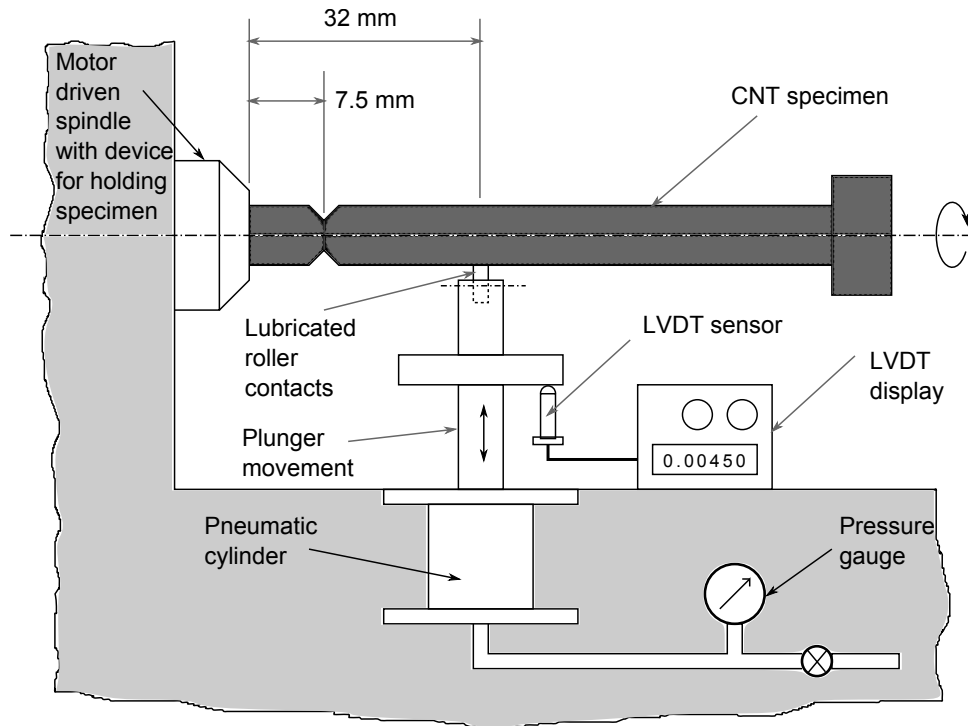


Fig. 3.4 Schematic of rotating bending machine used for fatigue pre-cracking.

notch was placed at 7.5 mm off the fixed end. It was subjected to bending load at a distance of 32 mm from the fixed end. The load was applied by a pneumatically operated plunger. A pair of lubricated rollers placed between the plunger and specimen helped to prevent any damage to the specimen surface during spinning. The plunger force was adjustable through manipulation of pneumatic pressure, which was constantly monitored by a pressure gauge.

The fatigue pre-crack initiated in the specimen was not visible directly and its size could not be measured easily. The size was monitored approximately through measurement of change in transverse deflection of the specimen. For this purpose, a linear variable differential transformer (LVDT) was employed (Fig. 3.4). The LVDT helped to measure movement of a plate attached conveniently to the pneumatic plunger. At the beginning of test, the specimen was set to spinning at a constant speed. The pneumatic pressure was adjusted to a fixed value and LVDT

reading was set to zero. Any growth in crack size lead to an increase in the transverse deflection of the specimen. This was measured by the LVDT. The combination of spinning speed, pneumatic pressure and transverse deflection required to achieve a fatigue crack depth was obtained by trial and error. The pre-cracking was stopped after attaining the critical deflection of the specimen.

In the present study, pre-cracking was done to the extent to achieve a crack root diameter of 4 mm approximately. The combination of parameters for this purpose is as follows: spindle speed rpm 2800, pneumatic pressure 250 kPa and LVDT display of 0.0045 units (1 display unit = 0.1 inch or 2.54 mm). The time needed for complete pre-cracking varied from 5 to 20 minutes. The stress intensity factor K_I during pre-cracking stage was restricted to $20 \text{ MPa} \sqrt{\text{m}}$ in order to restrict the size of crack tip plastic zone. K_I was calculated based on the plunger load and through relation given in Tada et al. (2000).

3.2.3 Test arrangement

After pre-cracking, specimen cylindrical surface was polished with SiC papers (upto 1200 grit). This was followed by cleaning with acetone and distilled water. The test specimen was wrapped by Teflon tape all over except over a 2.5 mm span on either side of the notch.

In the test setup, the specimen was enclosed by an acrylic environmental cell. The contact between the specimen and cell was plugged by Teflon seal at the bottom (Fig. 3.5). The cell was filled with 3.5% (weight) neutral NaCl solution. The cell top cover had openings for insertion of reference and counter electrodes. The solution inside cell was naturally aerated. The specimen was mounted vertically in the testing machine with a grease lubricated spherical washer provided at the bottom support. The washer helps to minimise minor misalignment, if any, in the loading axis. A few trial runs with and without the washer showed clearly its utility. A considerable reduction in scatter of load vs specimen elongation data was achieved using the spherical washer.

To measure the applied load, a load cell was fitted in between the cross-head and the specimen grip. Further, to measure specimen elongation, a special arrangement with two LVDTs (LVDT-1 and LVDT-2) was used. The two were adopted through two extension arm assemblies attached to the specimen, one 40 mm above and other 40 mm below the notch. The elongation

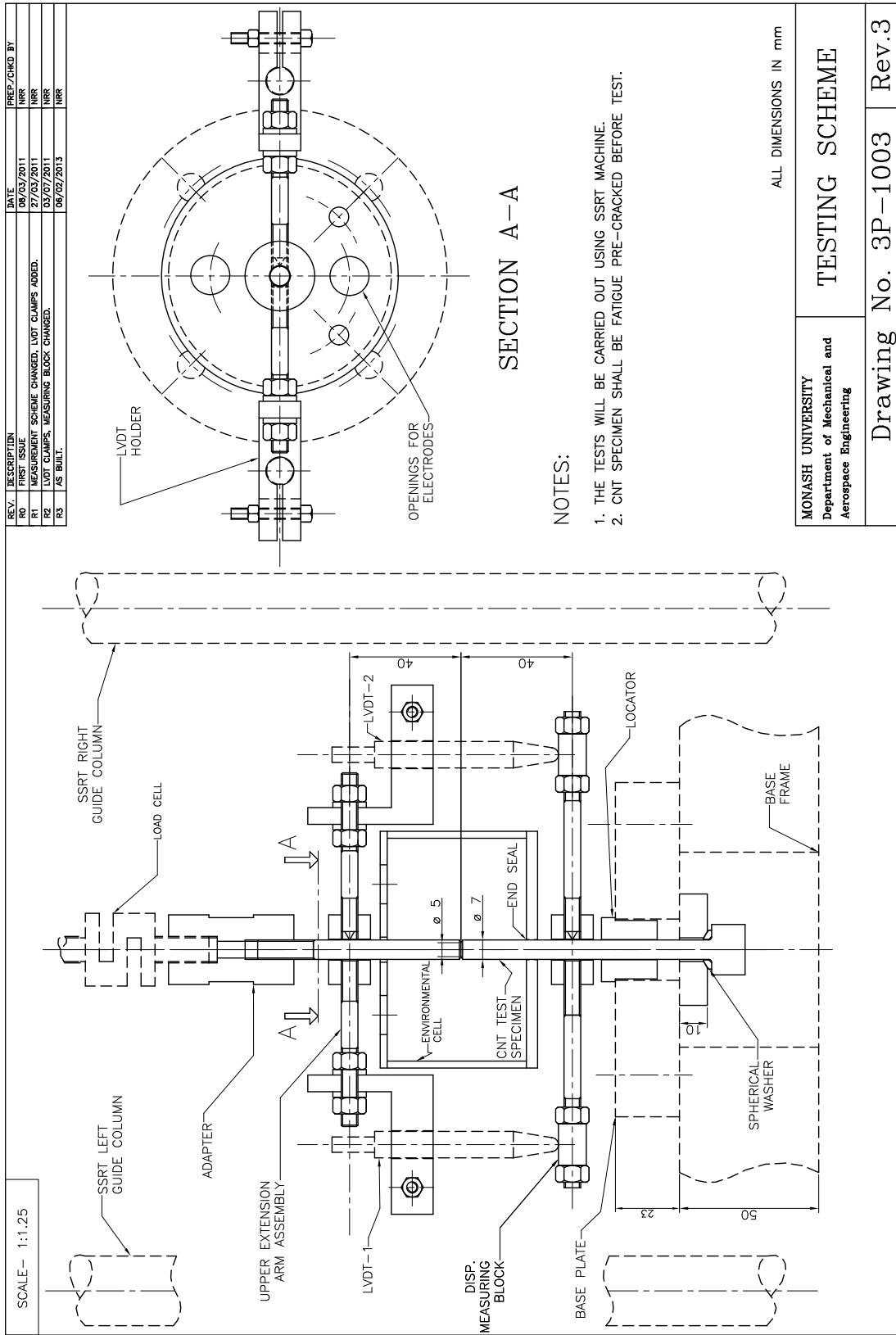


Fig. 3.5 Details of experimental arrangement.

δ_g over the gauge length of specimen was obtained from the change in the average reading of the two LVDTs. Readings from the two LVDTs were acquired through a data acquisition system. The electrical connection diagram for instruments is shown in Fig. 3.6.

Detailed drawings of components fabricated for the experimental set up, an outline of experimental procedure, instrument specifications and software employed are given in Appendix II.

3.2.4 Test details

All tests were conducted at room temperature under four environmental conditions: air, IHAC, HEAC and combination of IHAC and HEAC. For the IHAC investigations, the span of time for hydrogen charging was varied; whereas for the latter two cases (HEAC and IHAC+HEAC), the rate of loading (i.e., cross-head speed) was varied (Table 3.2).

During the HASCC experiments, the specimen was cathodically charged at a potential of -0.865 V (SCE) using a potentiostat for the entire duration of the test. For the IHAC investigations, the hydrogen charging was stopped and solution was drained from the environmental cell just before the cross-head motion commenced. A nominal load of less than 500 N was applied on the specimen during the pre-charging stage of IHAC and combined IHAC-HEAC tests. The charging potential was continuously monitored and recorded during the test period using the data acquisition system. For each test, the failure load was recorded. Using this data and the crack size K_{Ic}^H was computed.

The fracture surface of the test specimens was ultrasonically cleaned for removal of corrosion products and then examined by scanning electron microscope (SEM). The solution used during ultrasonic cleaning contained 6 mL concentrated hydrochloric acid + 10 mL of 30 g/L of 2-butyne-1,4-diol + 100 mL distilled water.

3.3 Determination of K_I

The fatigue pre-cracking through rotating bending operation generally leads to crack profiles which are eccentric with respect to the axis of test specimen (Fig. 3.7). The calculation of K_I requires consideration of additional bending moment arising out of this eccentricity. For this purpose, a method developed by Ibrahim and Stark (1990) has been used (R.K. Singh Raman

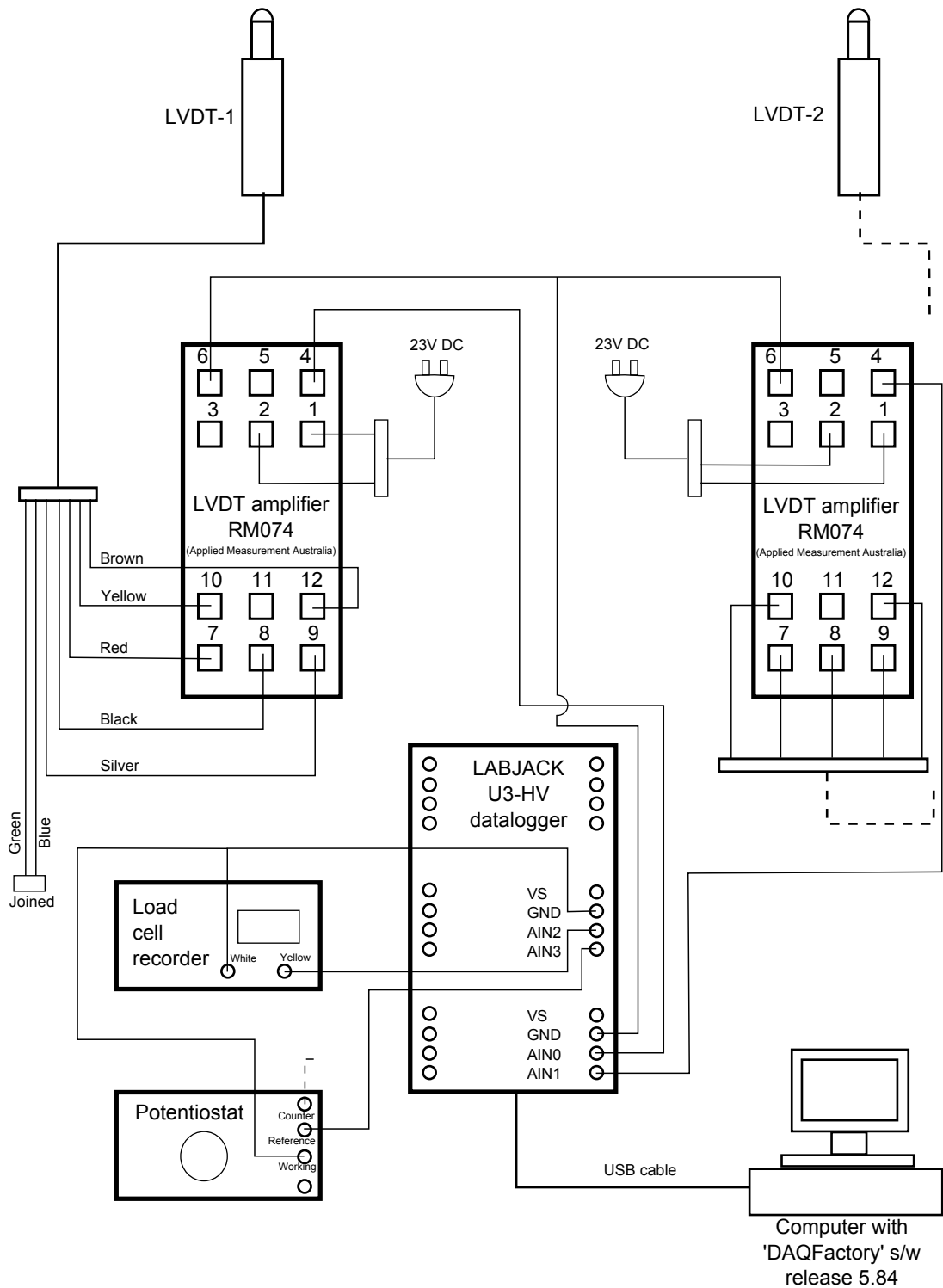


Fig. 3.6 Electrical connection diagram.

Table 3.2 Experimental details.

Case title	Specimen tag	Hydrogen pre-charging duration (h)	Cross-head speed (mm/h)	Strain rate in specimen (mm/mm/h)	d (mm)	e_1 (mm)
Air	S28	0	-	2.0×10^{-2}	3.40	0.90
	S30	0	-	2.0×10^{-2}	3.44	0.70
IHAC	S14	12	0.10	1.0×10^{-4}	3.32	0.66
	S27	12	0.10	1.0×10^{-4}	3.80	0.62
	S13	24	0.10	1.0×10^{-4}	4.00	0.16
HEAC	S20	0	0.0014	1.8×10^{-6}	4.40	0.24
	S17	0	0.0019	2.5×10^{-6}	3.52	0.26
	S21	0	0.0019	2.3×10^{-6}	3.48	0.36
	S22	0	0.02	1.9×10^{-5}	3.76	0.12
	S24	0	0.02	2.1×10^{-5}	3.48	0.54
	S25	0	0.10	1.5×10^{-4}	3.40	0.60
	S26	0	0.10	1.2×10^{-4}	3.40	0.52
IHAC+	S15	12	0.02	2.3×10^{-5}	4.08	0.26
	S18	12	0.02	2.1×10^{-5}	3.92	0.16
HEAC	S16	12	0.10	1.2×10^{-4}	3.08	0.14
	S19	12	0.10	1.2×10^{-4}	3.92	0.26

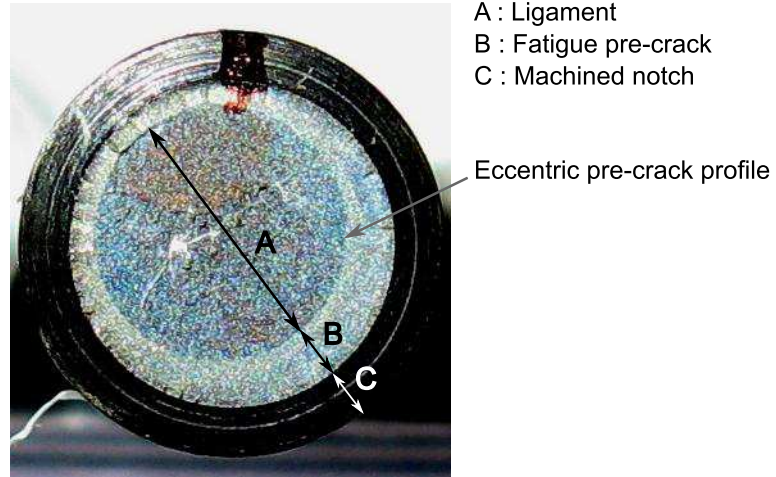


Fig. 3.7 Eccentricity of fatigue pre-crack profile.

et al., 2006, 2007a, 2007b; Rihan et al., 2007; Ibrahim et al., 2008; Wu et al., 2009). K_I is calculated using the following relations.

$$K_I = (\sigma_t + \sigma_b) \sqrt{a\pi F_0} \quad (3.1)$$

where

$$a = \frac{D - d}{2} \quad (3.2)$$

$$\sigma_t = \frac{4P}{\pi D^2} \quad (3.3)$$

$$\sigma_b = \frac{16Pe_1}{\pi D^3} \quad (3.4)$$

$$F_0 = F e^{\alpha(e_1/D)} \quad (3.5)$$

$$F = \frac{1.25}{[1 - (2a/D)^{1.47}]^{2.4}} \quad (3.6)$$

$$\alpha = 22.188e^{-4.889(2a/D)} \quad (3.7)$$

σ_t and σ_b are tensile and bending stresses respectively. F_0 and F are geometric factors for the

round specimen with and without eccentricity respectively. α is a constant. Functions for F_0 and α were obtained by Ibrahim and Stark (1990) to fit the experimental data for 56 specimen geometries with K_I calculated from finite element study for each individual specimen. P is the applied load, D is the specimen diameter, d is the equivalent ligament diameter, e_1 is the eccentricity and a is effective crack length (Fig. 3.8). The procedure for calculating d and e_1 is explained later in this section.

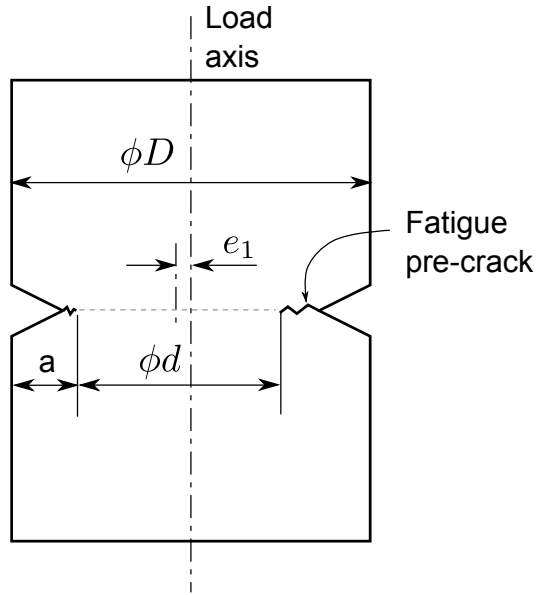


Fig. 3.8 Geometry of CNT specimen.

The initial K_I is first estimated using Eq. 3.1 for a given crack length a . The crack size a is corrected to \bar{a} using the Irwin correction factor r_y . That is,

$$r_y = \frac{1}{6\pi} \left(\frac{K_I}{\sigma_Y} \right)^2 \quad (3.8)$$

$$\bar{a} = \text{corrected crack size} = a + r_y \quad (3.9)$$

where σ_Y is the 0.2% offset tensile yield stress. The corrected K_I is then recalculated from Eq. 3.1 using \bar{a} .

3.3.1 Computation of d and e_1

After completion of test, the fractured surface of test specimen is examined under profile projector (Fig. 3.9). The coordinates of around 12 to 16 points on the circumference of both pre-crack and machined notch profiles are accurately recorded. This data are transferred to computer for digital reproduction of pre-crack and machined notch profiles. A geometric analysis (Fig. 3.10) is performed using drafting software to obtain d and e_1 as described below.

The center of machined notch (point O) is graphically located. Twelve equi-spaced radial lines are drawn through O. These rays intersect the pre-crack profile at points marked 1,2, ... Along each of these rays, the depth of machined notch a_{mi} and depth of pre-crack a_{fi} are measured. The area A_{pc} bounded by the pre-crack profile is obtained by summing areas A_{wi} , $i = 1,2, \dots, 12$, as follows.

$$A_{wi} = \frac{\pi}{12} \left(\frac{D}{2} - a_{mi} - a_{fi} \right)^2 \quad (3.10)$$

The equivalent diameter d of pre-crack profile is calculated by area equivalence. That is,

$$d = \sqrt{\frac{4}{\pi} A_{pc}} \quad (3.11)$$

Area moments of these sectors about the axes X and Y are as follows.

$$M_{xi} = \frac{\pi}{18} \left(\frac{D}{2} - a_{mi} - a_{fi} \right)^3 \sin \theta_i \quad (3.12)$$

$$M_{yi} = \frac{\pi}{18} \left(\frac{D}{2} - a_{mi} - a_{fi} \right)^3 \cos \theta_i \quad (3.13)$$

where $i = 1, 2, \dots, 12$; θ_i is the angular orientation of ray i with respect to X-axis. The location of centroid (\bar{X}, \bar{Y}) of the pre-crack area with respect to O is given by

$$\bar{X} = \frac{\sum_{i=1}^{12} M_{yi}}{\sum_{i=1}^{12} A_{wi}} \quad (3.14)$$



Fig. 3.9 Profile projector used to measure crack size (Pal, 2010).

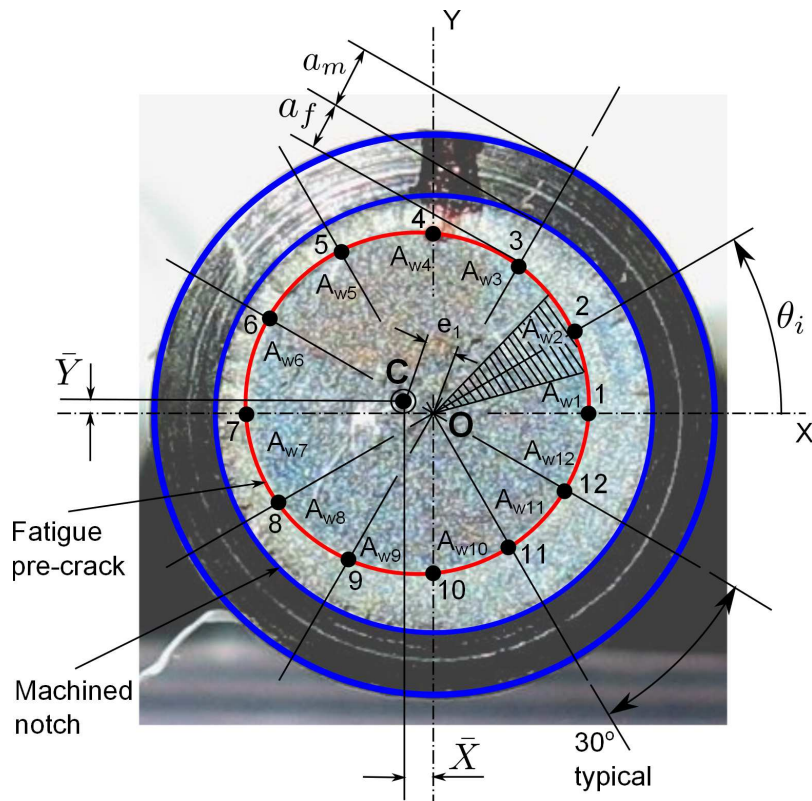


Fig. 3.10 Geometric analysis of pre-crack profile.

$$\bar{Y} = \frac{\sum_{i=1}^{12} M_{xi}}{\sum_{i=1}^{12} A_{wi}} \quad (3.15)$$

The eccentricity e_1 is calculated from \bar{X} and \bar{Y} .

$$e_1 = \sqrt{\bar{X}^2 + \bar{Y}^2} \quad (3.16)$$

3.3.2 Validity requirements

The concept of linear elastic fracture mechanics (LEFM) is valid for situations where the size of plastic zone near the crack tip is sufficiently small as compared to the crack size. According to Stark and Ibrahim (1986) and Ibrahim and Stark (1987) this is ensured provided the following conditions are satisfied.

- (a) Fatigue crack depth a_f should be at least twice the Irwin correction factor r_y

$$a_f \geq 2r_y \quad (3.17)$$

where $a_f = e_1 + (D - 2a_m - d)/2$ and a_m is the machined crack length.

- (b) Average axial stress in the final ligament σ_N should be less than 2.5 times the yield strength

$$\frac{\sigma_N}{\sigma_Y} \leq 2.5 \quad (3.18)$$

where the σ_N is the average axial stress across ligament.

Both these requirements have been ensured for all the tests reported here.

3.4 Results and discussion

The fracture toughness (K_{Ic}^H) for material AS-4340 steel has been determined in air and IHAC, HEAC and combined IHAC-HEAC. The toughness K_{Ic}^H and other data useful for checking va-

Validity are presented in Table 3.3. The validity requirements are fully satisfied.

Table 3.3 Calculated values of K_{Ic}^H and compliance with validity requirements.

$$\text{Validity requirements: } a_f > 2r_y \text{ and } \frac{\sigma_N}{\sigma_Y} < 2.5$$

Test condition	Specimen identification	K_{Ic}^H (MPa \sqrt{m})	$2r_y$ (mm)	a_f (mm)	$\frac{\sigma_N}{\sigma_Y}$
Air	S28	54.30 (= K_{Ic})	0.134	1.86	0.88
	S30	47.70 (= K_{Ic})	0.104	1.62	0.74
IHAC	S14	30.42	0.042	1.71	0.51
	S27	23.90	0.026	1.35	0.34
	S13	11.68	0.006	0.74	0.18
HEAC	S20	9.64	0.004	0.69	0.14
	S17	11.51	0.006	1.16	0.19
	S21	10.68	0.005	1.24	0.17
	S22	10.27	0.005	0.85	0.17
	S24	11.86	0.006	1.37	0.18
	S25	14.15	0.009	1.51	0.23
	S26	18.22	0.015	1.40	0.29
IHAC+	S15	11.37	0.006	0.87	0.17
	S18	8.80	0.004	0.83	0.14
HEAC	S16	15.19	0.011	1.21	0.28
	S19	12.00	0.007	0.92	0.18

3.4.1 IHAC tests

For the IHAC tests, the hydrogen concentration distribution around the crack tip was varied by changing duration of the pre-charging time. This is consistent with the practice in the literature (Dietzel and Pfuff, 1996). A plot of the SIF at failure (K_{Ic}^H) against the span of pre-charging time is shown in Fig. 3.11. As expected, the fracture toughness reduces with an increase in the average level of hydrogen concentration in the material immediately ahead of the crack tip with increasing pre-charging time.

The data K_{Ic}^H corresponding to 24 h pre-charging is $\sim 10 \text{MPa} \sqrt{m}$. The variation (Fig. 3.11) appears to be flat around this span of pre-charging time. This may indicate that, for pre-charging

span more than 24 h, the material may demonstrate no significant change in K_{Ic}^H value. This toughness can be considered to be close to the threshold SIF for this condition of testing, because further exposure does not cause any change in the damage in the material. K_{Ic}^H quoted in the literature for the material at 23 °C in NaCl and other environments, 10–15 MPa \sqrt{m} (R.K. Singh Raman et al., 2007b; Craig, 2003a), is close to the present data on the minimum K_{Ic}^H .

3.4.2 Analysis of hydrogen distribution during IHAC tests

The average hydrogen concentration immediately ahead of the crack tip has been computed through finite element analysis. The hydrogen distribution ahead of the crack tip is governed by the diffusion process. The diffusion of hydrogen during the pre-charging for the axi-symmetric geometry is governed by the following diffusion equation:

$$\frac{\partial C}{\partial t} = D_{eff} \left(\frac{\partial^2 C}{\partial r^2} + \frac{1}{r} \frac{\partial C}{\partial r} \right) \quad (3.19)$$

where t is time, r is radius, C is hydrogen concentration and D_{eff} is effective diffusivity of hydrogen in the material.

The diffusion equation has been solved using finite element code ABAQUS® (2006) neglecting any eccentricity of the ligament at $t > 0$. For the computations, the hydrogen concentration C was normalised, $C = \frac{C_{abs}}{C_{env}}$, where C_{abs} is the absolute concentration inside the material and C_{env} is the environmental concentration of hydrogen. This method avoids the need for a direct measurement of C_{env} which is usually a difficult task. The domain for analysis, finite element mesh and the boundary conditions are shown (Fig. 3.12). One half of CNT specimen was discretised with elements DCAX8 (axisymmetric mass diffusion element with single degree of freedom) of ABAQUS®. Total elements used are 13,825. The element size 0.1 mm was decided based on a convergence study. At $t = 0$, the hydrogen concentration $C = 0$ was assumed throughout the domain. The boundary condition considered is as follows: for $t \geq 0$, $C = 1$ on the external surface (PQR) up to 2.5 mm distance from the crack plane. The crack flanks are also assumed to be at the same state. The effective diffusivity D_{eff} for steel is in the range of 2×10^{-6} to 2×10^{-3} mm²/s. Due to their relatively higher trap density, D_{eff} of the high strength steels tends towards the lower values of this range (Gerberich et al., 1975). The diffusion analysis was done

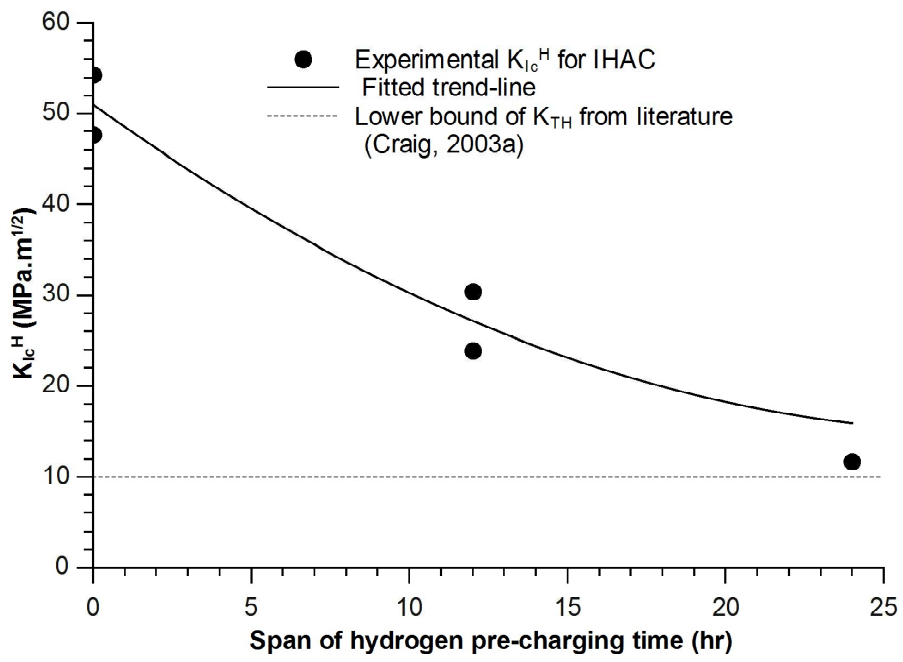


Fig. 3.11 K_{Ic}^H vs. hydrogen pre-charging span results for IHAC.

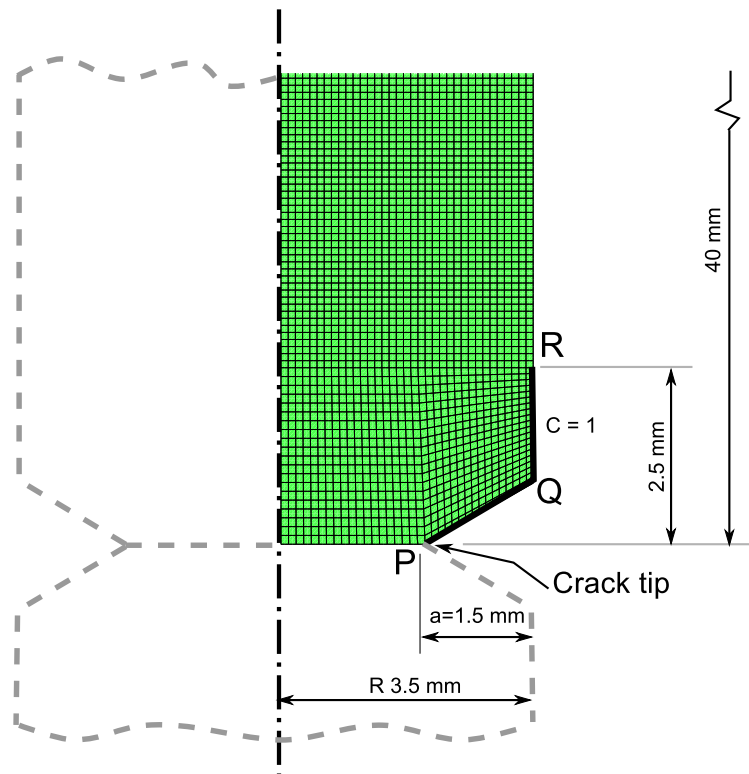


Fig. 3.12 Finite element mesh and boundary conditions.

for two values of D_{eff} : 2×10^{-6} and 5×10^{-6} mm²/s. A typical hydrogen distribution obtained after 12 hours of pre-charging is shown in Fig. 3.13.

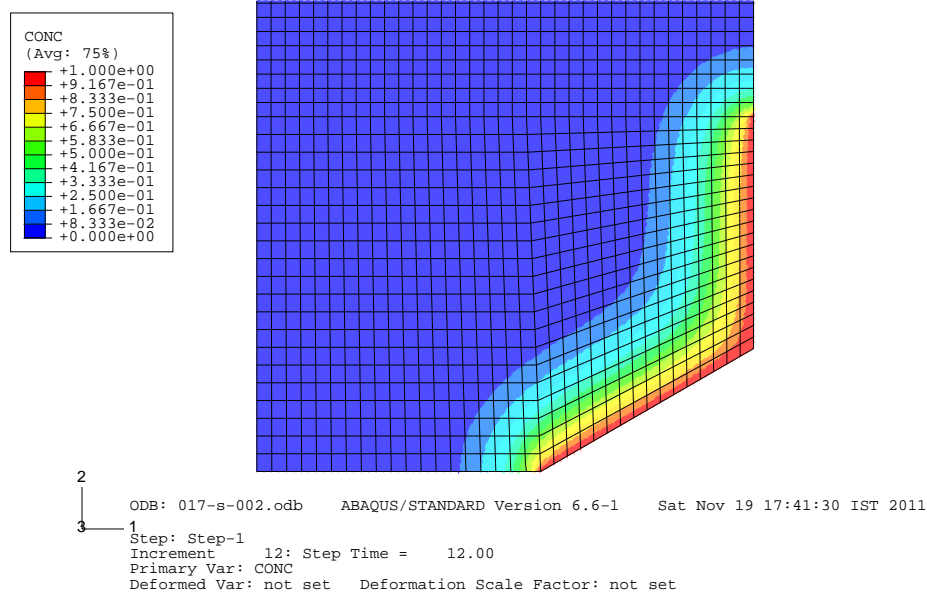


Fig. 3.13 Normalised hydrogen concentration distribution at $t = 12$ h for $D_{eff} = 2 \times 10^{-6}$ mm²/s.

The average hydrogen concentration C_{avg} was computed for different pre-charging durations and at different spans from the crack tip. A variation of average concentration C_{avg} over a distance of 0.3 mm from the crack tip with time is presented (Fig. 3.14). Some earlier studies (Scheider et al., 2008) have established that an increase in C_{avg} leads to a decrease in the decohesion resistance. Accordingly, the parameter $(1 - C_{avg})$ can be considered to be an indicator of the decohesion resistance of the material. Fig. 3.14 shows plots of both $(1 - C_{avg})$ and K_{Ic}^H against the pre-charging time for the two values of D_{eff} . The plots clearly show the dependence of the fracture toughness on the hydrogen concentration ahead of crack tip.

3.4.3 HEAC and combined IHAC-HEAC tests

For the HEAC tests carried out at the lowest cross-head speeds (0.0014–0.0019 mm/h), the durations of loading (130–230 h) were much longer as compared to the durations (3–20 h) for the other cross-head speeds. Because of the prolonged duration of the test at the lowest speed, the hydrogen distribution can be presumed to be uniform and the material can be considered to be fully saturated towards the later part of the tests. The additional pre-charging time span of

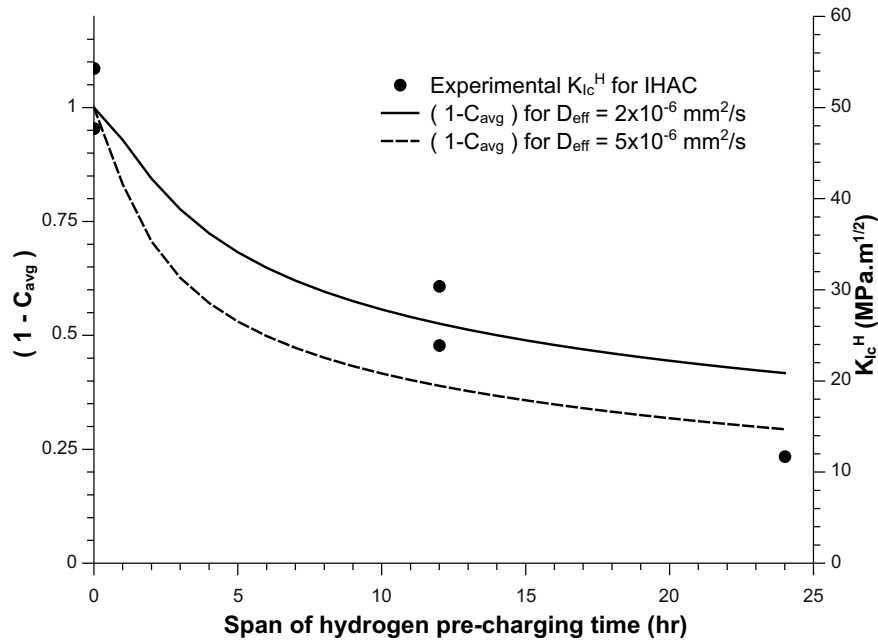


Fig. 3.14 Plots of $(1 - C_{avg})$ and K_{Ic}^H with hydrogen pre-charging time.

12 hours for the combined IHAC and HEAC test was assumed to have an insignificant effect on the hydrogen distribution, and hence negligible influence on the K_{Ic}^H at failure. Hence K_{Ic}^H data for the pure HEAC tests can be easily considered to correspond to the combined IHAC-HEAC situation. The data for combined IHAC-HEAC is presented as per this consideration.

For the HEAC and combined IHAC-HEAC experiments, the cross-head speed was varied for the purpose of changing the duration of hydrogen exposure at the crack tip. Figs. 3.15 and 3.16 respectively present the variations of stress intensity factor at failure (K_{Ic}^H) against the cross-head speed for the two situations, HEAC and combined IHAC-HEAC. The slower crack tip strain rate is reported to have an adverse effect on the fracture strength during HASCC (Krom et al., 1999). This is attributed to the longer time available for higher hydrogen ingress at the crack-tip at a slower loading rate. Consequently, K_{Ic}^H was found to decrease gradually with the reduction in cross-head speed in the case of HEAC (Fig. 3.15). The presence of additional hydrogen due to pre-charging in the case of combined IHAC-HEAC testing is manifested as a further drop in K_{Ic}^H (Fig. 3.16). K_{Ic}^H approached the K_{TH} towards the lowest range of the cross-head speed (0.0015–0.0020 mm/h). This regime corresponds to an infinitesimally slow cross-head speed.

The theoretical investigations into HEAC and combined IHAC-HEAC are more involved

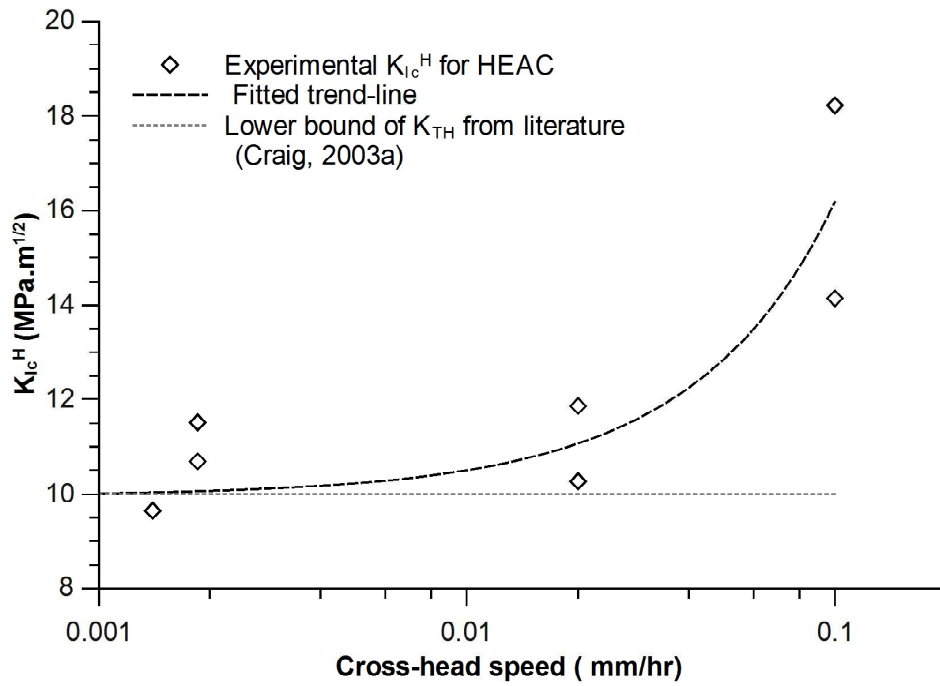


Fig. 3.15 K_{Ic}^H vs. cross-head speed for HEAC.

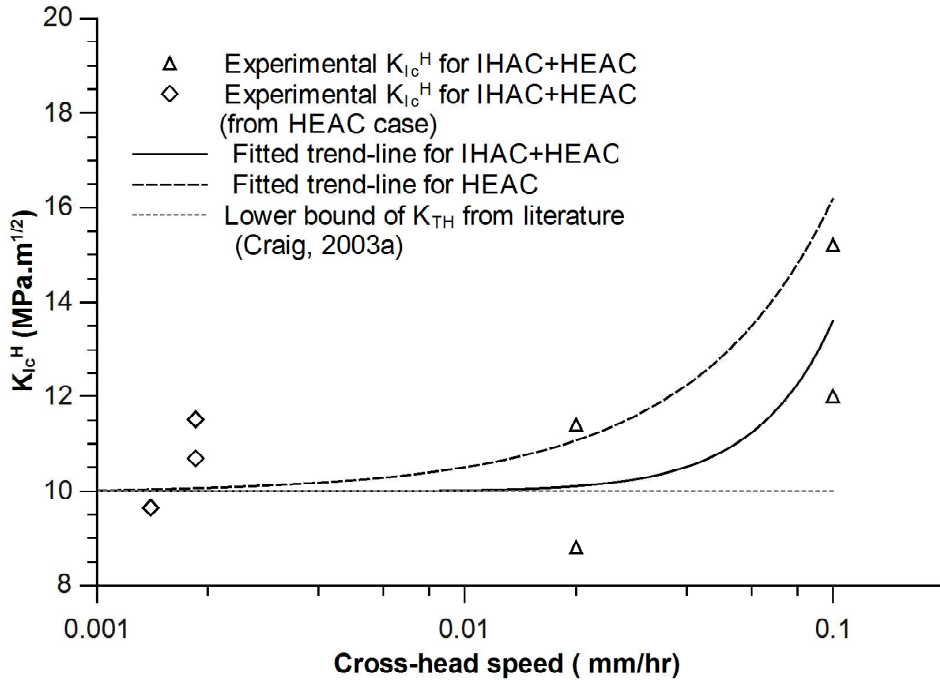


Fig. 3.16 K_{Ic}^H vs. cross-head speed for combined IHAC and HEAC.

compared to the case of IHAC due to the additional influences of the crack tip stress field and the strain rate on the hydrogen transport. Analyses of these situations are taken up in chapter 5.

3.4.4 Crack growth rate

The crack growth rate has been approximately calculated using the experimentally obtained data of axial load P and elongation δ_g of test specimen over gauge length. Typical variations of P vs. δ_g are shown in Fig. 3.17 for IHAC, HEAC and combined IHAC+HEAC cases. The variation of P vs. δ_g is linear prior to reaching the maximum load P_{max} for all the cases. The sharp deviation from the linearity after reaching P_{max} may be due to initiation of crack growth.

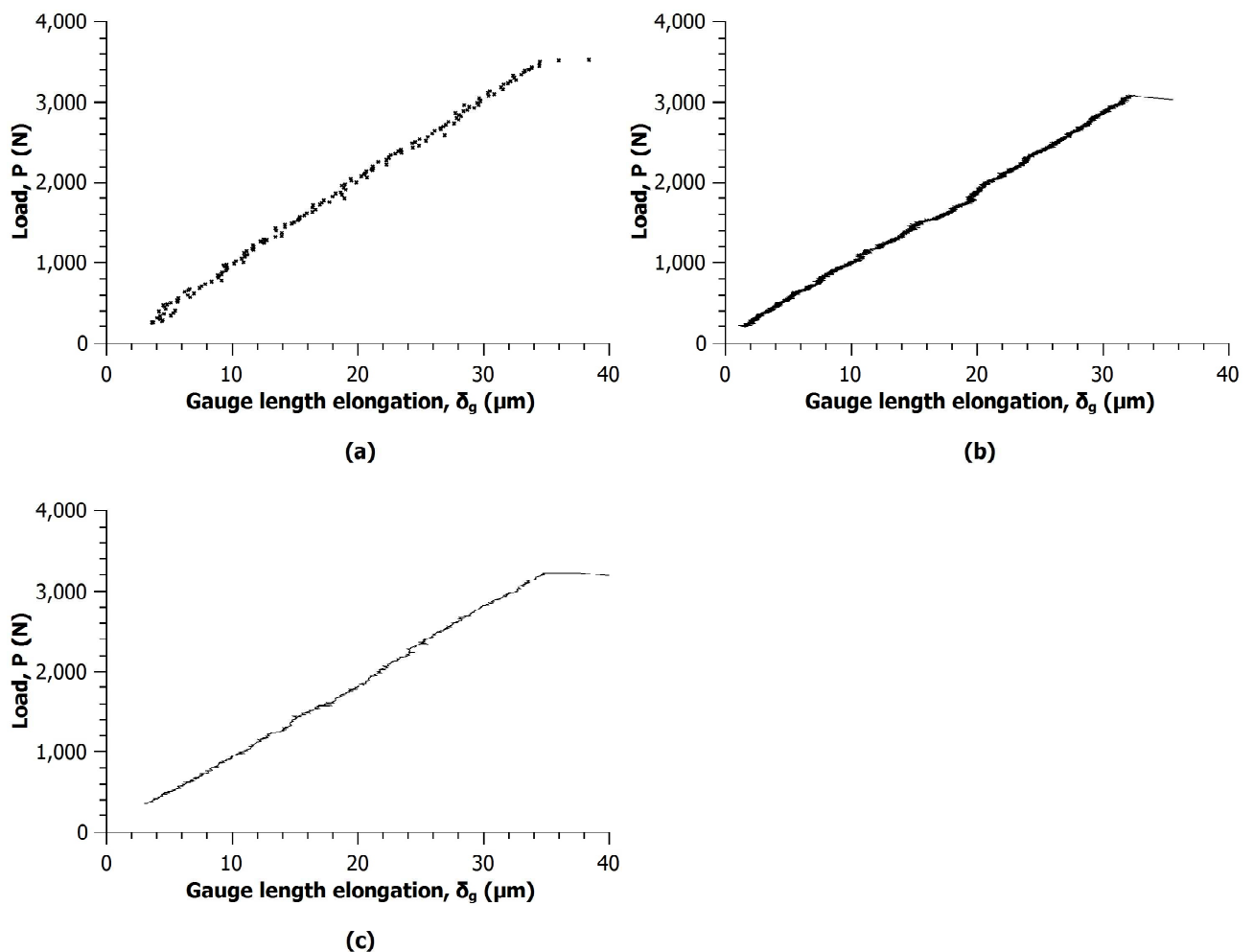


Fig. 3.17 Typical load vs elongation variation for (a) IHAC case, specimen S13; (b) HEAC case, specimen S20 and (c) combined IHAC and HEAC case, specimen S15.

The span of time Δt_f from this stage up to total separation/failure has been obtained through recoding of P vs. time data for each specimen. A typical P vs. time variation for specimen S15 is shown in Fig. 3.18. Δt_f is the time span between point A (crack initiation) and point B (total failure). During this span Δt_f the crack grows over entire ligament ($= d/2$). The average crack growth rate $\frac{da}{dt}$ over this span is given by

$$\frac{da}{dt} = \frac{\Delta a_f}{\Delta t_f} \quad (3.20)$$

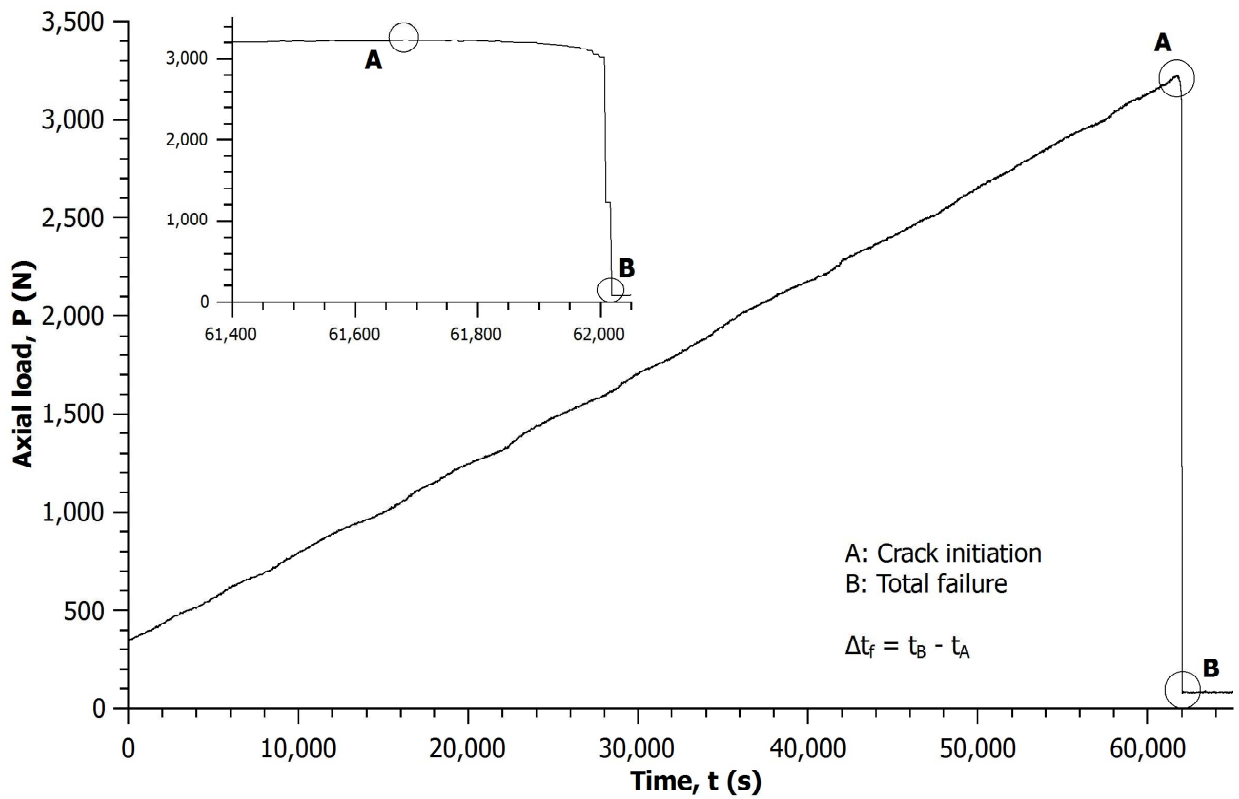


Fig. 3.18 Typical load vs time variation (specimen S15).

Table 3.4 shows $\frac{da}{dt}$ data for all the specimens. The average crack speed is observed to be higher for faster rates of loading dP/dt (Fig. 3.19). The interdependency is more or less linear. The similar trend is also reported by Mayville et al. (1989) and Dietzel and Ghosal (1997).

Kalnaus et al. (2011) conducted SCC experiments involving determination of $\frac{da}{dt}$ for almost identical grade of material (AISI-4340 steel, $\sigma_Y=1503$ MPa) and in aqueous NaCl environment. Circular CT specimen were employed in their test in neutral NaCl solution of varying concen-

Table 3.4 Crack growth rate calculations.

Case title	Specimen tag	Δa_f (mm)	Δt_f (s)	da/dt (mm/s)
IHAC	S14	1.7	22.5	7.38×10^{-2}
	S27	1.9	30.0	6.33×10^{-2}
	S13	2.0	130.0	1.54×10^{-2}
HEAC	S20	2.2	1470.0	1.50×10^{-3}
	S17	1.8	560.0	3.14×10^{-3}
	S21	1.7	680.0	2.56×10^{-3}
	S22	1.9	310.0	6.06×10^{-3}
	S24	1.7	520.0	3.35×10^{-3}
	S25	1.7	240.0	7.08×10^{-3}
	S26	1.7	210.0	8.10×10^{-3}
IHAC+	S15	2.0	332.0	6.13×10^{-3}
	S18	2.0	310.0	6.32×10^{-3}
HEAC	S16	1.5	160.0	9.63×10^{-3}
	S19	2.0	120.0	1.63×10^{-2}

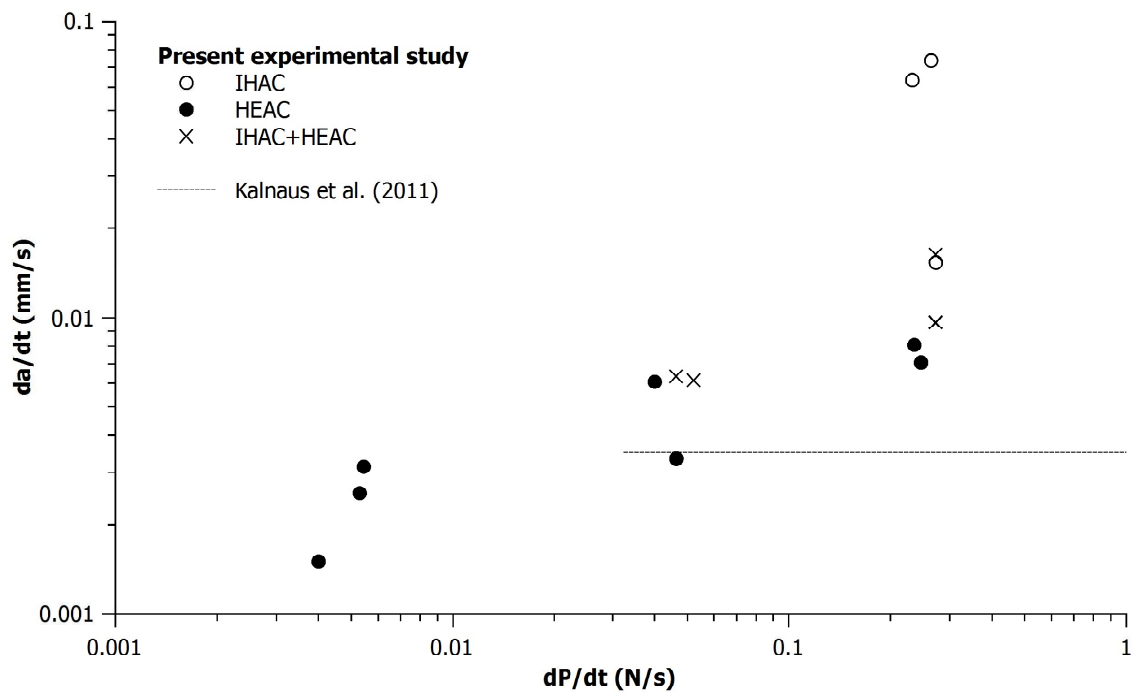


Fig. 3.19 Plot of crack growth rate vs. loading speed.

trations (0 to 3.5%). The experiments were conducted under HEAC condition, without cathodic charging. They tested for both steady and rising load conditions. $\frac{da}{dt}$ was reported for rates of loading ranging from 0.03 to 1.0 N/s. A nearly constant crack growth rate of 3.5×10^{-3} mm/s was observed (Fig. 3.19). The average crack velocity under HEAC conditions in the present study is observed as 4.5×10^{-3} mm/s. The higher crack growth rate in the current work and its variation with loading rate may be attributed to the greater availability of hydrogen near crack tip due to additional factor of cathodic charging.

The published data on HASCC crack growth rates for similar material and under similar environmental conditions vary widely from 10^{-5} to 10^{-1} mm/s (Ramamurthy et al., 2011) depending on specific experimental parameters. Crack growth rates obtained in the present work are in the range of 1.5×10^{-3} to 7.4×10^{-2} mm/s. Some of the related published data indicate similar crack growth rates, e.g., 1×10^{-3} to 1.6×10^{-3} mm/s (Sullivan, 1972), 4×10^{-3} to 9×10^{-3} mm/s (Macdonald and Chung, 1985) and 1×10^{-2} to 3×10^{-2} mm/s (Gerberich et al., 1988).

The data quoted for 4340 grade steel ($\sigma_Y=1470$ MPa) based on testing CNT specimen by Ibrahim et al. (2008) under constant load conditions is in the range of 1.0×10^{-7} to 3.0×10^{-6} mm/s. This range indicates a very low order of crack velocity. One of the reasons for the low rates is the fact that Ibrahim et al. (2008) conducted the tests near the threshold regime.

3.4.5 Fractography

Fig. 3.20a represents the overall fractograph of a failed CNT specimen under HEAC condition. Overall fractograph consist of four regions: machined notch, fatigue pre-crack, HASCC and sudden failure zone. The distinct features of each region become clear at higher magnification. The fatigue pre-crack region is exclusively characterised by striation marks running from the circumference (Fig. 3.20b). Fig. 3.20c shows the transition from fatigue pre-crack zone to HASCC zone. HASCC region is characterized by intergranular cracking/fracture (Fig. 3.20d). This presence of intergranular fracture is a typical hydrogen effect, which is generally caused by the preferential crack growth along the prior austenite grain boundaries. This observation is consistent with the features of hydrogen embrittlement reported for this steel (R.K. Singh Raman et al., 2007b; Shim and Byrne, 1990). The crack propagates in the intergranular fashion until the critical stress intensity K_{Ic}^H is attained. At this stage, mechanical overloading takes

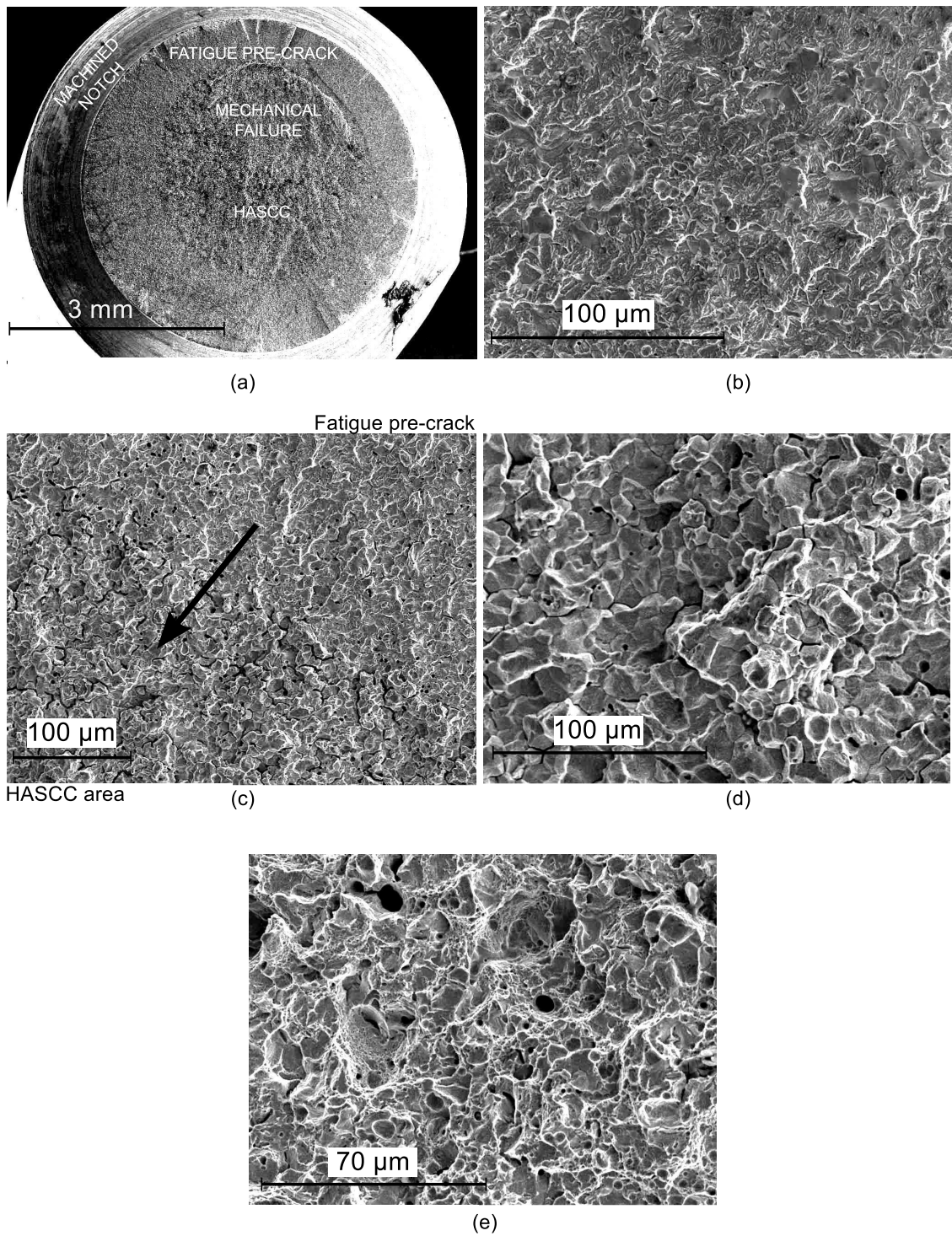


Fig. 3.20 SEM fractographs of CNT specimen (S17): (a) overall fracture surface; (b) fatigue pre-crack area; (c) transition from fatigue pre-crack to HASCC area (arrow indicates crack growth direction); (d) HASCC area suggesting intergranular crack propagation; (e) region of sudden failure.

over. Accordingly, the central part of the fracture surface reveals ductile failure characterised by dimple formations (Fig. 3.20e), thereby confirming that the final failure indeed occurs by mechanical overloading.

3.5 Closing remarks

The HASCC behaviour of high strength alloy steel AS-4340 has been studied experimentally, employing the novel CNT tests. During the IHAC, a progressive reduction in K_{Ic}^H with increasing amount of hydrogen is observed. During the HEAC and combined IHAC-HEAC tests, a reduction in the value of K_{Ic}^H with the decrease in rates of loading is noticed. The fracture toughness (K_{Ic}^H) approaches the threshold fracture toughness (K_{TH}) reported in the literature for similar material in the IHAC tests with longer duration of pre-charging, and in both HEAC and combined IHAC-HEAC tests with slower loading rates.

The computed hydrogen distribution ahead of the crack tip is observed to have a distinct influence on the fracture data obtained during the IHAC test. This confirms the existence of the HEDE mechanism. The crack growth speed $\frac{da}{dt}$ is observed to be directly dependent on the loading rate. Higher loading rates lead to higher crack speed. The present crack speed data for HEAC compare well with the data reported in the literature. This agreement may indicate that CNT geometry is a viable geometry for collection of material data under HASCC conditions for high strength steels. The present results provide distinct fractographic evidence of intergranular failure under HASCC. This too is in conformity with earlier observation reported in the literature.

Chapter 4

Analysis of HASCC through CT specimen

4.1 Introduction

The cohesive zone model (CZM) offers a relatively simple and effective approach for crack growth modelling under HASCC. A new approach involving uncoupled analytical solution of diffusion equation and finite element analysis of crack extension has been evolved to study HASCC growth through rectangular panels¹. The effects of hydrostatic stress and plastic strain at the crack tip region on the crack growth have also been examined.

4.2 Scheme I for HASCC modelling

Under HASCC, the specimen is surrounded by a corrosive medium. Hydrogen in the environment finds its way into the specimen material through diffusion. A simple diffusion equation can be written as

$$\frac{\partial C}{\partial t} = D_{eff} \nabla^2 C \quad (4.1)$$

¹Most data reported in this chapter have been published in the following two papers.

Raykar N. R., Maiti S.K., R. K. Singh Raman (2011), 'Modelling of mode-I stable crack growth under hydrogen assisted stress corrosion cracking', *Engineering Fracture Mechanics*, **78**(18), 3153-3165.

Raykar N. R., Maiti S.K., R. K. Singh Raman (2012), Influence of hydrostatic stress distribution on the modelling of hydrogen assisted stress corrosion crack growth, in 'Proceedings of 10th World Congress on Computational Mechanics (WCCM2012 CD-ROM), Sao Paulo, Brazil'

where C is hydrogen concentration and D_{eff} is effective diffusivity. If the specimen is simultaneously loaded in the presence of stress concentrators like a crack, the ingress of hydrogen into the material increases. Absorption of hydrogen leads to a reduction in its fracture resistance and cohesive strength. Thereby, the crack growth enhances. The growth of crack leads to creation of new surfaces, which, in turn, affects the diffusion of hydrogen. Thus the process of diffusion and crack growth gets coupled. An analysis of such crack growth requires solution of diffusion equation and crack growth analysis. Some investigators have analysed the diffusion equation through numerical methods, e.g., finite element method (FEM). Thereby concentration distribution of hydrogen in the component is obtained. With this knowledge of concentration distribution, the modification in fracture properties of the material around the crack tip is ascertained. A crack growth model based on, for example, finite element analysis and hydrogen concentration dependent material properties can help to study the crack growth. This sort of uncoupled or sequential analysis of diffusion followed by study of crack growth can help to evaluate the effects of various influential parameters.

The cohesive zone model (CZM) of crack growth has been exploited by some investigators (Serebrinsky et al., 2004; Scheider et al., 2008; Olden et al., 2009; Moriconi et al., 2011) in this connection. Through hydrogen concentration dependent cohesive zone model, termed here as HCD-CZM, the hydrogen distribution around crack tip and level of damage to the crack growth resistance of material can be simultaneously computed.

The hydrogen distribution is obtained through diffusion calculations. While a hydrogen atom generated near crack surface will generally combine with other hydrogen atom to form hydrogen gas (bubble) at the metal surface and escape, some hydrogen atoms diffuse into the metal (before getting an opportunity to combine with other atom). Such hydrogen atoms lodge themselves at several high energy locations, particularly, near crack tip. This transport of hydrogen atoms into metal is influenced by pressure, temperature, metal microstructure, hydrostatic stress, and plastic strain. The amount of hydrogen inside trap sites is related to the number of trap sites and the number depends on the magnitude of plastic strain. The quantum of hydrogen inside lattice sites depends on the hydrostatic stress. Although the peak concentration of lattice hydrogen occurs at a distance little ahead of crack tip, the distribution of total (trapped and lattice) hydrogen is dominated by the variation of plastic strain. Since the strain is highest at

the crack tip, so does the hydrogen concentration (Sofronis and McMeeking, 1989) . Here, the hydrostatic stress is assumed to have a minor influence on the distribution of total hydrogen near the crack tip. Therefore it can be neglected for diffusion analysis of hydrogen and subsequent damage calculations. The effective diffusivity D_{eff} chosen in the modelling is mostly adjusted to represent average effect of plastic strain on hydrogen diffusion. D_{eff} also takes into account the effects of microstructure. For situations where there are no thermal fluctuations, the effect of temperature on diffusion can be ignored.

In this chapter, stable crack growth through a compact tension specimen of structural steel is simulated under rising displacement loading and hydrogen charging corresponding to a typical sea water environment. While finite element method has been used by Scheider et al. (2008) and Olden et al. (2009) to solve the diffusion equation (Eqn. 4.1), here an analytical method, both one and two dimensional, is proposed to obtain the distribution of hydrogen concentration around the crack tip. The finite element code ABAQUS[®], version 6.6 (2006) has been employed for modelling crack extension using element COH2D4, which is based on cohesive zone model (CZM).

4.2.1 Specimen geometry and material

The CT specimens tested by Scheider et al. (2008) and Dietzel and Pfuff (1996) were considered for analysis. These specimens were 40 mm wide, 19 mm thick and pre-cracked to initial crack length to width ratio a_0/W of 0.55. The tests were conducted both in laboratory air and in the ASTM standard sea water with hydrogen generation promoted by cathodic charging. The test material was a medium strength low alloy structural steel (FeE 690T) with properties: yield strength $\sigma_Y = 695$ MPa and ultimate strength $\sigma_u = 820$ MPa. The true and engineering stress-strain curves obtained experimentally (Scheider et al., 2008) are shown in Fig. 4.1. The approximate stress-strain variation supplied for numerical simulation is also shown in Fig. 4.1.

The experiments (Dietzel and Pfuff, 1996) under hydrogen charging were carried out at three displacement rates: 0.1 mm/h, 0.01 mm/h, and 0.001 mm/h. The slower rates permitted more hydrogen to diffuse into the metal during crack growth and lead to greater damages. Through the experiments, CTOD resistance curves (R-curves) were generated in terms of δ_5 vs. Δa , where δ_5 (Schwalbe, 1995) is the displacement of two points that are located 2.5 mm above and below the

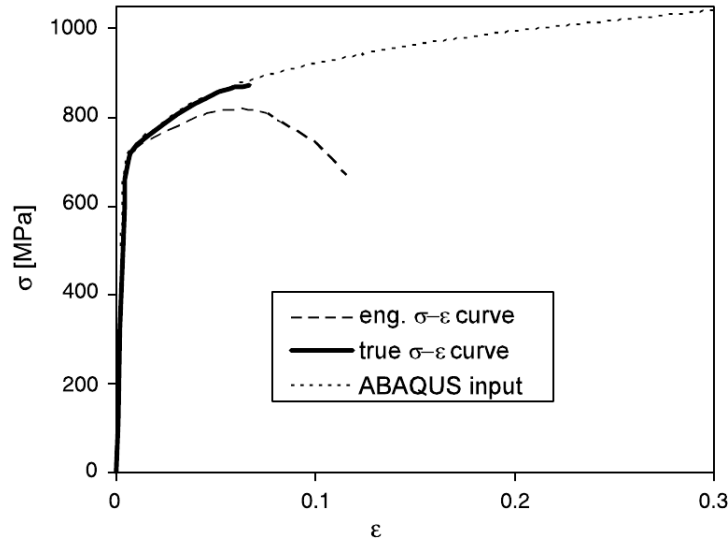


Fig. 4.1 Stress-strain curves for FeE690T, generated by Scheider et al. (2008).

original crack tip. δ_5 values were calculated from the measured load-line displacement record using the formula given in Hellmann and Schwalbe (1986); Schwalbe et al. (1988), which is a modified version of the formula given in British standard BS5762 (1979).

$$\delta_5 = \frac{K^2(1 - \nu^2)}{2\sigma_Y E} + \frac{0.6\Delta a + 0.4(W - a_0)}{0.6(a_0 + \Delta a) + 0.4W + z} v_{pl} \quad (4.2)$$

where v_{pl} is plastic portion of the crack mouth opening displacement, z is the distance between the load-line and the actual measuring position for v . It may be pointed out here that, in reference (Scheider et al., 2008; Schwalbe, 1995), there is a minus sign before $0.4W$ in the denominator of Eqn. 4.2. In the British standard BS5762 as well as in the references (Hellmann and Schwalbe, 1986; Schwalbe et al., 1988) the sign given is plus. In the present study all calculations are based on the plus sign.

4.2.2 Analytical solution to diffusion equation

The analytical solution to the diffusion equation can be obtained through the method of Laplace transform, variable separation, Fourier series, etc. The one dimensional solution to the diffusion equation in relation to the corrosion has been obtained by Olden et al. (2008). Here closed form solutions to the diffusion equation (Eqn. 4.1) for both one- and two-dimensional situations corresponding to the CT specimen geometry are obtained through the method of Fourier series.

The generation of hydrogen takes place at the crack tip from where it is transported along both the crack extension and crack-normal directions. The variation in generation of hydrogen in the thickness direction can be considered negligible for homogeneous material and environment, thereby reducing the case to a two dimensional problem. If the diffusion in the crack-normal direction is ignored, the situation further simplifies to a one dimensional problem. Both these situations have been examined here.

One dimensional solution

For this calculations, the hydrogen concentration is normalised, $C = \frac{C_{abs}}{C_{env}}$, where C_{abs} is the absolute concentration inside the domain and C_{env} is the environmental concentration of hydrogen. This method avoids the need for a direct measurement of C_{env} which will be a difficult task. At $t = 0$, $C = 0$ is assumed throughout the domain. The boundary conditions are as follows: for $t \geq 0$, $C = 1$ at the crack tip and for $t > 0$, $C = 0$ at the far right end of crack extension line.

The corresponding solution (Crank, 1975) for hydrogen concentration $C(x, t)$ with crack tip as the origin is given by

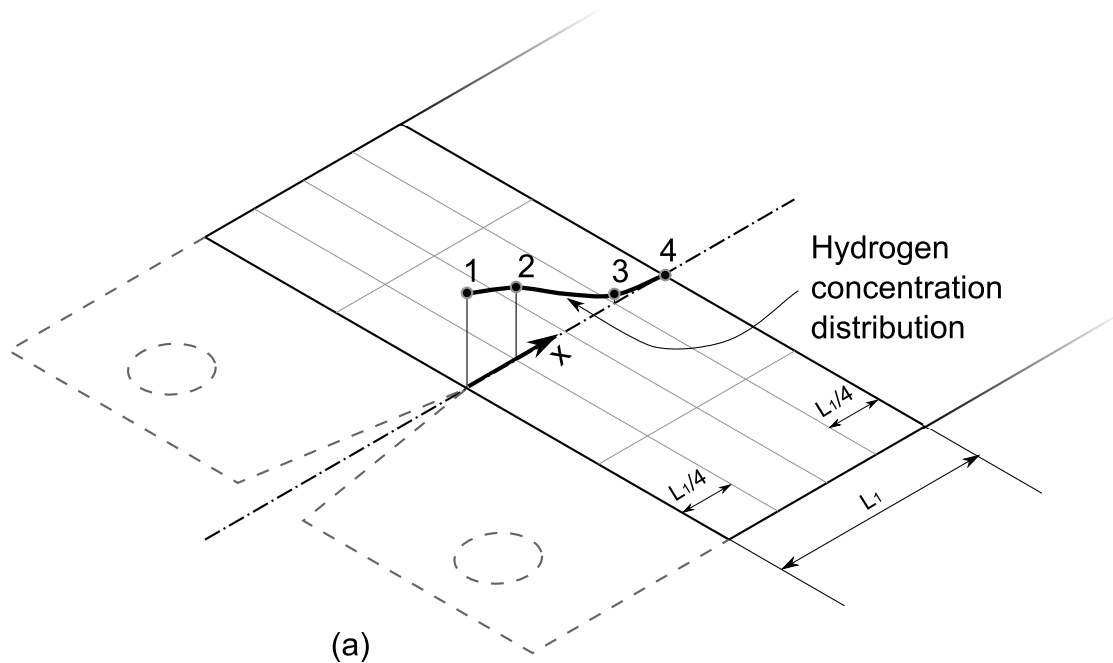
$$C(x, t) = 1 - \frac{x}{L} - \sum_{m=1}^{\infty} \frac{2}{m\pi} \sin\left(\frac{m\pi x}{L}\right) e^{-\frac{m^2\pi^2}{L^2} D_{eff} t} \quad (4.3)$$

After the failure of a single cohesive zone (CZ) element at $t = t_1$, the crack advances by one element span w and the remaining domain span becomes $L - w$. Again, it is observed that the concentration drops to almost zero at a distance L_1 from the crack tip which is much shorter than $L - w$. For further calculations, new domain size is set as L_1 .

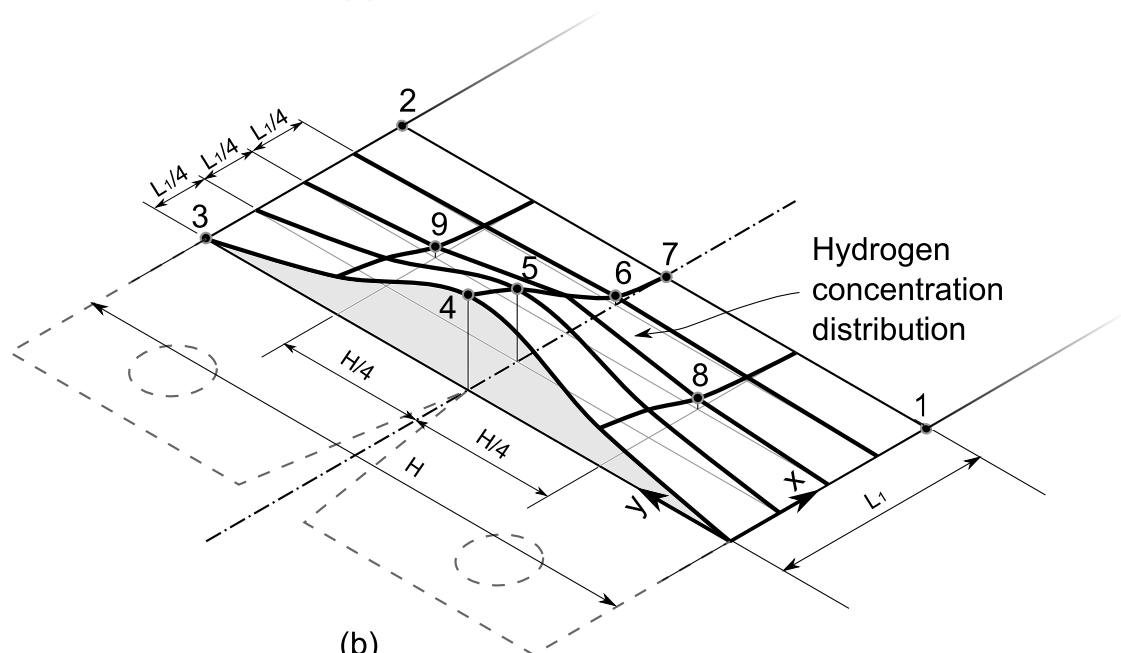
After the failure of the first CZ element, at $t = t_1$, the existing concentration variation along the x-axis (or crack extension direction) is the initial condition for subsequent solution to Eqn. 4.1. This concentration distribution is fitted by

$$C(x, t_1) = b_0 + b_1x + b_2x^2 + b_3x^3 \quad (4.4)$$

where b_i 's, for $i = 0$ to 3 , are obtained by passing the curve through four key points (Fig. 4.2a). The solution to the diffusion equation for $t \geq t_1$ is then obtained in the following form.



(a)



(b)

Fig. 4.2 Polynomial representing initial conditions to diffusion equation. (a) One dimensional
(b) Two dimensional

$$C(x, t - t_1) = 1 - \frac{x}{L_1} - \sum_{i=1}^3 \sum_{m=1}^{\infty} E_m^i \sin\left(\frac{m\pi x}{L_1}\right) e^{-\frac{m^2\pi^2}{L_1^2} D_{eff}(t-t_1)} \quad (4.5)$$

where E_m^i 's, for $i = 1$ to 3 , are given below.

$$E_m^1 = -\frac{2}{m\pi} [(b_1 L_1 + 1) \cos m\pi - (b_0 - 1)(1 - \cos m\pi)] \quad (4.6)$$

$$E_m^2 = 2b_2 L_1^2 \left[-\frac{2}{m^3 \pi^3} + \left(\frac{2}{m^3 \pi^3} - \frac{1}{m\pi} \right) \cos m\pi \right] \quad (4.7)$$

$$E_m^3 = 2b_3 L_1^3 \left[-\frac{1}{m\pi} + \frac{6}{m^3 \pi^3} \right] \cos m\pi \quad (4.8)$$

Two dimensional solution

Fig. 4.3 shows the rectangular domain and boundary conditions that are considered for the analytical solution. The boundary conditions are: $C = 1$ at the crack tip. C varies linearly from 1 to zero at locations (A) and (B) on the top and bottom edges respectively. At all other edges $C = 0$.

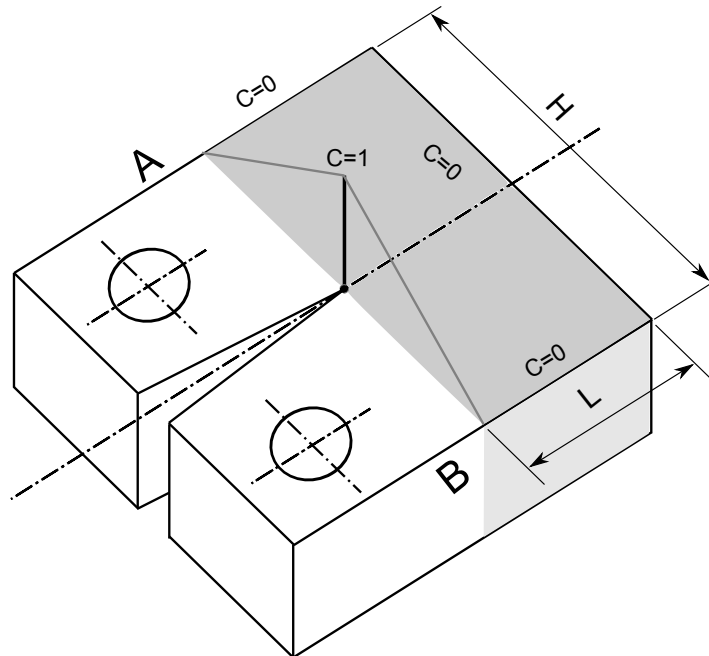


Fig. 4.3 Solution domain and boundary conditions for diffusion equation.

Although the whole specimen is subjected to hydrogen environment, the concentration of hydrogen will vary only if there is variation in stress level (affecting the rate of electrochemical reaction) and geometric features. The high stress concentration, low mobility of fluid and continuous formation of new virgin surfaces near the crack tip will facilitate accelerated electrochemical reaction leading to high hydrogen concentration. The condition existing at the outer boundary is much weaker than the condition existing at the crack tip. This justifies assumption of a much lower relative hydrogen concentration at all points of the outer boundary.

The actual variation in distribution of hydrogen arising out of diffusion through the whole outer boundaries with unit hydrogen concentration (at $t = 0$) was analysed by finite element method. The results are shown in Figs. 4.4 and 4.5. The figures show that the concentration of hydrogen at the crack tip after 440 hours for the slowest rate of loading is less than 0.06.

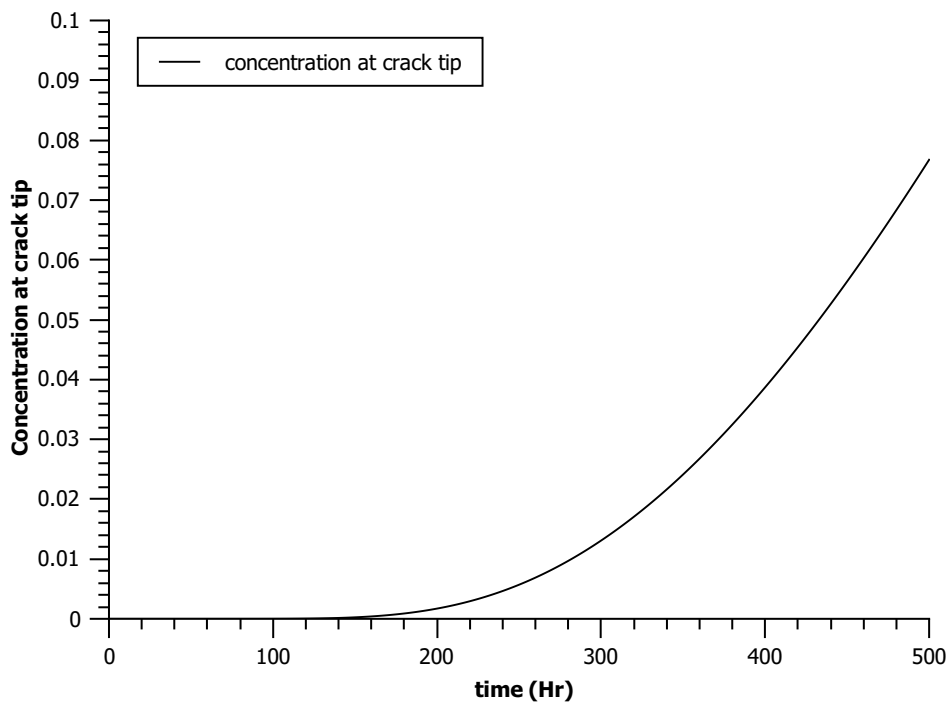


Fig. 4.4 Concentration at crack tip with $C=1$ at outer boundaries.

Since the differential equation governing the diffusion is linear, it is possible to obtain the solution for the given problem by superimposing two solutions: (i) The first corresponding to a unit concentration (at $t = 0$) at crack tip and zero at all points of the outer boundaries. (ii) The second corresponding to a unit concentration (at $t = 0$) at all points of the outer boundaries and

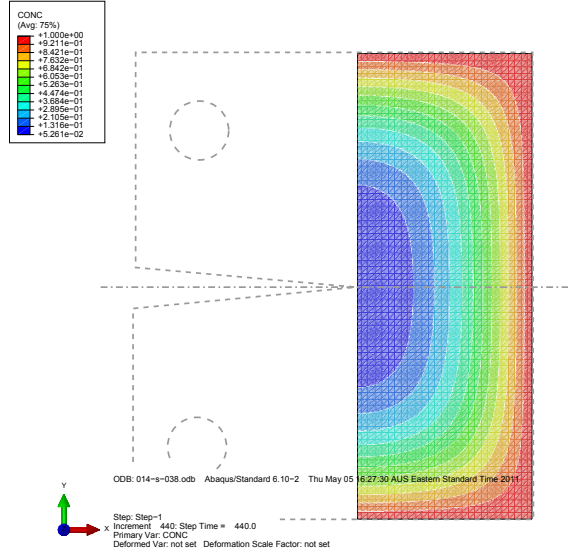


Fig. 4.5 Concentration contours with $C=1$ at outer boundaries, $t = 440$ h.

zero at the crack tip.

The solution due to the second part contributes to less than 6% change in hydrogen concentration at the crack tip region. The solution due to the first part, which can be easily obtained analytically, is sufficient and has been considered here. Incidentally, the boundary conditions at the outer boundary corresponding to the first part are in conformity with boundary condition, $C = 0$ at the far end of ligament, assumed for the one dimensional solution (section 4.2.2).

With the above boundary conditions the solution to Eqn. 4.1, for $t \geq 0$, is obtained as follows.

$$\begin{aligned}
 &\text{For } 0 \leq y \leq \frac{H}{2}, \\
 &C(x, y, t) = \left(1 - \frac{x}{L}\right) \left(\frac{2y}{H}\right) \\
 &\quad + \sum_{n=1}^{\infty} \sum_{m=1}^{\infty} B_{m,n} \sin\left(\frac{m\pi x}{L}\right) \sin\left(\frac{n\pi y}{H}\right) e^{-D_{eff}\lambda_{m,n}t} \\
 &\text{For } \frac{H}{2} < y \leq H, \\
 &C(x, y, t) = \left(1 - \frac{x}{L}\right) \left(2 - \frac{2y}{H}\right) \\
 &\quad + \sum_{n=1}^{\infty} \sum_{m=1}^{\infty} B_{m,n} \sin\left(\frac{m\pi x}{L}\right) \sin\left(\frac{n\pi y}{H}\right) e^{-D_{eff}\lambda_{m,n}t}
 \end{aligned} \tag{4.9}$$

where

$$\lambda_{m,n} = \pi^2 \left(\frac{m^2}{L^2} + \frac{n^2}{H^2} \right) \quad (4.10)$$

$$B_{m,n} = -\frac{16}{\pi^3 mn^2} \sin\left(\frac{n\pi}{2}\right) \quad (4.11)$$

The concentration distribution at time t_1 is represented by a polynomial of the form

$$C(x, y, t_1) = a_1x + a_2y + a_3x^2 + a_4xy + a_5y^2 + a_6x^3 + a_7x^2y + a_8xy^2 + a_9x^2y^2 \quad (4.12)$$

where a_i 's, for $i = 1$ to 9 , are obtained by fitting C at nine key points ahead of crack tip (Fig. 4.2). For Eqn. 4.12 origin is located at the intersection of the vertical line passing through the new crack tip and the bottom edge of the specimen. Similar to one dimensional solution, the new domain for further calculations is of size $L_1 \times H$. The solution to Eq.(4.1) is given by

$$\begin{aligned} \text{For } 0 \leq y \leq \frac{H}{2}, \\ C(x, y, t - t_1) &= \left(1 - \frac{x}{L_1}\right) \left(\frac{2y}{H}\right) \\ &+ \sum_{i=1}^{10} \sum_{n=1}^{\infty} \sum_{m=1}^{\infty} B_{m,n}^i \sin\left(\frac{m\pi x}{L_1}\right) \sin\left(\frac{n\pi y}{H}\right) e^{-D_{eff}\lambda_{m,n}(t-t_1)} \end{aligned} \quad (4.13)$$

$$\begin{aligned} \text{For } \frac{H}{2} < y \leq H, \\ C(x, y, t - t_1) &= \left(1 - \frac{x}{L_1}\right) \left(2 - \frac{2y}{H}\right) \\ &+ \sum_{i=1}^{10} \sum_{n=1}^{\infty} \sum_{m=1}^{\infty} B_{m,n}^i \sin\left(\frac{m\pi x}{L_1}\right) \sin\left(\frac{n\pi y}{H}\right) e^{-D_{eff}\lambda_{m,n}(t-t_1)} \end{aligned}$$

where $B_{m,n}^i$'s, for $i = 1$ to 10 are given below.

$$B_{m,n}^1 = -\frac{16}{\pi^3 mn^2} \sin \frac{n\pi}{2} \quad (4.14)$$

$$B_{m,n}^2 = \frac{4a_1L_1}{mn\pi^2} (\cos m\pi)(\cos n\pi - 1) \quad (4.15)$$

$$B_{m,n}^3 = \frac{4a_2H}{mn\pi^2} (\cos m\pi - 1)(\cos n\pi) \quad (4.16)$$

$$B_{m,n}^4 = \frac{4a_3L_1^2}{mn\pi^2} \left[\cos m\pi \left(\frac{2}{m^2\pi^2} - 1 \right) - \frac{2}{m^2\pi^2} \right] [1 - \cos n\pi] \quad (4.17)$$

$$B_{m,n}^5 = \frac{4a_4L_1H}{mn\pi^2} (\cos m\pi)(\cos n\pi) \quad (4.18)$$

$$B_{m,n}^6 = \frac{4a_5 H^2}{mn\pi^2} [1 - \cos m\pi] \left[\cos n\pi \left(\frac{2}{n^2\pi^2} - 1 \right) - \frac{2}{n^2\pi^2} \right] \quad (4.19)$$

$$B_{m,n}^7 = \frac{4a_6 L_1^3}{mn\pi^2} \left[\left(\frac{6}{m^2\pi^2} - 1 \right) \cos m\pi \right] [1 - \cos n\pi] \quad (4.20)$$

$$B_{m,n}^8 = \frac{4a_7 L_1^2 H}{mn\pi^2} \left[\cos m\pi \left(\frac{2}{m^2\pi^2} - 1 \right) - \frac{2}{m^2\pi^2} \right] [-\cos n\pi] \quad (4.21)$$

$$B_{m,n}^9 = \frac{4a_8 L_1 H^2}{mn\pi^2} [-\cos m\pi] \left[\cos n\pi \left(\frac{2}{n^2\pi^2} - 1 \right) - \frac{2}{n^2\pi^2} \right] \quad (4.22)$$

$$B_{m,n}^{10} = \frac{4a_9 L_1^2 H^2}{mn\pi^2} \left[\cos m\pi \left(\frac{2}{m^2\pi^2} - 1 \right) - \frac{2}{m^2\pi^2} \right] \left[\cos n\pi \left(\frac{2}{n^2\pi^2} - 1 \right) - \frac{2}{n^2\pi^2} \right] \quad (4.23)$$

4.2.3 Finite element (FE) model

The CT specimen is discretised using 4 noded quadrilateral plane strain elements (Fig. 4.6) of uniform size around the crack extension line. The cohesive elements of zero height and 0.025 mm width are placed along the crack path.

The plane strain element size was arrived at by trial and error using δ_5 vs. Δa results of Scheider et al. (2008) for test in air. The mesh size was initially estimated following the report of Turon et al. (2005). They specify an acceptable element dimension one half to one tenth of the cohesive zone size l_{cz} given by

$$l_{cz} = M \frac{K_{Ic}^2}{T_0^2} \quad (4.24)$$

where K_{Ic} is fracture toughness and T_0 is cohesive strength and M is model constant. Using $K_{Ic}=112.5 \text{ MPa} \sqrt{\text{m}}$ and $T_0= 2440 \text{ MPa}$ (Scheider et al., 2008) and $M=1$, $l_{cz} = 2.1 \text{ mm}$. It is relevant to note here is that K_{Ic} was not available for this material and it was estimated from CVN data listed by material manufacturer's catalogue (ThyssenKrupp Steel, 2005) as 35 J and the relation $\left(\frac{K_{Ic}}{\sigma_y} \right)^2 = \frac{5}{\sigma_y} \left(CVN - \frac{\sigma_y}{20} \right)$ (ASM Handbook, 2003). However, the acceptable mesh size was finally arrived at by trial and error. The variations of δ_5 vs. Δa for element sizes of 0.2, 0.125, 0.1 and 0.08 were obtained (Fig. 4.7). The size 0.1 mm is the best and it was selected for the present study. It may also be noted that the element size chosen is very small compared with plastic zone correction factor $r_{py} = \frac{1}{6\pi} \left(\frac{K_{Ic}}{\sigma_y} \right)^2 = 1.39 \text{ mm}$. Thus the chosen element size would accurately capture the stress distribution around the crack tip. For loading, the centre node of

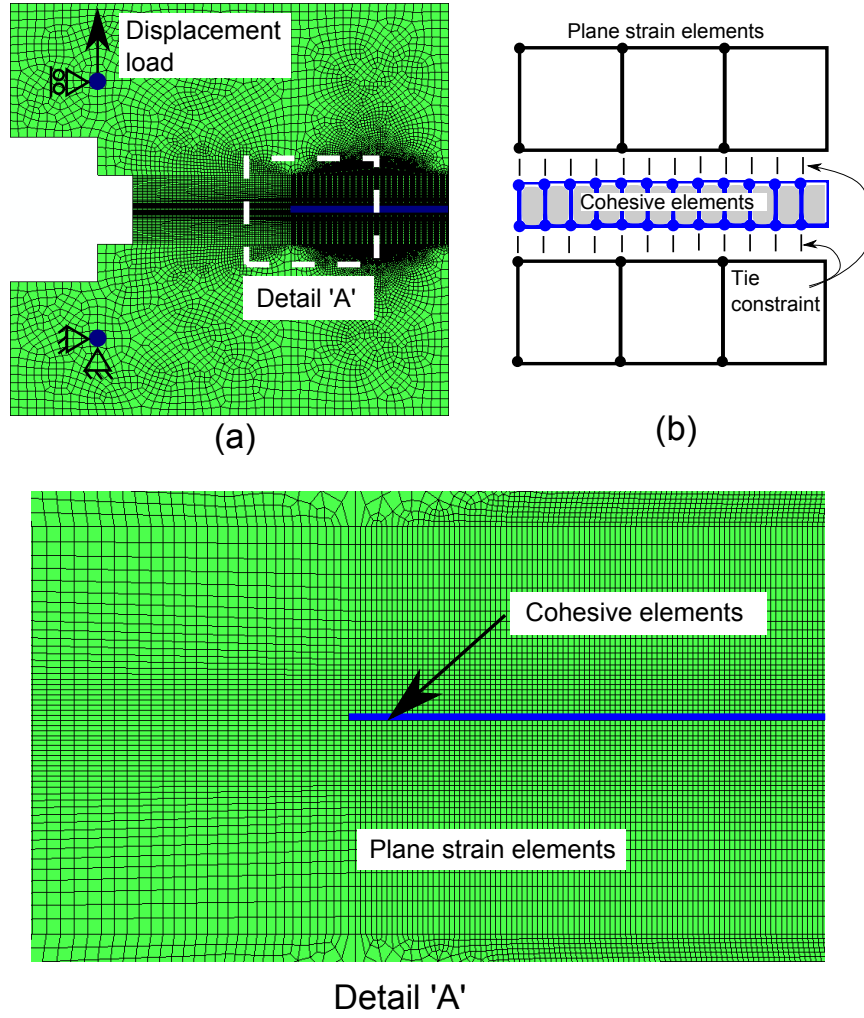


Fig. 4.6 Finite element discretisation:- (a) FE mesh and boundary conditions (b) schematic arrangement of cohesive elements

the bottom pin is held fixed while the displacement is applied at the centre of the top pin.

The traction separation law (TSL) used for cohesive elements (Fig. 4.8) is given as:

$$T = T_0(1 - \mu C) \begin{cases} 2\left(\frac{\delta}{\delta_1}\right) - \left(\frac{\delta}{\delta_1}\right)^2, & \delta \leq \delta_1, \\ 1, & \delta_1 < \delta \leq \delta_2, \\ 2\left(\frac{\delta - \delta_2}{\delta_0 - \delta_2}\right)^3 - 3\left(\frac{\delta - \delta_2}{\delta_0 - \delta_2}\right)^2 + 1, & \delta_2 < \delta \leq \delta_0. \end{cases} \quad (4.25)$$

The shape of TSL is defined (Scheider et al., 2008) by $\delta_1 = 0.05\delta_0$ and $\delta_2 = 0.65\delta_0$. μ links directly the rise in normalised hydrogen concentration C to drop in cohesive strength T_0 .

The diffusion calculations are coupled with the finite element model through user subroutine

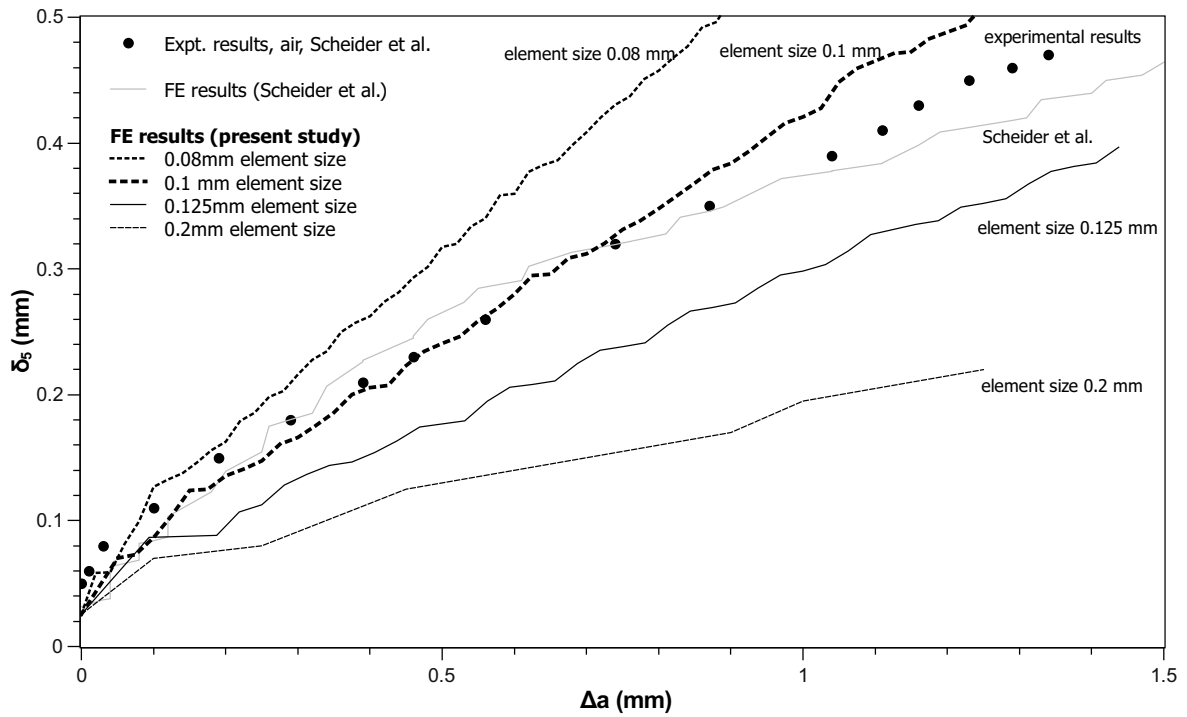


Fig. 4.7 Effect of mesh size on results.

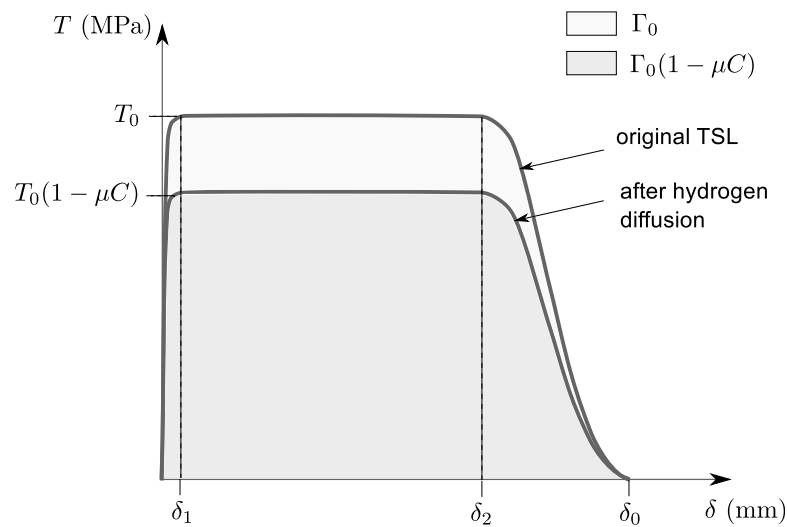


Fig. 4.8 Concentration dependent traction separation law (Scheider et al., 2008) and effect of strength reduction factor μ .

USDFLD of ABAQUS[®]. The ABAQUS[®] implementation of coupled calculations is explained in section 4.3.4.

Through the FE analysis, the load line displacement is obtained and the corresponding δ_5 is

calculated using Eqn. 4.2 with $z = 0$. The experimental δ_5 vs. Δa curve for testing in air has been the basis to determine the basic TSL parameters as $T_0 = 2390$ MPa and $\delta_0 = 0.016$ mm.

4.2.4 Comparison of predicted results with experimental data

The two parameters, effective diffusivity D_{eff} and strength reduction factor μ are the key factors while incorporating the effect of hydrogen to crack growth. These are obtained by matching the simulation results with experimental data for displacement loading rate of 0.01 mm/h iteratively. Initially, $\mu = 0.2$ and $D_{eff} = 2.5 \times 10^{-6}$ mm²/s were obtained, which are consistent with the data ($\mu = 0.2$ and $D_{eff} = 2 \times 10^{-6}$ mm²/s) obtained by Scheider et al. (2008). Fig. 4.9 present the comparison of theoretical and experimental variation of modified CTOD δ_5 with crack growth Δa for three loading rates. The experimental results are for tests in air and in hydrogen envi-

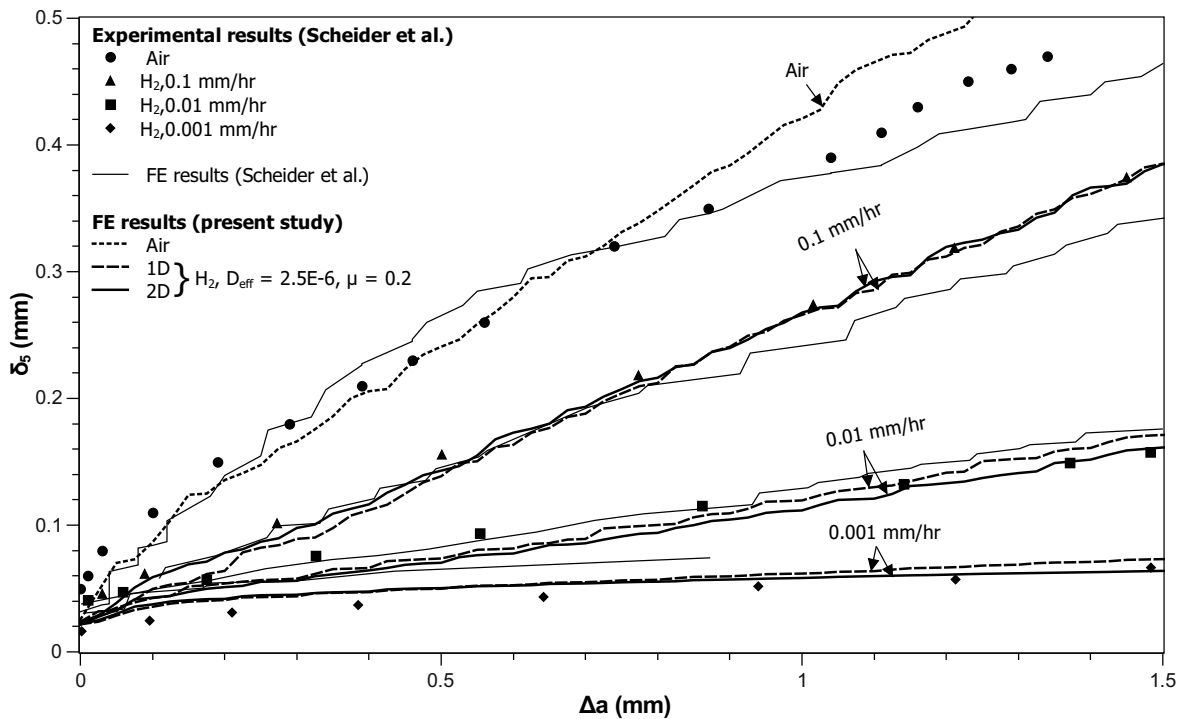


Fig. 4.9 Comparison of predicted and experimental results, for $D_{eff} = 2.5 \times 10^{-6}$ mm²/s and constant μ .

ronment for different loading rates. The present FE results based on one and two dimensional analytical solutions for diffusion have been compared with the data of Scheider et al. (2008) in

the figure. The theoretically predicted results based on both one and two dimensional analytical solutions for diffusion modelling are close to the experimental data.

D_{eff} is inversely related to the number of trap sites, which, in turn, depend directly on the plastic strain. That is, higher plastic strain means more trap sites and lower diffusivity, D_{eff} . The experimental D_{eff} data (Dietzel et al., 2006) are in the range 2×10^{-5} to 8×10^{-7} mm²/s for steel membranes deformed to plastic strains ϵ_p in the range of 0.02–1.0 (Fig. 4.10). The

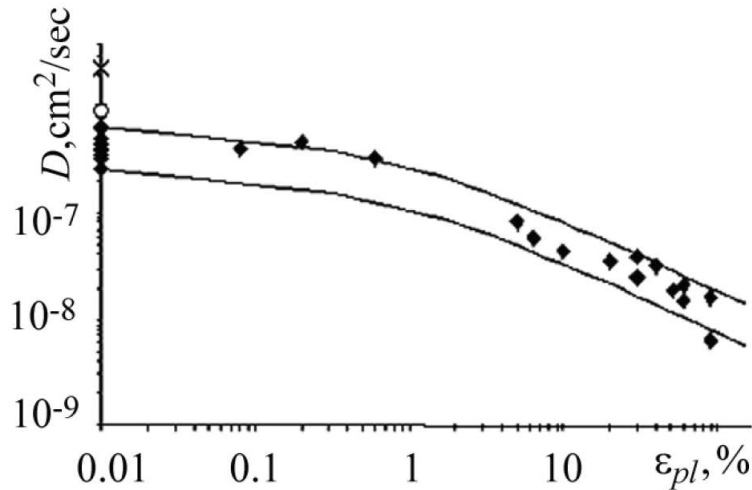


Fig. 4.10 Experimental D_{eff} vs ϵ_p data (Dietzel et al., 2006).

symbol D shown in Fig. 4.10 represents the effective diffusivity D_{eff} . In the present FE study, the plastic strain immediately ahead of the crack tip (Fig. 4.11) increases gradually from 0.011 to 0.030, which corresponds to the crack extension from 0.0 to 2.0 mm. Since in the present case the plastic strains are at lower levels, D_{eff} can be increased.

The average plastic strain rate too has an inverse relationship with the cohesive strength reduction factor μ . Higher average plastic strain rate means lower time span available for diffusion of trapped hydrogen into the lattice and hence lower reduction in cohesive strength, i.e., lower μ for higher $\dot{\epsilon}_p$ (Krom et al., 1999). It is relevant to note that lattice hydrogen concentration causes more damage to cohesive strength than trapped hydrogen (Krom et al., 1999). Thus it is reasonable to link μ as well to the loading rate. In the subsequent studies μ is gradually increased with decreasing rates of loading.

A new set of simulation results for two values of effective diffusivity, $D_{eff} = 2.0 \times 10^{-5}$ mm²/s and 5.5×10^{-6} mm²/s, are shown in Figures 4.12 and 4.13 respectively. The first

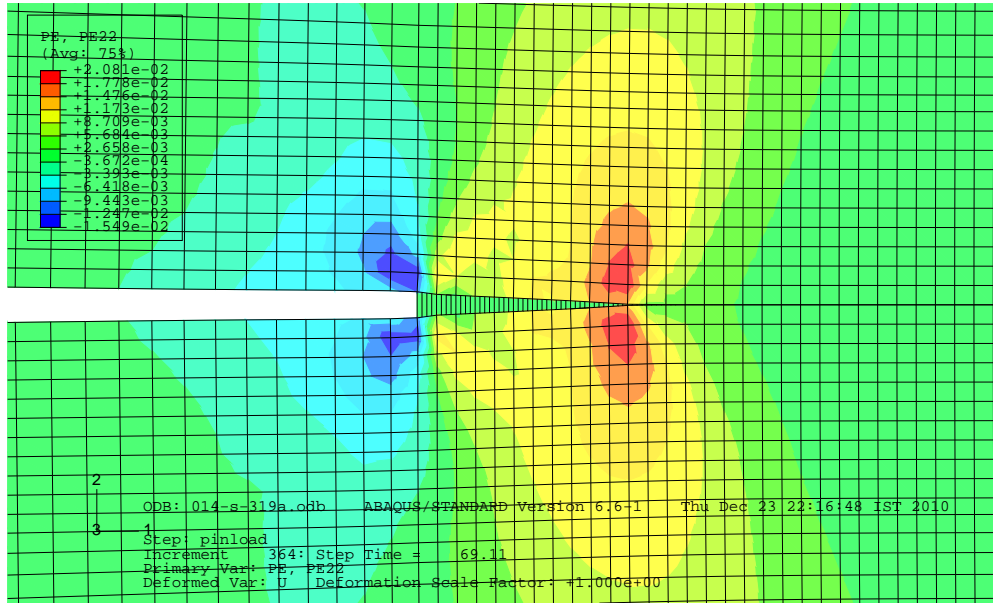


Fig. 4.11 Plastic strain ahead of crack tip along direction normal to crack extension for $\Delta a = 1$ mm.

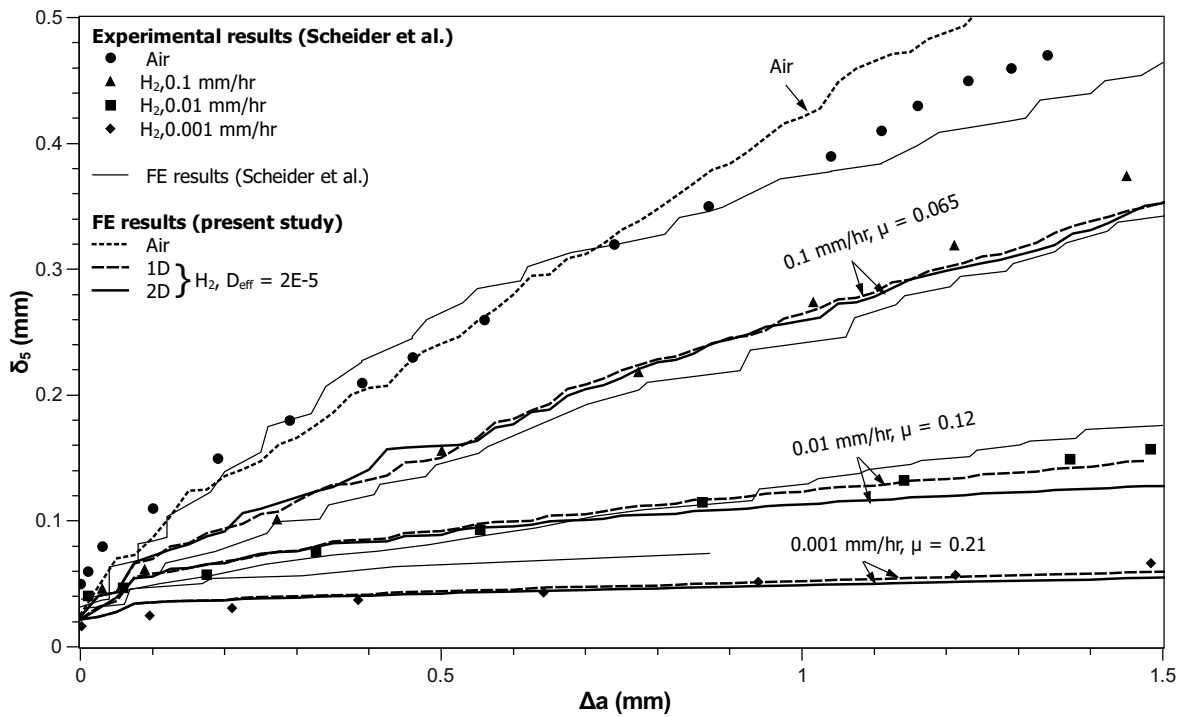


Fig. 4.12 Comparison of predicted and experimental results, $D_{eff} = 2.0 \times 10^{-5}$ mm²/s and variable μ .

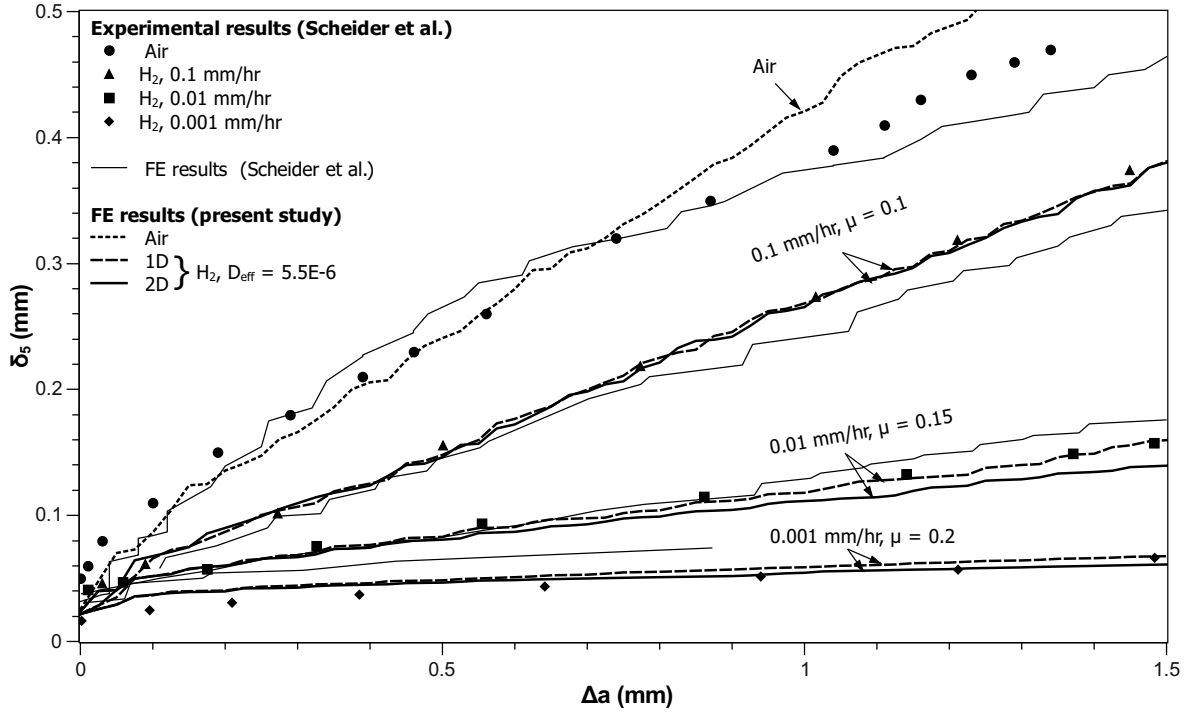


Fig. 4.13 Comparison of predicted and experimental results, $D_{eff} = 5.5 \times 10^{-6} \text{ mm}^2/\text{s}$ and variable μ .

corresponds to the reported experimental value for $\epsilon_{pl} = 0.02$ (Dietzel et al., 2006) and the latter is arbitrarily selected to examine the further influence of D_{eff} . The values of μ for different loading rates are shown in Table 4.1. The average crack tip plastic strain rate $\dot{\epsilon}_p$ was obtained for each of the loading rate. The variation of μ with $\dot{\epsilon}_p$ is shown in Fig. 4.14. An approximate relationship between μ and $\dot{\epsilon}_p$ can be obtained using these data.

$$\mu = -0.05079 - 0.05810 \log_{10}(\dot{\epsilon}_p) \quad (4.26)$$

where $\dot{\epsilon}_p$ is in mm/mm/h.

Table 4.2 presents comparison of δ_5 vs. Δa for all three cases. The results for variable μ are in better agreement than those based on constant μ . The predictions for δ_5 vs. Δa are also superior to the FE results of Scheider et al. (2008). The maximum error in δ_5 has reduced from 63.5% (Scheider et al., 2008) to 10.8% in 1-D analysis. However, when 2D analysis was employed, there was overall improvement of the prediction using small D_{eff} . It is observed that, particularly for one dimensional diffusion, $D_{eff} = 5.5 \times 10^{-6} \text{ mm}^2/\text{s}$ gives better match for

Table 4.1 Values of strength reduction factor μ .

	Rate of loading (mm/h)		
	0.1	0.01	0.001
μ for $D_{eff} = 2.0 \times 10^{-5} \text{ mm}^2/\text{s}$	0.065	0.12	0.21
μ for $D_{eff} = 5.5 \times 10^{-6} \text{ mm}^2/\text{s}$	0.10	0.15	0.20

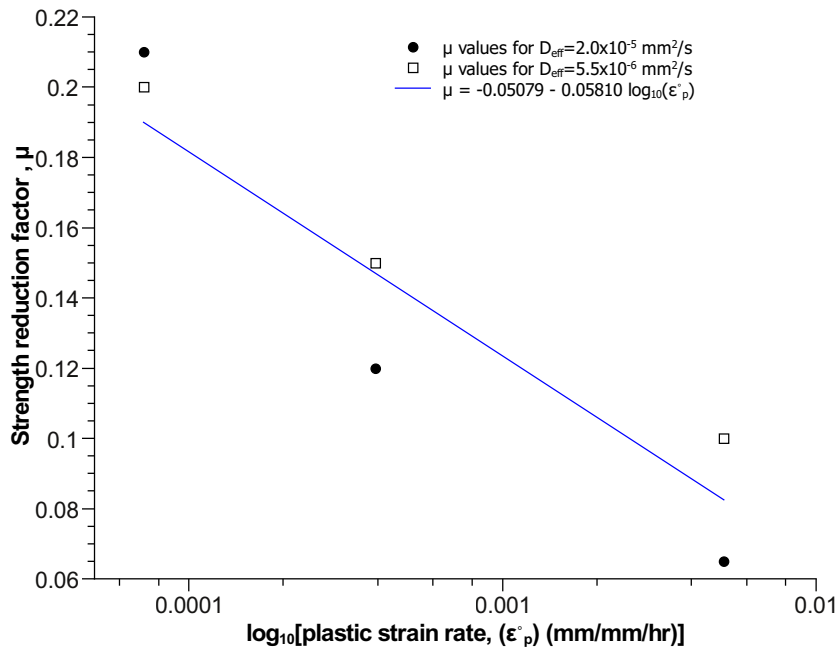


Fig. 4.14 Variation of μ with $\dot{\epsilon}_p$.

the faster rates of loading whereas $D_{eff} = 2.0 \times 10^{-5} \text{ mm}^2/\text{s}$ suits better for the slower rates of loading. However, in the two-dimensional analysis, variation of D_{eff} from $5.5 \times 10^{-6} \text{ mm}^2/\text{s}$ to $2.0 \times 10^{-5} \text{ mm}^2/\text{s}$ does not lead to an appreciable difference in the prediction of δ_5 vs. Δa .

The theoretically predicted results based on both one and two dimensional analytical modelling of diffusion are close to the experimental observations (Scheider et al., 2008) with variable μ . For loading rate of 0.1 mm/h, the FE results for both one and two dimensional analytical modelling of diffusion are almost identical whereas for slower loading rate (0.01 and 0.001 mm/h) the two dimensional analysis yields a slightly faster damage to the material. The effect of two dimensional modelling can be seen more clearly in the theoretically predicted variations in hydrogen concentration over the ligament (Fig. 4.15) after three stages of crack growth, i.e.,

Table 4.2 Comparison of experimental δ_5 with different theoretical predictions.

Rate of loading (mm/h)	Δa (mm)	Expt. ^a δ_5 (mm)	Scheider et al. δ_5 , % error	1-D solution, δ_5 , % error			2-D solution, δ_5 , % error		
				<i>b</i>	<i>c</i>	<i>d</i>	<i>b</i>	<i>c</i>	<i>d</i>
0.1	0.5	0.1558	-6.5	-11.0	-4.9	-3.6	-8.2	-6.2	+2.6
	1.0	0.2700	-10.6	-1.5	-0.6	-2.0	-0.9	-1.7	-4.0
	1.5	0.3859	-11.3	-0.2	-1.2	-8.5	-0.3	-1.5	-8.7
0.01	0.5	0.0893	-7.3	-17.5	-7.0	+3.0	-21.3	-9.5	-0.4
	1.0	0.1238	+4.2	-3.5	-4.7	-0.6	-9.9	-9.9	-8.6
	1.5	0.1587	+10.8	+7.9	+0.7	-6.6	1.6	-12.1	-19.3
0.001	0.5	0.0399	+63.4	+24.8	+21.6	+10.8	+26.1	+17.0	+5.8
	1.0	0.0529	-	+16.7	+11.3	-1.6	+10.1	+2.9	-7.6
	1.5	0.0670	-	+9.2	+1.0	-10.9	-4.7	-8.8	-17.8

^aInterpolated from experimental data

^b $D_{eff} = 2.5 \times 10^{-6} \text{ mm}^2/\text{s}$, $\mu = 0.2$

^c $D_{eff} = 5.5 \times 10^{-6} \text{ mm}^2/\text{s}$, $\mu = 0.10, 0.15, 0.20$

^d $D_{eff} = 2.0 \times 10^{-5} \text{ mm}^2/\text{s}$, $\mu = 0.065, 0.12, 0.21$

at $\Delta a = 0.025, 1, 2.5$ and 4 mm . The hydrogen concentration distribution obtained for the two dimensional modelling spreads up to a longer distance from the crack tip as compared to that for the one dimensional modelling. This effect is more pronounced for slower loading rates.

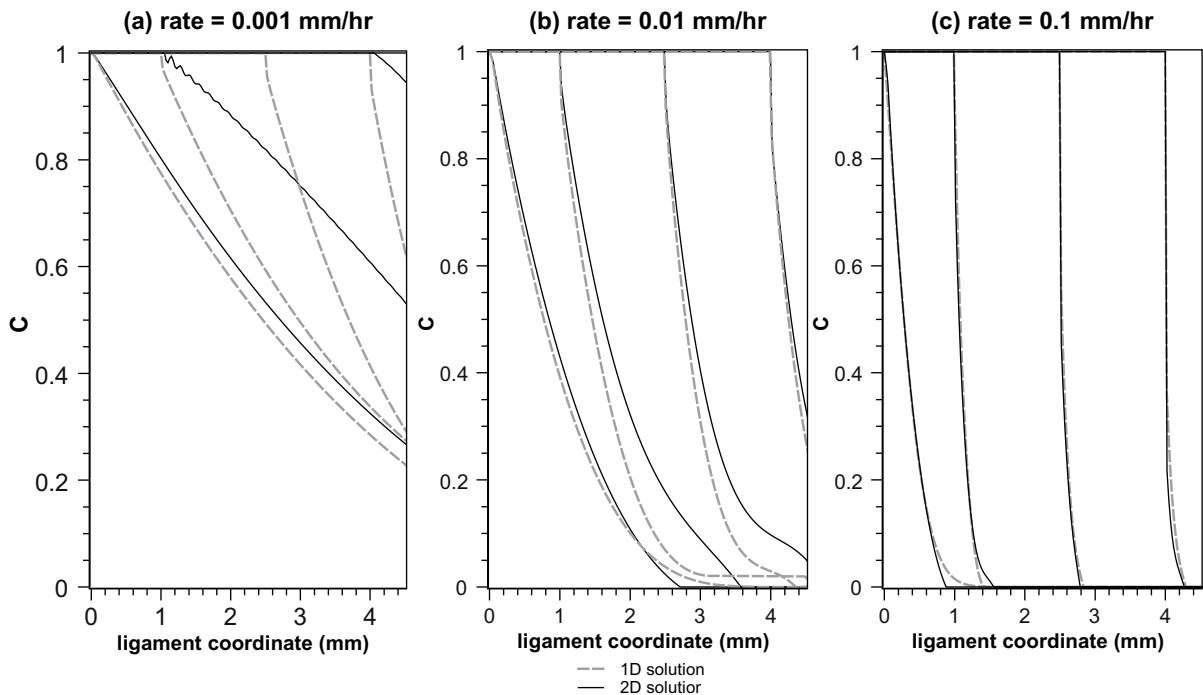


Fig. 4.15 Predicted values of normalised hydrogen concentrations in crack ligament with $D_{eff} = 5.5 \times 10^{-6} \text{ mm}^2/\text{s}$ and after crack growth $\Delta a = 0.025 \text{ mm}$, 1 mm , 2.5 mm and 4 mm respectively for three different loading rates: (a) 0.001 mm/h , (b) 0.01 mm/h and (c) 0.1 mm/h .

For loading rate of 0.01 mm/h, FE analysis was carried out for both diffusion and crack growth with the same mesh. A full FE approach took around 8 hours as compared to less than 2 hours taken for the combined analytical and FE approach. The two-tier FE analysis required more time as it involved three steps: diffusion analysis, transfer of hydrogen concentration data and crack growth calculation, which were repeated at the end of each crack increment. In the combined analytical and FE approach, the first two steps are almost eliminated. The faster solution process is particularly advantageous during the iterative part of simulation to determine the key parameters, D_{eff} and μ .

4.3 Scheme II for HASCC modelling

In the scheme I, the analysis of diffusion and crack growth have been done independently. Results of one analysis are used as input for the other. Therefore, the diffusion calculations are unaffected by the stress distribution obtained during crack growth analysis. This scheme has been modified here to include the effects of hydrostatic stress σ_h and plastic strain ϵ_p on the diffusion of hydrogen. This modification requires a bi-directional coupling between diffusion calculations and crack growth analysis. The scheme II too is verified against the same experimental data. In the scheme II, diffusion solution is obtained by a finite difference method to the governing equation and the crack growth is analysed by finite element based CZM.

The movement of hydrogen through material is influenced by σ_h and ϵ_p as follows. The hydrogen is considered to move inside the metal largely by normal interstitial lattice site (NILS) diffusion (Sofronis and McMeeking, 1989). The movement of hydrogen through NILS is arrested at various micro-structural trap sites such as, voids, inclusions, grain boundaries, collectively termed as traps (Taha and Sofronis, 2001) where the hydrogen gets accumulated. The approach of Oriani (1970) for modelling of hydrogen diffusion assumes that the dissolved hydrogen resides at either NILS or trap sites and the concentration of hydrogen at these two sites is always in local equilibrium. The hydrogen in NILS is influenced by hydrostatic stress σ_h (Sofronis and McMeeking, 1989). On the other hand, the hydrogen concentration in the trap sites depends on trap site density (i.e. number of traps per unit volume). This density is dependent on local equivalent plastic strain ϵ_p ; the dependence is shown experimentally by Kumnick

and Johnson (1980). Thus, the total hydrogen concentration and hence the damage to material is dependent on levels of both σ_h and ϵ_p .

Although both σ_h and ϵ_p have influence on HASCC, certain modelling (Scheider et al., 2008; Rimoli and Ortiz, 2010) have followed the scheme I (of section 4.2) and have assumed that, for an elastic-plastic material under moderate to strong levels of ϵ_p , the plastic strain plays a substantially dominant role in determination of hydrogen distribution near the crack tip and the effect of σ_h may be neglected. Further, the effect of ϵ_p can be accommodated into a modelling parameter such as D_{eff} . This assumption simplifies a computational study. However, hydrostatic stress may become an important factor in situations where plastic strain levels are sufficiently small. The scheme II of HCD-CZM proposed in this section can be used to analyse such a situation where σ_h and ϵ_p are important.

4.3.1 Modifications in scheme I

Hydrogen concentration C_L in NILS is affected by σ_h and concentration in traps C_T is related to ϵ_p . The new scheme thus involves two concentration related parameters C_L and C_T unlike a single concentration term C employed in the scheme I. Total hydrogen concentration $C_{tot} = C_L + C_T$ is employed to assess hydrogen assisted damage to the material cohesive strength.

C_L and C_T are considered to be always in equilibrium as per Oriani's law (Oriani, 1970).

$$C_T = \frac{K_{tr} \left(\frac{\alpha_{tr} N_T}{\beta N_L} \right) C_L}{1 + \left(\frac{K_{tr}}{\beta N_L} \right) C_L} \quad (4.27)$$

where trap equilibrium constant $K_{tr} = 2.7977 \times 10^{10}$ (at 300 K), α_{tr} represents number of hydrogen atom sites per trap, β is number of NILS per solvent atom and $\beta=6$ for iron considering tetrahedral site occupancy, $N_L (=8.46 \times 10^{28})$ atoms/m³ denotes number of solvent lattice atoms per unit volume (Sofronis and McMeeking, 1989; Taha and Sofronis, 2001). All data correspond to iron-hydrogen system. The trap density N_T measured in number of traps per unit volume is obtained in terms of equivalent plastic strain ϵ_p . $\alpha_{tr}=1$ is assumed in the present study (Sofronis and McMeeking, 1989). The experimental data of N_T vs. ϵ_p (Fig. 4.16) obtained by Kumnick

and Johnson (1980) is fitted (Sofronis and McMeeking, 1989; Krom et al., 1999) as

$$\log N_T = 23.26 - 2.33e^{-5.5\epsilon_p} \quad (4.28)$$

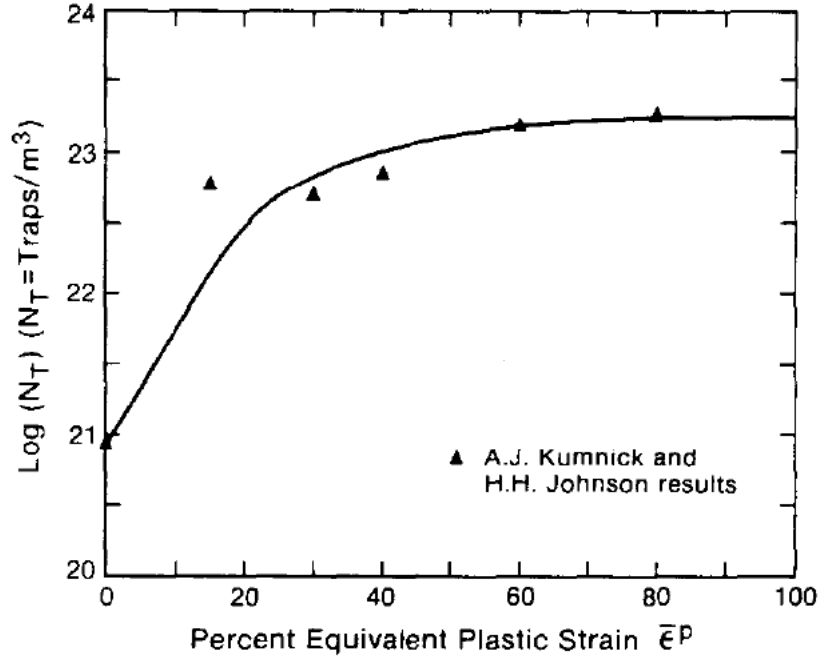


Fig. 4.16 Experimental data of N_T vs. ϵ_p obtained by Kumnick and Johnson (Sofronis and McMeeking, 1989).

The diffusion of hydrogen through metal is governed by a partial differential equation Eq. (2.1) which is reproduced below for ready reference.

$$\frac{\partial C_L}{\partial t} = \vec{\nabla} \cdot (D_{eff} \vec{\nabla} C_L) - \vec{\nabla} \cdot \left(\frac{D_{eff} V_H}{RT_a} C_L \vec{\nabla} \sigma_h \right) - f(\dot{\epsilon}_p)$$

The term $f(\dot{\epsilon}_p)$ of Eq. (2.1) was introduced by Krom et al. (1999) to account for the effect of plastic strain rate. This term is not included in the scheme II. Thus the governing diffusion equation can be re-written as:

$$\frac{\partial C_L}{\partial t} = \vec{\nabla} \cdot (D_{eff} \vec{\nabla} C_L) - \vec{\nabla} \cdot \left(\frac{D_{eff} V_H}{RT} C_L \vec{\nabla} \sigma_h \right) \quad (4.29)$$

where D_{eff} is effective diffusivity of material, V_H is partial molar volume of hydrogen in metal

(2×10^3 mm³/mol for iron), R is universal gas constant (8.3144 J/mol-K), T is 300 K. Eq. (4.29) is solved numerically to obtain transient hydrogen distribution along the crack line.

For crack growth analysis, the CZM based material representation followed earlier, defined by TSL (Eqn. 4.25), is adopted. The hydrogen concentration C used in TSL is normalised as $C = \frac{(C_{tot})}{(C_{tot})_{env}}$, where (C_{tot}) and $(C_{tot})_{env}$ are respectively the hydrogen concentrations in material and environment. $(C_{tot})_{env}$ is the same as C_{env} employed earlier. The material data indicated in section 4.2.1 have been utilised here.

4.3.2 Finite difference solution to the diffusion equation

The governing equation of diffusion, Eq. (4.29), is non-linear in the presence of the time-dependent term σ_h . A closed form solution to this equation such as the one obtained by Olden et al. (2008) or as described for scheme I (section 4.2.2) is not possible. A numerical solution using finite difference method has been considered. It has been shown in the scheme I that one dimensional solution to diffusion equation gives sufficiently accurate hydrogen distribution for the purpose of predicting stable crack growth; one dimensional solution to diffusion along the crack extension line has only been considered. Eq. (2.1) can be rewritten for one dimension as follows.

$$\frac{\partial C_L}{\partial t} = D_{eff} \frac{\partial^2 C_L}{\partial x^2} - E_H \frac{\partial C_L}{\partial x} \frac{\partial \sigma_h}{\partial x} - E_H C_L \frac{\partial^2 \sigma_h}{\partial x^2} \quad (4.30)$$

where x is the distance from the crack tip along the crack path and

$$E_H = \frac{D_{eff} V_H}{RT}. \quad (4.31)$$

The effective diffusivity of material D_{eff} is assumed to be constant and equal to the value employed earlier, i.e., $D_{eff} = 5.5 \times 10^{-6}$ mm²/s. At $t = 0$, $C_L = 0$, i.e. complete absence of hydrogen is assumed across entire crack path. The boundary conditions are: for $t \geq 0$, $C_L = C_{L0}$ at the crack tip and for $t > 0$, $C_L = 0$ at the far end D of crack path (Figure 4.17). C_{L0} is the concentration of hydrogen in environment. C_{L0} is assumed to be equal to the stress free equilibrium solubility of hydrogen in iron at 300 K, i.e. 2.084×10^{21} atoms/m³ (Sofronis and McMeeking, 1989). The equilibrium concentration in traps C_{T0} corresponding to C_{L0} is calculated from Eq. (4.27) as 8.4379×10^{20} atoms/m³.

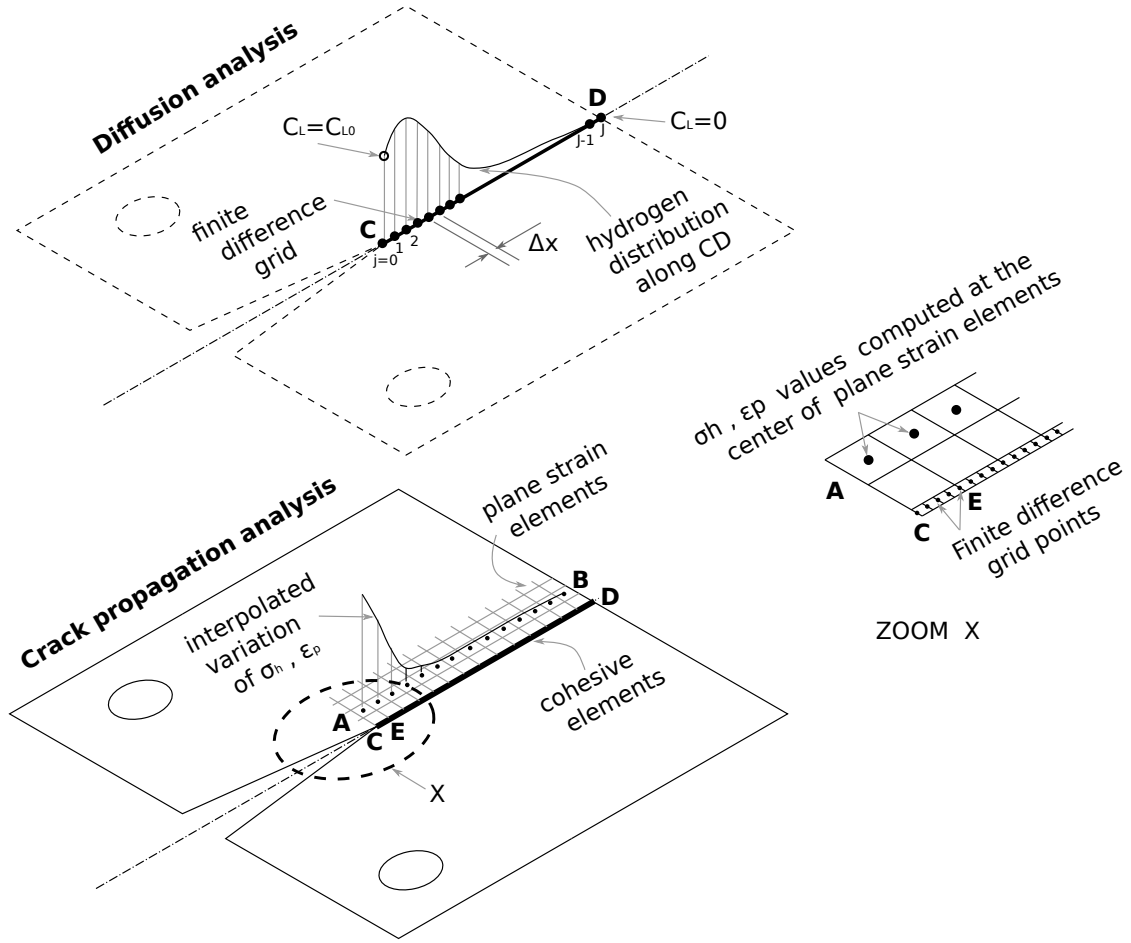


Fig. 4.17 Finite difference scheme used in HCD-CZM.

The finite difference representation of Eq. (4.30) is obtained (Press et al., 1998) using Crank-Nicholson scheme.

$$\begin{aligned}
 & \frac{(C_L)_j^{n+1} - (C_L)_j^n}{\Delta t} \\
 &= \frac{D_{eff}}{2} \left[\frac{[(C_L)_{j-1}^{n+1} - 2(C_L)_j^{n+1} + (C_L)_{j+1}^{n+1}] + [(C_L)_{j-1}^n - 2(C_L)_j^n + (C_L)_{j+1}^n]}{(\Delta x)^2} \right] \\
 & \quad - \frac{E_H}{2} \left[\frac{[(C_L)_{j+1}^{n+1} - (C_L)_{j-1}^{n+1}] + [(C_L)_{j+1}^n - (C_L)_{j-1}^n]}{2(\Delta x)} \right] \left[\frac{(\sigma_h)_{j+1}^n - (\sigma_h)_{j-1}^n}{2(\Delta x)} \right] \\
 & \quad - \frac{E_H}{2} [(C_L)_j^{n+1} + (C_L)_j^n] \left[\frac{(\sigma_h)_{j-1}^n - 2(\sigma_h)_j^n + (\sigma_h)_{j+1}^n}{(\Delta x)^2} \right] \quad (4.32)
 \end{aligned}$$

where $(C_L)_j^n$ is magnitude of C_L at time step n ; $j = 0, 1, 2, \dots, J$ are grid points; Δt is the time interval between step $(n + 1)$ and n ; Δx is the distance between grid points which is kept equal

to the cohesive element size used in the crack propagation analysis.

The diffusion and crack propagation analyses are coupled for each time interval Δt and are performed only once per time step. The selection of Δt is based on a numerical stability criterion (Press et al., 1998) for the diffusion solution.

$$\Delta t \leq \frac{(\Delta x)^2}{2D_{eff}}. \quad (4.33)$$

The values of σ_h and ϵ_p and current crack length required for solving Eqn.(4.32) are computed through the crack propagation analysis and passed on to diffusion analysis. Once a step increase in crack length occurs, the number of active grid points are correspondingly reduced to $j = i, i + 1, \dots, J$ where i is the grid point corresponding to the new position of crack tip and the boundary condition $C_L = C_{L0}$ is shifted to grid point i .

Starting with the specified initial condition, values of C_L at time step $(n + 1)$ can be obtained in terms of C_L at time step n through Eq. (4.32). This equation is applied at each of the inner grid points $j = (i + 1)$ to $(J - 1)$ and after rearrangement of terms in Eq. (4.32) this procedure gives a set of $(J - i - 1)$ linear equations.

$$\begin{aligned} &(-\alpha_1 + \beta_1)(C_L)_{j-1}^{n+1} + (1 + 2\alpha_1 - \gamma_1)(C_L)_j^{n+1} + (-\alpha_1 - \beta_1)(C_L)_{j+1}^{n+1} \\ &= (\alpha_1 - \beta_1)(C_L)_{j-1}^n + (1 - 2\alpha_1 + \gamma_1)(C_L)_j^n + (\alpha_1 + \beta_1)(C_L)_{j+1}^n \end{aligned} \quad (4.34)$$

where

$$\alpha_1 = \frac{D_{eff}\Delta t}{2(\Delta x)^2} \quad (4.35)$$

$$\beta_1 = \frac{E_H\Delta t}{8(\Delta x)^2} [(\sigma_h)_{j+1}^n - (\sigma_h)_{j-1}^n] \quad (4.36)$$

$$\gamma_1 = \frac{E_H\Delta t}{2(\Delta x)^2} [(\sigma_h)_{j-1}^n - 2(\sigma_h)_j^n + (\sigma_h)_{j+1}^n] \quad (4.37)$$

$$j = (i + 1), 2, 3, \dots, (J - 1)$$

These simultaneous equations are solved to obtain $(C_L)_j^{n+1}$ at the grid points j and this is repeated as many times as required in every time step.

4.3.3 Finite element (FE) based CZM

The CT specimen is discretised using 4 noded quadrilateral plane strain elements and the FE mesh details are identical to those used in the scheme I (Figure 4.6). The node positions of cohesive elements are identical to the spacing of grid points used in the finite difference solution. The node at the centre of bottom pin is held fixed while the centre of the top pin is subjected to the displacement load. The TSL for cohesive elements uses $T_0 = 2390$ MPa and $\delta_0 = 0.016$ mm; these values are the same as used earlier.

The coupled diffusion and finite element analysis is facilitated through user subroutine USDFLD of ABAQUS®. This routine computes the latest value of hydrogen concentration C_L on grid along CD (Figure 4.17) using Eq. (4.32). The values of σ_h and ϵ_p required at the same grid points are obtained through interpolation of the average values at centre of the plane strain elements along AB. The spacing between AB and CD is neglected for this purpose. It may be noted that there are four grid points over each element span, e.g. CE. The values along the single row of elements between AB and CD are not considered to avoid errors due to proximity of this row to the cohesive elements along CD. The term C used in Eq. (4.25) for modification of TSL is calculated as follows.

$$C = \frac{(C_L + C_T)}{(C_{L0} + C_{T0})} \quad (4.38)$$

The C_T is calculated from C_L using Eq. (4.27). The TSL is updated according to C at each integration point of the cohesive elements. The computation of damage to cohesive elements during crack propagation simulation proceeds with the updated TSL.

The load line displacement is obtained through the finite element based CZM analysis and the corresponding δ_5 is calculated using Eqn. (4.2) with $z = 0$.

4.3.4 Implementation of HCD-CZM in ABAQUS®

CZM based COH2D4 elements of ABAQUS® are placed along the crack path in the FE model. The concentration dependent TSL for these cohesive elements (Eqn. 4.25) is defined inside ABAQUS® using a user defined field variable. The variable is set equal to C . For computation of this variable, ABAQUS® provides a programmable interface through FORTRAN subroutine

USDFLD. This routine is invoked for every integration point of cohesive element at every time step. Based on the crack length at a given instant, and total time elapsed since the crack initiation, C at every integration point is obtained using the set of formulae in section 4.2.2 or 4.3.2. The TSL, which is defined in terms of C , gets updated and accordingly the damage to cohesive element is revised. The flow-chart and typical code for subroutine USDFLD is given in Fig. 4.18 and Appendix III respectively.

4.3.5 Results and discussion

The parameter D_{eff} is taken as 5.5×10^{-6} mm²/s. The same value has been used earlier in section 4.2.4. The parameter μ represents the extent of drop in strength corresponding to unit hydrogen concentration. The values of μ corresponding to the three loading rates have been obtained (Table 4.3) by matching the predicted results of δ_5 vs. Δa with the experimental data of Scheider et al. (2008). μ corresponding to scheme I are shown for comparison. Table 4.3

Table 4.3 Strength reduction factor μ obtained through scheme I and II.

	Rate of loading (mm/h)		
	0.001	0.01	0.1
μ^b without σ_h effect (scheme I)	0.200	0.150	0.100
μ^a with σ_h effect (scheme II)	0.140	0.080	0.025

shows that μ is highest for the slowest loading rate. This variation of μ is consistent with the findings of Krom et al. (1999) where the damage during HASCC is shown to be dependent on plastic strain rate. The lowest plastic strain rates lead to the highest drop in strength. The lowest plastic strain rates occur at the slowest loading rates and the corresponding value of μ is the highest.

Figure 4.19 shows a comparison of predicted and experimental δ_5 vs. Δa variation. The results of the scheme I are also included in Figure 4.19. The predicted results of the modified scheme, which includes the effects due to σ_h , are in agreement with the experimental data. Notably, it is also close to the results obtained using scheme I, without considering the effect of σ_h .

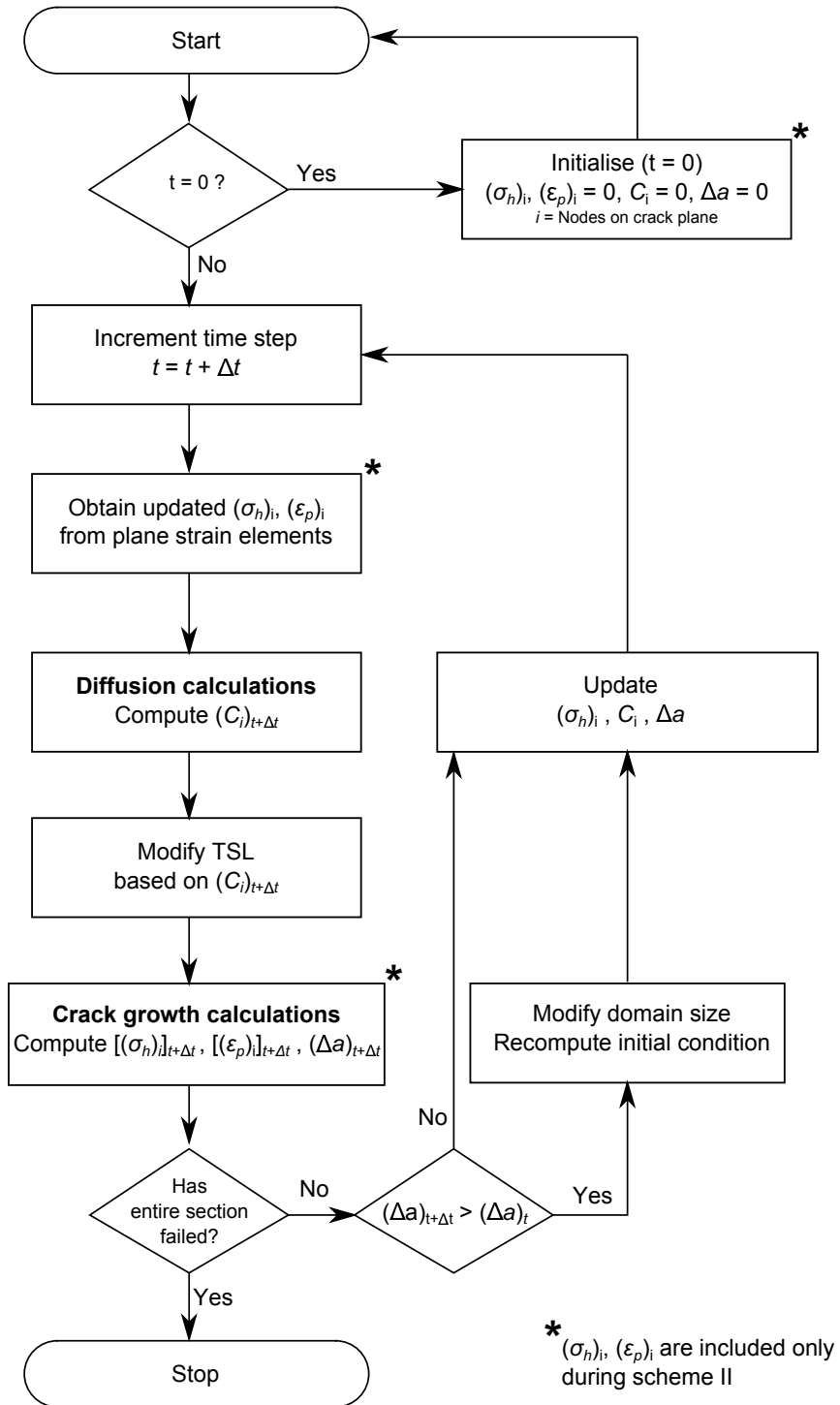


Fig. 4.18 Flow-chart of subroutine USDFLD.

Corresponding to $\Delta a = 0.025$ and $\Delta a = 1.0$ mm, the variations of C_L , C_T , σ_h and ϵ_p with distance from the crack tip for the three loading rates (0.001, 0.01 and 0.1 mm/h) are shown in Figures 4.20, 4.21 and 4.22 respectively.

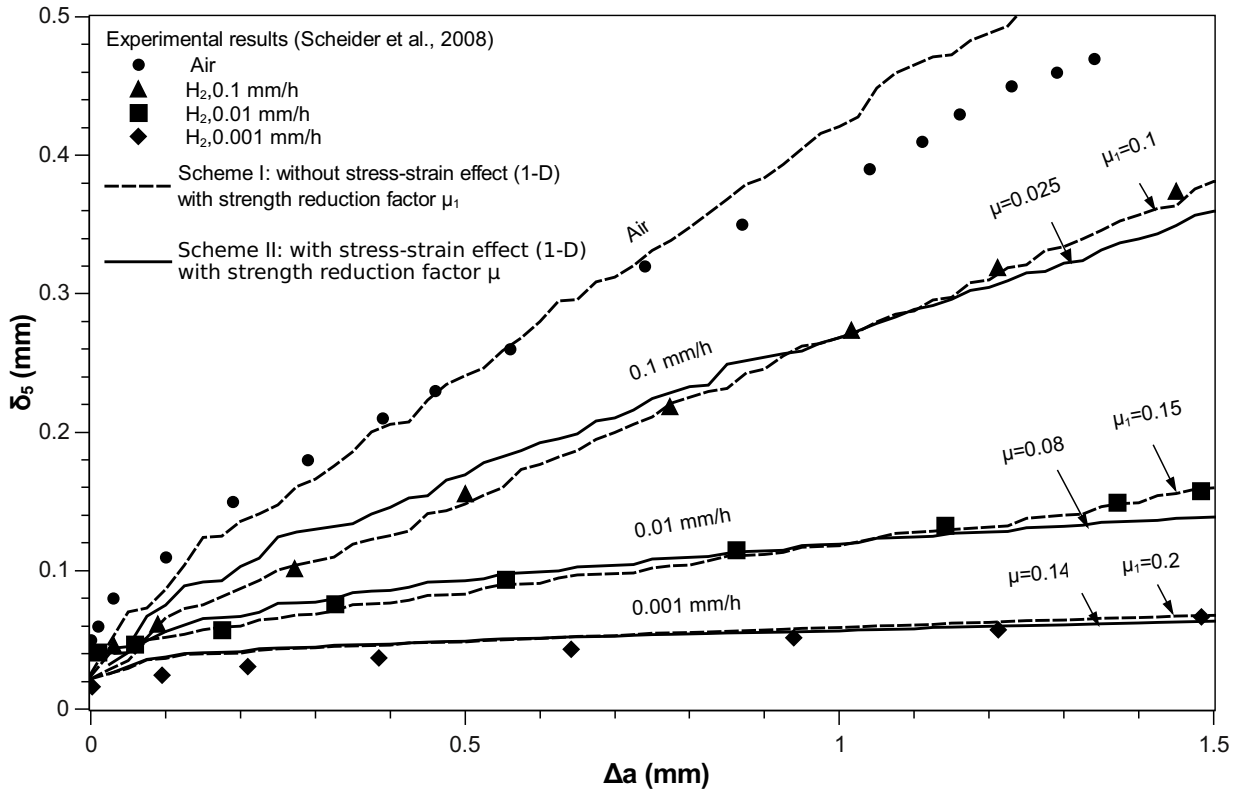


Fig. 4.19 Comparison of results with and without hydrostatic stress σ_h and plastic strain ϵ_p effect.

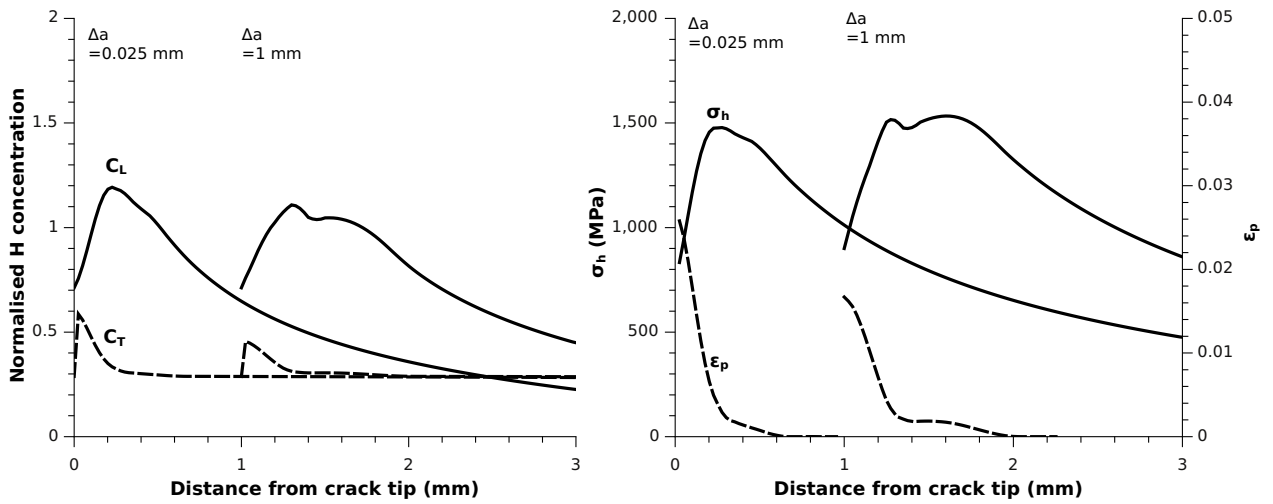


Fig. 4.20 Variation of C_L , C_T , σ_h and ϵ_p near crack tip, rate of loading = 0.001 mm/h.

There is resemblance between the distributions of C_L and σ_h on one hand, and C_T and ϵ_p on the other. This clearly indicates the influence of distribution of σ_h on C_L and ϵ_p on C_T . The distribution of total hydrogen concentration C is shown in Figures 4.23, 4.24 and 4.25 for the

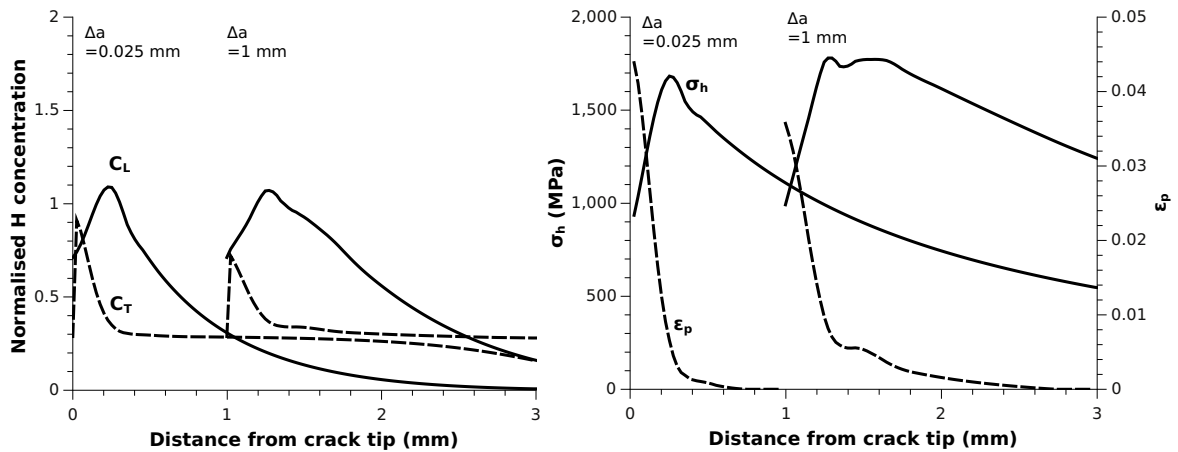


Fig. 4.21 Variation of C_L , C_T , σ_h and ϵ_p near crack tip, rate of loading = 0.01 mm/h.

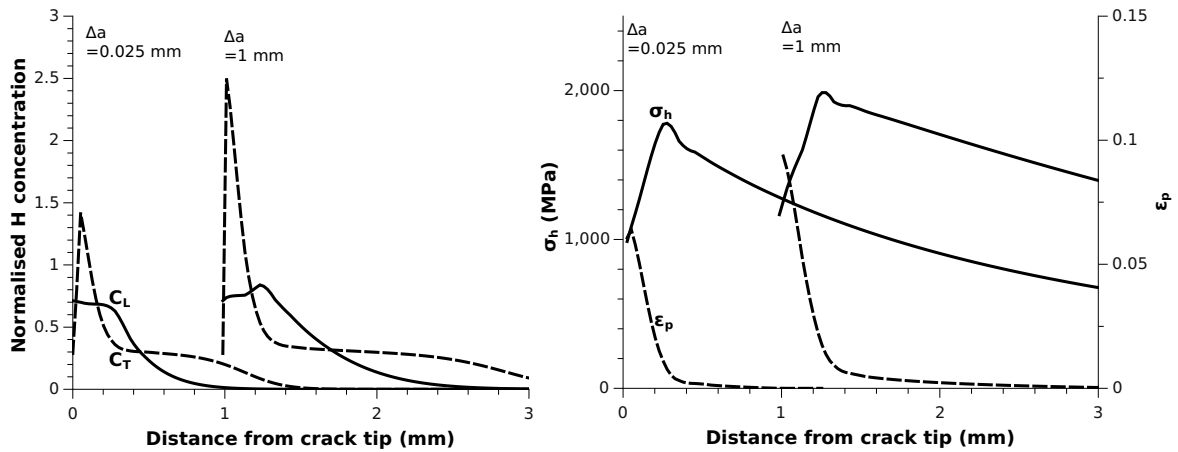


Fig. 4.22 Variation of C_L , C_T , σ_h and ϵ_p near crack tip, rate of loading = 0.1 mm/h.

three loading rates respectively. These figures also include the results of scheme I where the effects of σ_h on diffusion are neglected. In the scheme II, the maximum value of normalised hydrogen concentration occurs at a finite distance ahead of crack tip and it has values higher than 1. The peak location varies with loading rates and it occurs at a point closer to the crack tip at higher Δa loading rates. Further the hump in profile of C is the narrowest at the highest loading rate.

The average concentration C_{avg}^a of hydrogen in the three cases of loading rates were evaluated by numerically integrating the plot of C vs. distance up to 1 mm ahead of the crack tip. The same data C_{avg}^b was also computed in the case of scheme I. These two sets of average C are

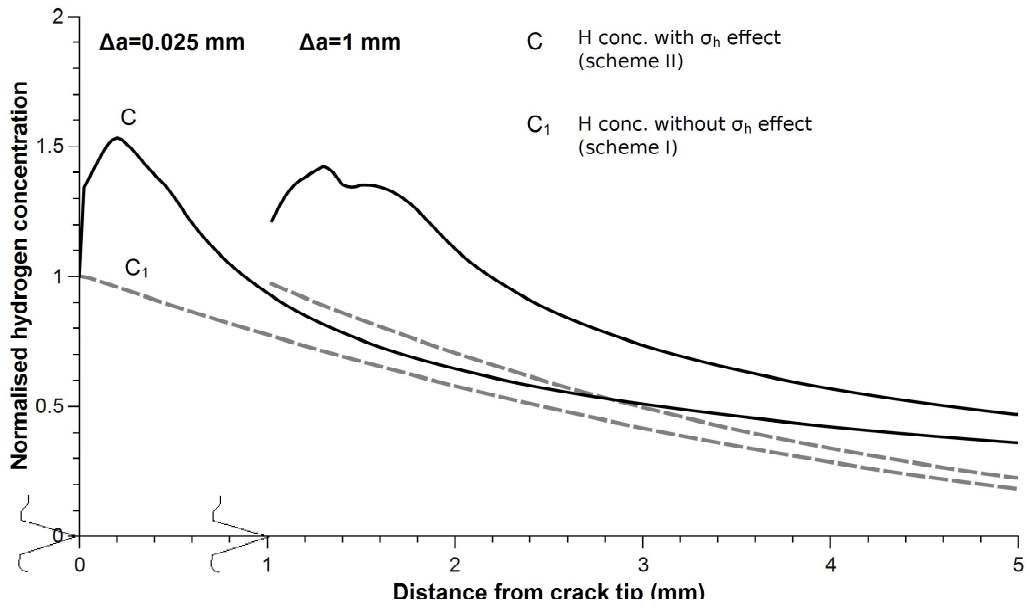


Fig. 4.23 Comparison of C with and without σ_h effect for loading rate of 0.001 mm/h.

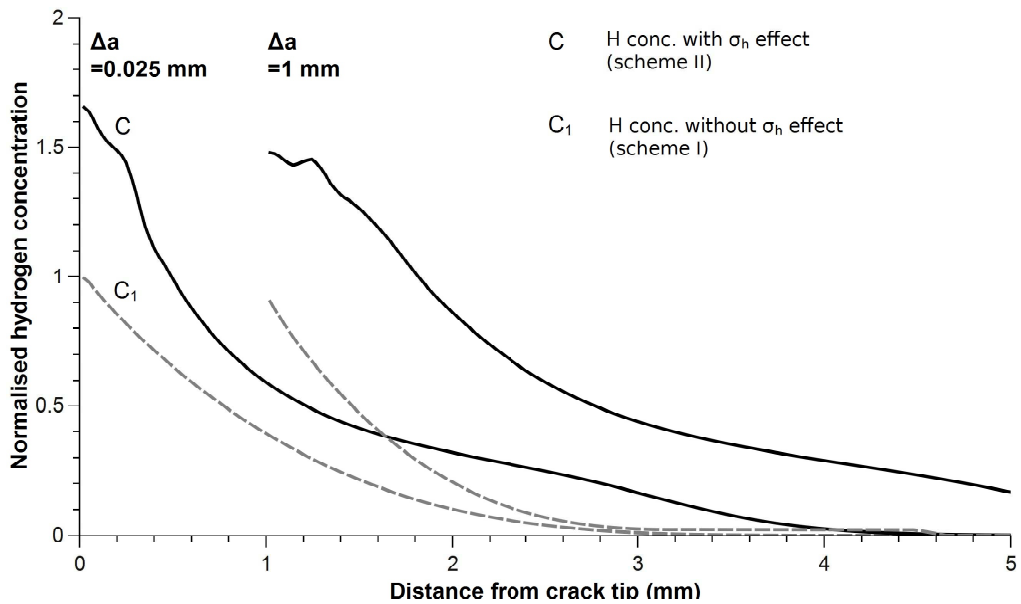


Fig. 4.24 Comparison of C with and without σ_h effect for loading rate of 0.01 mm/h.

compared in Table 4.4. The average hydrogen concentration by the scheme II is always higher. Since higher levels of average C indicate a higher damage and perhaps more crack growth rate, to predict the same experimental variation δ_5 with Δa , it is necessary to keep the same extent of reduction in the strength of cohesive elements. That is, μC must be closer in the two cases.

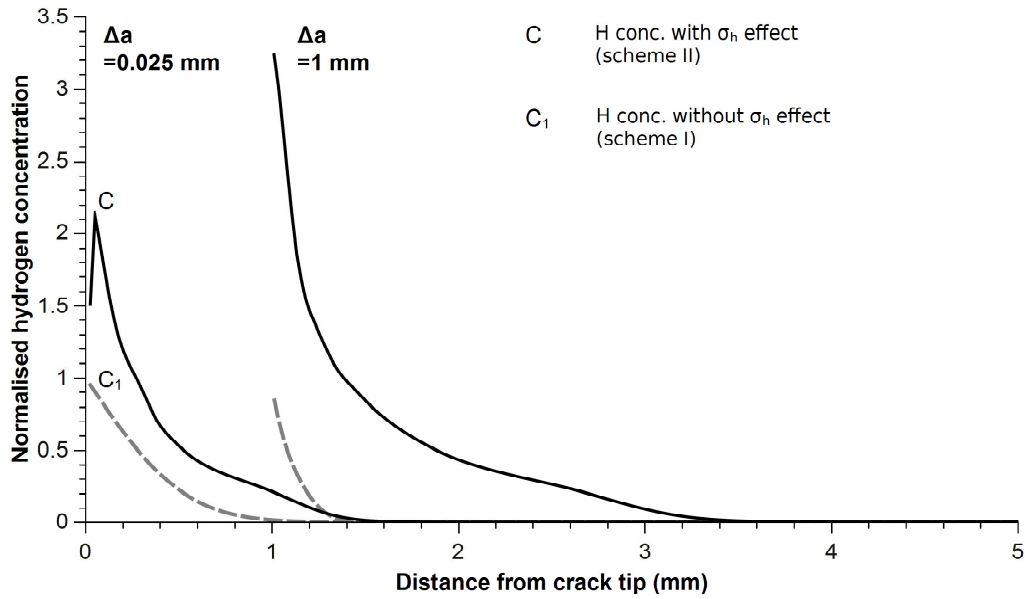


Fig. 4.25 Comparison of C with and without σ_h effect for loading rate of 0.1 mm/h.

This calls for lowering of μ 's in the scheme II matching the higher levels of hydrogen concentrations. μ 's obtained through the numerical studies (Table 4.4) tallies almost exactly with this expectation barring the case of highest loading rate.

The total hydrogen concentration C in the case of first two loading rates (0.001 and 0.01 mm/h) is dominated by the distribution of C_L than C_T . The maximum value of equivalent plastic strain $(\epsilon_p)_{max}$ near the crack tip at $\Delta a = 1$ mm for these two cases are 0.017 and 0.036 respectively. The total hydrogen concentration in the case of third loading rate (0.1 mm/h, $(\epsilon_p)_{max} = 0.099$) is dominated by that of C_T . This means that the total concentration distribution in the third case, where $\epsilon_p > 0.05$, is more dominated by the equivalent plastic strain ϵ_p distribution than σ_h distribution. Nevertheless, the average concentration C_{avg}^a in the third case of loading rate too is higher than in the corresponding value of the scheme I. This called for lowering of μ in this case too for the crack growth study.

4.4 Closing remarks

The stable crack growth under HASCC in structural steel can be predicted using a scheme developed using hydrogen concentration dependent cohesive zone model (HCD-CZM). The scheme

Table 4.4 Comparison of average hydrogen concentration C_{avg} and estimation of μ .

		Rate of loading (mm/h)		
		0.001	0.01	0.1
Scheme I	C_{avg}^b	0.87	0.64	0.30
Scheme II	C_{avg}^a	1.24	1.01	0.70
Scheme I	Damage $D_H = \mu^b \times C_{avg}^b$	0.174	0.096	0.030
Scheme II	Estimated $\mu = D_H / C_{avg}^a$	0.140	0.095	0.043
	Selected μ^a	0.140	0.080	0.025

is based on analytical solution for diffusion and FE analysis for crack growth. Two schemes are proposed. In the first scheme, the two processes are considered partially uncoupled. Specifically, the effect of stress distribution on the diffusion process are not considered. To address this situation, the second scheme has been evolved, where the effect of stress distribution on diffusion process has been properly accounted for. In the first scheme, the diffusion process has been analysed considering both 1-D and 2-D approaches. 1-D solution for diffusion combined with CZM of crack growth give good predictions for COD δ_5 vs. Δa variations at higher loading rates; 2-D solution combined with CZM of crack growth give good predictions for COD δ_5 vs. Δa even for lower loading rates. Further, these predictions give better agreement with the experimental δ_5 vs. Δa than the predictions of Scheider et al. (2008), whose analysis is based on FE approaches for both diffusion and crack growth. The proposed schemes eliminate the FE analysis of diffusion after every step of crack growth; thereby the time required for a case study reduces substantially. The uncoupled analysis has facilitated to obtain a correlation between the strength reduction factor μ and crack tip plastic strain rate $\dot{\epsilon}_p$, which can be exploited to account for the influence of strain rate on hydrogen damage indicated by Krom et al. (1999). In turn, this can help to improve the prediction for δ_5 vs. Δa variations.

For the coupled analysis, the following points are worth noting.

- (a) This approach of finite difference analysis of diffusion and CZM of crack growth are equally effective, though this scheme helps to bring out the effects of more process parameters.
- (b) The study with the inclusion of the effects of hydrostatic stress σ_h predicts the experimental crack growth behaviour (Scheider et al., 2008) employing lower values of μ and the same

value of D_{eff} as in the case of the first scheme.

- (c) An inclusion of the effect of hydrostatic stress in the diffusion process requires a reduction in the μ parameter for prediction of the same experimental COD δ_5 vs. Δa variation, since this method leads in general to higher concentration C of hydrogen. That is to say, to predict the same variation of COD δ_5 vs. Δa , it is necessary to maintain μC at the same level, hence μ must be reduced.
- (d) Ahead of crack tip, distribution of lattice hydrogen concentration C_L is dependent on the distribution of hydrostatic stress σ_h . Similarly the trap hydrogen concentration C_T is dependent on the distribution of plastic strain ϵ_p .
- (e) With the inclusion of the effect of hydrostatic stress in the diffusion analysis, the total hydrogen concentration is the highest at the point, where the hydrostatic stress is the highest. This location is slightly off the crack tip. If the effect of σ_h is not included in the analysis, the highest concentration occurs at the crack tip.
- (f) As a simplification of the process of analysis of HASCC, the effect of hydrostatic stress on the diffusion process can be neglected. Further, the full scheme can involve 1-D or 2-D analytical modelling of diffusion process plus CZM of crack growth.

Chapter 5

Analysis of HASCC through CNT specimen

5.1 Introduction

In this chapter the possibility of adopting the method of coupled diffusion and crack growth analysis for examining the growth of external circumferential crack in cylindrical notched tensile specimen¹ maintained under conditions that can promote IHAC and/or HEAC is explored. The theoretical predictions have been verified against experimental data reported in chapter 3.

5.2 HCD-CZM model for cylindrical geometry

The implementation of HCD-CZM to cylindrical geometry calls for modification in the solution of diffusion equation and crack growth. It is observed that the crack growth in a CNT specimen, during the fatigue pre-cracking stage as well as HASCC, occurs asymmetrically. However, the remaining ligament stays nearly circular, but its center becomes eccentric with respect to the specimen. To analyse the problem exactly, a 3-D approach is required. Such analysis is very expensive computationally. The experimental observation that the remaining ligament center

¹Most data reported in this chapter have been published in the following paper.

Raykar N. R., Maiti S.K., R. K. Singh Raman, Aryan Saurav (2013), 'Study of hydrogen concentration dependent growth of external annular crack in round tensile specimen using cohesive zone model', *Engineering Fracture Mechanics*, **106**, 49-66.

shifts in such a way that it is subjected to a bending moment along a plane of symmetry. This can be exploited to simplify the analysis. Taking advantage of the fact that the eccentricity is small, the diffusion process can still be analysed assuming axisymmetry. This will permit both analytical and finite difference (FD) analysis. The FD method will enable incorporating the effect of hydrostatic stress and plastic strain as in the case of modelling of CT specimen. Further, the cohesive zone model too can be simplified to a 2-D model to accommodate the effect of asymmetry appropriately.

5.2.1 Analysis of crack growth

As before, the shape of TSL can be rectangular, trapezoidal, exponential or triangular. For rectangular geometry of low alloy steel FeE690T, trapezoidal shape was found suitable (section 4.2.3). Both trapezoidal and triangular shapes were considered as candidates to simulate the tests in air. The triangular shape gave better agreement with experimental results. The suitability of triangular shape for similar brittle materials has been reported by Cornec et al. (2003). The triangular TSL (Fig. 5.1) is finally chosen for the present study.

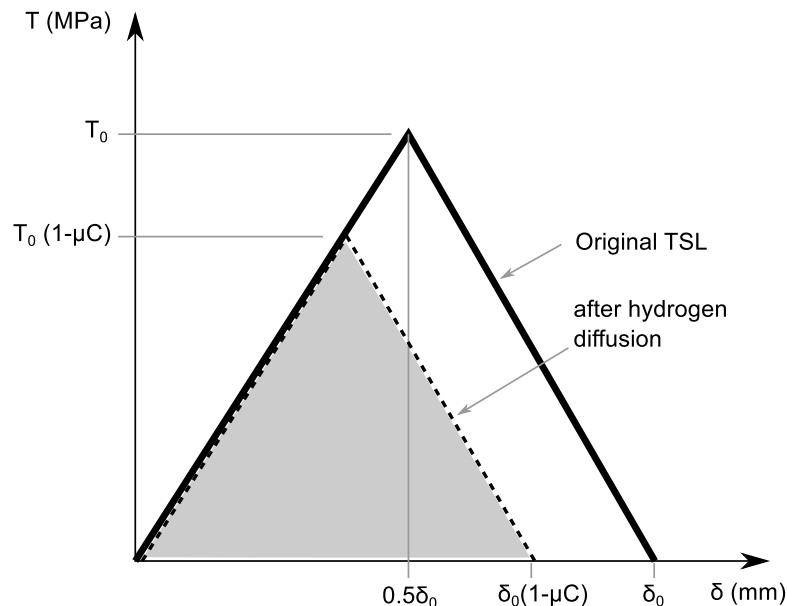


Fig. 5.1 Triangular TSL used in analysis.

There was choice for reducing the cohesive strength T_0 to $T_0(1 - \mu C)$ depending on the concentration C of hydrogen, where μ is the extent of reduction, as in the case of study of

CT specimen (chapter 4 and Scheider et al., 2008). There was also a choice for reducing both cohesive strength to $T_0(1 - \mu C)$ and the critical separation δ_0 to $\delta_0(1 - \mu C)$, which is illustrated in Fig. 5.1. Based on the experimental observations that there were reductions in both the ultimate strength and percentage elongation with hydrogen embrittlement for the material (Shim and Byrne, 1990), the second option was considered more appropriate.

5.2.2 Diffusion of hydrogen

As in the case of CT geometry (section 4.3), the total concentration of hydrogen within the material C_{tot} consists of two components, hydrogen in lattice C_L and in traps C_T . The diffusion of hydrogen through NLS is governed by the differential equation Eq. 2.1,

$$\frac{\partial C_L}{\partial t} = \vec{\nabla} \cdot (D_{eff} \vec{\nabla} C_L) - \vec{\nabla} \cdot \left(\frac{D_{eff} V_H}{RT_a} C_L \vec{\nabla} \sigma_h \right) - f(\dot{\epsilon}_p)$$

where the parameters are: partial molar volume of hydrogen in metal, $V_H = 2 \times 10^3 \text{ mm}^3/\text{mol}$ for iron; universal gas constant $R = 8.3144 \text{ J/mol-K}$; absolute temperature $T = 300 \text{ K}$. The last term, $f(\dot{\epsilon}_p)$ represents drift in the movement of hydrogen due to increase in number of trap sites depending on the plastic deformation. The situations considered here are mostly elastic, i.e., $\epsilon_p = 0$. Therefore $f(\dot{\epsilon}_p)$ in Eq. (2.1) can be neglected. Although effective diffusivity D_{eff} is dependent on C_L and C_T (Sofronis and McMeeking, 1989), in the present study D_{eff} is assumed to be constant for the full range of tests. This is similar to the approach adopted by Scheider et al. (2008) and given in chapter 4.

The distribution of C_L is obtained by employing the appropriate form of the above equation (i.e. Eq. (2.1) in polar coordinates). The distribution of C_T is obtained from that of C_L using Oriani's law (Eq. 4.27). The parameters of Oriani's law are kept the same as that of iron-hydrogen system considered in section 4.3.1. The trap density N_T depends on the equivalent plastic strain ϵ_p according to Eq. (4.28). For the present case $\epsilon_p = 0$, $N_T = 8.51 \times 10^{20} / \text{m}^3$ is employed.

The diffusion equation is solved to obtain the transient hydrogen concentration $C_{tot} = C_L + C_T$ along the crack plane. Thereby, the normalised hydrogen concentration $C = C_{tot}/C_{env}$, where C_{env} is the hydrogen concentration in the environment, is determined.

5.3 Study of crack growth

5.3.1 Overview of scheme of analysis

The problem involves solution of diffusion equation, CZM for crack growth and coupling of the two. The pre-crack edge profile in CNT specimen (Fig. 5.2) is generally non-circular and out-of-roundness is small. The ligament section can therefore be considered circular and diffusion can be considered axisymmetric. The diffusion of hydrogen in the axial direction can be neglected based on the observations associated with CT geometry (chapter 4) that the inclusion of diffusion in the direction normal to the crack plane does not affect appreciably the hydrogen concentration dependent crack growth. The two dimensional form in cartesian coordinates of the diffusion equation is given by Eq. (2.1). The corresponding axisymmetric form of the equation is given by the following.

$$\frac{\partial C_L}{\partial t} = D_{eff} \frac{\partial^2 C_L}{\partial r^2} + D_{eff} \frac{1}{r} \frac{\partial C_L}{\partial r} - E_H \frac{\partial C_L}{\partial r} \frac{\partial \sigma_h}{\partial r} - E_H C_L \left(\frac{\partial^2 \sigma_h}{\partial r^2} + \frac{1}{r} \frac{\partial \sigma_h}{\partial r} \right) \quad (5.1)$$

where r is the radial coordinate with respect to ligament center and $E_H = D_{eff} V_H / RT_a$.

The terms involving σ_h indicates the influence of hydrostatic stress on the diffusion process. An useful solution neglecting σ_h has been obtained earlier in connection with CT specimen (section 4.2), as a first approximation, an analytical solution has been obtained here in the absence of the effect of σ_h . The corresponding solution with the inclusion of σ_h is obtained here by finite difference method (FDM).

5.3.2 Finite element based CZM for crack growth

The consideration of axisymmetry of the ligament section is reasonable for the analysis of diffusion, but it is not tenable for the study of crack growth. The symmetry is lost because of the eccentricity of the external load with respect to the ligament centre. The ligament section is subjected to both tension and bending. During the crack growth the ligament center shifts along a diametral plane in which the bending moment acts. This fact can be conveniently utilised to evolve a 2-D analysis of crack growth.

The ligament area after fatigue pre-cracking is approximated by a circle of diameter d

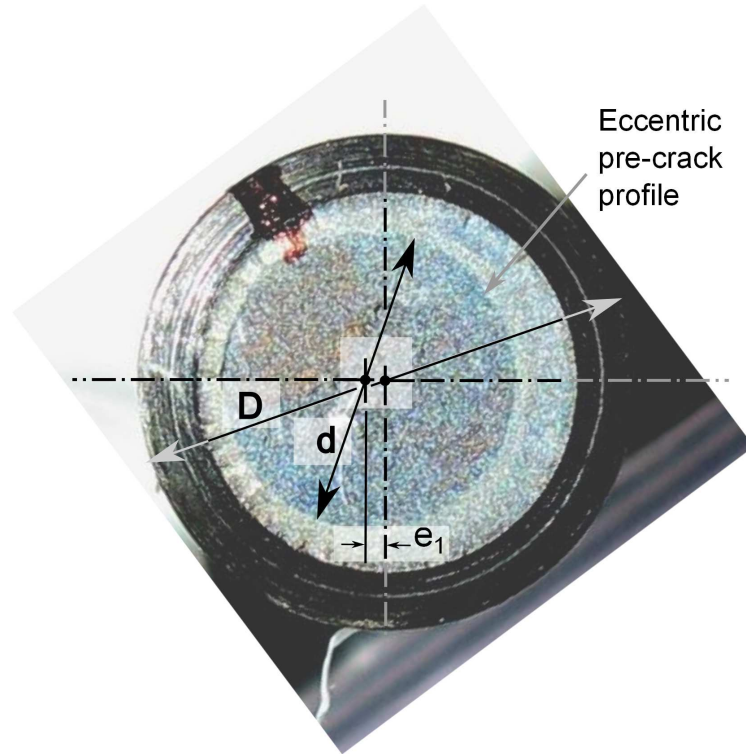


Fig. 5.2 Eccentric crack edge profile in CNT specimen.

(Fig. 5.3a). This circle is eccentric with respect to the specimen axis by e_1 . Because of the bending moment the vertical plane containing diameter AB always remains the plane of symmetry during the crack growth. After some crack extension, the new ligament circle diameter is d_i (Fig. 5.3b). The crack tip A on the left has extended by Δa_l and the tip B on the right has extended by Δa_r . d_i is equal to $d - \Delta a_r - \Delta a_l$ and crack growth $\Delta a = (\Delta a_r + \Delta a_l)/2$. The instantaneous eccentricity $(e_1)_i = e_1 + (\Delta a_r - \Delta a_l)/2$. The analysis is done considering a 2D discretisation in the plane (ABCD) of bending (Fig. 5.3c). Since the bending stresses do not vary in the z -direction for a particular x , it is sufficient to assume a two-dimensional analysis with thickness of an element to be equal to the total material width in the z -direction. That is, the dimension in z -direction for element n_1 is w_1 , for element n_2 it is w_2 , etc. The order of bending stress due to eccentricity is determined by distance x_1, x_2 , etc. for elements n_1, n_2 , etc., respectively. With the assignment of varying thickness the total bending load on an element in the vertical direction is preserved.

The ABAQUS® (2006) finite element code is employed for the FE calculations. The CNT specimen is discretised (Fig. 5.4) using four node quadrilateral plane strain elements (type

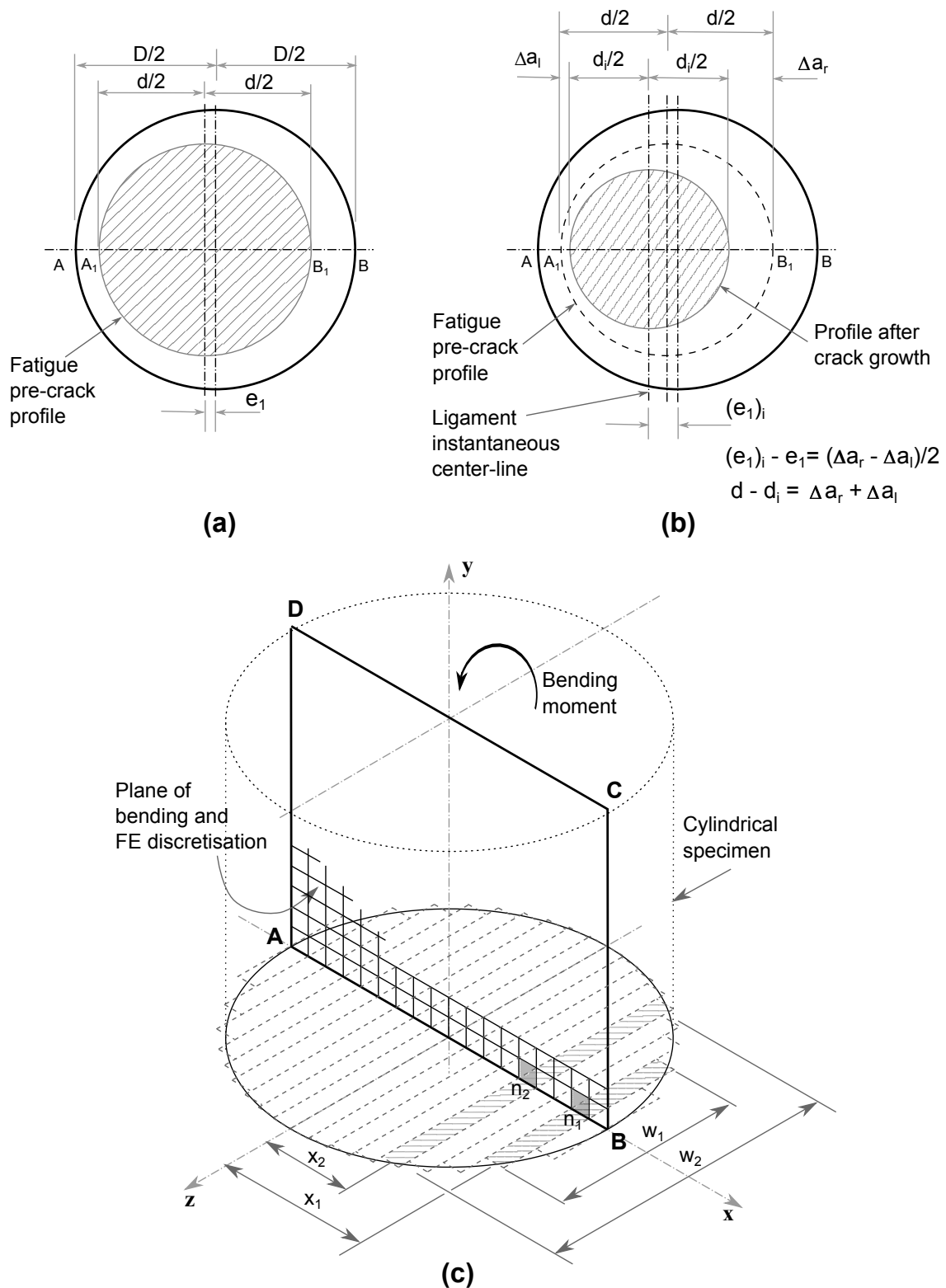


Fig. 5.3 Geometry for 2D analysis of CNT specimen. (a) Ligament circle after fatigue pre-cracking. (b) Ligament circle after crack growth. (c) Illustration of element thickness.

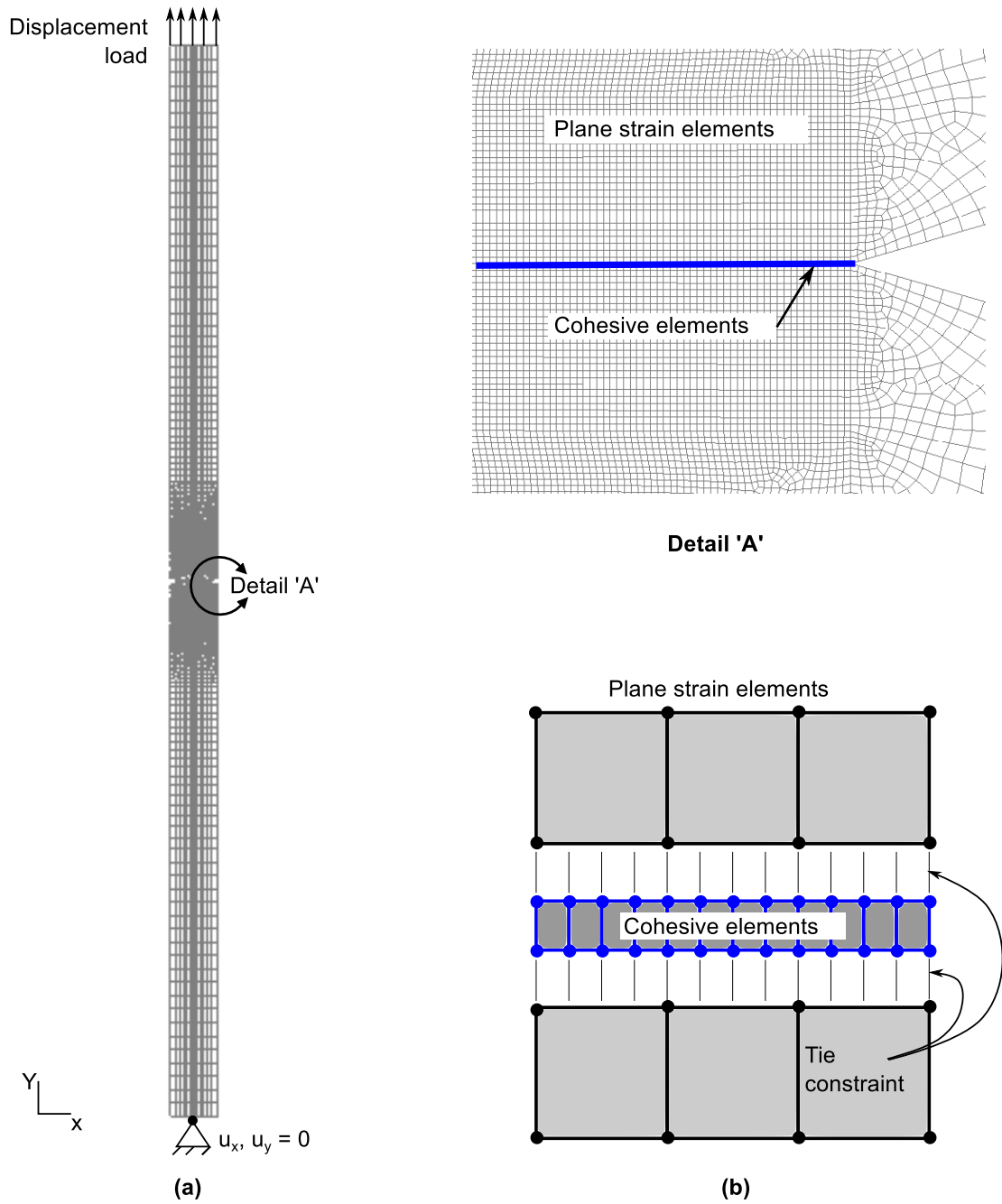


Fig. 5.4 Finite element discretisation: (a) FE mesh and boundary conditions (b) Schematic arrangement of cohesive elements.

CPE4). The width of these elements lying within 25 rows above and below the crack plane is kept uniformly 0.02 mm. The cohesive elements (type COH2D4) of height zero and width 0.005 mm are placed along the crack plane. The node positions of the cohesive elements are identical to the spacing of grid points in the finite difference analysis for diffusion. The thickness of each individual element is varied taking note of its dimension in the z-direction. It may be mentioned here that thickness of typical elements n_1 , n_2 and n_3 (Fig. 5.5), which are located at distances y_1 , y_2 and y_3 respectively from the crack plane ($y=0$) and x_1 , x_2 and x_3 respectively from y-z plane, are w_1 , w_2 and w_3 . As the crack extends, the ligament circle changes from P1 to P2. This calls for change in the thickness of cohesive elements. The thickness of cohesive element n_1 reduces upon crack growth from w_1 to $w_1' = r_t \times w_1$, where r_t is the thickness reduction ratio. The ABAQUS® code does not offer any technique to accommodate this change in the thickness during run-time. This has been accommodated as follows. The cohesive element with reduced thickness w_1' will offer resisting force, $F = b \times w_1' \times T$, where b is width of cohesive element along x-direction and T is the cohesive strength. The same resisting force $F = b \times w_1 \times r_t T$ is maintained by amending the traction to $r_t T$ and keeping the thickness w_1 unchanged. This sort of modification is done after every step of crack extension.

The tensile force in the CNT specimen corresponding to the rising displacement is continuously monitored. The maximum force on the specimen is noted to calculate K_{Ic}^H using Eq. (3.1).

5.3.3 Coupling of crack growth and diffusion analyses

The coupling between diffusion and crack growth analyses is done through USDFLD of ABAQUS®. Assuming crack tip is located at C (Figure 5.6) initially ($t = 0$), the concentration distribution of hydrogen along CD is obtained analytically or by FDM. At the beginning the hydrostatic stress σ_h along CD is assumed zero. Having obtained this concentration distribution, TSL is modified, CZM is carried out and σ_h distribution is obtained along CD. This variation of σ_h is taken to be the same as in the level AB. The span AC is negligible. The next step of analysis for $t = 0 + \Delta t$ begins. The diffusion calculation is done analytically ignoring σ_h distribution. The same calculation is done by FDM where the effect of σ_h distribution is included. The second cycle of crack growth analysis is then completed. If the critical state is arrived at one or more than one cohesive elements, crack is extended by the corresponding span of cohesive

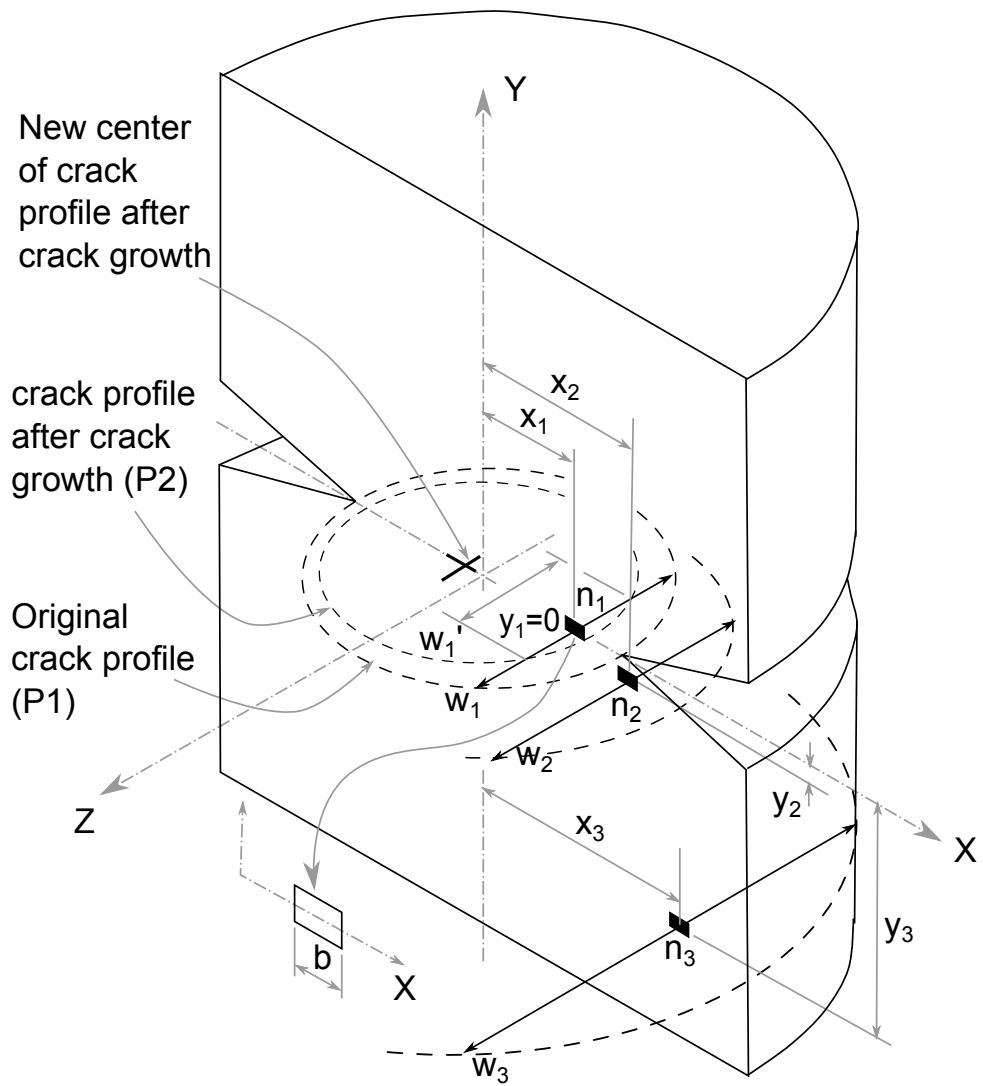


Fig. 5.5 Approximation for thickness of elements in 2D FE analysis.

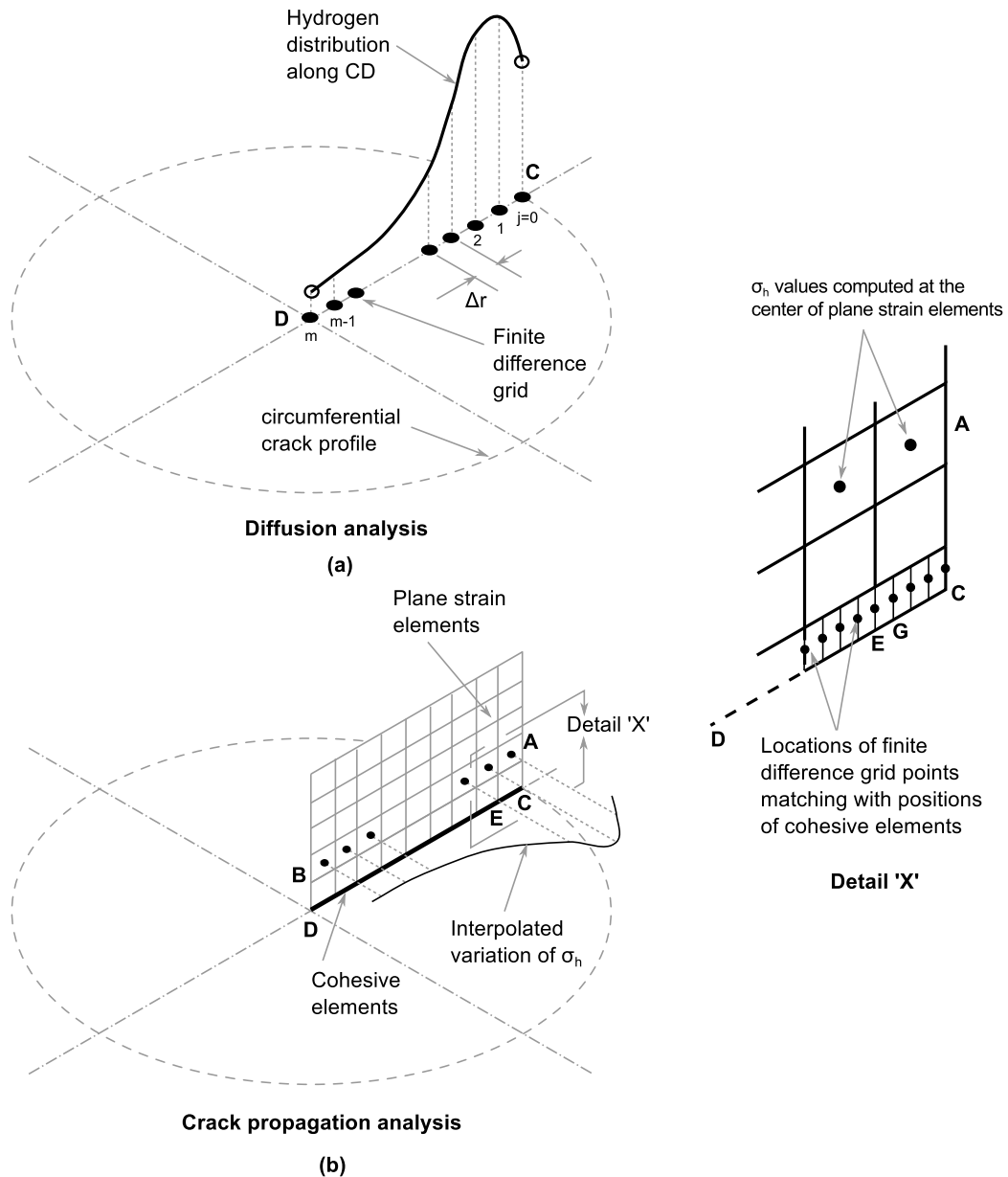


Fig. 5.6 (a) Hydrogen distribution over bending plane (b) Element arrangement on bending plane close to crack plane.

zone elements. Assuming crack extends by a 3-element span to G, the hydrogen concentration distribution over G to D is obtained from the distribution at the end of previous step of diffusion cycle, i.e., $t = \Delta t$. Thus the process continues till the crack extends over the whole ligament. At the end of each cycle of CZM, the load acting on the specimen is noted. The time step Δt is specified with an upper limit so as to restrict variation of hydrogen concentration and σ_h over Δt below an assigned level. The normalised concentration C is calculated using Eq. (4.38).

5.3.4 Boundary and initial conditions for diffusion analysis

Pre-charging stage of IHAC and combined IHAC+HEAC

During pre-charging stage, the concentration at the crack tip located at radius R_1 is maintained at a level equal to the hydrogen concentration C_{L0} in the environment for both $t = 0$ and $t > 0$ (Fig. 5.7a). C_{L0} is set equal to the stress free equilibrium solubility of hydrogen in iron at

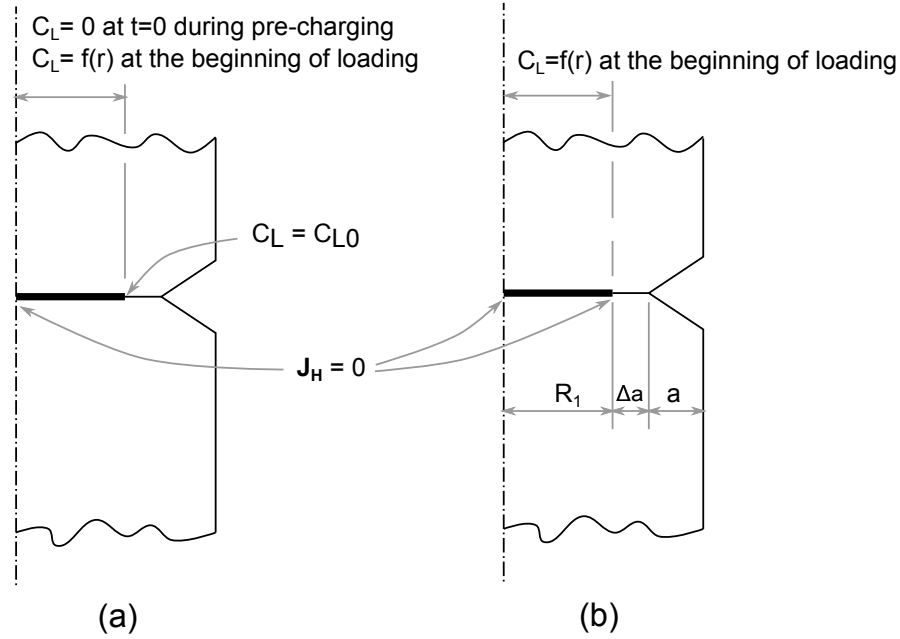


Fig. 5.7 Boundary and initial conditions for axisymmetric diffusion analysis. (a) Pre-charging stage for IHAC and combined IHAC+HEAC; also applicable to loading stage of HEAC and combined IHAC+HEAC. (b) Loading stage of IHAC.

300 K, i.e., 2.084×10^{21} atoms/m³ (0.00346 mol/m³) (Sofronis and McMeeking, 1989). The equilibrium concentration in traps C_{T0} corresponding to C_{L0} is calculated from Eq. (4.27) as 8.4379×10^{20} atoms/m³ (0.00140 mol/m³).

The hydrogen diffused inside material is driven by the distribution of hydrogen concentration and hydrostatic stress. It moves towards regions of lower driving potential, i.e., towards regions of lower hydrogen concentration and higher tensile hydrostatic stress. The flux of hydrogen at any point \mathbf{J}_H is given (Sofronis and McMeeking, 1989) by

$$\mathbf{J}_H = -D_L \nabla C_L + \frac{D_L C_L V_H}{RT} \nabla \sigma_h \quad (5.2)$$

where D_L is stress and concentration independent lattice diffusivity.

For axisymmetric geometry and axisymmetric boundary conditions, the hydrogen flux \mathbf{J}_H is zero at the center, $r = 0$. Hence $\frac{\partial C_L}{\partial r}, \frac{\partial \sigma_h}{\partial r} = 0$ always at $r = 0$. The boundary condition $\frac{\partial \sigma_h}{\partial r} = 0$ is enforced in the FDM by forcing σ_h to be equal at three consecutive grid points near the centre.

The virgin specimen is devoid of any hydrogen, i.e., at $t = 0$, $C_L = 0$ throughout the crack plane.

Loading stage of IHAC

The specimen for IHAC, after hydrogen pre-charging is loaded in air. During loading, the hydrogen trapped inside specimen is unlikely to escape into outside air. Therefore hydrogen flux \mathbf{J}_H at the crack tip in the radial direction can be taken as zero (Fig. 5.7b). Hence $\frac{\partial C_L}{\partial r}, \frac{\partial \sigma_h}{\partial r} = 0$ always at $r = R_1$ in addition to at $r = 0$. The boundary condition $\frac{\partial \sigma_h}{\partial r} = 0$ is enforced in the FDM in a manner similar to that described above for the pre-charging stage both at the center and crack edge/tip.

The hydrogen concentration distribution $C_L = f(r)$ obtained at the end of pre-charging stage becomes the initial condition for determination of changes in hydrogen concentration in the specimen after loading.

Loading stage of HEAC and combined IHAC+HEAC

During loading stage of HEAC and combined IHAC+HEAC, flux is zero at the centre and the concentration at the current crack tip located at radius R_1 is maintained at a level equal to the hydrogen concentration C_{L0} in the environment (Fig. 5.7a). Both these boundary conditions are identical to those occurring during pre-charging stage and are handled similarly.

During the initial state, the specimen for HEAC is free of any hydrogen, i.e., at $t = 0$, $C_L = 0$ throughout the crack plane. However, for the specimen for the combined IHAC+HEAC study, the hydrogen concentration distribution $C_L = f(r)$ obtained at the end of pre-charging stage becomes the initial condition.

For all cases, the initial condition after every step of crack growth Δa , is obtained in a manner described in section 5.3.3.

5.3.5 FDM based solution to diffusion equation

Eq. (5.1) is represented in finite difference form using the Crank-Nicholson scheme (Press et al., 1998).

$$\begin{aligned}
& \frac{(C_L)_j^{n+1} - (C_L)_j^n}{\Delta t} \\
&= \frac{D_{eff}}{2} \left\{ \frac{[(C_L)_{j-1}^{n+1} - 2(C_L)_j^{n+1} + (C_L)_{j+1}^{n+1}] + [(C_L)_{j-1}^n - 2(C_L)_j^n + (C_L)_{j+1}^n]}{(\Delta r)^2} \right\} \\
&+ \frac{D_{eff}}{2r_j} \left\{ \frac{[(C_L)_{j+1}^{n+1} - (C_L)_{j-1}^{n+1}] + [(C_L)_{j+1}^n - (C_L)_{j-1}^n]}{2(\Delta r)} \right\} \\
&- \frac{E_H}{2} \left\{ \frac{[(C_L)_{j+1}^{n+1} - (C_L)_{j-1}^{n+1}] + [(C_L)_{j+1}^n - (C_L)_{j-1}^n]}{2(\Delta r)} \right\} \left\{ \frac{(\sigma_h)_{j+1}^n - (\sigma_h)_{j-1}^n}{2(\Delta r)} \right\} \\
&- \frac{E_H}{2} \{(C_L)_j^{n+1} + (C_L)_j^n\} \left\{ \frac{(\sigma_h)_{j-1}^n - 2(\sigma_h)_j^n + (\sigma_h)_{j+1}^n}{(\Delta r)^2} \right\} \\
&- \frac{E_H}{2r_j} \{(C_L)_j^{n+1} + (C_L)_j^n\} \left\{ \frac{(\sigma_h)_{j+1}^n - (\sigma_h)_{j-1}^n}{2(\Delta r)} \right\} \tag{5.3}
\end{aligned}$$

where $(C_L)_j^n$, $(\sigma_h)_j^n$ are the magnitudes of C_L , σ_h at time step n ; $j = 0, 1, 2, \dots, m$. m is the number of grid points; Δt is the time step size; r_j is the radius of grid point j ; Δr is the distance between two adjacent grid points. Δr is kept equal to size of cohesive element employed for crack growth analysis. The maximum span of time Δt for the diffusion analysis is limited to $(\Delta r)^2/(2D_{eff})$. Eq. (5.3) can be rewritten in the form:

$$\begin{aligned}
& (-\alpha_1 + \beta_1 + \gamma_1)(C_L)_{j-1}^{n+1} \\
&+ (1 + 2\alpha_1 - \zeta_1 - \eta_1)(C_L)_j^{n+1} + (-\alpha_1 - \beta_1 - \gamma_1)(C_L)_{j+1}^{n+1} \\
&= (\alpha_1 - \beta_1 - \gamma_1)(C_L)_{j-1}^n + (1 - 2\alpha_1 + \zeta_1 + \eta_1)(C_L)_j^n \\
&+ (\alpha_1 + \beta_1 + \gamma_1)(C_L)_{j+1}^n \tag{5.4}
\end{aligned}$$

where

$$\alpha_1 = \frac{D_{eff}\Delta t}{2(\Delta r)^2} \quad (5.5)$$

$$\beta_1 = \frac{D_{eff}\Delta t}{4r_j\Delta r} \quad (5.6)$$

$$\gamma_1 = \frac{-E_H\Delta t}{8(\Delta r)^2} [(\sigma_h)_{j+1}^n - (\sigma_h)_{j-1}^n] \quad (5.7)$$

$$\zeta_1 = \frac{-E_H\Delta t}{2(\Delta r)^2} [(\sigma_h)_{j-1}^n - 2(\sigma_h)_j^n + (\sigma_h)_{j+1}^n] \quad (5.8)$$

$$\eta_1 = \frac{-E_H\Delta t}{4r_j\Delta r} [(\sigma_h)_{j+1}^n - (\sigma_h)_{j-1}^n] \quad (5.9)$$

$$j = (i + 1), (i + 2), \dots, (m - 1)$$

i is the grid point corresponding to current position of crack tip

The values of concentration $(C_L)_j^{n+1}$, at the grid points j at the end of time $t = \sum_{k=1}^n \Delta t_k$ are obtained by solving these simultaneous equations. This procedure is repeated at every time step.

5.3.6 Analytical solution to diffusion equation

Neglecting the effect of hydrostatic stress σ_h , the diffusion equation takes the following simplified form.

$$\frac{\partial C_L}{\partial t} = D_{eff} \frac{\partial^2 C_L}{\partial r^2} + D_{eff} \frac{1}{r} \frac{\partial C_L}{\partial r} \quad (5.10)$$

The solution to this second order differential equation can be obtained using the technique of separation of variables (Crank, 1975; Rosenheinrich, 2012). Although the governing equation remains the same for both IHAC and HEAC, the initial and boundary conditions are different for the two cases as described in section 5.3.4. Each situation is dealt with separately and the closed form solutions are obtained by imposing the appropriate boundary conditions.

Solution during pre-charging stage of IHAC and combined IHAC+HEAC:

$$C_L = C_{L0} \left[1 - \frac{2}{R_1} \sum_{k=1}^{100} \frac{1}{\alpha_k} \frac{J_0(r\alpha_k)}{J_1(R_1\alpha_k)} \exp(-D_{eff}\alpha_k^2 t) \right] \quad (5.11)$$

where J_0, J_1 are Bessel functions of the first kind of order zero and one respectively; α_k are the positive roots of $J_0(R_1\alpha_k) = 0$.

Solution during loading stage of IHAC:

$$C_L = \frac{2}{R_1^2} \left[\int_0^{R_1} r f(r) dr + \sum_{k=1}^{100} \exp(-D_{eff}\alpha_{k1}^2 t) \frac{J_0(r\alpha_{k1})}{J_0^2(R_1\alpha_{k1})} \int_0^{R_1} r f(r) J_0(\alpha_{k1} r) dr \right] \quad (5.12)$$

where α_{k1} are the positive roots of $J_1(R_1\alpha_{k1}) = 0$; $f(r)$ represents the concentration distribution of hydrogen after the pre-charging stage of IHAC.

Solution during loading stage of HEAC and combined IHAC+HEAC:

$$C_L = C_{L0} \left[1 - \frac{2}{R_1} \sum_{k=1}^{100} \frac{1}{\alpha_k} \frac{J_0(r\alpha_k)}{J_1(R_1\alpha_k)} \exp(-D_{eff}\alpha_k^2 t) \right] + \frac{2}{R_1^2} \sum_{k=1}^{100} \left[\exp(-D_{eff}\alpha_k^2 t) \frac{J_0(r\alpha_k)}{J_1^2(R_1\alpha_k)} \int_0^{R_1} r f(r) J_0(\alpha_k r) dr \right] \quad (5.13)$$

where $f(r)$ represents the concentration distribution of hydrogen after the pre-charging stage of combined IHAC+HEAC. $f(r) = 0$ at $t = 0$ for HEAC.

After every instance of crack growth, $f(r)$ in Eqs. (5.12) and (5.13) represents the distribution of hydrogen concentration on the crack plane at the time of crack growth. This distribution is approximated by a third order polynomial $f(r) = p_0 + p_1 r + p_2 r^2 + p_3 r^3$. With this approximation the definite integrals within Eqs. (5.12) and (5.13) are obtained as follows.

$$\int_0^{R_1} rf(r)dr = p_0 \frac{R_1^2}{2} + p_1 \frac{R_1^3}{3} + p_2 \frac{R_1^4}{4} + p_3 \frac{R_1^5}{5} \quad (5.14)$$

$$\begin{aligned} & \int_0^{R_1} rf(r)J_0(\alpha_{k_i}r)dr \\ &= \frac{p_0}{\alpha_{k_i}^2} R_1 \alpha_{k_i} J_1(R_1 \alpha_{k_i}) \\ &+ \frac{p_1}{\alpha_{k_i}^3} \left[R_1^2 \alpha_{k_i}^2 J_1(R_1 \alpha_{k_i}) - \phi(R_1 \alpha_{k_i}) \right] \\ &+ \frac{p_2}{\alpha_{k_i}^4} R_1 \alpha_{k_i} \left[2R_1 \alpha_{k_i} J_0(R_1 \alpha_{k_i}) - (R_1^2 \alpha_{k_i}^2 - 4) J_1(R_1 \alpha_{k_i}) \right] \\ &+ \frac{p_3}{\alpha_{k_i}^5} \left[(R_1^4 \alpha_{k_i}^4 - 9R_1^2 \alpha_{k_i}^2) J_1(R_1 \alpha_{k_i}) + 3R_1^3 \alpha_{k_i}^3 J_0(R_1 \alpha_{k_i}) + 9\phi(R_1 \alpha_{k_i}) \right] \end{aligned} \quad (5.15)$$

$$\phi(R_1 \alpha_{k_i}) = \frac{\pi R_1 \alpha_{k_i}}{2} [J_1(R_1 \alpha_{k_i}) H_0(R_1 \alpha_{k_i}) - J_0(R_1 \alpha_{k_i}) H_1(R_1 \alpha_{k_i})] \quad (5.16)$$

where α_{k_i} is either α_{k_1} or α_k corresponding to the computation of the integrals from Eq. (5.12) or (5.13) respectively. H_0, H_1 are Struve functions (Rosenheinrich, 2012).

5.4 Results and discussion

The HCD-CZM approach was applied to predict K_{Ic}^H for all test cases. Each of the 16 specimens used in the experiment were separately analysed. The basic TSL parameters for the test material are determined by matching the simulation results with experimentally obtained values of K_{Ic} for the tests in air with $T_0 = 2500$ MPa and $\delta_0 = 0.01$ mm. The other two modelling parameters D_{eff} and μ were found by iterations to give the best agreement between experimental and predicted K_{Ic}^H over the whole range of tests. The modelling involved diffusion calculations by both finite difference method (FDM) and analytical approach. The parameter D_{eff} obtained thereby is 1×10^{-5} mm²/s. This value lies within the experimentally measured range of 1×10^{-4} to 1×10^{-7} mm²/s for iron/steel at room temperature (Olden et al., 2008; Hirth, 1980). The strength reduction factor μ is known to depend on equivalent plastic strain rate $\dot{\epsilon}_p$ (shown in

section 4.2.4). As has been mentioned earlier, for all the current tests computed plastic strain ϵ_p and plastic strain rate $\dot{\epsilon}_p$ are zero. The absence of ϵ_p is consistent with the low level of nominal stress (~ 300 MPa) compared with material's yield strength 1525 MPa in the specimens at the time of failure. In the absence of plastic strain, μ is independent of the loading rate. It was therefore considered constant for all test cases. $\mu = 0.75$ has been determined through iterations. The absence of plastic strain ϵ_p also justifies the assumptions (section 5.2.2) of neglecting plastic strain rate term in Eq. (2.1) and eliminating ϵ_p term in Kumnick and Johnson's law (Kumnick and Johnson, 1980).

The time step Δt in the crack growth analysis is always maintained below $T_{tot}/100$, where T_{tot} is the total duration of an experiment. This consideration has helped to attain a small (less than 1% of the maximum) change of σ_h and C over Δt . This too justifies the assumption of constant σ_h and C over Δt for diffusion and crack growth analyses (section 5.3.3).

Hydrogen concentration distributions obtained analytically or by FDM ahead of the crack tip are shown in Figs. 5.8 and 5.9 for typical IHAC and HEAC tests (S27, S22 in Table 3.2) respectively. The results are presented at $t = 12$ h and 14h for IHAC and HEAC. In the case of IHAC, the curves corresponding to $t = 12$ h represent the concentration distribution computed at the end of the pre-charging stage. Both FDM and analytical approaches predict nearly identical distributions away from the crack tip. The concentrations predicted near the crack tip by FDM are higher than the analytical approach. This is expected because the effect of hydrostatic stress is included only in the FDM calculations. The concentration peaks occur at a location a little ahead of the crack tip. This distribution is very similar to that of the corresponding σ_h distribution (Figs. 5.8 and 5.9), which confirms the influence of σ_h on the hydrogen distribution.

The comparisons of the predicted values of K_{Ic}^H using both FDM and analytical approaches against the experimental data are presented in Figs. 5.10, 5.11 and 5.12, respectively for IHAC, HEAC and combined IHAC-HEAC cases. The percentage deviations of predicted results (fitted line) from the averaged experimental data are compared in Table 5.1. The predicted results of K_{Ic}^H based on both FDM and analytical approaches are close to the experimental observations except in the case of IHAC tests, where differences are generally much higher. There is no significant improvement in the accuracy of results by the inclusion of effect of σ_h .

The K -resistance curve, K_R vs Δa , obtained through FE analysis for three typical cases

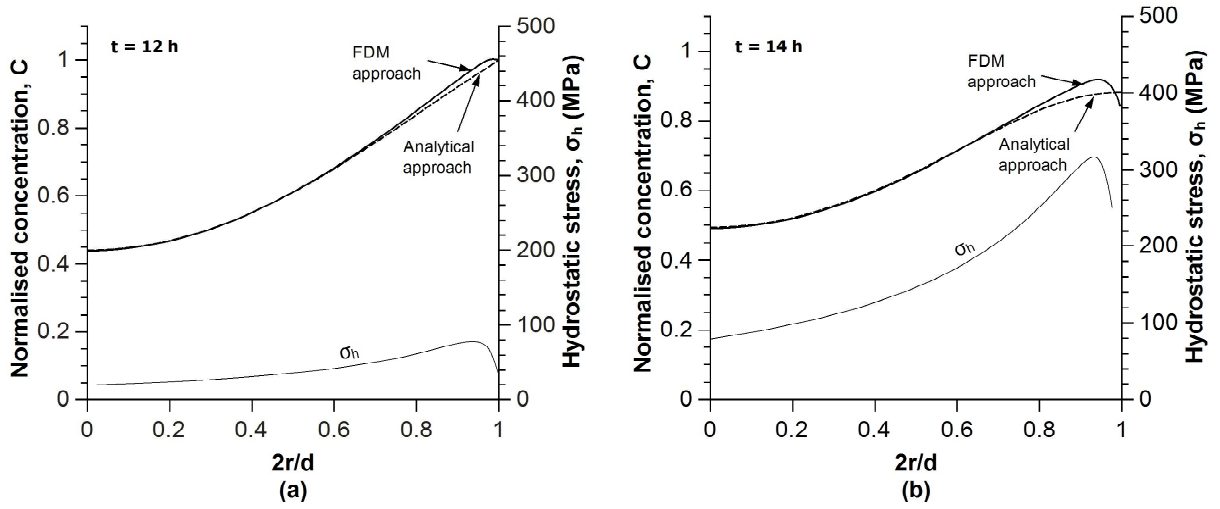


Fig. 5.8 Typical hydrogen concentration and σ_h distributions predicted during IHAC test for specimen S27 at (a) $t = 12$ h and (b) $t = 14$ h.

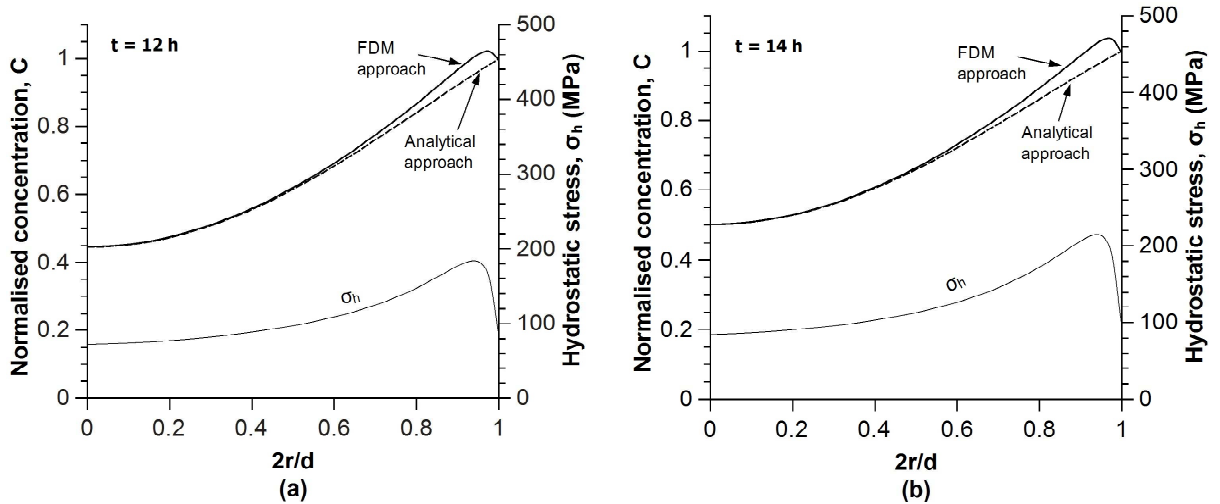


Fig. 5.9 Typical hydrogen concentration and σ_h distributions predicted during HEAC test for specimen S22 at (a) $t = 12$ h and (b) $t = 14$ h.

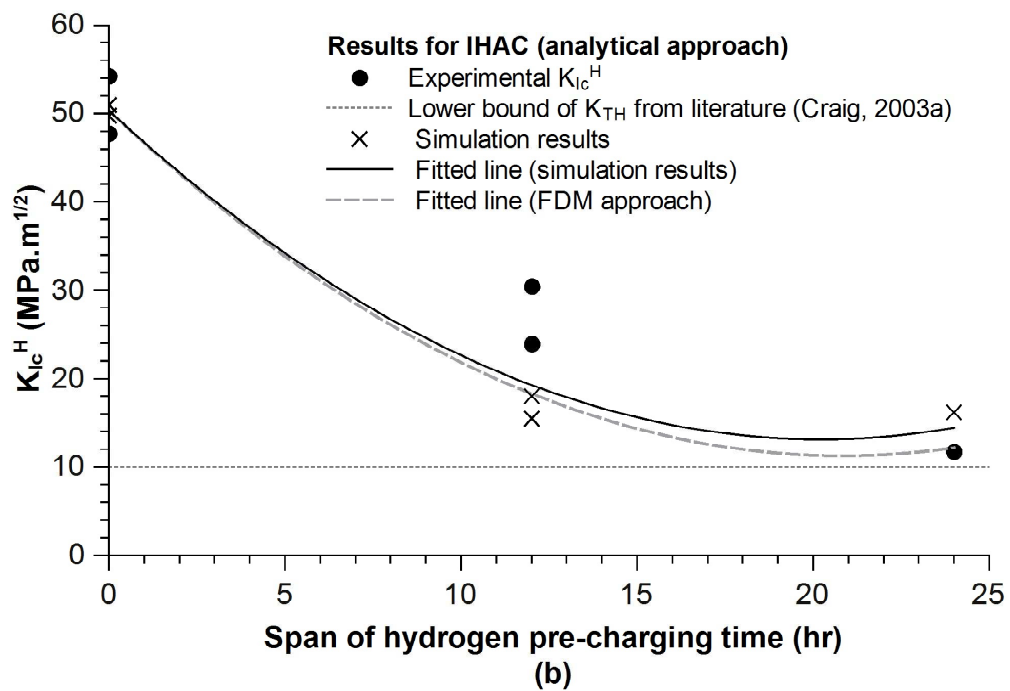
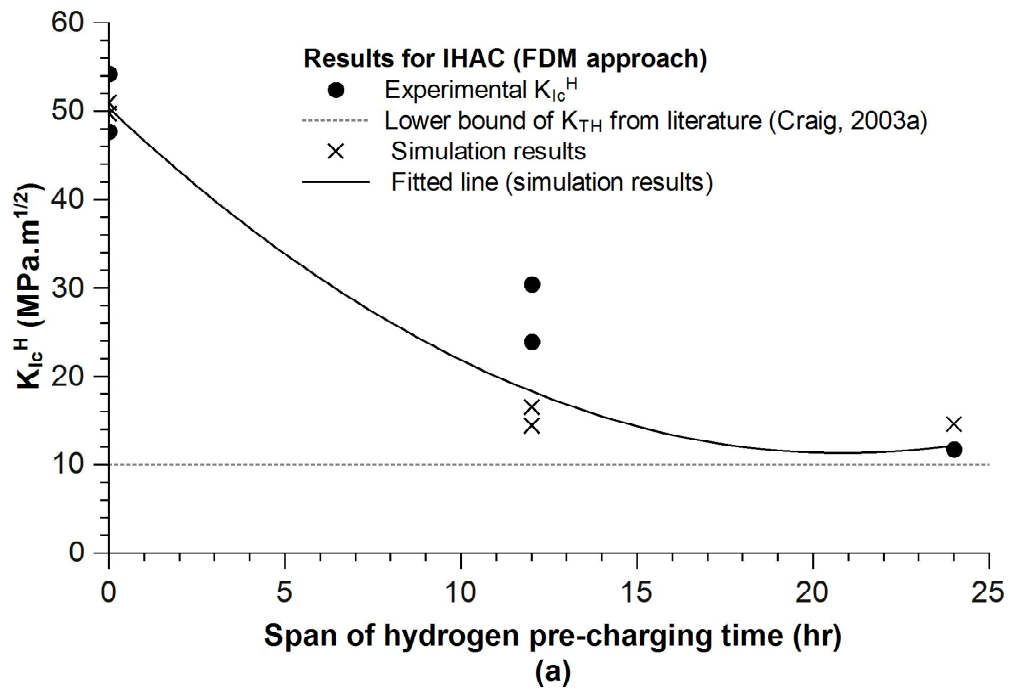


Fig. 5.10 Predicted K_{Ic}^H for IHAC using (a) FDM and (b) analytical approaches.

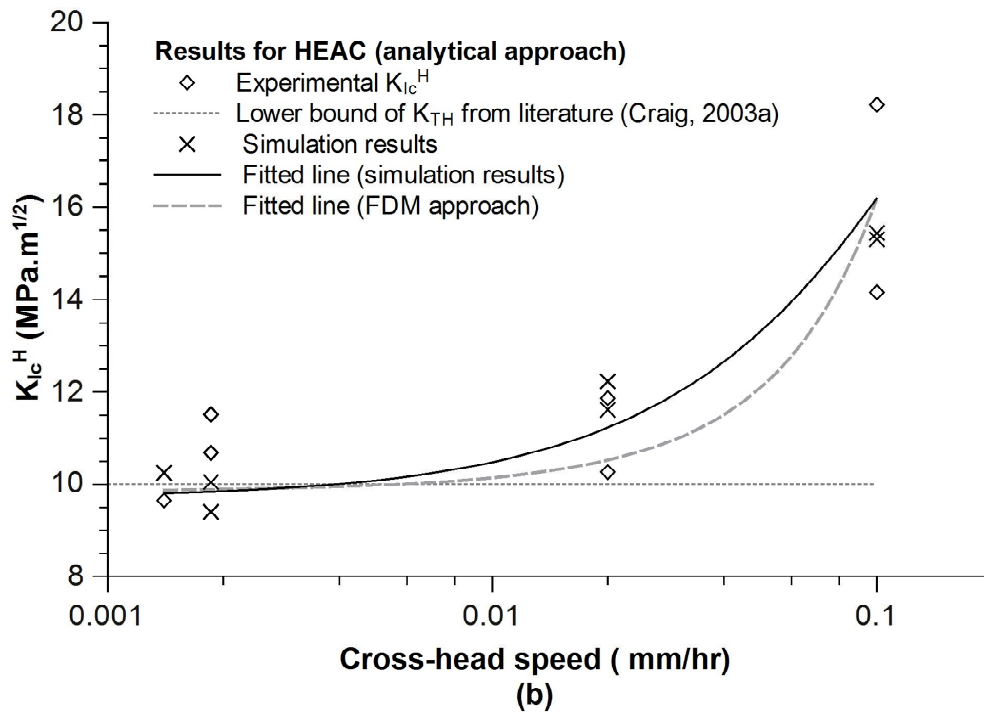
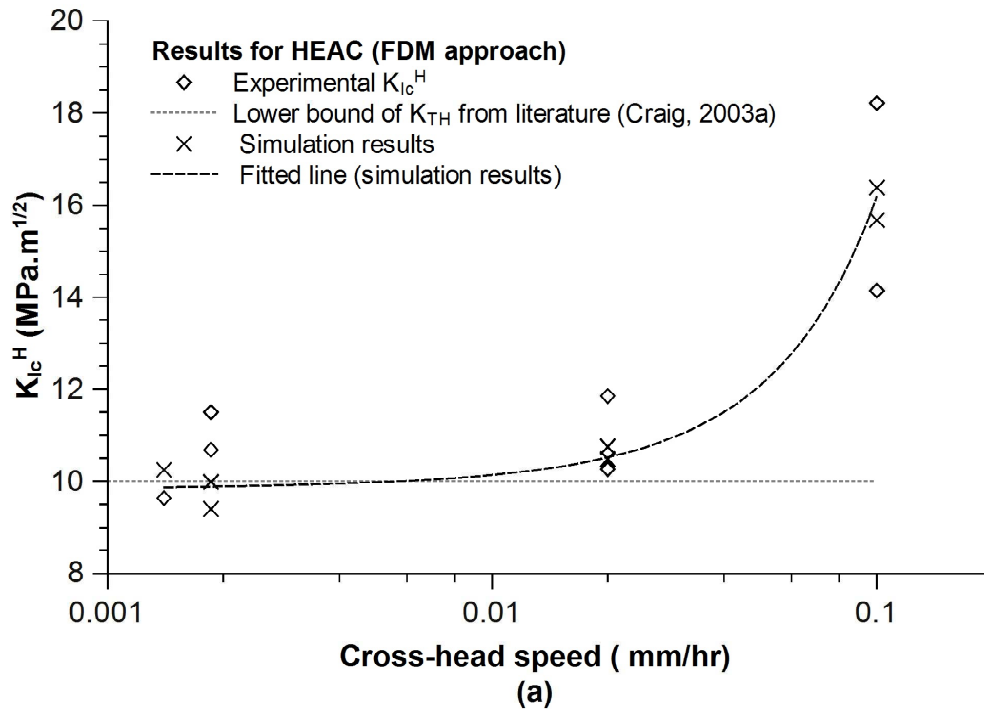


Fig. 5.11 Predicted K_{Ic}^H for HEAC using (a) FDM and (b) analytical approaches.

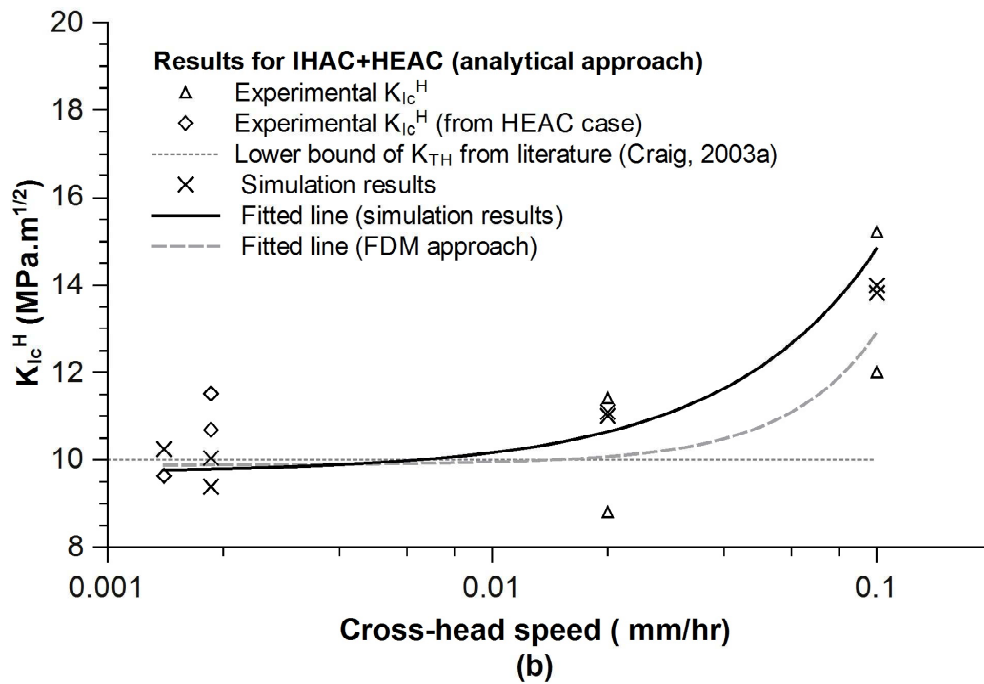
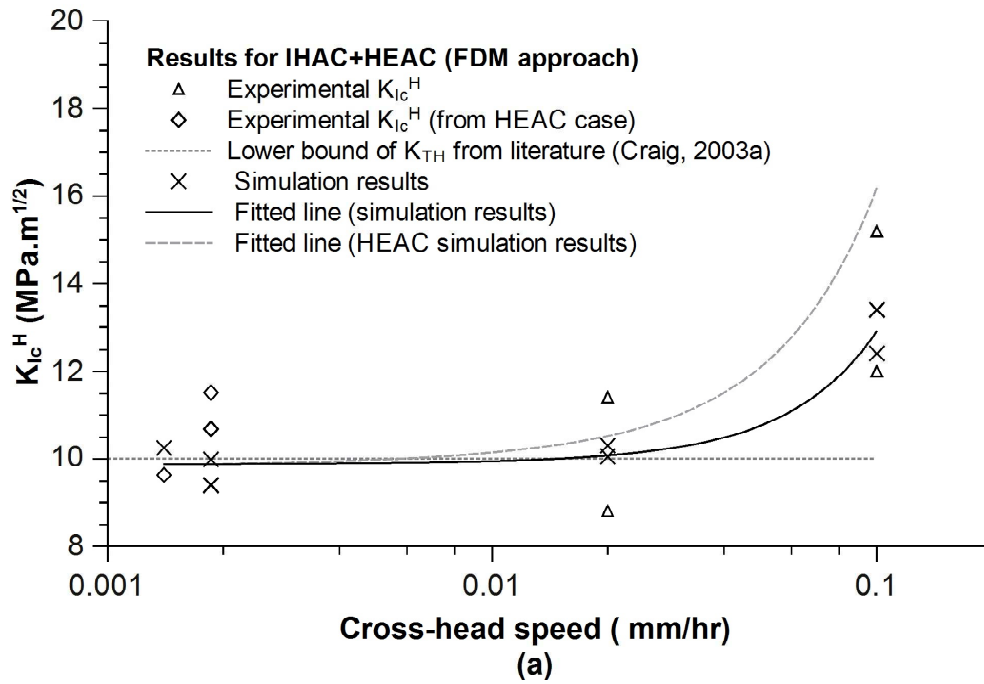


Fig. 5.12 Predicted K_{Ic}^H for IHAC+HEAC using (a) FDM and (b) analytical approaches.

Table 5.1 Experimental and predicted K_{Ic}^H in MPa.m^{1/2}. Values in parenthesis represent percentage deviation of predicted K_{Ic}^H from experimental data.

Approach	Tests in air	IHAC		HEAC			IHAC+HEAC		
		Pre-charge time (h)		Cross-head speed (mm/h)			Cross-head speed (mm/h)		
		12	24	0.1	0.02	0.0014, 0.0019	0.1	0.02	0.0014, 0.0019
Experimental	51.0	27.2	11.2	16.2	11.1	10.6	13.6	10.1	10.6
FDM	50.3	18.3 (-32.6)	12.0 (+2.6)	16.0 (-1.1)	10.5 (-4.7)	9.9 (-6.9)	12.9 (-5.1)	10.2 (+0.8)	9.9 (-6.9)
Analytical	(-1.3)	19.5 (-28.2)	14.3 (+22.2)	16.1 (-0.5)	11.2 (+1.2)	9.8 (-7.6)	14.8 (+8.8)	10.6 (+5.0)	9.8 (-7.6)

are shown in Fig. 5.13. The instantaneous crack growths, Δa_l at the left edge and Δa_r at the right edge (Fig. 5.3), were obtained from the spans of damaged cohesive elements. Almost entire crack extension occurred from the tension side, i.e., $\Delta a_l = 0$, except for a short period before the final failure. K_R was calculated at different $\Delta a = (\Delta a_r + \Delta a_l)/2$ using Eqs. (3.1) to (3.7) and considering $d_i = d - \Delta a$ and $(e_1)_i = e_1 + (\Delta a_r - \Delta a_l)/2$. This data could not be verified by experiments because there was no provision for monitoring Δa in the set-up. The rising nature of K_R vs Δa curve is in order because of the fact that crack grows gradually through regions of lower hydrogen concentration. As the hydrogen concentration reduces, the decohesion energy requirement increases and hence the fracture resistance. The decohesion energy increases because the cohesive strength and crack opening displacement increase with decreasing hydrogen concentration.

In general, the threshold stress intensity factor K_{TH} is associated with no crack growth. In the present experiments the test duration varied widely. In some cases the loading rates were were so low that the tests prolonged up to 9 days; the crack grew at a negligible rate. Such loading level was indicating a stress intensity level close to the K_{TH} of the material available from the literature. Thus the prolonged tests can perhaps be used to extract the threshold stress intensity factor. The lowest three stress intensity factors computed during HEAC tests are 10.25, 10.0 and 9.4; average = 9.9 MPa.m^{1/2}. The reported K_{TH} data for C-Mn and alloy steels including the test material at room temperature in NaCl and other environments facilitating hydrogen

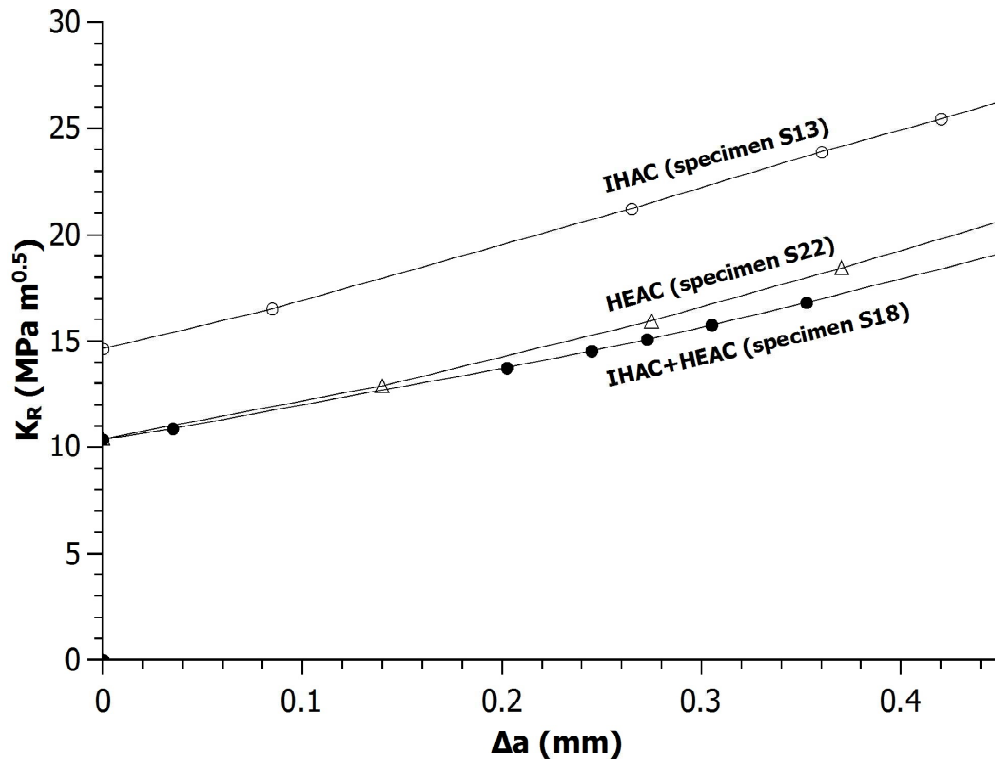


Fig. 5.13 Typical K -resistance curves obtained through FE analysis.

evolution lie in the range of 10–15 MPa.m^{1/2} (Brown and Beachem, 1965; Craig, 2003a; R.K. Singh Raman et al., 2007b). The present data, though approximate, is close to the lower range of the reported data.

It is observed that the strength reduction factor μ may be estimated using the experimental data of K_{Ic} and K_{TH} . The traction separation law on the crack plane corresponding to K_{Ic} and K_{TH} tests can be represented (Fig. 5.1) with $C = 0$ and 1 respectively. The cohesive energies of material corresponding to these states are $(\Gamma)_{Ic} = 0.5T_0\delta_0$ and $(\Gamma)_{TH} = 0.5T_0\delta_0(1 - \mu)^2$. Approximately

$$\frac{(\Gamma)_{Ic}}{(\Gamma)_{TH}} = \frac{(1 - \nu^2)\frac{K_{Ic}^2}{E}}{(1 - \nu^2)\frac{K_{TH}^2}{E}} = \frac{K_{Ic}^2}{K_{TH}^2} = \frac{1}{(1 - \mu)^2} \quad (5.17)$$

where ν is Poisson's ratio and E is modulus of elasticity. Considering $K_{Ic}=51$ MPa.m^{1/2} (chapter 3), the estimated range of μ is 0.71 to 0.80. The value of $\mu = 0.75$ obtained in the present study is well within this range. This method of calculation can help to estimate μ for numerical iterations for situations dominated by elastic deformation during crack growth. Alternatively it

can help check μ obtained through numerical studies.

5.5 Closing remarks

The hydrogen concentration dependent cohesive zone model (HCD-CZM) provides an effective scheme to analyse problems with coupled diffusion and crack growth under hydrogen assisted stress corrosion cracking (HASCC) in circumferentially notched specimen. A new modelling technique to handle the cylindrical specimen with eccentric ligament disposition using two dimensional finite element method has been proposed. This results in substantial reduction of the required computational efforts and time. The diffused hydrogen distribution under the conditions of internal hydrogen assisted cracking (IHAC) and hydrogen environment assisted cracking (HEAC) is computed using two approaches: a finite difference method (FDM) based analysis including the effect of hydrostatic stress σ_h and an analytical formulation excluding the effect. The fracture toughness K_{Ic}^H data predicted using both the approaches are in good agreement with the experimental data. The inclusion of effects of σ_h does not alter the results appreciably. But an exclusion of the effects helps to simplify the analysis. The K -resistance curve obtained through the finite element analysis shows a linearly rising curve which is in conformity with the physics of gradual crack growth through the regions of decreasing hydrogen concentrations. The lowest stress intensity factors K_{Ic}^H obtained from the tests and predicted by the computational method lie at the lower range of the published threshold stress intensity factor data for the material. A possibility of estimating the strength reduction factor μ using K_{Ic} and K_{TH} is indicated.

Chapter 6

Conclusions

6.1 Introduction

In this chapter a brief discussion on the important observations is presented and significant conclusions are given. Also, important contributions of the study are highlighted and some suggestions for further work are provided.

6.2 Discussion

Investigations have been carried out to analyse theoretically the crack growth process in high strength steels under hydrogen assisted stress corrosion cracking (HASCC). Modelling results are compared with experimental observations, wherever possible. Three modes of HASCC, i.e., internal hydrogen assisted cracking (IHAC) and hydrogen environment assisted cracking (HEAC), and combination of these two, have been examined. The process of HASCC involves interaction of diffusion of hydrogen into, or within, the material in the presence of external loading. The diffusion is influenced by the hydrostatic stress and plastic strain in the material. The hydrostatic stress influences the interstitial movements of hydrogen and plastic strain affects the movements of hydrogen into trap sites and evolution of the traps. An analysis of such a process calls for a coupled examination of diffusion and crack growth. This has been accomplished in the present study by interspersing the analyses of the two processes. In one scheme of solution, only effect of diffusion on crack growth is considered and the effects of stress-strain field

on diffusion, i.e., interdependencies, are neglected. In the second scheme, the interdependencies/coupling has been properly implemented. The diffusion has been analysed by analytical and finite difference approaches. The crack growth has been analysed adopting the CZM based FE modelling. This strategy has helped to take care of the effect of hydrogen concentration on the cohesive strength of the material and it is termed as hydrogen concentration dependent cohesive zone model (HCD-CZM).

The HCD-CZM has been used to analyse crack growth in CT specimens. The results predicted by the model employing both the schemes, i.e., the one excluding and the other including the effect of hydrostatic stress and plastic strain, are in good agreement with experimental data. Incidentally, the agreement is better compared to the results reported by earlier investigators (Scheider et al., 2008), who resorted to analysis of both diffusion and crack growth by FEM. Both one- and two-dimensional diffusion solutions combined with FE analysis of crack growth give similar results at higher loading rates; but, two-dimensional diffusion solution combined with FE analysis of crack growth shows better agreement at slower loading rates. The predictions obtained by the strategy of combined analytical and FE based CZM, or FDM and FE based CZM, have helped to considerably bring down the time required for analysis of a problem from that required for analysis of both diffusion and crack growth by FEM. Even the influence of hydrostatic stress and plastic strain fields on the diffusion process has been evaluated. This has been possible by resorting to FDM in place of analytical solution. On the whole, it appears that reasonably good results are obtainable by even if the interdependencies of stress-strain field and diffusion process are neglected.

The hydrogen concentrations distribution obtained with the two schemes are different. The variation of the concentration distributions near crack tip is observed to follow closely the variation of hydrostatic stress for lower range of plastic strain.

The study has brought out the fact that more accurate predictions are obtained by correlating plastic strain rate ahead of crack tip with hydrogen concentration dependent strength reduction factor μ .

The present study has examined the HASCC experimentally using circumferentially notched tensile (CNT) specimens for the first time. Thereby fracture toughness at different hydrogen pre-charging spans and various loading rates have been obtained under the IHAC, HEAC and

combined IHAC-HEAC conditions. The fracture toughness progressively reduces with an increase in availability of hydrogen near the crack tip. This condition can be ensured through an increase in pre-charging time during IHAC and decrease in loading rate during HEAC. The crack growth rates have been obtained under various test conditions. These are found to be in good agreement with the published data.

The crack growth through the CNT specimen gives rise to an asymmetric growth during both pre-cracking and HASCC. In spite of this asymmetry, the ligament section remains nearly circular. This has been exploited in a 2-D analysis of the diffusion process. The crack growth mostly occurs under combined tension and bending. The ligament profile too remains circular. Additionally, the crack grows in such a way that the ligament center shifts in the plane of bending which is fixed. The actual crack growth in the CNT specimen is three dimensional. Taking note of the existence of plane of bending, an approximate 2-D analysis has been worked out, which has been found to be effective. The diffusion in this case has been analysed by either analytical method or FDM. The crack growth has been analysed as before by FE based CZM. Triangular traction separation law has been found suitable for the material of CNT specimens as opposed to the trapezoidal shape employed for a relatively low strength material during study of CT specimen. The diffusion analysis has also been done by including or neglecting the effects of hydrostatic stress. The inclusion of these effects leads, in general, to higher hydrogen concentration, however, it does not significantly affect the accuracy of the predicted crack growth results.

The study with CNT specimen has facilitated generation of K -resistance curve for the material under HASCC conditions. The fracture resistance of the material increases with crack extension. The gradual increase in the resistance is in line with the fact that the crack grows gradually through the regions of lower hydrogen concentration or higher fracture resistance.

The toughness data obtained at the lower range of loading rate approach a constant value, which happens to be close to the lower range of threshold SIF quoted for the material in the literature. This observation may be exploited to advantage for the collection of K_{TH} experimentally.

The gradual reduction in toughness data has a direct linkage with the strength reduction factor, μ . The ratio of the toughnesses corresponding to the threshold K_{TH} and resistance in

air K_{Ic} has been shown to be a useful parameter for the approximate calculation of cohesive strength reduction factor.

The study has demonstrated that appropriate combination of diffusion analysis with crack growth can permit an examination of wide range of specimen geometry and evaluation of the effect of different process parameters. The diffusion analysis involves an important material parameter, diffusivity (D_{eff}), whereas the crack growth analysis involves material parameters like traction, critical displacement and cohesive strength reduction factor. These four parameters are first adjusted with sample experimental data. Subsequently, the analysis can be extended to predict results for new situations.

The theoretical modelling has helped to understand the HASCC mechanism, evaluate the influence of some process parameters, and utility of 1-D/2-D analyses of diffusion. The theoretical solution methodology developed may be exploited in practice for predicting the load capacity or life of component with geometry similar to CT or CNT specimens. Prior to applications, the four model parameters (T_0 , δ_0 , D_{eff} and μ) must be obtained for the material. The cohesive zone parameters (T_0 , δ_0) can be settled through experimental data on crack growth generated by normal air tests. The other two parameters (D_{eff} , μ) can be adjusted through 2–3 cases of HASCC tests.

6.3 Conclusions

The main conclusions of the study are as follows.

Modelling of HASCC

1. Hydrogen concentration dependent cohesive zone model (HCD-CZM) with coupled diffusion and crack growth analysis, is found suitable for generating quality toughness vs. crack growth data for both CT and CNT specimens.
2. The difference in the accuracy of predicted crack growth results obtained through 1-D and 2-D diffusion analysis for CT specimens is not much significant.
3. The inclusion of effects of hydrostatic stress and plastic strain on diffusion does not alter predictions for crack growth with time appreciably. Therefore the simplification of analysis without the inclusion of their effects is acceptable.

4. The combined analytical/FDM and FE based CZM approach is computationally much faster (nearly 4 times faster), and gives better accuracy as compared to a full FEM approach (e.g., error in predicted result improved from 64% to 11%).
5. The HCD-CZM can accommodate differences in geometry, material type and mode of hydrogen supply, i.e., IHAC or HEAC, equally well.
6. The hydrogen concentration distribution just ahead of crack tip shows a variation similar to that of hydrostatic stress for situations with plastic strains less than 5%. In general, the peak of hydrogen distribution is located a little away from crack tip.
7. Better crack growth predictions are obtained by employing a variable cohesive strength reduction factor μ depending on the plastic strain rate ahead of the crack tip.
8. In spite of non-axisymmetric crack growth in the CNT specimens, a 2-D modelling has been found quite effective and could predict the experimental results with good accuracy.
9. Shape of traction separation law (TSL) has a significant effect on the crack growth results depending on susceptibility of material towards embrittlement. The triangular shape is found suitable for the high strength steels (e.g., AS-4340) and trapezoidal shape is found suitable for the relatively low strength steels (e.g., FeE 690T).
10. The rising K-resistance curve obtained through HCD-CZM can be attributed to gradual extension of crack through regions of decreasing hydrogen concentration.

Experimental study

11. The circumferentially notched tensile (CNT) specimen appears to be a viable geometry for evaluating process parameters associated with HASCC. This validation was accomplished upon testing of high strength steel AS-4340.
12. The increased concentration of hydrogen in the material, which can arise through increased span of exposure during IHAC, or slow rate of loading during HEAC, or combined IHAC and HEAC, leads to reduction in toughness of the material.
13. The fracture toughness obtained at the lowest rates of present tests are close to those of the published data for threshold fracture toughness (10 to 15 MPa.m^{1/2}) for the steel.

14. The variation of K_{Ic}^H , obtained through IHAC tests, with the computed average hydrogen concentration ahead of the crack tip confirms the existence of a hydrogen concentration dependent decohesion (HEDE) mechanism.
15. The crack growth rates computed from the experimental data are in the range of 1.5×10^{-3} to 7.4×10^{-2} mm/s, which is in reasonable agreement with the published experimental data. For example, the average crack growth rate during the current HEAC is 3.5×10^{-3} mm/s. This is also in agreement with published data.
16. Fractographs of the fracture surface of CNT specimens indicate intergranular HASCC for the high strength steel AS-4340, which is consistent with the reported observations on this steel.

6.4 Contributions

The present study has thus contributed:

1. to develop a scheme of analysis based on analytical or finite difference solution of diffusion combined with FE modelling of crack growth to study hydrogen assisted stress corrosion cracking in CT and CNT specimens,
2. to reduce considerably the time required for analysing opening mode crack growth through CT specimens,
3. to establish the insignificant difference between 1-D and 2-D analyses of diffusion on the final results of crack growth prediction through CT specimens,
4. to show the influence of coupled analysis of diffusion and crack growth on the prediction of experimental results,
5. to develop a 2-D scheme of analysis of crack growth through CNT specimens in the presence of asymmetric crack extension,
6. to establish viability of CNT specimen for collecting HASCC data,

7. to give a method for evaluation of the important process parameters through combined experimental and theoretical study and,
8. above all, to the understanding of the three forms (IHAC, HEAC and combined IHAC and HEAC) of HASCC.

6.5 Suggestions for future work

In the present study, the effective diffusivity D_{eff} has been assumed constant. In reality, it varies with the hydrogen concentration C , which is equal to sum of C_L and C_T . It may be worthwhile examining the effect of this dependency of D_{eff} and C .

In the analysis of diffusion, the strain rate dependency of C_L has been disregarded. An improved modelling is possible through the inclusion of the effect. This can be considered for further investigations.

In the present two-dimensional finite element simulation of the cylindrical CNT specimen, the variation in hydrogen concentration in the direction perpendicular to the plane of bending has been fully disregarded. It is necessary to examine if this variation can be taken care of easily and if it is possible to assess the extent of error caused by such disregard. An improved simulation of the problem calls for a fully three dimensional FE modelling. Further studies along this line can be a worthy exercise.

During the test, the fatigue pre-crack profile was assumed to correspond to the onset of unstable crack extension and the corresponding fracture load was taken as the maximum load recorded in a test. In order to find out the crack edge profile corresponding to the initiation of crack extension and the fracture load, it is necessary to monitor the changes in crack edge profile with load continuously. This will help to determine correctly K_{Ic}^H and crack growth rate.

Appendix I

Commonly used HASCC test standards

A list of commonly used HASCC test standards is given below (Katz et al., 2000).

Designation	Title
ASTM A143	Practice for Safeguarding against Embrittlement of Hot-Dip Galvanized Steel Products and Procedure for Detecting Embrittlement
ASTM B577	Standard Test for Detection of Cuprous Oxide (Hydrogen Embrittlement Susceptibility) in Copper
ASTM F326	Standard Test for Electronic Hydrogen Embrittlement Test for Cadmium-Electroplating Processes
ASTM F519	Mechanical Hydrogen Embrittlement Evaluation of Plating Processes and Service Environments
ASTM F1113	Standard Test Method for Electrochemical Measurement of Diffusible Hydrogen in Steels (Barnacle Electrode)
ASTM F1459	Determination of the Susceptibility of Metallic Materials to Gaseous Hydrogen Embrittlement
ASTM F1624	Standard Test Method for Measurement of Hydrogen Embrittlement Threshold in Steel by the Incremental Step Loading Technique
ASTM G129	Slow Strain Rate Testing to Evaluate the Susceptibility of Metallic Materials to Environments
ASTM G142	Determination of Susceptibility of Metals to Embrittlement in Hydrogen Containing Environments

Designation	Title
ASTM G168	Standard Practice for Making and Using Precracked Double Beam Stress Corrosion Specimens
ASTM G1681	Standard Test Method for determining Threshold Stress Intensity Factor for Environment-Assisted Cracking of Metallic Materials
BS 5899	Method for Hydrogen Embrittlement Test for Copper
BS-EN 2831	Hydrogen Embrittlement of Steels, Test by Slow Bending
BS-EN 2832	Hydrogen Embrittlement of Steels, Notched Specimen Test
ISO 2626	Copper-Hydrogen Embrittlement Test
ISO 15330	Fasteners-Preloading Test for the Detection of Hydrogen Embrittlement Parallel Bearing

Appendix II

Details of experimental arrangement

This appendix provides detailed fabrication drawings for all components used in experimental arrangement and the an outline procedure for setting up the experiment. The details of instruments and software used is also included.

Instrumentation and software

1. LVDT: Model LBB375TA-100 by Measurement Specialities Inc. with RM074 signal conditioner by Measuring Instrument Australia.
2. Load cell: Model STC-1K by Scale Components Pvt. Ltd.
3. Potentiostat: Model 2125 by CORTEST Instrument Systems.
4. Datalogger: Model U3-HV by LabJack Corporation.
5. Data acquisition software: DAQFactory Express, version 5.84 by AzeoTech Inc.

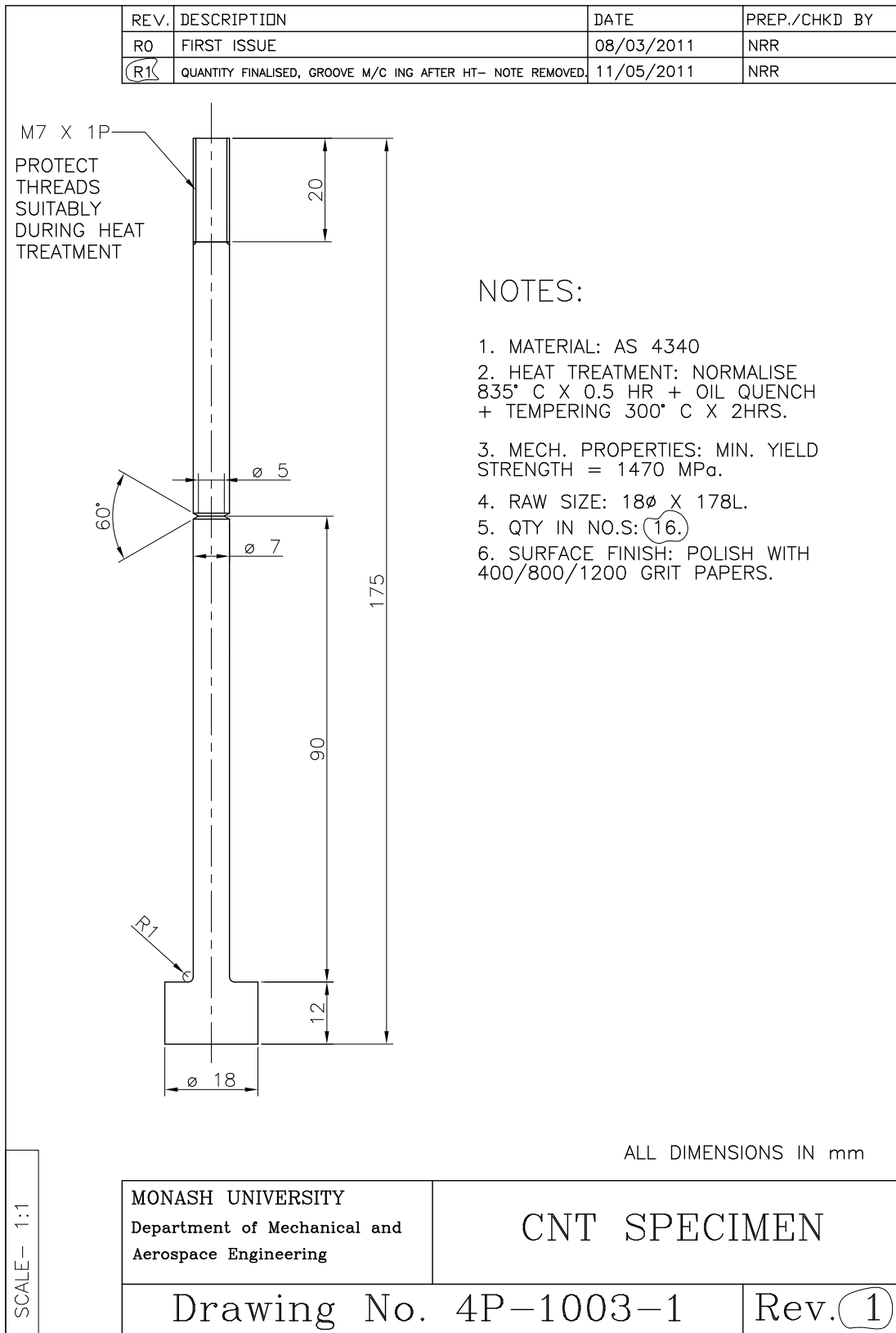


Fig. II.1 CNT specimen.

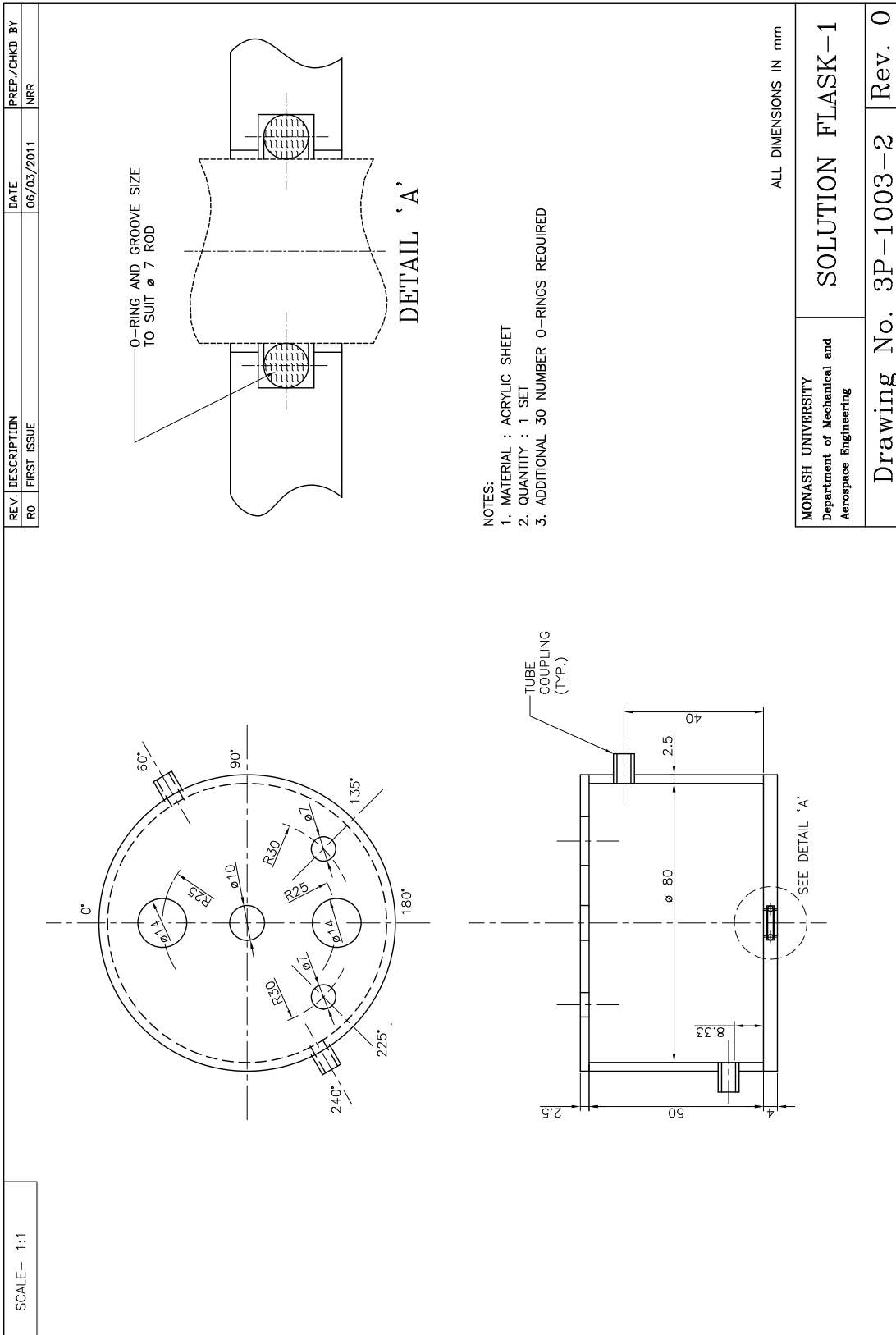


Fig. II.2 Environmental cell.

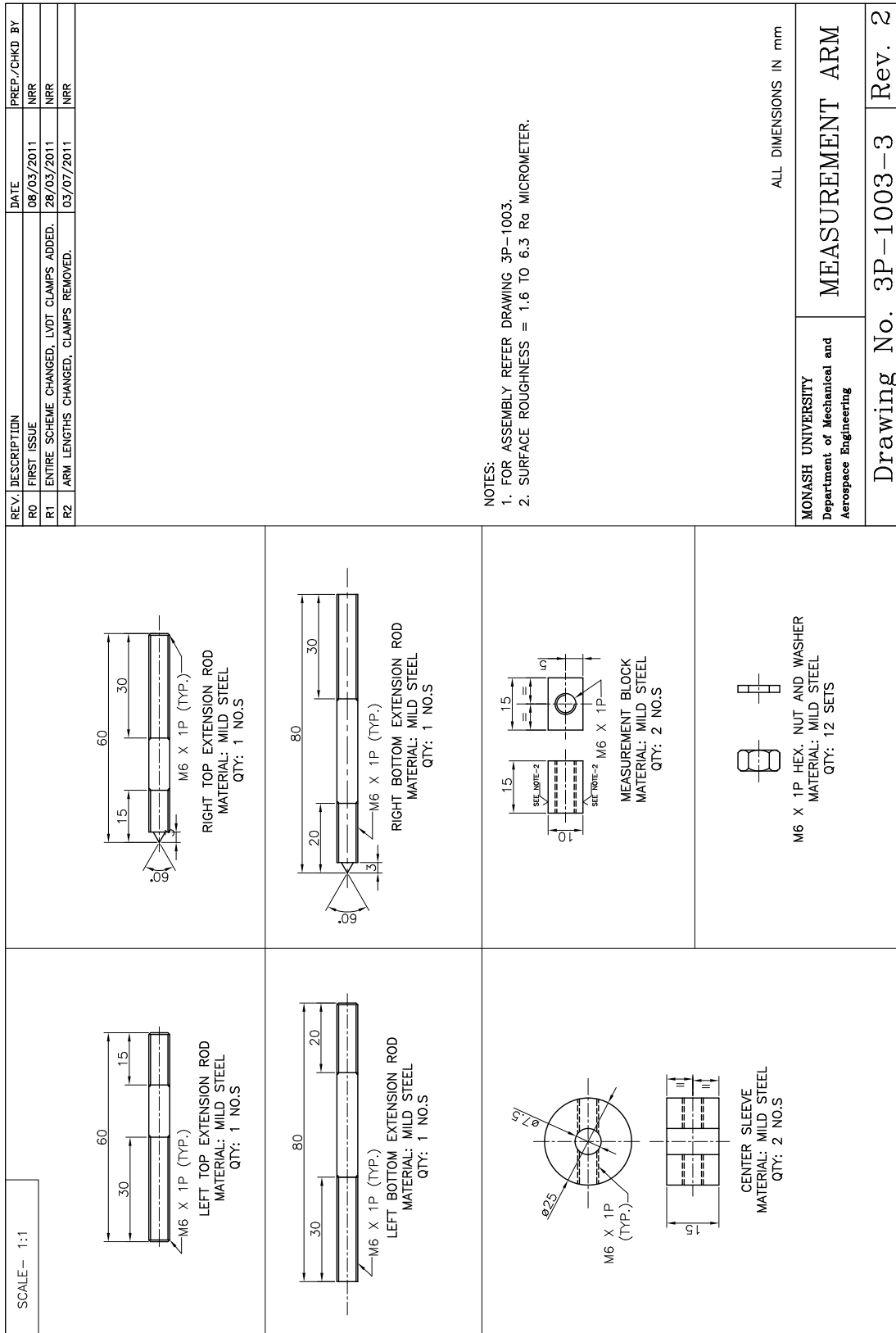


Fig. II.3 Measurement arm.

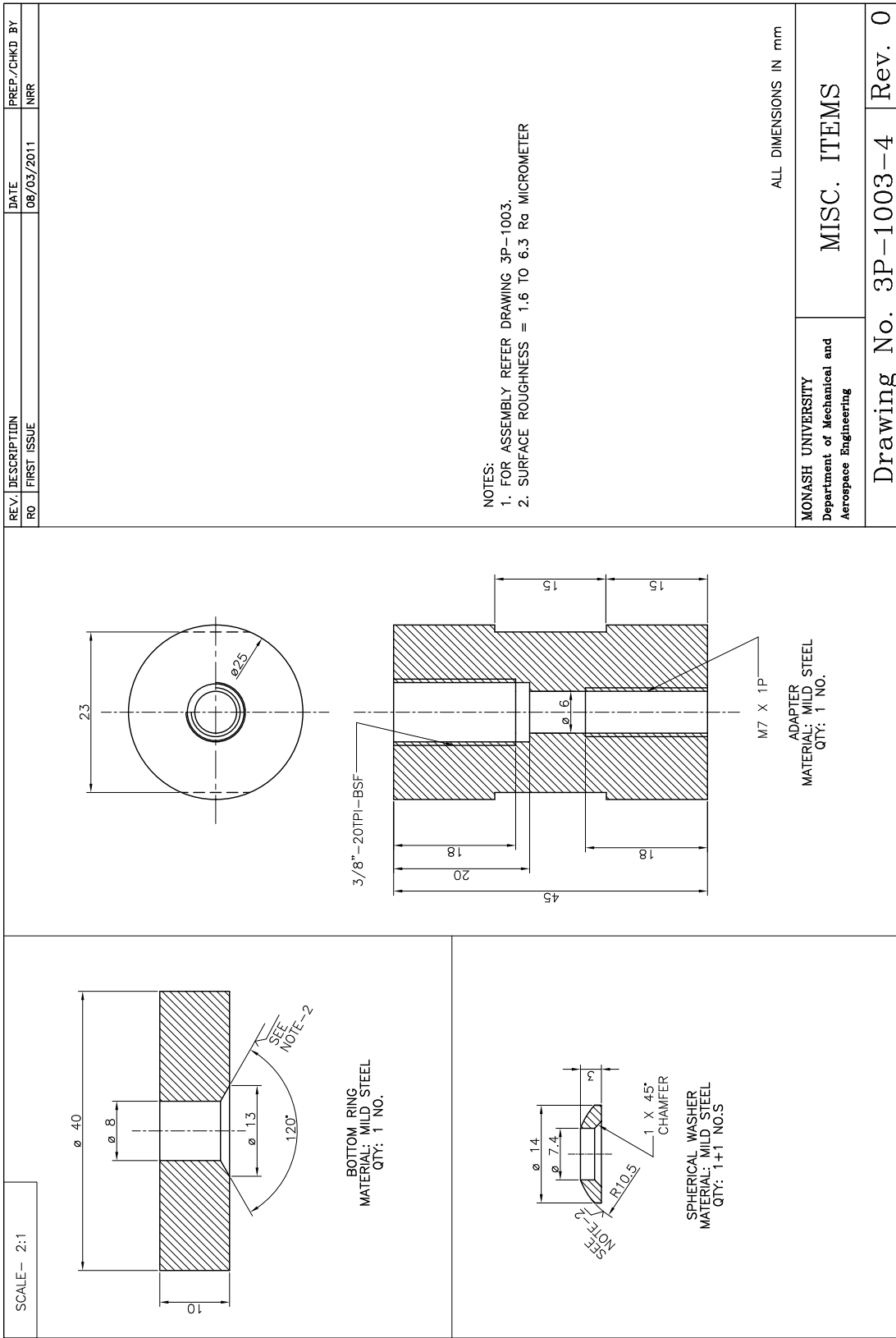
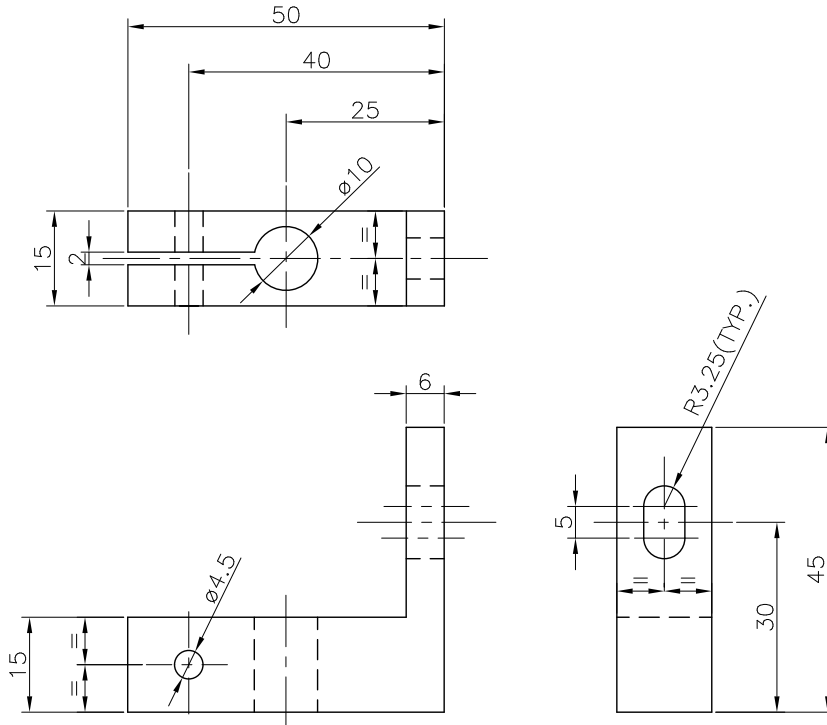
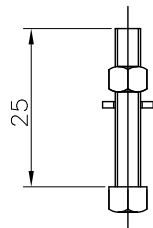


Fig. II.4 Miscellaneous items.

REV.	DESCRIPTION	DATE	PREP./CHKD BY
R0	FIRST ISSUE	29/03/2011	NRR
R1	CLAMP DESIGN CHANGED.	03/07/2011	NRR



LVDT CLAMP
MATERIAL: ALUMINIUM
QTY: 2 NO.S



M4 X 0.7P HEX. HD. BOLT
AND HEX. NUT AND WASHER
MATERIAL: MILD STEEL
QTY: 2 SETS

NOTES:

1. FOR ASSEMBLY REFER DRAWING 3P-1003.

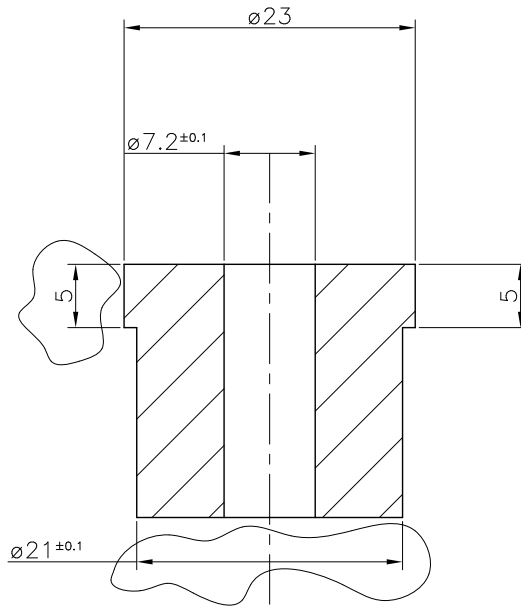
ALL DIMENSIONS IN mm

SCALE- 1:1

MONASH UNIVERSITY Department of Mechanical and Aerospace Engineering	LVDT CLAMPS
Drawing No. 4P-1003-6	Rev. 1

Fig. II.5 LVDT clamps.

REV.	DESCRIPTION	DATE	PREP./CHKD BY
R0	FIRST ISSUE	18/05/2011	NRR
R1	21 DIA STEP ADDED.	09/06/2011	NRR



NOTES:

1. MATERIAL: MILD STEEL
2. QUANTITY = 1 NO.
3. FOR ASSEMBLY REFER TO DRAWING 3P-1003.

ALL DIMENSIONS IN mm

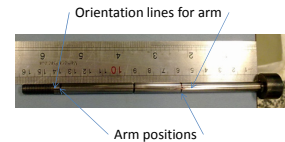
SCALE- 1:1

MONASH UNIVERSITY Department of Mechanical and Aerospace Engineering	LOCATOR PIECE
Drawing No. 4P-1003-7	Rev. 1

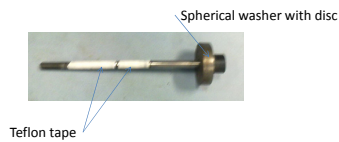
Fig. II.6 Locator piece.

1. Fatigue pre-crack the specimen. For AS-4340 material (Q+T) and 5 mm notch diameter following parameters give ~0.5 mm radial crack growth
 - 2800 rpm
 - Pressure = 250 Kpa
 - LVDT reading = 0.004
 - Process takes approximately 10 to 20 minutes.

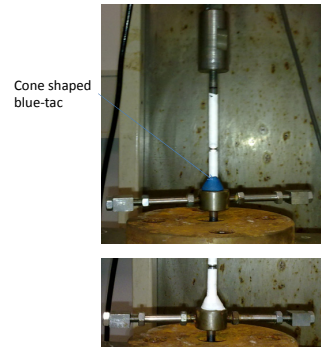
2. Polish specimen with 800, 1200 grit emery paper and wipe clean with acetone and distilled water.
3. Mark positions on the specimen for measuring arms and also orientation lines for arm.



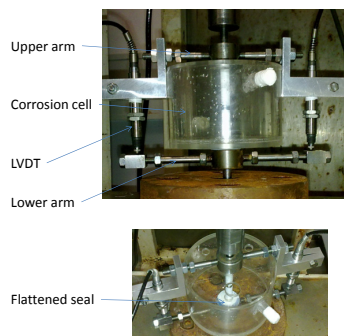
4. Insert spherical washer (with grease coating) and disc
5. Cover specimen with teflon tape except for about 2.5 mm on either side of notch.



6. Assemble the specimen and lower measuring arm in SSRT machine
7. Cast cone shaped blue-tac on to the specimen and above lower arm. Cover cone with teflon tape.



8. Insert acrylic corrosion cell and top measuring arm
9. Push down cell till conical seal flattens out.
10. Position top arm with respect to lower arm
11. Hold LVDTs in position with nuts on upper arm



12. Connect counter electrode, reference electrode and specimen to potentiostat
13. Set potentiostat to isolate state and set it to desired potential

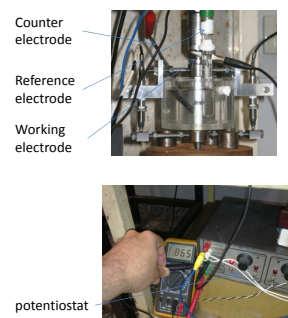


Fig. II.7 Procedure for setting up the experiment.


```

IF (CMNAME.EQ.'TOP20FCOH') THEN
IF (TIME(2).EQ.0) THEN
IF ((NPE.EQ.0).AND.(NPT.EQ.1)) THEN
NPE=1
PEORG(1)=NOEL
P(1)=0.0
PSTRN(1)=0.0
PEX(1)=COORD(1)
ELSE
IF (INLIST(NOEL,PEORG,NPE).EQ.0) THEN
NPE=NPE+1
PEORG(NPE)=NOEL
P(4*NPE-3)=0.0
PSTRN(4*NPE-3)=0.0
PEX(4*NPE-3)=COORD(1)
ELSE
P(4*NPE-(4-NPT))=0.0
PSTRN(4*NPE-(4-NPT))=0.0
PEX(4*NPE-(4-NPT))=COORD(1)
ENDIF
ENDIF
ENDIF
CALL GETVRM('SINV',ARRAY,JARRAY,FLGRAY,JRCD,JMAC,JMATYP,MATLAYO,
1 LACCFLA)
DO I=1,NPE
IF (PEORG(I).EQ.NOEL) THEN
P(4*I-(4-NPT))=ARRAY(3)
ENDIF
ENDDO
CALL GETVRM('PE',ARRAY,JARRAY,FLGRAY,JRCD,JMAC,JMATYP,MATLAYO,
1 LACCFLA)
DO I=1,NPE
IF (PEORG(I).EQ.NOEL) THEN
PSTRN(4*I-(4-NPT))=ARRAY(7)
ENDIF
ENDDO
PECHK1=0
RETURN
ENDIF
IF (TIME(2).EQ.0) THEN
LMAX=18.0
HMAX=48.0
CEWID=0.025
CRITSEP=0.0159835
NULLSTR=1E-12
DA=0.0
DDA=0.0
DT=0.0
T0=0.0
TIMETOL=0.05
C Deff used by Scheider is 7.2E-3.
DEFF=19.8E-3
VH=2000.0
R=8314.2
TEMPZERO=0.0
TEMPROOM=298.0
EH=DEFF*VH/(R*(TEMPROOM-TEMPZERO))
STATEV(1)=TIME(2)
STATEV(2)=0.0
STATEV(3)=COORD(1)
STATEV(4)=1
STATEV(5)=0.
PREVTIME(NOEL,NPT)=TIME(2)
PREVCONC(NOEL,NPT)=0.0
FIELD(NFIELD)=0.0
C Count original number of elements and store their labels
IF (NEORG.EQ.0) THEN
NEORG=1
EORG(1)=NOEL
CHK1=0
CHK2=0
STATEV(2)=1.0
PREVCONC(NOEL,NPT)=1.0
FIELD(NFIELD)=1.0
ELSE
IF (INLIST(NOEL,EORG,NEORG).EQ.0) THEN
NEORG=NEORG+1
EORG(NEORG)=NOEL
ENDIF
ENDIF
RETURN
ENDIF
C At the begining, determine the first,last ele label & then set CHK1=1
IF (CHK1.EQ.0) THEN
EFIRST=EORG(1)
ELAST=EORG(NEORG)
CHK1=1
ENDIF
C Restore undeformed x coord from state variable
XUNDEF=STATEV(3)
X=XUNDEF-X0
C If time at the time of this increment equals to that of previous
C increment, then set the concentration same as that in the previous
C increment. Otherwise store this time into PREVTIME
IF (ABS(TIME(2)-PREVTIME(NOEL,NPT)).LE.1E-10) THEN
FIELD(NFIELD)=PREVCONC(NOEL,NPT)
RETURN
ELSE
DT=TIME(2)-PREVTIME(NOEL,NPT)
STATEV(1)=TIME(2)
PREVTIME(NOEL,NPT)=TIME(2)
C Count current number of elements and store their labels
IF (CHK2.EQ.0) THEN
NECUR=1
ECUR(1)=NOEL
CHK2=1
ELSE
IF (INLIST(NOEL,ECUR,NECUR).EQ.0) THEN
NECUR=NECUR+1
ECUR(NECUR)=NOEL
ENDIF
ENDIF
C If last elem label and IP=2, reset CHK2=0, check for ele failures,
C and accordingly compute DA
IF ((NOEL.EQ.ELAST).AND.(NPT.EQ.2)) THEN
CHK2=0
IF (ABS((NEORG-NECUR)*CEWID-DA).GE.(CEWID/2)) THEN
PRINT *, 'CRK EXTENDED',TIME(2),T0,DA,DDA,NEORG,NECUR
DDA=(NEORG-NECUR)*CEWID-DA
DA=DA+DDA
T1=TIME(2)-T0
NDEADELE=INT(DA/CEWID)
LD=LD1
T0=TIME(2)
ENDIF
ENDIF
C If IP is behind crack tip then set conc as 1.0
IF (XUNDEF.LE.(X0+DA)) THEN
FIELD(NFIELD)=1.0
PREVCONC(NOEL,NPT)=1.0
PREVTIME(NOEL,NPT)=TIME(2)
STATEV(1)=TIME(2)
STATEV(2)=1.0
RETURN
ENDIF
C Now calculate the conc at this IP and store into field and state
C variables
X=XUNDEF-X0
T1=TIME(2)-T0
LD=LD1
C*****
IF (PECHK1.EQ.0) THEN
C Form CONC() array for FDM
NGRID=NEORG-NDEADELE+1
CONC(1)=1.0
DO I=NDEADELE+2,NEORG
CONC(I-NDEADELE)=PREVCONC(EORG(I),1)
ENDDO
CONC(NGRID)=0.0
C Rearrange P and PSTRN array in ascending order of x-coord
DO I=1,NPE
P1(I)=(P(4*I-3)+P(4*I-2)+P(4*I-1)+P(4*I))/4.
PSTRN1(I)=(PSTRN(4*I-3)+PSTRN(4*I-2)+
1 PSTRN(4*I-1)+PSTRN(4*I))/4.
PEX1(I)=(PEX(4*I-3)+PEX(4*I-2)+PEX(4*I-1)+PEX(4*I))/4.
ENDDO
CALL SORT(NPE,PEX1,P1,PSTRN1)

```

```

C      Form PHYD() array for FDM
      DO I=1,NGRID
        GX=X0+(NDEADELE+I-1)*CEWID
C      Locate position of this gridpoint in PEX array
        CALL LOCATE(PEX1,NPE,GX,GPOSN)
C      Calculate posn of leftmost pt in PEX for NINTP pt selection
        LPOSN=MIN(MAX(GPOSN-(NINTP-1)/2,1),NPE+1-NINTP)
        CALL POLINT(PEX1(LPOSN),P1(LPOSN),NINTP,GX,PGRID(I),ERRINTP)
        CALL POLINT(PEX1(LPOSN),PSTRN1(LPOSN),NINTP,GX,PSTRNGRD(I),
1      ERRINTP)
      ENDDO

      CALL GETCFDM(CONC,PGRID,CEWID,DT,DEFF,EH,NGRID)

      PECHK1=1

      ENDIF
C*****
      DO I=1,NGRID-1
        IF (EORG(NDEADELE+I).EQ.NOEL) THEN
          IF (NPT.EQ.1) THEN
            C=CONC(I)
            STATEV(5)=PGRID(I)
          ELSE
            C=CONC(I+1)
            STATEV(5)=PGRID(I+1)
          ENDIF
        ENDIF
      ENDDO

      FIELD(NFIELD)=C
      STATEV(2)=C

      IF ((NOEL.EQ.ELAST).AND.(NPT.EQ.2)) THEN
        DO I=1,NGRID-1
          PREVCONC(EORG(NDEADELE+I),1)=CONC(I)
          PREVCONC(EORG(NDEADELE+I),2)=CONC(I+1)
        ENDDO
        PECHK1=0
      ENDIF

C      WRITE(*,100)NOEL,NPT,KINC,X,TIME(2),DA,FIELD(NFIELD)
100  FORMAT(3I5,3F10.4,2E15.4E2)

      RETURN
      END
CCCCCCCCCCCCCCCCCCCCCCCCCCCCCCCCCCCCCCCCCCCCCCCCCCCCCCCCCCCC

```

```

C      SUBROUTINE GETCFDM
CCCCCCCCCCCCCCCCCCCCCCCCCCCCCCCCCCCCCCCCCCCCCCCCCCCCCCCCCCCC
      SUBROUTINE GETCFDM(C,P,DX,DT,DEFF,EH,J)
      REAL DX,DT,DEFF,EH,ALPHA,BETA,GAMMA
      INTEGER I,J,NMAX,N
      REAL C(J),P(J),AA(J),BB(J),CC(J),RR(J),CN(J)
      PARAMETER (PI=3.14159265358, NMAX=10000)

      DT1=DX**2/2/DEFF
      IF (DT1.LT.DT) THEN
        N=INT(DT/DT1)+1
        DT1=DT/N
      ELSE
        N=1
        DT1=DT
      ENDIF

      ALPHA=(DEFF*DT1)/(2.*(DX**2))

      DO I=1,N
C      Populate vectors for tridiagonal solver
        DO JJ=1,J-2
          BETA=EH*DT1*(P(JJ+2)-P(JJ))/(8.*(DX**2))
          GAMMA=EH*DT1*(P(JJ)-2.*P(JJ+1)+P(JJ+2))/(2.*(DX**2))
          AA(JJ)=-1.0*ALPHA+BETA
          BB(JJ)=1.0+2.0*ALPHA-GAMMA
          CC(JJ)=-1.0*ALPHA-BETA

          RR(JJ)=(ALPHA-BETA)*C(JJ)
1      +(1.0-2.0*ALPHA+GAMMA)*C(JJ+1)
1      +(ALPHA+BETA)*C(JJ+2)

          IF (JJ.EQ.1) RR(JJ)=RR(JJ)+(ALPHA-BETA)*C(JJ)
          IF (JJ.EQ.(J-2)) RR(JJ)=RR(JJ)+(ALPHA+BETA)*C(JJ+2)

        END DO
        CALL TRIDAG(AA,BB,CC,RR,CN,J-2)
        DO JJ=2,J-1
          C(JJ)=CN(JJ-1)
        END DO
      END DO

      IF (J.EQ.719) THEN
        PRINT *, 'GETCFDM'
      ENDIF

      RETURN
      END

```

References

- ABAQUS (2006), *Version 6.6, Analysis users' manual*, ABAQUS Inc.
- Ahmad, J. and Purbolaksono, J. (2010), 'Hydrogen damage in a rear riser water wall tube of a power plant', *Engineering Failure Analysis* **17**(5), 1239 – 1245.
- Ahn, D., Sofronis, P. and Dodds, R. (2007), 'Modeling of hydrogen-assisted ductile crack propagation in metals and alloys', *International Journal of Fracture* **145**(2), 135–157.
- Akhurst, K. and Baker, T. (1981), 'The threshold stress intensity for hydrogen-induced crack growth', *Metallurgical and Materials Transactions A* **12**, 1059–1070.
- Akstens, F. W., Gialamas, J., Bueche, E. J. and Madvod, T. P. (1990), Threaded steel fasteners, properties and selection: irons, steels and high performance alloys, in 'ASM Handbook, Volume 1', ASM International.
- Alam, T., Khan, M. K., Pathak, M., Ravi, K., Singh, R. and Gupta, S. (2011), 'A review on the clad failure studies', *Nuclear Engineering and Design* **241**(9), 3658 – 3677.
- Anderson, T. L. (2002), *Fracture Mechanics: Fundamentals and Applications*, 3 edn, Taylor Francis, Singapore.
- Arnoux, P. (2010), 'Atomistic simulations of stress corrosion cracking', *Corrosion science* **52**, 1247–1257.
- ASM Handbook (2003), Fracture mechanics properties of carbon and alloy steels, in 'ASM handbook Volume 19', ASM International, Metals Park, OH.
- ASTM special committee (1962), 'Screening tests for high-strength alloys using sharply notched cylindrical specimens', *Materials research and standards* **2**(2), 196–203.
- ASTM Standard (2006a), *G129-00: Standard Practice for Slow Strain Rate Testing to Evaluate the Susceptibility of Metallic Materials to Environmentally Assisted Cracking*, ASTM International.
- ASTM Standard (2006b), *G168-00: Standard Practice for Making and Using Precracked Double Beam Stress Corrosion Specimens*, ASTM International.
- ASTM Standard (2010), *E699-09: Standard Test Method for Linear-Elastic Plane-Strain Fracture Toughness K_{Ic} of Metallic Materials*, ASTM International.

- ASTM Standard (2011), *E1681-03: Standard Test Method for determining Threshold Stress Intensity Factor for Environment-Assisted Cracking of Metallic Materials*, ASTM International.
- ASTM Standard (2012a), *F1459-06: Standard Test Method for Determination of the Susceptibility of Metallic Materials to Hydrogen Gas Embrittlement (HGE)*, ASTM International.
- ASTM Standard (2012b), *F1624-12: Standard Test Method for Measurement of Hydrogen Embrittlement Threshold in Steel by the Incremental Step Loading Technique*, ASTM International.
- ASTM Standard (2012c), *F519-12a: Standard Test Method for Mechanical Hydrogen Embrittlement Evaluation of Plating/Coating Processes and Service Environments*, ASTM International.
- Baboian, R. and Treseder, R. S., eds (2002), *NACE corrosion engineer's reference book*, 3 edn, NACE International, TX.
- Bandyopadhyay, N., Kameda, J. and McMahon, C. (1983), 'Hydrogen-induced cracking in 4340-type steel: Effects of composition, yield strength, and hydrogen pressure', *Metallurgical and Materials Transactions A* **14**, 881–888.
- Banerjee, A. and Manivasagam, R. (2009), 'Triaxiality dependent cohesive zone model', *Engineering Fracture Mechanics* **76**(12), 1761 – 1770.
- Barenblatt, G. I. (1962), 'The mathematical theory of equilibrium cracks in brittle fracture', *Advanced Applied Mechanics* **7**, 55–129.
- Benson, J. and Edyvean, R. G. J. (1998), 'Hydrogen permeation through protected steel in open seawater and marine mud', *Corrosion* **54**(9), 732–739.
- Bhaskaran, R., Palaniswami, N. and Rengaswami, N. S. (2003), Global cost of corrosion - a historical review, corrosion: Fundamentals, testing, and prediction, in S. D. Cramer and B. S. J. Covino, eds, 'ASM Handbook', Vol. 13A, ASM International, Metals Park, OH.
- Bhowmik, S., Acharyya, S. K., Sahoo, P., Dhar, S. and Chattopadhyay, J. (2013), 'Estimation and comparative study of J_{Ic} using different methods for 20MnMoNi55 steel', *Materials & Design* **46**(0), 680 – 687.
- Boellinghaus, T., Viyanit, E. and Hoffmeister, H. (2001), Numerical modelling of hydrogen assisted cracking (paper no. 01226), in 'Corrosion 2001', NACE International.
- Brocks, W., Falkenberg, R. and Scheider, I. (2012), 'Coupling aspects in the simulation of hydrogen-induced stress-corrosion cracking', *Procedia IUTAM* **3**, 11–24.
- Brown, B. and Beachem, C. (1965), 'A study of the stress factor in corrosion cracking by use of the pre-cracked cantilever beam specimen', *Corrosion Science* **5**(11), 745 – 750.
- Carrasco, J., Barbosa, J., Silva, A. and da Silva Irmão, M. (2012), 'Application of elastic fracture and damage mechanics models for numerical simulation of hydrogen embrittlement in steels', *Engineering Computations* **29**(6), 596–604.

- Charles, Y., Gasperini, M., Disashi, J. and Jouinot, P. (2012), 'Numerical modeling of the disk pressure test up to failure under gaseous hydrogen', *Journal of Materials Processing Technology* **212**, 1761–1770.
- Chateau, J., Delafosse, D. and Magnin, T. (2002), 'Numerical simulations of hydrogen dislocation interactions in FCC stainless steels. Part I: hydrogen dislocation interactions in bulk crystals', *Acta Materialia* **50**, 1507–1522.
- Cho, T. and Kim, T. (2008), 'A prediction model for hydrogen induced cracking in a prestressed wire with a fracture analysis', *ISIJ international* **48**(4), 496–505.
- Cornec, A., Scheider, I. and Schwalbe, K.-H. (2003), 'On the practical application of the cohesive model', *Engineering Fracture Mechanics* **70**(14), 1963–1987.
- Craig, B. (2003a), Hydrogen damage, corrosion: Fundamentals, testing, and prediction, in S. D. Cramer and B. S. J. Covino, eds, 'ASM Handbook', Vol. 13A, ASM International, Metals Park, OH, pp. 367–380.
- Craig, B. (2003b), Introduction to environmentally induced cracking, corrosion: Fundamentals, testing, and prediction, in S. D. Cramer and B. S. J. Covino, eds, 'ASM Handbook', Vol. 13A, ASM International, Metals Park, OH.
- Crank, J. (1975), *The mathematics of diffusion, 2nd edn.* Clarendon, Oxford.
- Cwiek, J. (2010), 'Prevention methods against hydrogen degradation of steel', *Journal of Achievements in Material and Manufacturing Engineering* **43**(1), 214–221.
- Dayal, R. K. and Parvathavarthini, N. (2003), 'Hydrogen embrittlement in power plant steels', *Sadhana* **28**, 431–451.
- Dean, S. W., Pugh, E. N. and Ugiansky, G. M., eds (1982), *ASTM STP 821: Environment-Sensitive Fracture: Evaluation And Comparison Of Test Methods*, ASTM, Philadelphia.
- Delafosse, D. and Magnin, T. (2001), 'Hydrogen induced plasticity in stress corrosion cracking of engineering systems', *Engineering Fracture Mechanics* **68**, 693–729.
- Dietzel, W. and Ghosal, S. K. (1997), 'Stress corrosion cracking - a new approach to testing methods', *Materials Science* **33**, 516–523.
- Dietzel, W. and Mueller-Roos, J. (2001), 'Experience with rising load/rising displacement stress corrosion cracking testing', *Materials Science* **37**, 264–271.
- Dietzel, W. and Pfuff, M. (1996), Effect of deformation rates on hydrogen embrittlement, in A. W. Thompson and N. Moody, eds, 'Hydrogen effects in materials', Minerals, Metals & Materials Soc (TMS), pp. 303–311.
- Dietzel, W., Pfuff, M. and Juilfs, G. (2006), 'Hydrogen permeation in plastically deformed steel membranes', *Materials Science* **42**, 78–84.

- Dietzel, W., Pfuff, M. and Juilfs, G. G. (2005), 'Studies of scc and hydrogen embrittlement of high strength alloys using fracture mechanics methods', *Materials Science Forum* **482**, 11–16.
- Doig, P. and Jones, G. (1977), 'A model for the initiation of hydrogen embrittlement cracking at notches in gaseous hydrogen environments', *Metallurgical and Materials Transactions A* **8**(12), 1993–1998.
- Eliasz, N., Eliezer, D. and Olson, D. (2000), 'Hydrogen-assisted processing of materials', *Materials Science and Engineering: A* **289**(1), 41–53.
- Elliott, P. (2003), Gallery of corrosion damage, corrosion: Fundamentals, testing, and prediction, in S. D. Cramer and B. S. J. Covino, eds, 'ASM Handbook', Vol. 13A, ASM International, Metals Park, OH.
- Falkenberg, R., Brocks, W., Dietzel, W. and Scheider, I. (2010), 'Simulation of stress-corrosion cracking by the cohesive model', *Key Engineering Materials* **417-418**, 329–332.
- Fontana, M. G. (2005), *Corrosion Engineering*, 3rd edn, Tata McGraw Hill, New Delhi.
- Ford, F. P. (1982), Current understanding of the mechanisms of stress corrosion and corrosion fatigue, in S. W. Dean, E. N. Pugh and G. M. Ugiasky, eds, 'ASTM STP 821: Environment-Sensitive Fracture: Evaluation And Comparison Of Test Methods', ASTM, Philadelphia, pp. 32–51.
- Ford, F. P. (1996), 'Quantitative prediction of environmentally assisted cracking', *Corrosion* **52**, 375–395.
- Freeman, S. R. (2003), Corrosion related failures - hydrogen damage and prevention, in W. T. Becker and R. J. Shipley, eds, 'ASM Handbook-vol.11-Failure analysis and prevention', Vol. 11, ASM International, Metals Park, OH.
- Frohberg, R. P., Barnett, W. J. and Troiano, A. R. (1954), Delayed failure and hydrogen embrittlement in steel, Technical report, Case Institute of Technology, Wright Air Development Center.
- Gangloff, R. (2009), Science-based prognosis to manage structural alloy performance in hydrogen, in B. Somerday, P. Sofronis and R. Jones, eds, 'Effects of Hydrogen on Materials, Proceedings of the 2008 International Hydrogen Conference', ASM International, Metals Park, OH, pp. 1–21.
- Gangloff, R. P. (2003), Hydrogen assisted cracking in high strength alloys, in 'Comprehensive Structural Integrity, Environmentally-Assisted Fracture', Vol. 6, Elsevier, Oxford.
- Gangloff, R. P. (2006), Critical issues in hydrogen assisted cracking of structural alloys, in S. Shipilov, ed., 'Environment induced cracking of metals (EICM-2)', Elsevier.
- Gao, M. and Wei, R. (1985), 'A "Hydrogen partitioning" model for hydrogen assisted crack growth', *Metallurgical and Materials Transactions A* **16**, 2039–2050.

- Gavrilov, S., Vankeerberghen, M., Nelissen, G. and Deconinck, J. (2007), 'Finite element calculation of crack propagation in type 304 stainless steel in diluted sulphuric acid solutions', *Corrosion Science* **49**, 980–999.
- Gerberich, W. and Chen, Y. (1975), 'Hydrogen-controlled cracking-an approach to threshold stress intensity', *Metallurgical and Materials Transactions A* **6**, 271–278.
- Gerberich, W., Chen, Y. and John, C. (1975), 'A short-time diffusion correlation for hydrogen-induced crack growth kinetics', *Metallurgical and Materials Transactions A* **6**, 1485–1498.
- Gerberich, W., Livne, T., Chen, X. and Kaczorowski, M. (1988), 'Crack growth from internal hydrogen-temperature and microstructural effects in 4340 steel', *Metallurgical and Materials Transactions A* **19**, 1319–1334.
- Gutierrez-Solana, F., Gonzalez, J., Varona, J. M. and Biezma, M. V. (1993), 'Modelling the stress corrosion cracking of low alloy steels', *Corrosion Science* **35**(1-4), 499–505.
- Hall, M. J. (2007), Crack tip strain rate equation with applications to crack tip embrittlement and active path dissolution models of stress corrosion cracking, in S. Shipilov, R. Jones, J. Olive and R. Rebak, eds, 'Environment-Induced Cracking of Materials: Chemistry, Mechanics and Mechanisms', Vol. 1, Elsevier, Oxford.
- Hassan, S. (2010), 'Hydrogen induced premature failure of massive cast medium carbon steel anchor fluke', *Materials & Design* **31**(2), 956–964.
- Hellmann, D. and Schwalbe, K. H. (1986), On the experimental determination of CTOD based R-curves, in K. H. Schwalbe, ed., 'The crack tip opening displacement in elastic-plastic fracture mechanics', Springer, Heidelberg.
- Hirth, J. (1980), 'Effects of hydrogen on the properties of iron and steel', *Metallurgical and Materials Transactions A* **11**, 861–890.
- Hudson, M. S. L., Dubey, P., Pukazhselvan, D., Pandey, S. K., Singh, R. K., Raghubanshi, H., Shahi, R. R. and Srivastava, O. (2009), 'Hydrogen energy in changing environmental scenario: Indian context', *International Journal of Hydrogen Energy* **34**(17), 7358 – 7367.
- Ibrahim, R. N. and Stark, H. L. (1987), 'Validity requirements for fracture toughness measurements obtained from small circumferentially notched cylindrical specimens', *Engineering Fracture Mechanics* **28**, 455–460.
- Ibrahim, R., Rihan, R. and R.K. Singh Raman (2008), 'Validity of a new fracture mechanics technique for the determination of the threshold stress intensity factor for stress corrosion cracking (K_{Isc}) and crack growth rate of engineering materials', *Engineering Fracture Mechanics* **75**, 1623–1634.
- Ibrahim, R. and Stark, H. (1990), 'Establishing K_{Ic} from eccentrically fatigue cracked small circumferentially grooved cylindrical specimens', *International Journal of Fracture* **44**, 179–188.

- Interrante, C. G. and Raymond, L. (2005), *Environmental cracking-corrosion fatigue (ASTM manual series, MNL20)*, ASTM International, PA, chapter 27, pp. 322–340.
- Johnson, H. H. and Paris, P. C. (1968), ‘Sub-critical flaw growth’, *Engineering Fracture Mechanics* **1**(1), 3 – 45.
- Johnson, W. (1874), ‘On some remarkable changes produced in iron and steel by the action of hydrogen and acids’, *Proceedings of the Royal Society of London* **23**(156-163), 168–179.
- Jones, R. H. (2003), Stress-corrosion cracking, corrosion: Fundamentals, testing, and prediction, in S. D. Cramer and B. S. J. Covino, eds, ‘ASM Handbook’, Vol. 13A, ASM International, Metals Park, OH.
- Jones, R., Li, H. and Hirth, J. (2001), ‘Effects of mixed mode i/iii loading on environment-induced cracking’, *Corrosion* **57**, 52–59.
- Kain, V., Gupta, V. and De, P. K. (2007), Embrittlement cracking of a stabilized stainless steel wire mesh in an ammonia converter, in S. Shipilov, R. Jones, J. Olive and R. Rebak, eds, ‘Environment-induced Cracking of Materials: Prediction, Industrial Developments and Evaluation’, Vol. 2, Elsevier, Oxford.
- Kalnaus, S., Zhang, J. and Jiang, Y. (2011), ‘Stress corrosion cracking of AISI 4340 steel in aqueous environments’, *Metallurgical and Materials Transactions A* **42A**, 434–447.
- Kameda, J. (1986), ‘A microscopic model of hydrogen-induced intergranular cracking–i. equilibrium crack growth’, *Acta Metallurgica* **34**(5), 867 – 882.
- Kane, R. D. (2000), *ASTM STP-1401: Environmentally Assisted Cracking: Predictive Methods for Risk Assessment and Evaluation of Materials, Equipment, and Structures.*, ASTM, Philadelphia.
- Katz, Y., Tymiak, N. and Gerberich, W. W. (2000), Evaluation of environmentally assisted crack growth, in ‘ASM handbook Volume 8’, ASM International, Metals Park, OH.
- Kim, J.-S., An, D.-H., Lee, S.-Y. and Lee, B.-Y. (2009), ‘A failure analysis of fillet joint cracking in an oil storage tank’, *Journal of Loss Prevention in the Process Industries* **22**(6), 845 – 849.
- Kim, N., Oh, C., Kim, Y., Yoon, K. and Ma, Y. (2012), ‘Hydrogen-assisted stress corrosion cracking simulation using the stress-modified fracture strain model’, *Journal of Mechanical Science and Technology* **26**(8), 2631–2638.
- Koch, G., Brongers, M., Thompson, N., Virmani, Y. and Payer, J. (2002), Corrosion cost and preventive strategies in the united states, Technical report, Turner-Fairbank Highway Research Center.
- Krom, A. H. M., Bakker, A. and Koers, R. W. J. (1997), ‘Modelling hydrogen-induced cracking in steel using coupled diffusion stress finite element analysis’, *International journal of pressure vessel and piping* **72**, 139–147.

- Krom, A. H. M., Koers, R. W. J. and Bakker, A. (1999), 'Hydrogen transport near a blunting crack tip', *Journal of the Mechanics and Physics of Solids* **47**, 971–992.
- Kumnick, A. and Johnson, H. (1980), 'Deep trapping states for hydrogen in deformed iron', *Acta Metallurgica* **28**(1), 33 – 39.
- Liu, H. W. (2008), 'A unified model of environment-assisted cracking', *Acta Materialia* **56**, 4339–4348.
- Louthan, M.R., J. (2008), 'Hydrogen embrittlement of metals: A primer for the failure analyst', *Journal of Failure Analysis and Prevention* **8**, 289–307.
- Lynch, S. (2007), Progress towards understanding mechanisms of hydrogen embrittlement and stress corrosion cracking, in 'NACE - International Corrosion Conference Series', NACE International, pp. 074931 – 0749355.
- Lynch, S. P. (2003), 'Failures of engineering components due to environmentally assisted cracking', *Practical Failure Analysis* **3**, 33–42.
- Macdonald, D. D. and Chung, H. H. (1985), 'A study of transient crack growth in AISI 4340 steel in NaCl solution', *Corrosion* **41**, 151–159.
- Magnin, T., Chambreuil-Paret, A., Chateau, J. P., Delafosse, D. and Bayle, B. (1997), Chapter 2: The corrosion enhanced plasticity model: Single crystal experiments and numerical simulations, in T. Magnin, ed., 'Corrosion-Deformation Interactions, CDI-96', The Institute of Materials.
- Magnin, T., ed. (1995), *Advances in Corrosion-Deformation Interactions, Materials Science Forum*, Vol. 202, Trans Tech Publications, Switzerland.
- May, I. L. and Bagnall, C. (2007), Case studies of corrosion and environmentally induced cracking in industry, in S. Shipilov, R. Jones, J. Olive and R. Rebak, eds, 'Environment-induced Cracking of Materials: Prediction, Industrial Developments and Evaluation', Vol. 2, Elsevier, Oxford.
- Mayville, R. A., Warren, T. J. and Hilton, P. D. (1989), The Crack Velocity- K_I Relationship for AISI 4340 in Seawater Under Fixed and Rising Displacement, in R. P. Wei and R. P. Gangloff, eds, 'ASTM STP-1020 Fracture mechanics perspectives and directions', ASTM International, PA, pp. 605–614.
- McLaughlin, B. D. (1997), 'Stress corrosion cracking simulation', *Modelling Simul. Mater. Sci. Eng.* **5**, 129–147.
- McNitt, R., Sawyer, S. and Thompson, W. (1972), 'Stress-intensity factors of hollow notched bars and hydrogen-embrittled specimens', *Experimental Mechanics* **12**, 229–234.
- Mohanty, S., Majumdar, S. and Natesan, K. (2012), A review of stress corrosion cracking/fatigue modeling for light water reactor cooling system components, Technical report, Nuclear Engineering Division, Argonne National Laboratory, Argonne, IL.

- Moody, N. R., Baskes, M. I., Robinson, S. L. and Perra, M. W. (2001), 'Temperature effects on hydrogen-induced crack growth susceptibility of iron-based superalloys', *Engineering Fracture Mechanics* **68**(6), 731 – 750.
- Moriconi, C., Henaff, G. and Halm, D. (2011), 'Influence of hydrogen coverage on the parameters of a cohesive zone model dedicated to fatigue crack propagation', *Procedia Engineering* **10**, 2663–2668.
- Mousson, J. L., Vuillemin, B., Oltra, R. and Cottis, R. A. (2004), 'Use of a general purpose finite element package for modeling of crevice corrosion (paper no. 04066)'.
- Newman, R. C. (1995), Stress-corrosion cracking mechanisms, in P. Marcus and J. Ouder, eds, 'Corrosion Mechanisms in Theory and Practice', Marcel Dekker Inc., NY.
- Olden, V., Alvaro, A. and Akselsen, O. M. (2012), 'Hydrogen diffusion and hydrogen influenced critical stress intensity in an api x70 pipeline steel welded joint - experiments and fe simulations', *International Journal of Hydrogen Energy* **37**(15), 11474 – 11486.
- Olden, V., Thaulow, C. and Johnsen, R. (2008), 'Modelling of hydrogen diffusion and hydrogen induced cracking in supermartensitic and duplex stainless steels', *Materials and Design* **29**, 1934–1948.
- Olden, V., Thaulow, C., Johnsen, R., Ostby, E. and Berstad, T. (2008), 'Application of hydrogen influenced cohesive laws in the prediction of hydrogen induced stress cracking in 25% Cr duplex stainless steel', *Engineering Fracture Mechanics* **75**, 2333–2351.
- Olden, V., Thaulow, C., Johnsen, R., Ostby, E. and Berstad, T. (2009), 'Influence of hydrogen from cathodic protection on the fracture susceptibility of 25%Cr duplex stainless steel - Constant load SENT testing and FE-modelling using hydrogen influenced cohesive zone elements', *Engineering Fracture Mechanics* **76**(7), 827 – 844.
- Oriani, R. (1987), 'Hydrogen—the Versatile Embrittler', *Corrosion* **4**(7), 390–397.
- Oriani, R. A. (1970), 'The diffusion and trapping of hydrogen in steel', *Acta Metallurgica* **18**, 147–157.
- Oriani, R. A. (1978), 'Hydrogen embrittlement of steels', *Annual review of material science* **8**, 327–357.
- Oriani, R. A., Hirth, J. P. and Smialowski, M., eds (1985), *Hydrogen degradation of ferrous alloys*, Noyes publication, USA.
- Oriani, R. and Josephic, P. (1974), 'Equilibrium aspects of hydrogen-induced cracking of steels', *Acta Metallurgica* **22**(9), 1065 – 1074.
- Page, R. and Gerberich, W. (1982), 'The effect of hydrogen source on crack initiation in 4340 steel', *Metallurgical and Materials Transactions A* **13**, 305–311.
- Pal, S. K. (2010), Role of Microstructure and Environment in Stress Corrosion Cracking Susceptibility, PhD thesis, Monash University, Clayton campus, Australia.

- Parkins, R. N. (1975), 'Environmental effects in crack growth', *Journal of strain Analysis* **10**(4), 251–257.
- Pidaparti, R. M. and Patel, R. R. (2011), 'Modeling the evolution of stresses induced by corrosion damage in metals', *Journal of Materials Engineering and Performance* **20**(7), 1114–1120.
- Prescott, G. R. and Shannon, B. (2001), 'Process equipment problems caused by interaction with hydrogen-an overview', *Process Safety Progress* **20**(1), 63–72.
- Press, W. H., Teukolsky, S. A., Vetterling, W. T. and Flannery, B. P. (1998), *Numerical recipes in FORTRAN, The art of Scientific Computing*, 2nd edn, Cambridge University Press.
- Prior, R., Kirby, P., Jr., R. L. and Alt, M. (1991), 'Severe accident analysis of a 1300 MWe PWR to address the hydrogen issue', *Nuclear Engineering and Design* **130**(1), 51 – 58.
- Ramamurthy, S., Lau, W. and Atrens, A. (2011), 'Influence of the applied stress rate on the stress corrosion cracking of 4340 and 3.5NiCrMoV steels under conditions of cathodic hydrogen charging', *Corrosion Science* **53**(7), 2419 – 2429.
- Raymond, L., ed. (1972), *ASTM STP-543 Hydrogen embrittlement testing*, ASTM International, PA.
- Rhodes, P. (2001), 'Environment-assisted cracking of corrosion-resistant alloys in oil and gas production environments: A review', *Corrosion* **57**(11), 923–966.
- Rihan, R., R.K. Singh Raman and Ibrahim, R. (2005), 'Circumferential notched tensile (CNT) testing of cast iron for determination of threshold (K_{Isc}) for caustic crack propagation', *Materials Science & Engineering-A* **407**, 207–212.
- Rihan, R., R.K. Singh Raman and Ibrahim, R. (2006), 'Determination of crack growth rate and threshold for caustic cracking (K_{Isc}) of a cast iron using small circumferential notched tensile (CNT) specimens', *Materials Science & Engineering-A* **425**, 272–277.
- Rihan, R., R.K. Singh Raman and Ibrahim, R. (2007), Circumferential notch tensile (CNT) tests for determination of K_{Isc} , using small fracture mechanics specimens, in S. Shipilov, R. Jones, J. Olive and R. Rebak, eds, 'Environment-induced Cracking of Materials: Prediction, Industrial Developments and Evaluation', Vol. 2, Elsevier, Oxford.
- Rimoli, J. and Ortiz, M. (2010), 'A three-dimensional multiscale model of intergranular hydrogen-assisted cracking', *Philosophical Magazine* **90**, 2939–2963.
- R.K. Singh Raman, Rihan, R. and Ibrahim, R. (2006), 'A novel approach to the determination of the threshold for stress corrosion cracking (K_{Isc}) using round tensile specimens', *Metalurgical and Materials Transactions A* **37**, 2963–2973.
- R.K. Singh Raman, Rihan, R. and Ibrahim, R. (2007a), 'Role of imposed potentials in threshold for caustic cracking susceptibility (K_{Isc}): Investigations using circumferential notch tensile (CNT) testing', *Corrosion Science* **49**, 4386–4395.

- R.K. Singh Raman, Rihan, R. and Ibrahim, R. (2007b), ‘Validation of a novel approach to determination of threshold for stress corrosion cracking (K_{Isc})’, *Materials Science and Engineering: A* **452-453**, 652–656.
- Rosenheinrich, W. (2012), ‘Tables of some indefinite integrals of Bessel functions’, University of Applied sciences Jenna, Germany.
- San Marchi, C. and Somerday, B. (2008), Technical reference on hydrogen compatibility of materials (SAND2008-1163), Technical report, Sandia National Laboratories, California, USA.
- Sandoz, G. (1972), ‘A unified theory for some effects of hydrogen source, alloying elements, and potential on crack growth in martensitic AISI 4340 steel’, *Metallurgical and Materials Transactions B* **3**, 1169–1176.
- Saxena, S., Ramakrishnan, N. and Chouhan, J. (2010), ‘Establishing methodology to predict fracture behaviour of piping components by numerically predicting specimen fracture data using tensile specimen test’, *Engineering Fracture Mechanics* **77**(7), 1058 – 1072.
- Scheider, I., Pfuff, M. and Dietzel, W. (2008), ‘Simulation of hydrogen assisted stress corrosion cracking using the cohesive model’, *Engineering Fracture Mechanics* **75**, 4283–4291.
- Schwalbe, K.-H. (1995), Introduction of δ_5 as an operational definition of the CTOD and its practical use, in W. G. Reuter, J. H. Underwood and J. C. J. Newman, eds, ‘ASTM STP 1256: Fracture mechanics 26th volume’, ASTM, Philadelphia, pp. 763–778.
- Schwalbe, K. H., Neale, K. and Ingham, T. (1988), ‘Draft EGF recommendations for determining the fracture resistance of ductile materials: EGF procedure EGF P1-87d’, *Fatigue & Fracture of Engineering Materials and Structures* **11**(6), 409–420.
- Serebrinsky, S., Carter, E. and Ortiz, M. (2004), ‘A quantum-mechanically informed continuum model of hydrogen embrittlement’, *Journal of the Mechanics and Physics of Solids* **52**, 2403–2430.
- Shim, I.-O. and Byrne, J. (1990), ‘A study of hydrogen embrittlement in 4340 steel I: Mechanical aspects’, *Materials Science and Engineering: A* **123**(2), 169 – 180.
- Shipilov, S. A. (2007), Stress corrosion cracking and corrosion fatigue: a record of progress, 1873-1973, in S. Shipilov, R. Jones, J. Olive and R. Rebak, eds, ‘Environment-Induced Cracking of Materials: Chemistry, Mechanics and Mechanisms’, Vol. 1, Elsevier, Oxford.
- Shirband, Z., Shishesaz, M. and Ashrafi, A. (2011), ‘Hydrogen degradation of steels and its related parameters, a review’, *Phase Transitions* **84**(11-12), 924–943.
- Simmons, G., Pao, P. and Wei, R. (1978), ‘Fracture mechanics and surface chemistry studies of subcritical crack growth in aisi 4340 steel, vol. 9a, pp. 1147-1158, 1978’, *Metallurgical Transactions A* **9A**, 1147–1158.
- Smith, R. W. (2000), ‘Computer simulation of intergranular stress corrosion cracking via hydrogen embrittlement’, *Modelling Simulation Material Science Engineering* **8**, 629–648.

- Sofronis, P. and McMeeking, R. (1989), 'Numerical analysis of hydrogen transport near a blunting crack tip', *Journal of the Mechanics and Physics of Solids* **37**(3), 317 – 350.
- Srawley, J. E. and Brown Jr., W. F. (1964), Fracture toughness testing methods, in 'ASTM STP-381 Fracture toughness testing and its applications', ASTM International, PA, pp. 133–196.
- Staeble, R. W. (2000), Framework for predicting stress corrosion cracking, in R. D. Kane, ed., 'ASTM STP-1401: Environmentally Assisted Cracking: Predictive Methods for Risk Assessment and Evaluation of Materials, Equipment, and Structures.', ASTM, Philadelphia, pp. 131–165.
- Stansbury, E. E. and Buchanan, R. A. (2000), *Fundamentals of Electrochemical Corrosion*, ASM International, Ohio.
- Stark, H. L. and Ibrahim, R. N. (1986), 'Estimating fracture toughness from small specimen', *Engineering fracture mechanics* **25**, 395–401.
- Stark, H. L. and Ibrahim, R. N. (1992), 'Crack propagation in aluminium gas cylinder neck material at constant load and room temperature', *Engineering Fracture Mechanics* **41**, 569–575.
- Sujata, M., Bhuvana, R., Madan, M., Venkataswamy, M. and Bhaumik, S. (2009), 'Hydrogen-assisted cracking in boiler steam drums', *Journal of Failure Analysis and Prevention* **9**, 213–221.
- Sullivan, A. M. (1972), 'Stress corrosion crack velocity in 4340 steel', *Engineering Fracture Mechanics* **4**(1), 65 – 76.
- Tada, H., Paris, P. C. and Irwin, G. R. (2000), *The stress analysis of cracks handbook*, ASME press, NY, USA.
- Taha, A. and Sofronis, P. (2001), 'A micromechanics approach to the study of hydrogen transport and embrittlement', *Engineering Fracture Mechanics* **68**(6), 803 – 837.
- Takayama, K., Matsumoto, R., Taketomi, S. and Miyazaki, N. (2011), 'Hydrogen diffusion analyses of a cracked steel pipe under internal pressure', *International Journal of Hydrogen Energy* **36**(1), 1037–1045.
- Tan, H. (2002), Combined atomistic and continuum simulation of fracture and corrosion (ch. 8.12), in 'Comprehensive Structural Integrity', Vol. 8, Elsevier, pp. 413–451.
- Thomas, R., Scully, J. and Gangloff, R. (2003), 'Internal hydrogen embrittlement of ultrahigh-strength aermet 100 steel', *Metallurgical and Materials Transactions A* **34**, 327–344.
- ThyssenKrupp Steel (2005), 'Material specification N-A-XTRA'.
- Toribio, J. and Kharin, V. (2006), 'Effect of residual stress-strain profiles on hydrogen-induced fracture of prestressing steel wires', *Materials Science* **42**(2), 263–271.

- Toribio, J., Kharin, V., Vergara, D. and Lorenzo, M. (2011), 'Optimization of the simulation of stress-assisted hydrogen diffusion for studies of hydrogen embrittlement of notched bars', *Materials Science* **46**, 819–833.
- Traidia, A., Alfano, M., Lubineau, G., Duval, S. and Sherik, A. (2012), 'An effective finite element model for the prediction of hydrogen induced cracking in steel pipelines', *International Journal of Hydrogen Energy* **37**(21), 16214 – 16230.
- Turnbull, A. (1993), 'Modelling of environment assisted cracking', *Corrosion Science* **34**, 921–960.
- Turnbull, A. (1997), 'Modelling of crack chemistry in sensitized stainless steel in boiling water reactor environments', *Corrosion Science* **39**, 789–805.
- Turnbull, A. (2000), Issues in modeling of environment assisted cracking, in R. D. Kane, ed., 'ASTM STP-1401: Environmentally Assisted Cracking: Predictive Methods for Risk Assessment and Evaluation of Materials, Equipment, and Structures.', ASTM, Philadelphia, pp. 23–39.
- Turnbull, A. (2001a), Environment assisted cracking of steam turbine steels - modelling of crack chemistry (paper no. 01237), in 'Corrosion-2001', NACE International.
- Turnbull, A. (2001b), 'Modeling of the chemistry and electrochemistry in cracks - a review', *Corrosion* **57**(2), 175–189.
- Turnbull, A., Ferriss, D. and Anzai, H. (1996), 'Modelling of the hydrogen distribution at a crack tip', *Materials Science and Engineering: A* **206**(1), 1 – 13.
- Turon, A., Davila, C. G., Camanho, P. P. and Costa, J. (2005), An engineering solution for using coarse meshes in the simulation of delamination with cohesive zone models, Technical Report NASA/TM-2005-213547, NASA, Langley Research Center.
- Tvergaard, V. and Hutchinson, J. W. (1992), 'The relation between crack growth resistance and fracture process parameters in elastic-plastic solids', *J. Mech. Phys.Solids* **40**(6), 1377–1397.
- Van Der Sluys, W. (1969), 'Mechanisms of environment induced subcritical flaw growth in AISI 4340 steel', *Engineering Fracture Mechanics* **1**(3), 447 – 462.
- Van Leeuwen, H. (1974), 'The kinetics of hydrogen embrittlement: a quantitative diffusion model', *Engineering Fracture Mechanics* **6**(1), 141–161.
- Vankeerberghen, M. (2004), A mechanico-electrochemical diagram for crack growth under EAC conditions (Paper no. 04573), in 'Corrosion 2004', NACE International.
- Vankeerberghen, M., Gavrilov, S. and Nelissen, G. (2001), 'Finite element calculation of the polarisation behaviour of a metal in an aqueous solution using the dilute solution model', *Corrosion Science* **43**, 37–51.
- Viyanit, E. and Boellinghaus, T. (2007), Numerical modelling of hydrogen-assisted cracking, in S. Shipilov, R. Jones, J. Olive and R. Rebak, eds, 'Environment-Induced Cracking of Materials: Chemistry, Mechanics and Mechanisms', Vol. 1, Elsevier, Oxford.

- Wang, M., Akiyama, E. and Tsuzaki, K. (2006), 'Determination of the critical hydrogen concentration for delayed fracture of high strength steel by constant load test and numerical calculation', *Corrosion science* **48**(8), 2189–2202.
- Wanhill, R., Barter, S., Lynch, S. and Gerrard, D. (2011), Prevention of hydrogen embrittlement in high strength steels, with emphasis on reconditioned aircraft components (Chap. 20 of RTO-AG-AVT-140), Technical report, NATO Science and Technology Organization.
- Williams, D. P., Rao, P. S. and Wei, R. P. (1977), 'The combined influence of chemical, metallurgical and mechanical factors in scc'.
- Wintle, J. and Pargeter, R. (2005), 'Technical failure investigation of welded structures (or how to get the most out of failures)', *Engineering Failure Analysis* **12**(6), 1027 – 1037.
- Woodtli, J. and Kieselbach, R. (2000), 'Damage due to hydrogen embrittlement and stress corrosion cracking', *Engineering Failure Analysis* **7**, 427–450.
- Wu, F. W., Ibrahim, R. N., Das, R. and R.K. Singh Raman (2009), 'Fracture toughness for CNT specimens from numerically obtained critical CTOD values', *Theoretical and Applied Fracture Mechanics* **52**, 50–54.
- Yokobori, A., Nemoto, T., Satoh, K., Yamada, T. et al. (1996), 'Numerical analysis on hydrogen diffusion and concentration in solid with emission around the crack tip', *Engineering fracture mechanics* **55**(1), 47–60.
- Young, G. A., Wilkening, W. W., Morton, D. S., Richey, E. and Lewis, N. (2005), The mechanism and modeling of intergranular stress corrosion cracking of nickel-chromium-iron alloys exposed to high purity water, in T. Allen, P. King and L. Nelson, eds, 'Proceedings of the 12th International Conference on Environmental Degradation of Materials in Nuclear Power System- Water Reactors', TMS (The Minerals, Metals & Materials Society), pp. 913–924.

Publications by candidate

1. Raykar N. R., Maiti S.K., Raman Singh R. K. (2011), 'Modelling of mode-I stable crack growth under hydrogen assisted stress corrosion cracking', *Engineering Fracture Mechanics*, **78**(18), 3153-3165.
2. Raykar N. R., Raman Singh R. K., Maiti S.K., Choudhary Lokesh (2012), 'Investigation of hydrogen assisted cracking of a high strength steel using circumferentially notched tensile test', *Material Science and Engineering A*, **547**, 86-92.
3. Raykar N. R., Maiti S.K., Raman Singh R. K. (2012), Influence of hydrostatic stress distribution on the modelling of hydrogen assisted stress corrosion crack growth, in 'Proceedings of 10th World Congress on Computational Mechanics (WCCM2012 CD-ROM), Sao Paulo, Brazil'.
4. Raykar N. R., Maiti S.K., Raman Singh R. K., Aryan Saurav (2013), 'Study of hydrogen concentration dependent growth of external annular crack in round tensile specimen using cohesive zone model', *Engineering Fracture Mechanics*, **106**, 49-66.

Acknowledgements

I am deeply indebted to my mentors, Prof. S. K. Maiti and Prof. Raman Singh, for their valuable guidance, inspiration and encouragement throughout the course of my work. The high standards of academic discipline, professional values and passion for research exemplified by them would ever keep me driving to better myself.

I am grateful to my research progress committee members, Prof R. Ibrahim and Prof D. N. Pawaskar, for their critical assessment and thoughtful inputs at various stages of my work.

My sincere thanks to Mr. Hughes Venables and his workshop team for their excellent manufacturing support at Monash university.

I am highly thankful to my colleagues and friends (Dr.) Lokesh Choudhary and (Dr.) Mahesh Venkataraman for acquainting me with the Australian culture. I acknowledge the efforts taken by Lokesh while supporting me in the use of experimental facilities and scanning electron microscope. I would like to thank Mr. Saurav Aryan for his contribution towards development of the analytical solution for cylindrical geometry.

My research journey has been made memorable by the bubbling enthusiasm and wonderful personality of my colleague and friend Mr. Nelson Muthu. Thank you Nelson for the numerous stimulating discussions and for the sharing of spiritual wisdom.

My special thanks to my friends Mr. Bharat Padekar, Mr. Shardatva Pan, Mr. Dattatray Jadhav, Mr. Vivek Chavan, and laboratory group members at Monash university and IITB for their enthusiasm, cheerful company and help.

I am glad to acknowledge the excellent coordination and support offered by Mr. Adrian Gertler, Monash university, in dealing with academic and personal matters. I sincerely appreciate the warm and generous administrative support provided by Ms. Anasuya Banerji, Ms. Mamta Bhattacharyya, Ms. Kuheli Banerji, Mr. Rahul Krishna and staff members of IITB-Monash Research Academy.

Finally I would like to thank my parents Mr. Ramkrishna Raykar and Mrs. Pushpalata Raykar, wife Kavita and son Tejas for their patient understanding and loving support which immensely helped me to focus on my research.

September 2013


Nilesh R. Raykar